ISSN 0915-6348

NATIONAL INSTITUTE FOR FUSION SCIENCE

JSPS-CAS Core University Program Seminar
Proceedings of Japan-China Joint Seminar on Atomic and Molecular Processes in Plamsa
Oct. 8 - 12, 2007, Dunhuang, China

(Eds.) F. Koike and C. Dong

(Received - Feb. 21, 2008)

NIFS-PROC-73

Mar. 2008

RESEARCH REPORT
NIFS-PROC Series

TOKI, JAPAN

JSPS-CAS Core University Program Seminar

Proceedings of Japan-China Joint Seminar on Atomic and Molecular Processes in Plasma

October 8 – 12, 2007, Dunhuang, China

Edited by

Fumihiro Koike and Chenzhong Dong

Abstract

As one of the activities of JSPS-CAS Core University Program, Japan-China Joint Seminar on Atomic and Molecular Processes in Plasma was held on October 8 - 12, 2007 in Dunhuang, China. The total number of the officially registered participants was 41, in which 12 from Japan, 25 from China, and 4 from EU. And this seminar is an extension of the last seminar that was held on March 6 – 11, 2004 in Lanzhou, China.

In the nuclear fusion plasma, there are quite a variety of atomic processes such as ionization, excitation, radiative recombination, non-radiative recombination (di-electronic recombination, collisional electron transfer), cascade radiation, and cascade Auger decay over the wide range of plasma temperature. The knowledge of such processes is indispensable for the evaluation and improvement of the plasma properties, which is desirable to be investigated by international collaboration groups. The present seminar constitutes one of such activities to realize the above stated aim; especially it has given an opportunity for the collaborative workers to illustrate their achievements.

Key words:
atomic processes, plasma spectroscopy, excitation, ionization, recombination, charge transfer, X-ray, polarization spectroscopy, atomic database, tokamak, divertor, LHD, molecular processes, atomic structures, radiative recombination, di-electronic recombination

Preface

As one of the activities of the Core University Program (CUP) entitled "atomic and molecular processes in plasma", a seminar "China-Japan Joint Seminar on Atomic and Molecular Processes in Plasma" was held from the 8'th to 12'th October 2007 at Silkroad Dunhuang Hotel, Dunhuang, China. This is the seminar that was organized under the CUP agreement between Chinese Academy of Science (CAS) and Japan Society for the Promotion of Science (JSPS), which was initiated in 2000 and will last 10 years. And, further, this seminar is an extension of the last seminar that was held from the 6'th to 11'th March 2004 in Northwest Normal University, Lanzhou, China.

Since the last seminar in 2004, the researchers from both Japan and China carried out a number of significant studies in atomic and molecular processes in relation to the fusion plasma. The proposal of the present joint seminar has placed its intention not only on the presentations of the collaborative studies, but also on offering an opportunity for the wide range of researchers from both countries to be acquainted with each other, who would have made an extensive exchange of information about the recent progress of the research activities, and also would have made an extensive discussion about the plan of the future collaborations.

In the present seminar, the total number of 26 oral talks was presented by experts from Japan, China and EU, and the total number of 11 posters was presented by experts from China. The total number of the audience was about 40. In the opening remarks, firstly, Mr. Yulong Sun, who is the Mayor of Dunhuang City, delivered a warm address of his welcome. He is followed by Professor Limin Wang, President of Northwest Normal University, who presented a warm address. Professor Baonian Wan of Institute of Plasma Physics, Chinese Academy of Sciences, gave a cordial greeting to the seminar as the Coordinator of the Core University Program. Finally, Dr. Fumihiro Koike, gave also a cordial greetings to the seminar and expressed his sincere thanks to the local organizers as a representative of Japanese delegates.

The seminar was in always a friendly and active atmosphere. As of the intermission of the seminar, participants visited the Museum of Dunhuang City and they further enjoyed many kinds of tasty and ethnic foods. On the last day of the seminar, many of the participants visited Mogao Grottoes, Mingsha Mountain, and Crescent Moon Spring in the suburbs of Dunhuang City. During the seminar, the participants exchanged their new research results, discussed about the outlook for new research fields. They tried to promote further developments in mutual collaborations between the countries and the experts. It has given an atmosphere that a subsequent meeting should be desirable to be planned in the near future.

The present issue of the proceedings has collected 23 oral talks and 11 posters that are presented in the seminar. They covers the spectroscopic properties of atoms and ions in the plasma, the collisions of electrons or ions with atoms or ions in the plasma, the analysis and diagnostics of the confinement fusion plasma, the atomic data compilations and the database constructions, the molecular processes in the confinement fusion plasma, and, further, topics from wide area of atomic physics related to plasma. The present issue also includes the scientific program of the seminar, the group photo as well as the list of participants.

On behalf of the organizing committee, we would like to express our sincerest thanks to all the participants who made active contributions not only in the formal presentations but also in the fruitful discussions. We would like to acknowledge everybody who devoted very hard work for preparing the seminar. We also would like to express our special thanks to Professor Shunsuke Ohtani and Professor Baonian Wan; it was beyond our competence to prepare a nice seminar without their help. We also would like to express here our sincere thanks to Professor Mineo Kimura, who, regrettably, passed away on the 2'nd February 2008. As a member of the organizing committee, he has made a great effort to realize the present seminar and he has shown an excellent leadership by chairing a session and giving a nice talk at the seminar.

Finally, we would like to acknowledge the administrative as well as the financial supports from Northwest Normal University, Gansu Province, Dunhuang City, and the National Institute for Fusion Science.

Chenzhong Dong
Local Chairperson,
Northwest Normal University, Lanzhou, China

Fumihiro Koike
Organizing Committee,
Kitasato University, Sagamihara, Japan

Contents

Talks

Posters

Seminar Program

Participants List

JSPS-CAS Core University Program Seminar
Japan-China Joint Seminar on Atomic and Molecular Processes in Plasma

Short Wavelength Sources and Atoms and Ions

E. T. Kennedy
National Centre for Plasma Science and Technology and School of Physical Sciences,
Dublin City University, Dublin 9, Ireland

Abstract

The interaction of ionizing radiation with atoms and ions is a key fundamental process. Experimental progress has depended in particular on the development of short wavelength light sources. Laser-plasma and synchrotron sources have been exploited for several decades and most recently the development of short wavelength Free Electron Laser (FEL) sources is revolutionizing the field. This paper introduces laser plasma and synchrotron sources through examples of their use in studies of the interaction of ionizing radiation with atoms and ions, ranging from few-electron atomic and ionic systems to the many-electron high atomic number actinides. The new FEL source (FLASH) at DESY is introduced.

Keywords: vacuum ultraviolet, extreme ultraviolet, laser plasma, absorption spectra, photoionization, atoms, ions, free electron laser.

1. Introduction:

Experiments on the interaction of ionizing photons with atoms and ions improve our basic understanding of fundamental photoionisation processes and provide data essential for modelling of laboratory, fusion and astrophysical plasmas. Progress is enabled by advances in atom/ion beams and detectors for the resulting ions, electrons or photons but most critically by the development of improved light sources. In this paper we describe some examples of experiments on atoms and ions carried out with table-top laser-plasma and large-scale facility synchrotron light sources. The paper concludes with a brief description of the new short wavelength Free Electron Laser (FLASH) developed at Hamburg in Germany, which is ushering in a new era in the study of the interaction of ionizing photons with matter. First results are described in the accompanying paper by John Costello.

2. Synchrotron light sources

Accelerator-based light sources have developed over the last forty years or so, through distinctive generations. The potential of storage rings as short wavelength light sources for the study of photon-atom interactions was demonstrated in the sixties through the pioneering work of Madden and Codling (1963), when they observed the striking and unanticipated strong and weak asymmetric resonance series associated with the simultaneous excitation of both 1s electrons of helium. The interpretation of the spectra required consideration of the *correlated motions* of the two electrons and the introduction of new correlation quantum numbers by Cooper, Fano and Prats (1963). These impressive results stimulated the atomic and molecular physics communities world-wide and investigations of other atomic species soon followed. This early work relied on parasitic use of storage rings which had been designed and built for particle physics investigations; often termed first generation synchrotron light sources. Second generation machines specifically designed as light sources soon followed and introduced multiple beam-lines to cater for rapidly growing user communities quickly realizing the potential for a wide range of science investigations.

The introduction of straight, periodic, permanent magnetic structures (known as undulators or wigglers) which force the electrons to rapidly oscillate sideways and more efficiently emit light, led to the third generation phase of development. The systematic introduction of undulators together with improvements in the quality of the circulating electron bunches, at facilities such as ALS, APS, BESSY II, Elettra, ESRF, Max II, Spring 8, has provided orders of magnitude improvement in performance compared with the earlier second generation facilities (Bilderback *et al* 2005).

3. Laser Plasma light sources and the Dual Laser Plasma technique

For low-to-medium atomic number targets the spectral emission of laser-produced plasmas mainly consists of discrete lines. If however, a high atomic number target, such as tungsten or a rare-earth target, is used then a clean relatively uniform continuum is emitted throughout the VUV and EUV spectral regions (Carroll, O'Sullivan and Kennedy 1978, 1980). When a laser plasma continuum source is used as a back-lighter to a second laser generated plasma (which creates the absorbing atomic or ionic species of interest), the combination provides a flexible table-top approach to the study of inner-shell and multiple electron excitations in atoms and ions. The technique, termed the Dual Laser Plasma (DLP) photoabsorption technique, has been used to investigate short wavelength photon interactions with a wide range of atoms and ions. The method is versatile as solid targets are used and trends along isoelectronic and isonuclear sequences can be explored. In its earliest formulations the DLP technique used photographic detection (Carroll and Kennedy 1977, Carroll and Costello 1986). Photoelectric detection was introduced by the Padova group of Tondello and co-workers (Jannitti et al1984).

The DLP results briefly reviewed here, were obtained with the facility developed at Dublin City University, (Kennedy et al. 1994). The output of a pulsed Nd:YAG laser (~1J in < 10 ns) is focused tightly onto a tungsten surface *in vacuo* to generate the back-lighting plasma source of continuum radiation. A second laser, fired earlier, produces the absorbing plasma on the optical axis between the back-lighting plasma and the entrance slit of a spectrometer. By appropriate choices of target material, position of the absorbing plasma with respect to the optical axis, laser irradiation conditions and inter-plasma time delay the absorbing plasma conditions can be optimized for the atom or ion of interest. The continuum output from the back-lighting plasma is coupled, via a toroidal mirror, into the 10-μm entrance slit of a McPherson 2.2m grazing incidence spectrometer equipped with a multi-channel detector. By firing the back-lighting laser alone the background continuum spectrum (I_O) is obtained. By firing both lasers together the transmitted intensity (I) is recorded.

4. Some examples of the interaction of short wavelength photons with atoms and ions

4.1 Single photon - few electron atom/ion interactions

Since the sixties, there has been a continued interest in the interaction of ionizing radiation with two-electron helium atoms, particularly in the photon energy regimes leading to the formation of doubly excited states or to double ionization. More recently these interests have extended to few-electron ionized systems and triply excited states.

Singly-excited and doubly-excited states of Li$^+$. Mosnier et al (2000) exploited the DLP technique to carry out the first systematic experimental study of the relative photoionization cross-section of Li$^+$ in its ground state over the photon energy range (60 to 190 eV) extending from the discrete region up to two-and-a-half times the ionisation threshold energy. The figure alongside shows the experimental relative cross-section spectrum. The cross section shows the first *doubly excited state* at 150 eV, which is seen to make an almost negligible contribution to the total cross-section due to its very low oscillator strength. Absolute cross section measurements have been recently achieved for Li$^+$ at the ALS synchrotron facility through the range of doubly excited states (Scully et al 2006).

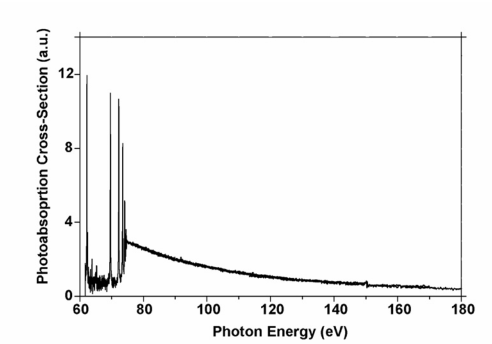

Photon-Induced Triply Excited States in Lithium: Neutral lithium makes possible the formation of *triply excited states* in which all three electrons are excited leaving the K shell unoccupied. Such triply excited states have been termed hollow atom states and lithium is a model system for the study of electron correlation in a three-electron atom (the Coulombic four-body problem). Studies of hollow lithium received a major stimulus from the first DLP photogeneration experiment (Kiernan et al 1994), which provided sufficient sensitivity and resolution to observe the profile of the lowest lying triply-excited resonance. To produce a sufficiently absorbing atomic lithium column it was necessary to use a long-pulse-duration (~1μs) dye laser to produce a high density of neutrals in a 22-mm-long line focus. The resulting lowest lying triply excited $1s^22s^2S \rightarrow 2s^22p\ ^2P$ resonance was observed at 142.3 eV (Kiernan et al 1994).

The successful observation of the triply excited state $2s^2 2p$ stimulated subsequent synchrotron-based investigations. Photoion spectrometry experiments at the HASYLAB (Kiernan et al 1995) and Photon Factory (Azuma et al 1995) synchrotrons had greater spectral resolution and sensitivity and discovered many new hollow atom resonances at higher photon energies. Photoelectron spectrometry at the ALS (Diehl *et al*1996), allowed very weak resonances such as the $2p^3$ state to be investigated in detail. Doubly hollow states (both K and L shells empty) have been observed (Diehl et al 1997a and Azuma et al 1997). Angular resolved measurements have been made on both the $2s^2 2p$ (Diehl et al 2000a) and $2p^3$ (Diehl et al 2000b) resonances. Extended Rydberg series have also been detected (Diehl et al 1997b). For further details and more complete sets of references on the study of triply excited states in lithium see the reviews (Wuilleumier et al 1998, Wuilleumier 2000, Kennedy 2001 and Madsen 2003)

4.2 The neon isoelectronic sequence: The strange case of Si^{4+}

The neon isoelectronic sequence: The importance of photoabsorption data for ions of the neon sequence,for astrophysical modelling was emphasized as part of the Opacity Project by Hibbert and Scott (1994). The near threshold cross section behaviour for the early members of the neon sequence has been examined theoretically and experimentally and the results indicate the importance of including fully the role of inner-shell resonances (Chakraborty et al 1999). The calculations were performed, using the Relativistic Random Phase Approximation plus multi-channel quantum defect theory. The results of the calculations for the cross section at the $2s^2 2p^5$ $^2P_{1/2}$ threshold are shown in the adjoining figure (solid points) for the first few sequence members. The smooth evolution of the cross section along the sequence is broken by the Si^{4+} results, which are smaller by more than an order of magnitude. Fig. 3 (continuous line) shows the calculated results with the coupling between 2s and 2p channels omitted, and a marked difference from the full RRPA result is seen. Without the coupling, the omission of which essentially excludes the inner shell excitations, the threshold 2p cross section for Si^{4+} falls into the smooth pattern of the neighboring members of the isoelectronic sequence. It is the presence of the inner-shell resonance in the vicinity of the threshold that causes the disruption in the series.

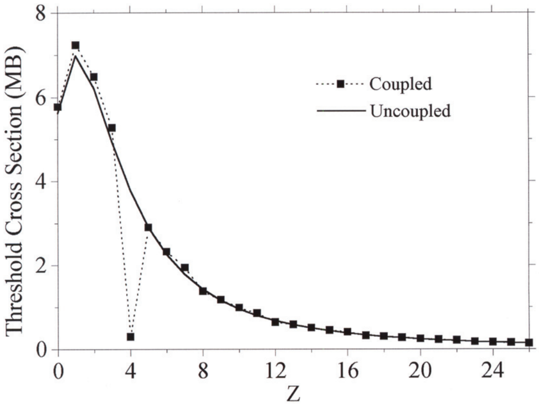

The movement of the inner shell resonance to the vicinity of the threshold region was confirmed by the DLP experiments which were carried out for the sequence members Na^+ through Si^{4+}. For the ions Na^+ to Al^{3+} the valence transitions (2p→ns, nd) were observed to run to the series limits in the normal way, with a smooth continuation in the cross section across the limits. For Si^{4+} the behaviour was strikingly different. The near-threshold cross section is now dominated by the inner-shell 2s→3p resonance which has moved down to 165.4 eV, just below the photoionization limits $^2P_{3/2}$ and $^2P_{1/2}$, which lie at 166.7 and 167.2 eV, respectively. This example shows that experiments are important to benchmark theoretical calculations for ion sequences and that simple theoretical interpolation may be unreliable.

4.3 4p excitations in Mo^+

High temperature furnaces to obtain significant vapour pressures for transition row elements are subject to chemical attack. In consequence only one 4p-subshell spectrum of an element of the 4d transition row, that of Y I (Z = 39) has been recorded using such a method. The dual laser plasma technique has been applied to molybdenum and provided, for the first time, photoabsorption results arising from excitation of the 4p-subshell of Mo^+ ions (Mansfield et al 2003). The figure below reproduces the overall absorption spectrum between 200 000 cm^{-1} (26 eV) and 500 000 cm^{-1} (62 eV) recorded at an optimized inter-plasma time delay of 350 ns. The spectrum can be interpreted as a 4p → 4d giant resonance on which extensive discrete structure is superposed. The discrete lines are ordered into six Rydberg series converging on the three limits $4p^5(4d^5\ ^6S)^7P_{4,3,2}$. The relative simplicity of the observed Mo$^+$ spectrum can be attributed to the stable nature of the $4d^5$ half-filled subshell ground state. The five 4d electrons couple with their spins parallel in the ground state and retain this alignment when the 4p subshell is excited.

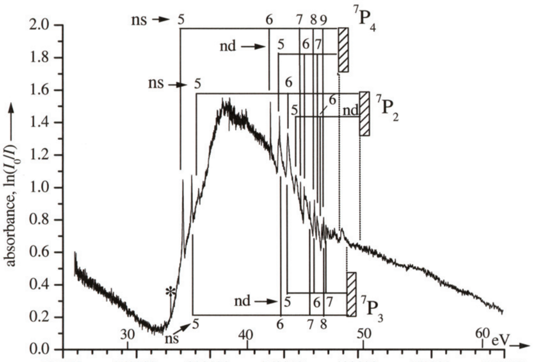

The Mo$^+$ spectrum provides a nice example of a Rydberg series straddling a giant resonance. The asymmetric profiles of the discrete lines arise from the interaction with the giant resonance and the reversal of the sign of q (the Fano profile index) as the series passes through the giant resonance is as predicted by Connerade and Lane (1987).

4.4 Evolution of giant 4d resonances in the lanthanides

The DLP technique has been used (Köble et al 1995) to compare the 4d excitation behaviour of Ba^{2+} with its isoelectronic partner La^{3+}. The results confirm that the collapse of the 4f ^1P orbital along the xenon sequence has a gradual nature. Calculations based on configuration interaction and many body perturbation techniques show that the giant dipole resonance in La^{3+} associated with the 4d subshell excitation has acquired a definite discrete $4d^{10} \rightarrow 4d^94f(^1P)$ character at the expense of the $4d^{10} \longrightarrow 4d^9\epsilon f$ continuum transitions. Most noticeable for La^{3+} is the strong resonance at the photon energy 118-9 eV and the further reduction in the continuum absorption background, when compared to Ba^{2+} (see the figure on the left).

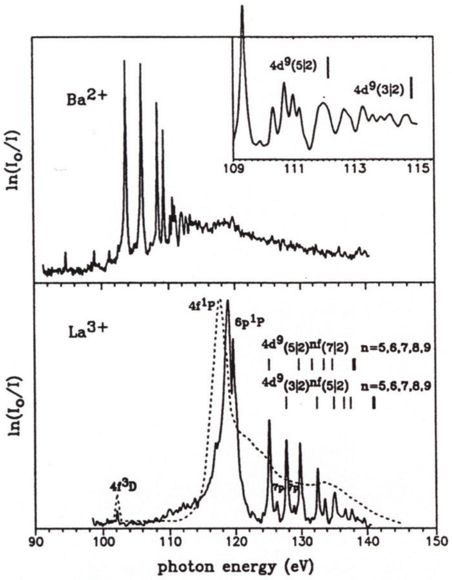

The corresponding photoabsorption cross section for solid LaF$_3$ (Olsen and Lynch 1982) is indicated by the dashed line. Both the free La^{3+} and the solid LaF$_3$ spectra show the dominant $4d^94f(^1P)$ resonance and the weak $4f(^3D)$ line at about 102 eV. The shoulder at 118.8 eV in the solid state spectrum corresponds to the $4d^9_{(3/2)}6p_{(1/2)}$ state in La^{3+}. The main $4f(^1P)$ resonance of La^{3+} in its solid state is influenced albeit moderately by the environment, which causes the resonance to be broadened and shifted by about 1.3 eV toward lower energy. The effects of the 4d excitations into higher levels are also recognizable in the solid state spectrum but the disappearance of the pronounced line structure indicates their non-localized character.

4.5 Photoabsorption of the actinide U: DLP - Synchrotron comparison

An understanding of the actinides is of fundamental interest. 5*f* electrons in the actinides experience a double-well potential (in a similar way to the 4f electrons in the lanthanides) but do not become as localized due to the additional node in the 5*f* wave function. Many of the physical properties peculiar to the actinides can be attributed to this fact (Haire 1995).

DLP experiments were performed for uranium in the normal incidence (15 –40 eV) and the grazing incidence (30 – 150 eV) regions, covering the 6p and 5d excitation spectral ranges, respectively (see van Kampen et al 2000 for a detailed description). To interpret the experimental spectra, calculations were carried out using the Cowan code and the results compared favourably with the experimental data. The 6p excitations are separated into two groups of resonances, about 9 eV apart, attributable to the spin-orbit splitting of the 6p core hole. The resonances around 21.5 eV can be ascribed to $6p_{3/2} \rightarrow 6d$ transitions; the second group, around 30 eV, is due to $6p_{1/2} \rightarrow 6d$ transitions. Both peaks are the result of many unresolved transitions between electrostatically split terms. In contrast to the 6p case, two overlapping peaks at 97.5 and 110 eV in the 5d region are not exclusively due to spin-orbit splitting and must be discussed within an intermediate coupling scheme. The calculations reveal that the 5d-5f electrostatic and spin-orbit terms are of comparable importance.

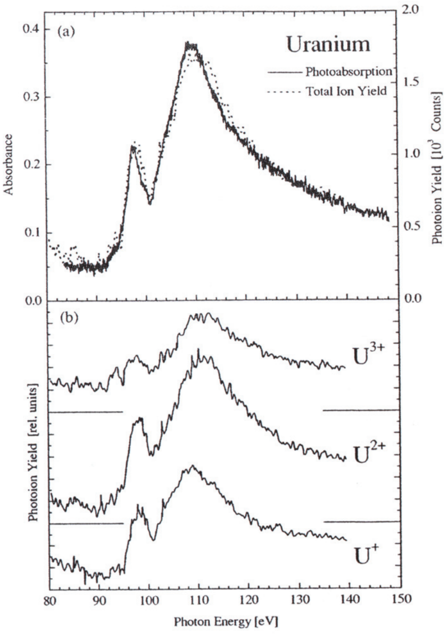

Complementary photoion data for the 80-140 eV region was obtained using synchrotron radiation from the electron storage ring at BESSY I (See the adjoining figure). The uranium metal was heated in a molybdenum crucible producing an atomic number density in the interaction region ≈ 10^{11} cm^{-3}. The photoion experiments provided individual yields for U^{+}, U^{2+} and U^{3+} ions over the 5d excitation regime. No U^{4+} ions were detected. The figure shows the individual yields and a comparison of the summed photoion yield and the DLP photoabsorption data. The latter agree very well and provide a mutual check on the reliability of the experimental results.

4.6 Photoabsorption from excited states: The role of metastables

Many atoms and ions have low-lying excited states, some of which may be metastable, and these states can enable the study of photoabsorption from excited states (Kennedy and Carroll 1977). The presence of substantial populations of excited states is generally undesirable however as they make it difficult to deduce the individual relative cross sections. Comparisons with theory require superposition of calculated cross sections for the different possible contributing levels, weighted according to the distribution of populations.

3p excitations in singly and doubly ionized chromium: Members of the iron group of the transition elements play important roles in astrophysics, in addition to having useful magnetic properties and forming the basis for many solid-state laser materials.

The spectrum of singly ionized chromium was first studied by Costello et al (1991) using the DLP technique, in the photon energy range 35-70 eV. Subsequently, Dolmatov used the spin-polarised RPAE(SPRPAE) technique to compute the Cr^{+} photoionisation cross section (Dolmatov 1996). Good agreement was found with the experimental data at low photon energies, where 3p→4s transitions and the onset of the 3p→3d giant resonance dominate, but serious disagreement at photon energies was evident and later confirmed by R-matrix calculations of Donnelly el al (1997).

To understand the discrepancies a new series of DLP experiments was carried out and supplemented by calculations aimed at assessing possible contributions to the measured absorption by excited states within the plasma. The nearest metastable state to the ground state of Cr^{+}, the $3d^4(^5D)4s\ ^6D$ multiplet, lies only 1.5 eV above the $3d^5\ ^6S$ ground state. Contributions to the observed spectrum due to photoabsorption from these levels may therefore be expected. The later DLP experiments on both Cr^{+} and Cr^{2+} ions confirmed that excited states play an important role in determining the observed spectra. Further details on the experiments and the extensive series of supporting calculations are provided in the original publications (McGuinness et al 1999, 2000).
The role of metastables is also important in synchrotron-based photoion experiments.
For an overview of developments in photoionization of ions see the reviews by West (2001) and Kennedy et al (2004)

5. Free Electron Laser developments: The FLASH User facility at DESY Hamburg

The concept of using highly relativistic electrons traversing magnetic undulators to generate short wavelength photons is exemplified in the most recent *4^{th} generation* of accelerator light source development. Single-pass Free Electron Lasers (FELs) based on the principle of Self Amplified Spontaneous Emission (SASE) provide uniquely intense, polarised, short pulse (<~100fs) and tunable coherent radiation at short wavelengths. A unique user facility termed FLASH (**F**ree Electron **Las**er at **H**amburg) based on this concept has recently become operational.

In a SASE FEL lasing occurs as an electron bunch passes through a long (~30m) ultra-precise magnetic undulator. The forward emitted electromagnetic radiation interacts with the electron bunch leading to a density modulation (micro-bunching - with a spacing equal to the wavelength) which enhances the power and coherence of the radiation emitted by the bunch. *This process of self-amplification leads to exponential growth of the radiation field and to saturated laser-quality output.* The fundamental emission wavelength is given by $\lambda = \lambda_u(1+K^2/2)/2\gamma^2$ where λ_u is the period length of the undulator (2.7 cm at FLASH), $\gamma = E/mc^2$ is the relativistic factor of the electrons and the undulator parameter $K = eB_0\lambda_u /2\pi mc$ where B_o is the peak magnetic field in the undulator. Because λ_u is of the order of cms and γ is of the order of 2000 for a 1Gev accelerator, the FEL emission wavelength λ_n is extremely short. The wavelength can be tuned by varying the energy of the electrons from the accelerator.

The very short emission wavelength may be simply understood as follows. An electron traverses the length of the undulator in a time $t = N\lambda_u /v$. The N wavelengths, of the associated electromagnetic wave, are therefore squeezed into a length ~ (c-v).t and the wavelength determined by $\lambda \sim (c-v).\ \lambda_u /v$. The ultra-relativistic nature of the electron bunch implies v >> (c-v) and the emitted wavelength can therefore be very short. It can be expressed in terms of the Lorentz γ factor as $\lambda = \lambda_u/2\gamma^2$. When the curved path of the electron trajectory is taken into account a corrective factor $(1+K^2/2)$ depending on the magnetic field results. Furthermore the FEL can emit harmonics (λ_n) of the fundamental wavelength.

The monochromatized output of the FEL is essentially a resonance phenomenon. In each period of the undulator the oscillating relativistic electron slips behind with respect to its emitted light by λ so that the waves emitted by an individual electron, as a result of each sideways oscillation, add coherently. The induced micro-bunching builds up the coherence between the electromagnetic waves emitted by different electrons in the bunch. The combination of the two effects leads to the unique and unprecedented nature of the final output beam brilliance.

DESY achieved a decisive milestone in February 2000 when the first coherent output was observed and by 2001 the FEL had produced the first saturated output and achieved GW pulses in the femto-second regime (Ayvazyan *et al*). The first scientific results obtained with the DESY Phase 1 FEL were reported by Wabnitz *et al* (2002) and involved the interaction of the VUV photons (at ~ 90nm) with xenon atoms and clusters. The behaviour was strikingly different to that which occurs with intense optical laser light.

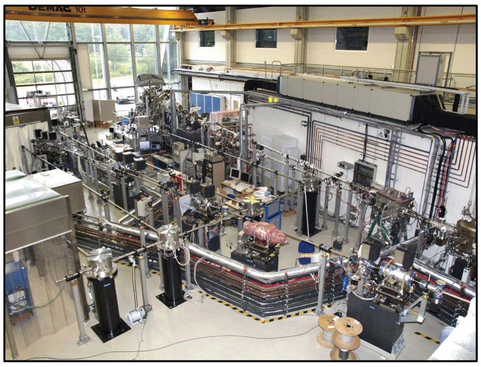

The success of the Phase 1 facility led to a Phase 2 (1 GeV) FEL development aimed at providing wavelengths extending down to 6 nm. This unique user facility, renamed as **FLASH** (**F**ree Electron **Las**er at **H**amburg), has enabled, during 2005, 2006 and 2007, laser operation at several wavelengths extending from 32 nm to as low as 7nm. Beam parameters of FLASH include virtually full transverse coherence, pulse duration < 100 fsec and ~ 10^{13} photons per pulse, making it a revolutionary new source. Several beamlines are being exploited by user groups addressing scientific areas including physics, chemistry, biology, plasma and materials science.

The figure above (Courtesy of DESY) shows the FLASH experimental hall. The FEL radiation is diverted to different beamlines by use of grazing incidence mirrors. The hall also includes a laser hutch which houses a time-synchronized femtosecond optical laser facility, providing an important added dimension by enabling pump-probe techniques (Meyer *et al* 2006). The FEL's performance is described in Ackermann *et al* (2006) where wavelengths reached include the water window region through the FEL harmonic emission.

The revolutionary nature of these sources is illustrated in the figure below (taken from Ackermann *et al* (2006)), which shows the peak brilliance of FLASH at three different wavelengths compared to existing synchrotron facilities and also indicates the anticipated performance of Stanford (LCLS) and DESY (European XFEL) FELs aimed at operation down to x-ray wavelengths. The figure shows the fundamental wavelength emission of FLASH and the 3rd and 5th harmonics.

The success of FLASH and the further prospects of SASE FELs extending down to x-ray wavelengths (Feldhaus *et al* 2005) introduce a new era in the study of photon-atom/ion interactions at short wavelengths. The availability of intense tunable laser radiation pulses of very short duration and at ionizing wavelengths is expected to pay rich dividends in terms of science and technology applications and will undoubtedly lead to many new and unforeseen developments in our understanding of fundamental photon-atom/ion interactions.

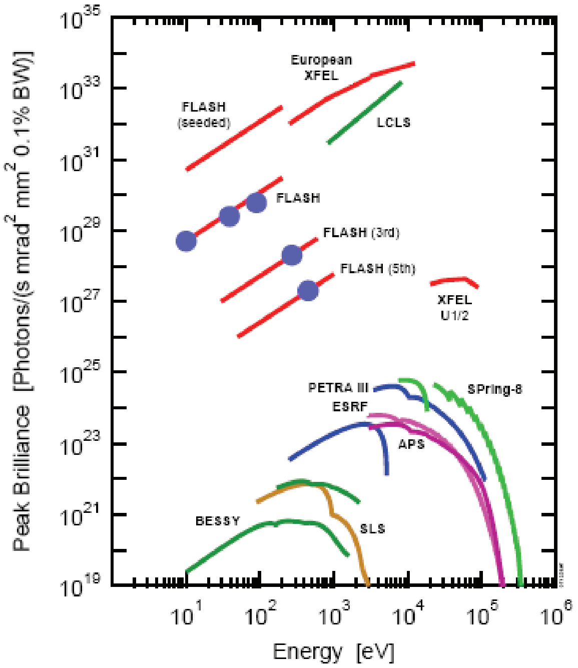

6. Acknowledgements

I would like to express my appreciation to my colleagues who over many years have worked on and developed the dual-laser plasma technique into a very versatile tool for the study of the interaction of short wavelength radiation with atoms and ions. I pay tribute to the support teams at FLASH and to the accelerator and diagnostics groups who are continuing to improve its performance. I acknowledge support of Enterprise Ireland under Project No. SC/2003/0180.

References

Ackermann W *et al*. 2007 *Nature Photonics* **1** (6) 336 - 342
Ayvazyan V *et al* 2002 *Phys Rev Lett* **88** (10) 104802
Ayvazyan V *et al* 2006 *Eur Phys J D* **37** (2) 297 - 303
Azuma Y *et al* 1995 *Phys Rev Lett* **74** 3678
Azuma Y *et a*l 1997 *Phys Rev Lett* **79** 2419 - 2422
Bilderback D H, Elleaume P and Weckert E 2005 *J Phys B* **38** S773 - S797
Carroll P K and Kennedy E T 1977 *Phys Rev Lett* **38** 1068 -1071
Carroll P K and Costello J T 1986 *Phys Rev Lett* **57** 1581 - 1583
Carroll P K, O'Sullivan G and Kennedy E T 1978 *Opt Lett* **2** 72 - 74
Carroll P K, O'Sullivan G and Kennedy E T 1980 *Appl Opt* **19** 1454 - 1462
Connerade J P and Lane A M *J Phys B* **20** L181 - L186
Cooper J W, Fano U and Prats F 1963 *Phys Rev Lett* **10** 518 - 521
Costello J T *et al* 1991 *Phys Rev A* **43** 1441
Chakraborty *et al* 1999 *Phys Rev Lett* **83** 2151 - 2154

Diehl S *et al* 1996 *Phys Rev Lett* **76** 3915 - 3918
Diehl S *et al* 1997a *Phys Rev A* Rapid Comm **56** R1071 - R1074
Diehl S *et al* 1997b *Phys Rev Lett* **79** 1241 - 1244
Diehl S *et al* 2000a *Phys Rev Lett* **84** 1677 - 1680
Diehl S *et al* 2000b *J Phys B* **33** L487 - L494
Dolmatov V K 1996 *J Phys B* **29** L 673 - L676
Donnelly D 1997 *et al J Phys B* **30** L285 - L291
Feldhaus J 2005 *J Phys B* **38** S799 - S819
Haire R G J Alloys Compd **223** 185 - 196
Hibbert A and Scott M P *J Phys B* **27** 1315 -1323
Jannitti E, Nicolosi P and Tondello G 1984 *Opt Commun* **50** 225 - 230
Kennedy E T and Carroll P K 1977 *Phys Lett A* **64** 37 - 38
Kennedy E T *et al* 1994 *Opt Eng* **33** 3964 -3992
Kennedy E T 2001 *Phys Scripta* **T95** 32 - 42
Kennedy E T *et al* 2004 *Rad Phys and Chem* **70** 291 - 321
Kiernan L *et al* 1994 *Phys Rev Lett* **72** 2359 - 2362
Kiernan L *et al* 1995 *J Phys B* **28** L161 - L168
Koble U *et al* 1995 *Phys Rev Lett* **74** 2188
Madden R P and Codling K 1963 *Phys Rev Lett* **10** 516 - 518
Madsen L B 2003 *J Phys B* **36** R223 - R278
Mansfield M *et al* 2003 *J Phys B* **36** 2611 - 2628
McGuinness C *et al* 1999 *J Phys B* **32** L583 - L591
McGuiness C *et al* 2000 *J Phys B* **33** 5077 - 5090
Meyer M *et al* 2006 *Phys Rev A* **74** 01140(R)
Mosnier J-P *et al* 2000 *J Phys B* **33** 5203 - 5214
Olsen C G and Lynch D W *J Opt Soc Amer* **72** 88
Scully SWJ *et al* 2006 *J Phys B* **39** 3957 - 3968
Wabnitz H *et al* 2002 *Nature* **420** (6915) 482 - 485
Van Kampen *et al* 2000 *Phys Rev A* 61 2706 - 2712
West J B 2001 *J Electr Spectr Related Phen* **123** 247 - 256
Wuilleumier F J *et al* 1998 *J Electr Spectr Relat Phen* **41** 88 - 91
Wuilleumier F J 2000 *Phys Essays* **13** 230 - 247

Two Colour Photoionization with the Ultrafast EUV Laser 'FLASH' – Free Electron Laser in Hamburg: Progress Report

John. T. COSTELLO

School of Physical Sciences and National Centre for Plasma Science and Technology (NCPST), Dublin City University, Glasnevin, Dublin 9, Ireland

John.Costello@DCU.IE

Abstract. The Free Electron Laser at Hamburg (FLASH) emits pulses of up to 150 μJ with durations in the 10 – 30 fs range in the Extreme-UV (EUV), 6 – 60 nm, at repetition rates of (currently) 5 – 300 Hz. The system opens up new research pathways in few photon-few electron processes and photoionization processes with ultra-low cross sections and/or ultra-dilute targets. In combination with an ultrafast optical laser synchonised to FLASH, two colour photoionization experiments, where both fields are of comparably high intensity but orders of magnitude different in photon energy, have become possible. We focus here on coherent photoionization processes in intense superposed EUV and optical fields. Apart from fundamental interest it provides a mechanism to measure EUV-Optical field jitter in femtotime.

Keywords: Free Electron Laser, Extreme-UV, Atoms, Photoionization, Coherent Processes.

1. Introduction

Photoionization is the predominant outcome of the interaction of Extreme-UV (EUV) radiation with matter. It has been a rich source of many electron interactions and quantum interferences which go way beyond the simple single particle picture of Einstein so insightfully proferred more than a century ago to explain the photoelectric effect. Experiment and theory have worked hand in glove in recent decades to deliver complete experiments along with a deep understanding of the role of many electron effects in photoionization [1]. In all of these studies, the EUV field has been weak and so each atom or molecule absorbs one, and only one, photon.

The competing field of ionization of atoms and molecules in intense infrared and visible laser fields has revealed many new dynamical processes such as multi-photon, above-threshold and optical-field ionization [2] as well as short wavelength coherent radiation via high order harmonic generation or HOHG [3]. An interesting, but until recently hypothetical, question is: *what happens if the intense driving field is ramped up to high optical frequency – into the EUV ?* Although HOHG can provide coherent EUV radiation of moderate peak intensity, even highly optimised systems are just about at the threshold for driving non-linear physics at short wavelengths [4]. Plasma based lasers have also tried to meet this grand challenge, starting with the first observation of population inversion/ gain in a recombining plasma in the 1970s [5], followed by the first convincing demonstration of a practical collisionally-excited EUV laser at Livermore [6] in the mid 1980s. Despite heroic efforts to improve these systems over the intervening decades by e.g., injection seeding [7], they have not resulted (as yet) in high average power, GW level pulses.

All this has recently changed with development of FLASH, the Free Electron Laser, located in DESY, Hamburg. The EUV output of FLASH possesses unprecedented average and peak intensity and is fully spatially coherent. For the first time, atomistic systems, bathed in intense and coherent ultrahigh frequency electromagnetic fields, can be uniquely studied using photon, photoion and photoelectron spectroscopies. Experiments on dilute samples and/or species with ultralow photoionization cross sections, few photon processes in few electron systems, two colour (EUV + IR/EUV + EUV) pump-probe experiments on a femtosecond (even attosecond) time scale are all made possible with the advent of ultrafast EUV and soon the XFEL [8] and LCLS [9].

FLASH started operation at a fundamental wavelength of 32 nm in mid 2005 [10]. Experiments have been performed on rare gas atoms and simple molecules with single EUV pulses and also with bichromatic fields using a two colour facility [11] which provides 800 nm/120 fs/20 μJ pulses synchronised to the FEL. The objective of this contribution is to provide an update on our two colour photoionization experiments at FLASH performed by a collaboration involving LIXAM-Orsay, NCPST-DCU, IRCEP-QUB and DESY-Hamburg.

This paper is organised as follows. Section 2 comprises only a brief introduction to FLASH as Eugene Kennedy discusses FEL physics and FLASH in detail towards the end of his contribution to these proceedings. Section 3 comprises an introduction to our experimental setup at FLASH. Section 4 contains salient results from our first experiments. A brief perspective is given in Section 5.

2. ***FLASH***: ***F***ree-electron ***LAS***er in ***H***amburg

A vacuum-UV (VUV) free electron laser (FEL), operating at the then record short wavelength of 98 nm was reported by DESY in 2000 [12]. It soon reached GW peak power levels [13] and was used to perform what was ostensibly the first VUV multiphoton experiment on rare gas clusters [14]. FLASH recently achieved world record peak and average coherent power [15] at a wavelength of 13.7 nm while the 5th harmonic (~2.7 nm) reached into the 'water window' (figure 2). FLASH is based on a linear accelerator coupled to a series of long and precisely aligned undulators acting in concert .

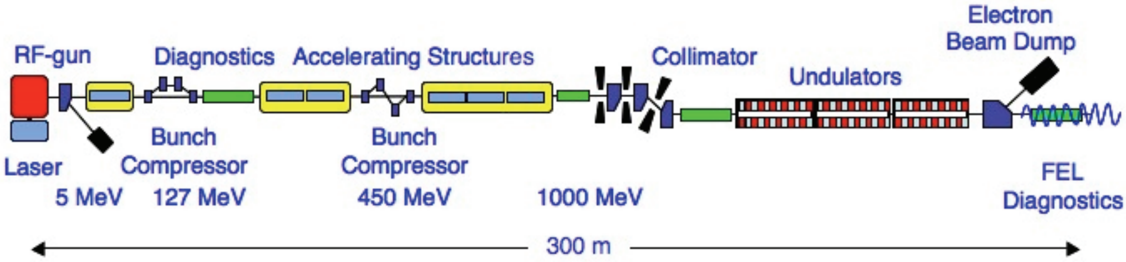

Figure 1. (Colour online). Layout of the EUV FEL 'FLASH' at DESY, Hamburg [10].

Referring to figure 1, ultrashort charge packets (~1nC) are ejected from a photocathode, accerelerated and compressed to produce a bunchtrain of low emittance and low energy spread. Electron bunches are injected into the undulator chain, where they undergo a zig-zag motion and emit synchrotron radiation. Radiation emitted by deflected electrons moves faster than the electron bunches and interacts with electrons further up the beam, accelerating or decelerating them leading to a periodic bunching of the electrons that imposes a density modulation period equal to the undulator fundamental period. The imposition of a well defined spatial periodicity in the emitting bunches results in increasing coherence, collimation and an exponential growth in the intensity of the laser-like radiation field as the bunchtrain travels down the train of undulators. Since the FEL output grows out of spontaneous emission (effectively the photon noise), the process is referred to as *SASE–'Self Amplified Spontaneous Emission'* [16]. For further details on FLASH see the contribution from Eugene Kennedy in these proceedings and also reference [15].

3. Two Colour AMO Experiment at FLASH

The experimental setup has been described in detail recently [11] and so only a brief outline is given here. The femtosecond EUV/Optical laser facility at DESY was built in the frame of a Framework 5, EU-Resarch and Technology Development grant by a collaboration involving Orsay (LIXAM), DCU (NCPST), Lund (LLC), MBI, BESSY and DESY. The optical laser provides 20 μJ/120 fs/800 nm pulses locked to the EUV FEL. The FEL provides trains of pulses (each 10-30 fs, average energy of 50 μJ) at a macro (bunch-train) repetition rate of 5 or 10 Hz with currently up to 30 'micro' pulses in each 'macro' pulse. The optical laser has recently had a new amplifier added to it to boost the pulse energy up to mJ level. The underlying principle of the setup is illustrated in figure 2.

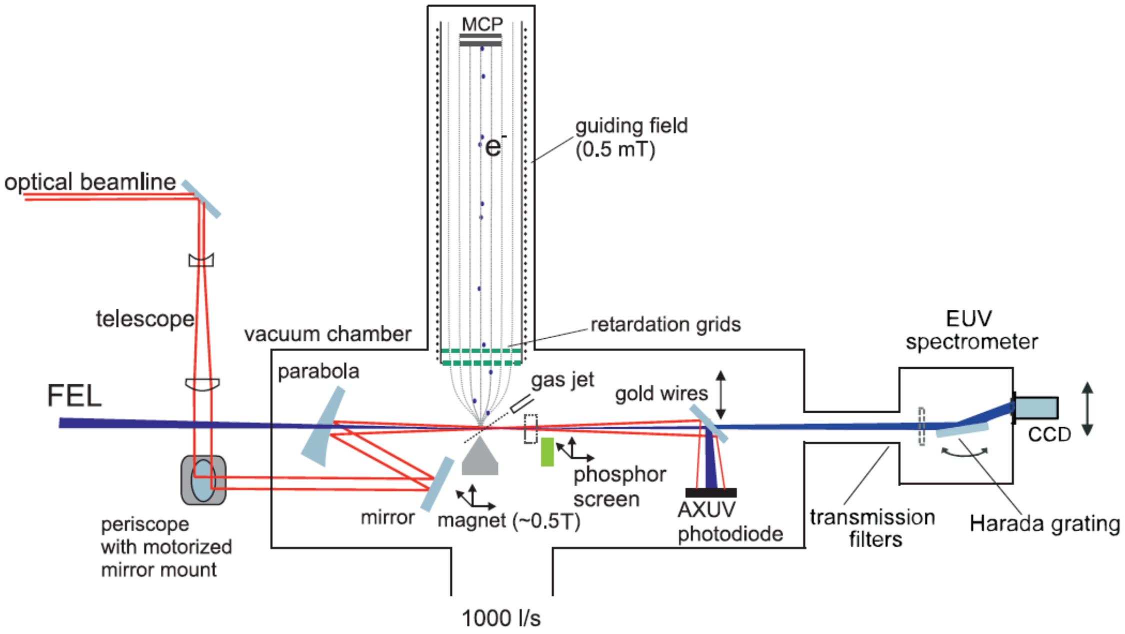

Figure 2. Detailed layout of the EUV FEL 'FLASH' at DESY, Hamburg [11].

The converging EUV beam is transported through a hole in the parabolic mirror used to focus the optical laser. The collinear EUV and 800 nm beams are brought to a focus at the intersection point of a gas jet and a time of flight electron (TOF) spectrometer entrance aperture. The TOF is of the magnetic bottle type which ensures 4π collection efficiency. The output from the TOF is fed to a LeCroy 8600A fast digital oscilloscope. A photoelectron spectrum (PES) trace is obtained and stored for each FLASH shot. FLASH and the 800 nm oscillator are driven off the same radio frequency source and are hence phase locked. The delay between these pulses is adjusted via an optical delay line (increment - 3.3 fs/micron). Obtaining spatial and temporal overlap of the beams is a non-trivial task as the experimental chamber is sited some 70 m from the exit port of the final undulator and 20 m from the optical laser. We use phosphor screens and fast (picosecond) photodiodes are used to obtain rough spatial (< 10 μm) and temporal (20 ps) overlap. We have found the HS3 photodiode from International Radiation Detectors Inc. (80 ps risetime) to offer the best compromise between responsivity at EUV/NIR wavelengths and time resolution while possessing very good radiation hardness. To obtain the absolute time delay we must find the overlap point of the EUV and 800 nm pulses not in picotime, but in femtotime – this will be the main subject of the results section.

As with any undulator based device the FEL emits not just at the fundamental wavelength but also at its harmonics [17]. So our experimental setup has the option of including a flat field spectrometer with back illuminated CCD to monitor the harmonic ratios on a shot to shot basis. When optimized, FLASH emits only odd harmonics at which point the beam is fully plane polarized and so one can perform experiments on aligned atomic and molecular systems. As FLASH is basically a shot noise amplifier, its output fluctuates from shot to shot with respect to spectral distribution, pulse width, peak intensity, beam profile, beam pointing, etc. Hence it is essential to measure all beam parameters for each and every FEL shot so that one can post-correlate measured data with its associated shot. To achieve this objective, DESY have developed an integrated diagnostics package which provides users with these data sets after each measurement campaign.

4. Two colour experiments with FLASH

The atomic, molecular and optics (AMO) community at FLASH is focused on a number of key domains which utilize the unique characteristics on an EUV FEL, high peak intensity, high average intensity and/or short pulse width. Before focusing on our own pathfinder results I should advert to a couple of other important AMO domains at FLASH. A summary of these experiments is given in an upcoming progress report from the 25th ICPEAC Conference which was held in july 2007 [18]. A number of experiments on few photon multiple ionization (FPMI) experiments with the rare gas atoms have been performed. For example Sorokin et al. [19] have performed systematic measurements on the photoion spectra of He and Ne under high irradiance (up to 10^{14} W.cm^{-2}). Using an analysis similar to that done earlier on N_2 ionization [20], these authors were able to derive two photon ionization cross section for Ne, Ne^+ and Ne^{2+}.

Moshammer et al. [21] have measured direct two photon double ionization of Ne in intense EUV fields. For low intensity, the concentration of events around the zero momentum origin led to the conclusion that electrons are ejected into opposite directions (hemispheres) with roughly equal energies in stark contrast to the one photon double ionization case where such a dynamical decay pattern is suppressed for equal energy sharing. A resonant two photon absorption experiment on helium has been performed by a University of Hamburg/DESY collaboration [22]. Föhlisch et al [23] have also recently reported an intriguing EUV field dependence of the valence photoelectron distribution of N_2. Two other recent results demonstrate how FLASH has made possible meaningful measurements on very dilute targets. In [24] Pedersen et al. report fragmentation of a molecular system of astrophysical significance (HeH^+) while in [25] Epp et al. illustrate how FLASH has brought a mature, but key technique, namely resonance laser induced fluorescence (LIF) into the EUV.

Two colour coherent experiments at FLASH

The femtosecond two colour facility at FLASH can be used to perform both pump-probe and laser assisted photoionization (LAP) studies [26]. In this contribution we focus on the latter *coherent* process. In LAP experiments, when the EUV and optical laser fields overlap in space and time, a photoelectron is born into the optical dressing field where it can exchange (i.e., gain or lose) one or more quanta of energy. The resultant photoelectron spectrum displays sidebands adjacent to the main photoelectron line separated by the optical photon energy. Each sideband intensity depends on the EUV photon energy and dressing field strength and so can be used to monitor the relative time delay jitter between overlapping pulses.

Many such experiments have been performed using a single optical laser split into two parts. One part is focused into a rare gas jet to generate a comb of EUV high order (odd) harmonics (HOH), (….H_{2N-1}, H_{2N+1},...) where '2N±1' refers to the (odd) harmonic number. The harmonics are then focused into a second gas jet where they produce a corresponding comb of photoelectron lines separated by twice the optical laser photon energy. The other part of the beam is overlapped in space/time with the EUV harmonics so that photoelectrons sense an intense dressing field with which they can exchange optical photons (hυ). The sidebands so induced are disposed either side of the main photoelectron lines at ±nhυ. In figure 3 a typical LAP spectrum is shown where the vertical axis corresponds to time delay between EUV HOH and optical pulses while the horizontal axis corresponds to the photoelectron kinetic energy [27].

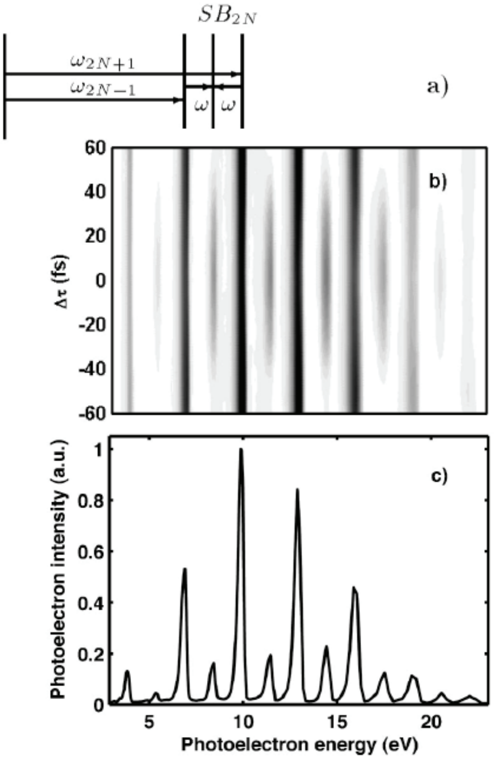

Referring to figure 3, the intense vertical bars correspond to the main photoelectron lines produced under direct ionization by the high order harmonic (HOH) light source ….H_{2N-1}, H_{2N+1},... The weaker interspersed lines are separated by the optical laser photon energy and appear only when the EUV and optical pulses are overlapped (in a window of ± 30 fs determined by the optical pulse duration in this particular experiment). The sideband signal is proportional to the degree of overlap of the EUV and optical fields and is hence a measure of the cross-correlation between them. At very high intensities the sidebands become subject to a strong ponderomtive shift and are even streaked [28]. However, the sidebands are also complicated by interference effects. Imagine that each photoelectron can absorb (or emit) just one optical photon. Then, each sideband results from the superposition of two sidebands - the upper sideband of one main line (say $H_{2N-1} + h\upsilon$) lies at the same photon energy as lower sideband of the next main photoline ($H_{2N+1} - h\upsilon$).

Figure 3. Coherent photoelectron sidebands [27]

However, the measured signal is not simply the sum of the two sideband intensities. As the EUV harmonics are derived from a single driving laser pulse, they are phase coherent (in fact if the phases can be locked with almost zero phase shift, the system approximates a mode locked laser and a train of attosecond pulses results). Hence the free electron waves or main photolines which the HOH produce are phase coherent as are, in turn, the sidebands since they are formed by exchanging quanta with the dressing laser field. So for any single sideband we cannot distinguish between the free electron waves which form it and in addition both these waves are phase coherent – in effect we have a classic two slit experiment and we add the probability amplitudes rather then the free wave intensities. In fact, at sufficient dressing fields intensities, a free electron can exhange 'n' photons with the dressing field and so we have, in effect, a 'n' slit experiment.

Since FLASH could produce high flux at a single photon energy, it presented us with the first opportunity to study this effect in the interference free regime. In our first experiment [29] we operated with a 12 ps, 527 nm pulse so that we did not have to worry about relative jitter between the EUV and optical laser pulses. In a more recent experiment [30] we have been able to carry out a comprehensive study of these sidebands with femtosecond pulses. Theoretical studies by Maquet and Taieb employ either the soft photon approximation or the time dependent Schrodinger equation [31]. They have been very successful and able to accurately predict sideband intensities and dependence on the polarization state of the dressing optical laser field. Importantly, theory shows that sideband intensity depends on not just the laser intensity but also the kinetic energy of the photoelectron.

In figure 4 we show a comparison between theory and experiment for the case of He where the main $1s^{-1}$ photoline was produced by the FLASH operating at a wavelength of 25.5 nm (48.5 eV). The sidebands are observed to straddle this line at ±1.55 eV (800 nm) energy separation as expected. From a fit of the theoretical trace to the experimental spectrum we were able to derive EUV and optical laser intensities independent of direct measurements to be both few 10^{12} W.cm^{-2}.

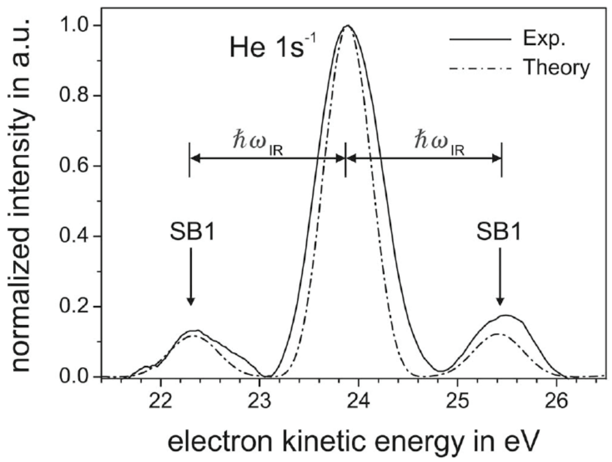

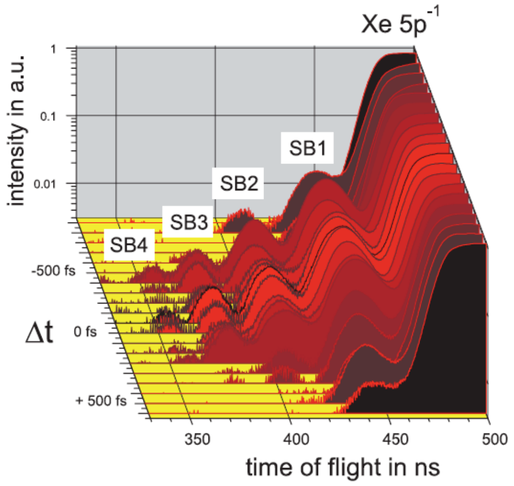

Figure 4. Comparison between measured and computed PE sideband spectra for He [30]

Figure 5. Multiple sidebands formed by 13.7 nm EUV and 800 nm laser fields [11]

In figure 5 we show a photoelectron (PE) spectrum for the case of Xe irradiated by superposed 13.7 nm and 800 nm radiation fields. Sidebands of up to order 4 corresponding to gaining up to four photons from the dressing laser field (800 nm) are observed. By analyzing Xe sideband numbers and intensities and comparing them with theory we have been able to determine the relative delay between the FEL and optical laser. The schematic in figure 6 illustrates the basic principle.

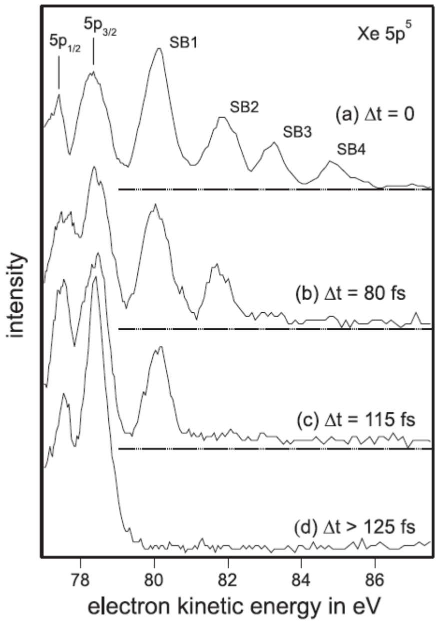

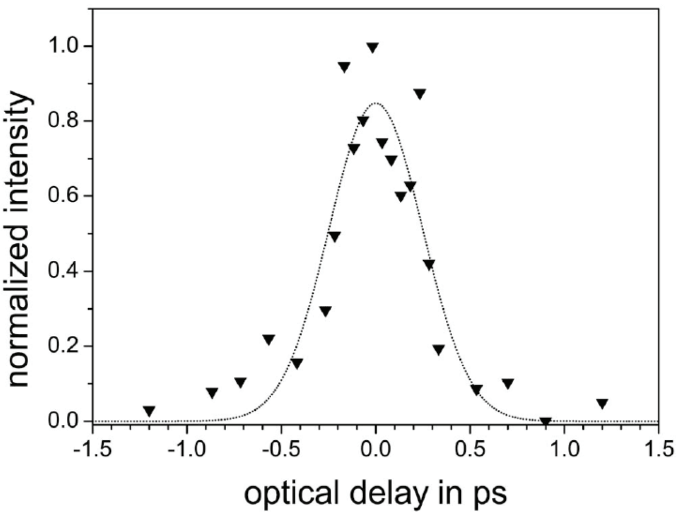

Figure 6. Time delay analysis derived from a study of Xe sidbands [11]

Figure 7. EUV-Optical pulse jitter obtained by recording sideband at various nominal delays [30]

In this figure we show how the number of sidebands generated in the case of Xe for 13.7 nm/ 800 nm irradiation depends on the relative delay between the two pulses. Hence simple sideband counting may be used to measure the relative delay between the pulses. In figure 7 we show the absolute jitter between the EUV and optical laser which is ~500 fs (FWHM). The trace is obtained by sweeping the optical time delay and measuring the average sideband intensity at each delay.

5. Near Future Perspective

In 2008 we will focus on the polarization dependence of the sidebands. Theoretical predictions are available and preliminary data from a recent measurement campaign compare well with them. We will also measure sideband data for a range of atomic and molecular gases so that we can study Z dependent effects (e.g., ionization threshold). We will also carry out further experiments on molecular ionization/fragmentation in intense EUV fields using both pump-probe experiments, for which we have preliminary data, and optical fluorescence techniques.

Acknowledgements

Sincere thanks are due to many collaborators for their contributions to the two colour photoionization experiments, especially Stefan Duesterer, Paul Radcliffe, Mikhail Yurkov, Josef Feldhaus (DESY), Ciaran Lewis (Belfast), Eugene Kennedy (DCU) and members of the DCU team. It is a particular pleasure to pay tribute to Michael Meyer for the lead role he has played in our two-colour collaboration. DCU work is supported by Science Foundation Ireland and the Higher Education Programme for Research in Third Level Institutions. Orsay-DCU work is supported by the Ulysses France-Irl. Exchange programme.

References

[1] Becker U and Shirley D A (Eds) 1996 *VUV and Soft X-ray Photoionization* Plenum Press (NY)
[2] Protopapas M et al. 1997 *Rep. Prog. Phys.* **60** 389
[3] Agostini P and DiMauro L F 2004 *Rep. Prog. Phys.* **67** 813
[4] Hasegawa H et al. 2005 *Phys. Rev. A* **71** 023407
[5] Dixon R H and Elton R C 1977 *Phys. Rev. Lett* **38** 1072
[6] Matthews D L et al. 1985 *Phys. Rev. Lett* **54** 110
[7] Zeitoun Ph. et al. 2004 *Nature* **431** 426
[8] http://xfel.desy.de
[9] http://www-ssrl.slac.stanford.edu/lcls
[10] Ayvazyan et al. 2006 *Eur. Phys. J. D* **37** 297
[11] Radcliffe P et al., 2007 *Nuc. Inst. Meth. Res, A.* (under review)
[12] Andruszkow J et al. 2000 *Phys. Rev. Lett.* **85** 3825
[13] Ayvazyan V et al. 2002 *Phys. Rev. Lett.* **88** 104802
[14] Wabnitz H et al. 2002 *Nature* **420** 482
[15] Ackermann W et al. 2007 *Nature Photonics* **1** 336
[16] Feldhaus J et al. 2005 *J. Phys. B:At. Mol. Opt. Phys* **38** S799
[17] Duesterer S et al. 2006 *Opt. Lett.* **31** 1750
[18] Costello J T, 2008 J. Phys. Conf. Ser. (to appear)
[19] Sorokin A A et al. 2007 *Phys. Rev. A* **75** 033411 051402(R)
[20] Sorokin A A et al. 2006 *J. Phys. B:At. Mol. Opt. Phys* **39** L299
[21] Moshammer R et al. 2007 *Phys. Rev. Lett.* **98** 203001
[22] Nagasona M et al. 2007 *Phys. Rev. A* **75** 051406(R)
[23] Föhlisch A et al, 2007 *Phys. Rev. A* **76** 013411
[24] Pedersen H B et al. 2007 *Phys. Rev. Lett.* **98** 223202
[25] Epp S et al. 2007 *Phys. Rev. Lett.* **98** 183001
[26] Schins J M et al., 1994 *Phys. Rev. Lett.* **73** 2180
[27] O'Keeffe P et al., 2004 *Phys. Rev. A* **69** 051401(R)
[28] Toma E S et al., 2000 *Phys. Rev. A* **62** 061801(R)
[29] Meyer M et al. 2006 *Phys. Rev. A* **74** 011401(R)
[30] Radcliffe P et al. 2007 *Appl. Phys. Lett.* **90** 131108

CHARGE-TRANSFER PROCESSES IN COLLISIONS OF H^+ AND He^{2+} IONS WITH H_2, N_2, O_2, CO, CO_2 AND HYDROCARBON MOLECULES BELOW keV/u ENERGY REGIME

T. Kusakabe[a], and M. Kimura[b]

[a]*Department of Science, Kinki University: Kowakae, Higashi-osaka, Osaka, Japan, 577-8501*
[b]*Graduate School of Sciences, Kyushu University: Fukuoka, Japan, 812-8581*

Charge transfer cross sections and dynamics are investigated jointly by experimental and theoretical approaches below keV-energy regime. We have identified a few significant aspects in dynamics relevant to molecular targets, and these are: (i) temperature effect, (ii) isotope effect, (iii) isomer effect and (iv) steric effect even in low keV- to high eV-energy regions. These effects have been considered to be negligible in this energy collision in most of earlier studies because of huge disparity between interaction time and rovibrational time of a target. These observations are shown to be significant to analyze experimental results and give correct interpretation for them.

I. INTRODUCTION

In current fusion devices and ITER with carbon-based plasma-facing materials, many kinds of hydrocarbon molecules as well as other impurities are produced in their edge and divertor plasma regions.[1] In order to understand the behavior of impurity molecules and plasma diagnostics, cross-section data for charge-transfer processes of H^+ and impurity ions colliding with simple molecules, such as H_2, N_2, O_2, CO and CO_2, and hydrocarbons (C_mH_n, where $m = 1, 2, 3$) are important. However, only a few data sets for these plasma-impurity molecules collisions are available so far. Therefore, we undertook a project to jointly investigate experimentally and theoretically charge-transfer processes in the collision energies below 4 keV/u.[2-5]

In this paper, our recent works concerning with determination of charge-transfer dynamics and cross sections will be reviewed for He^{2+} ions in collisions with simple molecules[5] and H^+ ions in collisions with hydrocarbons.[3,4] A simple empirical scaling relation will be also discussed as a function of molecular properties such as a number of active electrons N_{AE} in target molecules.

II. EXPERIMENTAL AND THEORETICAL APPRFOACHES

II. A. EXPERIMENTAL SET UP

The charge transfer cross sections were derived based upon the so-called growth rate method. Only some important features of the present experimental apparatus and methods are highlighted here.

Figure 1 shows the schematic view of the experimental arrangement. The mass-analyzed ion beam extracted from an electron impact ion source was introduced into a 40 mm long collision cell. The target gases of high purity (> 99.5 %) were fed into the collision cell which pressure was measured with a calibrated Pirani gauge. After collisions, both the incident ions and product *fast* particles formed in charge transfer collisions were charge-separated with the electrostatic parallel plates and were detected with a micro-channel plate position-sensitive detector (MCP-PSD). The charge-transfer cross sections were determined from the slope of the linear part in the curve of observed fractions for product particles versus the target gas thickness.

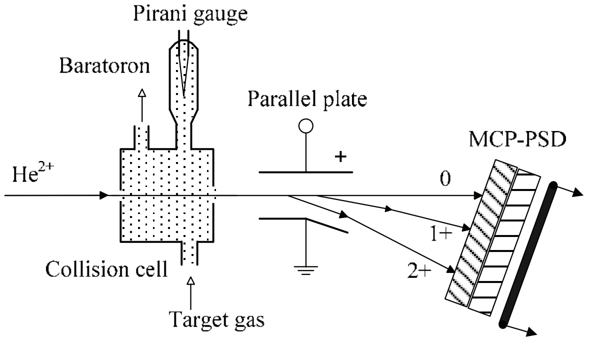

Fig. 1. Schematic view of the experimental arrangement.

In the case of He^{2+} ion collisions, the isotope ^3He gas was supplied to the ion source, in order to avoid the contamination of the He^{2+} ion beam by H_2^+ ions. Single- and double-charge transfer cross sections (σ_{21} and σ_{20}) were derived for He^{2+} ions, while single-charge transfer cross sections (σ_{10}) for H^+ ions.

II. B. THEORETICAL MODEL

In the collision energies below a few keV, it is believed that a molecular description of a collision system within a semi-classical picture is adequate. Therefore, we employed the so-called molecular orbital closed coupling method (MOCC). Briefly in this, electronic states are described quantum mechanically, while relative nuclear motion is classical mechanically. Then time-dependent coupled equations are derived and solved numerically to yield transition probabilities and hence cross sections.

III. RESULTS AND DISCUTION

Some of representative results for all molecular systems we conducted will be shown and discussed in details.

III. A. He^{2+}-H_2, N_2, O_2, CO and CO_2 Collisions

III. A. 1. Energy-Dependence and Magnitude of Cross Sections

The charge transfer cross sections, as an example, for He^{2+} + H_2 collisions are displayed for single σ_{21}, and double σ_{20} charge transfer in Fig.2 (a) and (b).

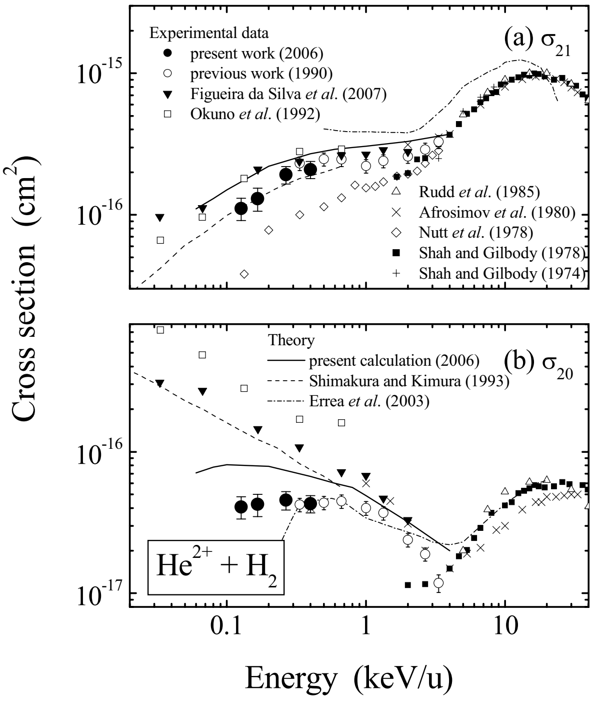

Fig. 2. Single- and double-charge transfer cross sections of He^{2+} ions with H_2 molecules as a function of the He^{2+} energy (keV/u).

There have been many experimental as well as theoretical studies on this system earlier. Double charge transfer process, however, is known to diverge each other at low energies. For double charge transfer, σ_{20}, in Fig. 2 (b), below around 1 keV/u, there are some measurements that show a linearly increasing feature, while most of others including the present results appear to level off around 1 keV/u with decreasing trend as the energy much decreases. The present theoretical results (solid curves) also suggest the decreasing trend in accord with the measurement, although the theory gives somewhat higher cross-section values. For single charge transfer, all measured except for one and theories are in reasonably agreement.

As a second example, the charge transfer cross sections for He^{2+} + CO collisions are displayed for single σ_{21}, and double σ_{20} charge transfer in Fig.3 (a) and (b). Again, for double charge transfer, below around 1 keV/u, one set of the measurement shows sharp increasing trend with the decreasing energy, while the present results level off and somewhat decrease. The present theory (solid curves) is not in good qualitative accord, but quantitatively shows the similar trend. In addition to these two examples, other cases also shows that one set of data consistently shows the increasing trend for double charge transfer as the energy decreases. Therefore we tentatively conclude that there may be a systematic problem in another set of the measurement.

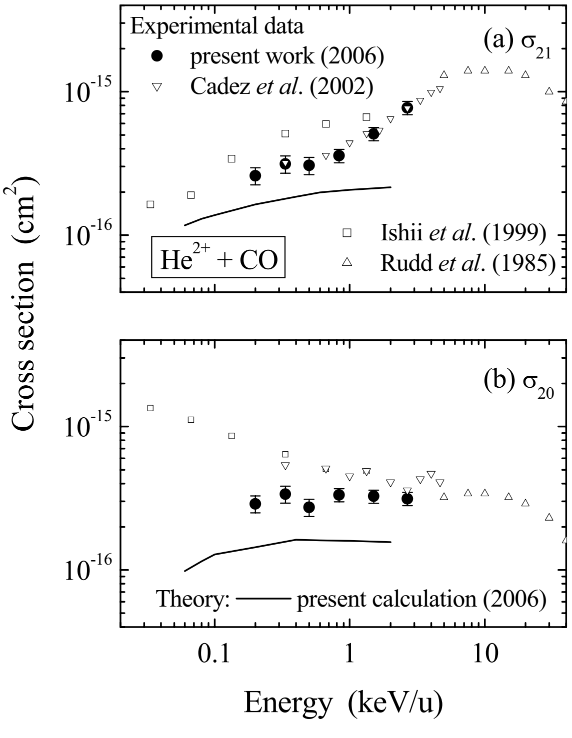

Fig. 3. Single- and double-charge transfer cross sections of He^{2+} ions with CO molecules as a function of the He^{2+} energy (keV/u).

III. A. 2. Scaling Property of Double-Charge Transfer Cross Sections

The present double-charge transfer cross sections σ_{20} for N_2, O_2, CO, and CO_2 molecules have a nearly equivalent value for all molecules in the collision energy range from 0.2 keV/u to 3 keV/u. However their magnitudes appear to somewhat increase as the molecular size increases. We have examined the dependence of the σ_{20} cross sections on the number of active electrons N_{AE} in target molecules, which is one of the molecular parameters and reflects the “molecular size”. The number of the active electrons N_{AE} in the outer-most shell is considered to play a primary role and hence to be active in the charge transfer processes at low energies.

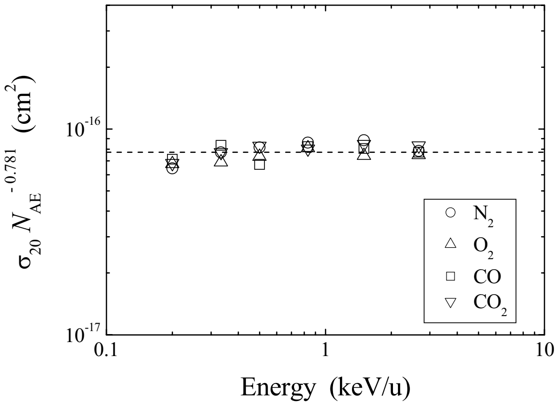

Fig. 4. Reduced plot of double-charge transfer cross sections as a function of the He^{2+} energy. The dashed line has a constant value of 7.72 × 10^{-17} (cm^2).

As seen in Fig. 4, the present double-charge transfer cross sections are found to be scaled well over the energy region from 0.2 to 3 keV/u. The analytical form to fit the data is proposed as follows:

$$\sigma_{20} = 7.72\times 10^{-17}\cdot N_{\mathrm{AE}}^{0.781}\ (\mathrm{cm}^2) \qquad (1)$$

Eq. (1) could be useful for the practical applications which shows the scaling relations to guide future experiments and theories.

Note that the behavior of the double capture cross section for H_2 is found to show somewhat a different characteristic compared to all other molecular cases, and hence, we exclude H_2 case from this analysis. However, in the recent measurements for hydrocarbons, the σ_{20} values for some hydrocarbons are found to possess the similar feature, and hence these cross sections combined with H_2 can be scaled as the similar formula of eq. (1) but with different coefficients.

III. B. H^+-Hydrocarbons Collisions

We have at first studied experimentally and theoretically on the single-charge transfer cross sections σ_{10} of H^+ ions colliding with CH_4, C_2H_2, C_2H_6 and C_3H_8 at energies below 4 keV.[4] Janev *et al.* compiled charge transfer cross sections data including those of ours and proposed a scaling law to predict cross section values based on a perturbative approach. They covered a wide range of collision systems, such as those of $H^+ + C_3H_4$, for which no data are available.[6] To provide more complete and accurate data sets for hydrocarbons, however, we have kept studying continuously a single-charge transfer cross sections of H^+ ions in collisions with C_2H_4, C_3H_4 [allene and propyne], C_3H_6, $(CH_2)_3$, n–C_4H_{10} and i–C_4H_{10} molecules in the energy range of 0.20 to 4.0 keV.[7,8]

III.B.1. Energy-Dependence and Magnitude of Cross Sections

When the energy defect between the initial and final channels in charge transfer reaction is equal to zero, this collision is so-called a “resonant” charge transfer process. In this case, the cross sections gradually decrease with the increasing incident energy at low energy regime.[9] While the energy defect is not zero, the cross section curve versus the collision energy has a maximum[9] at the intermediate energy.

If all of the particles before and after the charge-transfer collision stay electronically, vibrationally, and rotationally in the ground state, the energy defect of this charge transfer reaction can be described as the difference between the ionization potential of product neutral hydrogen atoms and that of target hydrocarbons. In the present collision, the energy defects of all collision partners are exothermic for the ground state to ground state transition. However, the near resonant condition for the charge transfer process is expected to be fulfilled through the vibrational and rotational excited states of the product target molecular ions.

In our results, we have observed that the cross sections for C_2H_2 and C_3H_4 [allene and propyne] targets behave as the non-resonant case, while those for other hydrocarbons show the resonant type energy dependence.[4,7,8]

As one example of the non-resonant case, the cross sections for charge transfer in $H^+ + C_3H_4$ collisions are shown in Fig. 5. To the best of our knowledge, the cross sections for these molecules have not been reported so far. The present cross sections are practically the same for both allene and propyne within each other’s experimental uncertainties, but the cross sections for allene are slightly larger than those for propyne. The difference gradually increase as the collision energy increases and reach maximum at about 1.5 keV. This means that these collisions are not fully resonant. In Fig. 5, a dot-chain curve, which is the prediction by Janev *et al.*,[7] is close to the present cross sections, but slightly smaller and almost flat in our investigated energy region.

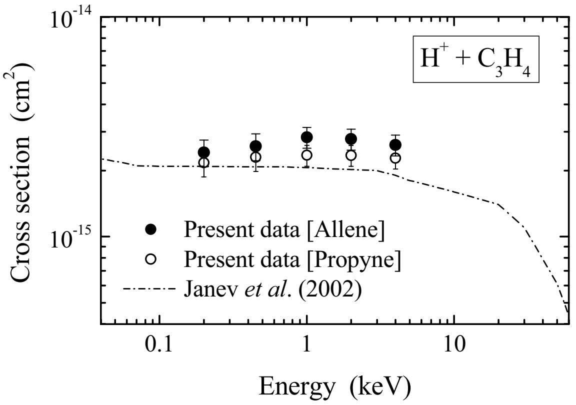

Fig. 5. Charge-transfer cross sections for H^+ ions in collisions with C_3H_4 (allene and propyne) molecules.

As one example of the near resonant case, the cross sections for charge transfer in H^+ + C_3H_6 and $(CH_2)_3$ collisions are shown in Fig. 6. The present cross sections are practically the same for both C_3H_6 and $(CH_2)_3$ molecules. Both cross sections decrease as the collision energy increases. This means that these collisions are fully resonant. The prediction by Janev *et al.*,[7] is in good accordance with the present measurements.

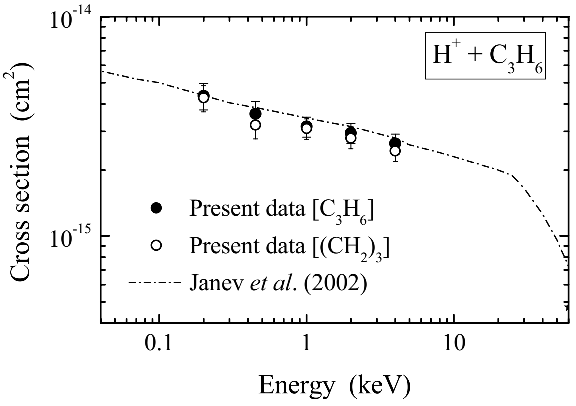

Fig. 6. Charge-transfer cross sections for H^+ ions in collisions with C_3H_6 and $(CH_2)_3$ molecules.

III.B.2. Scaling Property of Cross Sections of Fully Resonant Type

Some scaling relations for the cross sections are useful for application to other fields of science and technology. Generally, the dependence on the first ionization potential I_1 (eV) of target molecules is sometimes examined for the charge-transfer cross sections of slow ions. For the previous our σ_{10} data[4,7] together with recent our data of C_2H_4,[8] however, a simple relation to I_1 could not be determined.

We have examined the dependence of the present σ_{10} data of fully resonant type, except the C_2H_2 and C_3H_4 molecules, on the active electrons N_{AE} into the target hydrocarbons. A fairly good systematic dependence of these σ_{10} data of fully resonant type on N_{AE} was observed, and a following best fit relation

$$\sigma_{10} \text{ (at 1.0 keV)} = 7.8 \times 10^{-16} \cdot N_{AE}^{0.49} \text{ (cm}^2\text{)} \qquad (2)$$

was obtained.

In general, the resonant charge-transfer cross section σ_{RES} is represented by

$$\sigma_{RES} = (a - b\cdot\log \upsilon)^2 \qquad (3)$$

where a and b are constants and υ is the velocity of the incident ions.[9] Combining eq. (3) with eq. (2), we proposed the following empirical relation for the single-charge transfer cross sections of H^+ ions in collisions with hydrocarbons in the energies below about 20keV:

$$\sigma_{10} = 7.8\times10^{-16} \cdot(1 - 0.20\cdot\log_{10} E)^2 \cdot N_{AE}^{0.49} \text{ (cm}^2\text{)} \qquad (4)$$

where E is the kinetic energy of the incident ions in keV.

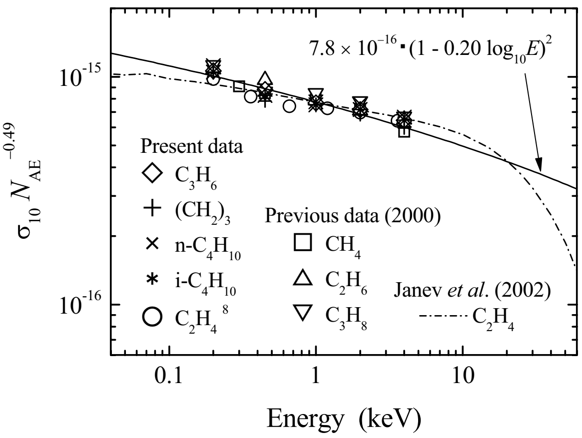

Fig. 7. Reduced plot of charge-transfer cross sections for H^+ ions colliding with some hydrocarbons.

Figure 7 shows the reduced plot ($\sigma_{10} \cdot N_{AE}^{-0.49}$ values) of the single-charge transfer cross sections versus incident energy E. A good correlation of the experimental data for the hydrocarbons to eq. (4) can be seen in Fig. 7.

ACKNOWLEDGMENTS

This work was supported in part by the Ministry of Education, Science, Sport, Culture and Technology, Japan, and a collaborative research program of the National Institute for Fusion Science, Japan.

REFERENCES

[1] H. KUBO, "Atomic and Molecular Processes for Heat and Particle Control in Tokamaks", *3rd Int. Conf. At. Mol. Data and Their Applications*, CP636, p.161, (2002).

[2] T. KUSAKABE, K. HOSOMI, H. NAKANISHI, H. TAWARA, M. SASAO, Y. NAKAI, AND M. KIMURA, "Charge-Transfer Processes in Collisions of Ground-State C^+ Ions with H_2, D_2, CO, and CO_2 Molecules in the Energy Range from 0.15 to 4.5 keV", *Phys. Rev. A*, **60**, 344 (1999).

[3] T. KUSAKABE, K. ASAHINA, J. P. GU, G. HIRSCH, R. J. BUENKER, M. KIMURA, H. TAWARA, AND Y. NAKAI, "Charge-Transfer Processes in Collisions of H^+ Ions with H_2, D_2, CO, and CO_2 Molecules in the Energy Range 0.2 - 4.0 keV", *Phys. Rev. A*, **62,** 062714 (2000).

[4] T. KUSAKABE, K. ASAHINA, A. IIDA, Y. TANAKA, Y. LI, G. HIRSCH, R. J. BUENKER, M. KIMURA, H. TAWARA, and Y. NAKAI, "Charge-Transfer Processes in Collisions of Slow H^+ Ions with Hydrocarbon Molecules: CH_4, C_2H_2, C_2H_6, and C_3H_8", *Phys. Rev. A*, **62**, 062715 (2000).

[5] T. KUSAKABE, Y. MIYAMOTO, M. KIMURA, and H. TAWARA, "Charge-Transfer Processes in Collisions of He^{2+} Ions with H_2, N_2, O_2, CO, and CO_2 Molecules below 4 keV/u" *Phys. Rev. A*, **62**, 062715 (2000).

[6] R. K. JANEV, J. G. WANG, and T. KATO, "Charge Exchange Cross Section Database for Proton Collisions with Hydrocarbon Molecules," *At. Plasma-Mater. Interact. Data Fus.*, **10,** 129 (2002).

[7] T. KUSAKABE, K. GOTANDA, H. SAKAUE, and M. KIMURA, "Charge-Transfer Cross Sections of H^+ Ions in Collisions with Some Hydrocarbon Molecules in the Energy Rande of 0.2 to 4 keV", *Trans. Fusion Sci. Techno*l., **51**, 132 (2007).

[8] T. KUSAKABE, K. GOTANDA, M. KIMURA, S. RAI, H.-P. LIEBERMANN, AND R. J. BUENKER, "Vibrational Effect on Charge-Transfer Processes in Collisions of H^+ and O^+ Ions with C_2H_4 Molecules at Energies below 10 keV/u" *Phys. Rev. A*, **76**, 042711 (2007).

[9] D. RAPP and W. E. FRANCIS, "Charge Exchange between Gaseous Ions and Atoms," *J. Chem. Phys.*, **17**, 2631 (1962).

Theoretical Study of EUVL-Emissions from $4d$ Open-Shell Atomic Ions of Heavy Ion Plasmas and Charge Transferred Excited States

KOIKE Fumihiro and FRITZSCHE Stephan[1]
Physics Laboratory, School of Medicine, Kitasato University
1-15-1 Kitasato,Sagamihara 228-8555 Japan
1) Gesellschaft fuer Schwerionenforschung (GSI), D-64291 Darmstadt, Germany
e-mail: koikef@kitasato-u.ac.jp

Abstract

Wavelengths and intensities of extreme ultra-violet(EUV) optical emissions are studied for $4d$ open shell atomic ions in plasmas, which are of interest from the view point of EUV light source development. The $4d - 5p$ transitions of Xe^{10+} ions have been calculated in detail. We have employed a method based on a multi-configuration Dirac-Fock approximation. Dipole transition rates have been calculated allowing the non-orthogonal orbital wavefunctions between the initial and final electronic states. The orbital relaxations and electron correlations have substantial effects on the formation of the transition arrays.

For atomic ions with atomic numbers ranging 48 to 56, the intra N shell transitions are calculated in detail. The effect of correlations in $4p-4d$ and $4d-4f$ transitions are investigated. This effect is pointed out to be common to the atomic ions with atomic numbers near to the range 48 to 56.

Keywords: EUV, atomic structure, atomic transition, optical emission, relativistic theory, MCDF, configuration interaction, electron correlation

1. Introduction

The extreme ultra-violet light (EUVL) emissions of 4d open-shell atomic ions are of interest in relation to the semiconductor technologies and also to the study of highly charged heavy atomic ions in plasmas. Extensive efforts have been made in recent years for understanding the emission spectra from the plasmas[1][2][3][4][5]. Those spectral structures are of interest also from the view point of academic atomic spectroscopy, whereas they are obtained mainly on the purpose of EUV light source development.

During the last years, a series of sophisticated charge transfer experiments have been carried out for xenon ions[6][7] and for tin ions[7][8] by Tanuma and his co-workers. In these experiments, a beam of charge selected atomic xenon or tin ions has been introduced into the gas chamber and the EUV emissions from the excited atomic ions that were created by collisional electron capture from neutral gas atoms have been observed. Because the gas pressure has been kept as low as to maintain a single collision condition, their individual spectral data are of the ions with a unique charge state. This gives a great advantage for comparison of the data with theory.

To give a theoretical counterpart of these experimental data, we performed a set of accurate calculations of electronic states and optical processes based on a Multi-Configuration Dirac-Fock (MCDF) approximation. In these computations, the General purpose Relativistic Atomic Structure Program 92 (GRASP92)[9] and the Relativistic Atomic Transition and Ionization Properties (RATIP)[10] computer codes are used. An advantage of these programs is that we can treat the two electron non-local exchange integrals as they are.

In the present paper, we, firstly, consider the EUV emission wavelengths and transition rates of Xe^{10+} ions. We calculate the $4p^6 4d^8$ - $4p^6 4d^7 5p$ electric-dipole transition array. In a standard treatment of the MCDF method, an atomic state function (ASF) is responsible for representing the individual multi-electron atomic state. An ASF is expanded in terms of configuration state functions (CSF), which are antisymmetrized products of a common set of orthonormal single electron orbitals. Including the excited orbitals in CSF's, we can evaluate the electron correlations through configuration interactions.

To consirer, on the other hand, the role of the intra N-shell optical transitions, which are relevant for the 13.5 nm EUV emissions from $4d$-open shell Sn ions, we calculate the $4p-4d$ and $4d-4f$ transitions for ions with atomic numbers Z ranging 48 to 56. We have pointed out the important role of the configuration interactions between the $4p$ sub-vallence hole configurations and $4f$ intra-shell excited configurations. It has been pointed out that the modifications of the optical emission spectral structures due to those type of configuration interactions are common to those ionic species.

2. Calculation

2.1. $4d-5p$ *Transitions of* Xe^{10+} *Ions*

Einstein spontaneous emission rates, i.e., the A-factors, have been calculated for all the combinations of excited and ground states relevant to the $4d-5p$ electric dipole transitions. Firstly, we calculate the $4d-5p$ transition probabilities of Xe^{10+} ions including only the minimal set of orbitals, say, $1s$, $2s$, $2p$, $3s$, $3p$, $3d$, $4s$, $4p$, $4d$, and $5p$. The ground configuration is $1s^2 2s^2 2p^6 3s^2 3p^6 3d^{10} 4s^2 4p^6 4d^8$ of 14 multiplet levels. The excited configuration is $1s^2 2s^2 2p^6 3s^2 3p^6 3d^{10} 4s^2 4p^6 4d^7 5p^1$ and consists of, in contrast, already 110 multiplet levels. Secondly, we calculate them including the correlation configurations. In these computations, we start from the $4p^6 4d^8$ and $4p^4 4d^{10}$ reference configurations and include all the single and double excitations into the $4f$, $5p$, $6s$, $6p$, $6d$, $6f$, and $6g$ sub-shells from the $4p^6 4d^8$ configuration. This approach then results in 16140 CSF. A similar scheme of virtual excitations is employed also for the excited states. Owing to the size of the calculations, the total computation required more than 750 hours (≈ 1 month) of CPU time on a present-day high-end PC.

In Figure 1, the calculated distribution of the A-factors for Xe^{10+} ions is plotted as a function of the wave lengths of optical emission[11]. In order to synthesize the 'real' spectra, the calculated lines have been convoluted with a Lorentzian profile for the natural width (width = 0.02 nm) and a triangular profile for the spectrometer (width = 0.02 nm). The broken curve is of the minimal base calculation and the solid curve is of the basis set with large scale correlation functions. It can be seen that, on the level of individual peaks, the two curves appear to be quite different. The electron correlation has a substantial influence on the poputations of A-factors with respect to the combination of total angular momenta of the upper and lower levels.

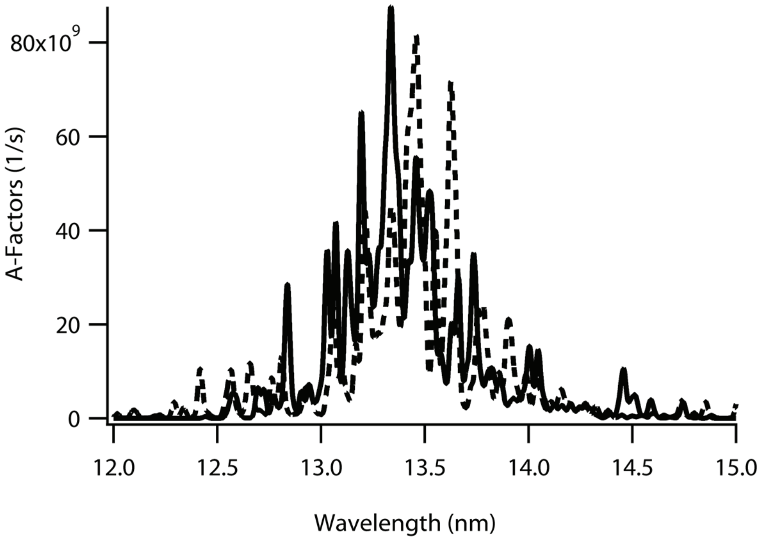

Figure 1. A-factor distributions for $4d-5p$ transitions of Xe^{10+} ions. The broken curve: the minimal base calculation. The solid curve: the large basis set calculation with correlation orbitals $4f$, $5p$, $6s$, $6p$, $6d$, $6f$, and $6g$.

In Table 1 and 2, we have listed our results from the calculation including the correlation effects, and also listed the corresponding values by Saloman[4] for comparison.

2.2. $4p-4d$ *and* $4d-4f$ *Transition Arrays of* $Z=46-56$ *Ions*

One of the best candidates for 13.5 nm region EUV light source are considered to be of the intra N shell ($n = 4$ shell) transitions of tin (Sn) multiplly charged atomic ions. It is normally indispensable to take into account the electron correlations if we are to evaluate the the transition energies within the accuracy of a few electron volts, because the correlation energy of the atomic valence electrons falls in this range. To gain an insight of the effects that are pointed out by O'Sullivan and Faukner[12], we have carried out careful MCDF calculations for $4d^q$ (q = 0 to 10) atomic ions with atomic number Z = 48 to 56. Although, they argued only the Sn atomic ions, those effects should be present also in other atomic species. As an

Table 1. Wavelegths and rates of $4d-5p$ electric dipole transitions in the region 12 to 15 nm.

Upper level angular momentum	Lower level angular momentum	Wavelength present calc. (nm)	A-factor Coulomb gage $\times 10^{10}(1/s)$	A-factor Babushkin gage $\times 10^{10}(1/s)$	Wavelength Saloman[4] (nm)	Intensity Saloman[4] (arb. unit)
1	2	12.7251	1.68824	2.00702	–	–
1	0	12.8409	5.25589	6.62560	–	–
4	4	13.0243	2.10509	1.61826	–	–
0	1	13.0295	4.41445	4.68371	–	–
1	0	13.0703	7.25224	7.91344	–	–
1	1	13.0735	3.54107	3.78470	–	–
4	4	13.1224	4.68160	4.73013	–	–
3	4	13.1313	1.07094	1.04687	13.1515	156
1	2	13.1871	4.19585	4.38572	–	–
5	4	13.1964	5.73363	5.48372	–	–
2	2	13.1983	3.57149	3.81152	–	–
2	2	13.2288	2.93902	3.06610	–	–
3	3	13.2340	1.59934	2.06908	–	–
1	2	13.2521	2.10563	2.14968	–	–
1	0	13.2775	2.76620	2.76423	–	–
3	4	13.2800	1.74243	1.83735	13.2573	170
0	1	13.2836	2.83040	2.83080	–	–
3	4	13.2981	2.20060	2.20617	–	–
2	2	13.3063	3.95639	4.08706	–	–
1	2	13.3081	2.15152	1.92982	–	–
1	2	13.3086	3.97931	3.67144	–	–
3	2	13.3247	2.29188	2.23569	–	–
1	2	13.3250	3.32820	3.99064	–	–
2	2	13.3296	3.16620	2.83941	–	–
2	2	13.3350	2.99325	3.29167	–	–
4	3	13.3395	4.17141	4.26180	13.4987	392
5	4	13.3406	6.19201	6.45949	13.5072	518
2	3	13.3463	2.43870	2.65455	–	–
3	2	13.3551	2.85879	2.95628	13.5100	179
1	2	13.3656	5.65392	5.82819	–	–
3	2	13.3763	2.01688	2.13407	13.5334	165
2	2	13.3770	2.43871	2.47897	–	–
4	4	13.3827	2.43699	2.26594	–	–

example, we show ,in Fig.2, the single electron atomic orbital energies for Sr-like atomic ions of $Z=48$ to 56. To obtain the single electron atomic orbitals and their energies, we have made their MCDF optimizations including the basis wavefunctions up to $6p, 5d, \text{and} 5f$. In this figure, we can find that the differences of orbital energies between $4p$ and $4d$ orbitals, and $4d$ and $4f$

Table 2. Continued from Table 1.

Upper level angular momentum	Lower level angular momentum	Wavelength present calc. (nm)	A-factor Coulomb gage $\times 10^{10}(1/s)$	A-factor Babushkin gage $\times 10^{10}(1/s)$	Wavelength Saloman[4] (nm)	Intensity Saloman[4] (arb. unit)
3	2	13.4220	4.15326	4.03751	–	–
4	4	13.4453	4.53258	4.44106	–	–
2	2	13.4550	3.29967	3.45749	13.5334	165
2	3	13.4608	1.41478	1.42233	13.4962	222
1	0	13.4628	7.33049	7.06751	–	–
3	3	13.4808	3.63103	3.33794	13.4037	309
1	2	13.4895	2.09521	2.08123	13.4927	218
1	0	13.5113	2.51755	2.38080	–	–
3	4	13.5291	1.47865	1.49451	13.4091	156
4	4	13.5340	4.82794	4.98559	13.5614	339
4	4	13.5354	2.13754	2.10283	13.6401	236
1	1	13.6304	3.85344	3.93575	–	–
3	4	13.6625	4.65111	4.49136	–	–
4	4	13.7317	1.48114	1.49973	13.6605	315
5	4	13.7339	3.47433	2.96986	13.6401	236
1	0	13.7446	1.91193	2.05482	–	–
2	1	13.7627	1.05335	1.08050	13.6605	315
1	0	14.0077	2.53333	1.83530	–	–
1	0	14.0452	3.45158	3.80649	–	–
1	0	14.4596	2.64676	2.33983	–	–

orbitals coincide within the range of a few %. The $4p^6 4d^1 4f^1$ and $4p^5 4d^3 4f^0$ configurations may mix strongly, and the optical $4p - 4d$ and $4f - 4d$ transitions may take place coherently, providing us with quite a peculiar EUV emission spectrum. The result of the orbital energy calculation stands for the argumentation made by O'Sullivan and FauknerOSullivan1994. Also, we find, from this figure, that we may expect that the so called the effect of spectral narrowing and shift is quite common to the atomic specieds with the atomic numbers in the range $Z = 48$ to 56. As an example of the effect of spectral narrowing and shift, we illustrate, in Fig.3 the calculated A-factor distributions of Y-like ions of atomic species with $Z = 49, 50, \mathrm{and} 51$. In this figure, we can also observe the change of the spectral shape in the atomic number Z. Due to the interference between the $4p^6 4d^4 - 4p^6 4d^3 4f^1$ and $4p^6 4d^4 - 4p^5 4d^5 4f^0$ transitions, we can observe a strong enhancement of the EUV emissions in 13.5 nm region of $Z = 50$, which provides us with the narrowing and shift in appearance of the emission spectra. Due to the term splitting both in the ground and the excited states, the spread of the A factor distribution would have been a couple of ten eV without the interference between the $4p - 4d$ and $4d - 4f$ transitions.

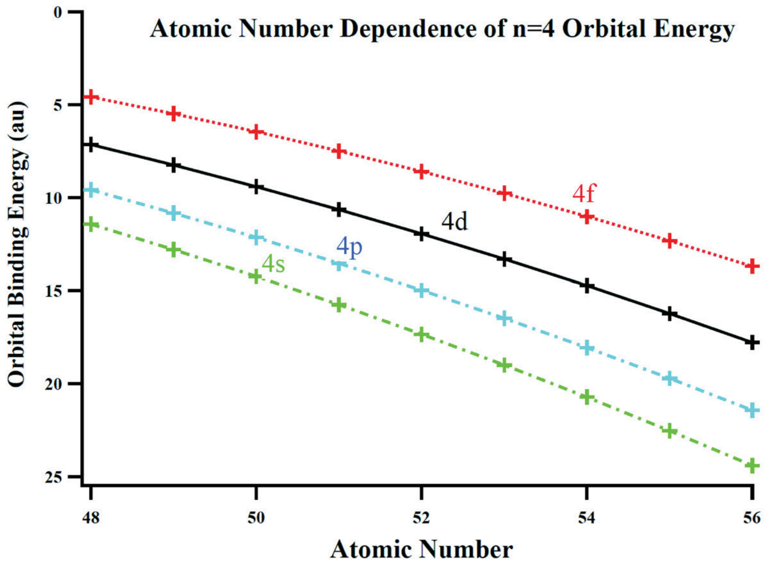

Figure 2. Atomic number Z dependence of the energies of $N = 4$ atomic orbitals. The calculated range of the atomic number is $Z = 48$ to $Z = 56$. Dotted curve: $4f$ orbital, Solid curve: $4d$ orbital, Dot-dashed curve in upper entry: $4p$ orbital, and Dot-dashed curve in lower entry: $4s$ orbital.

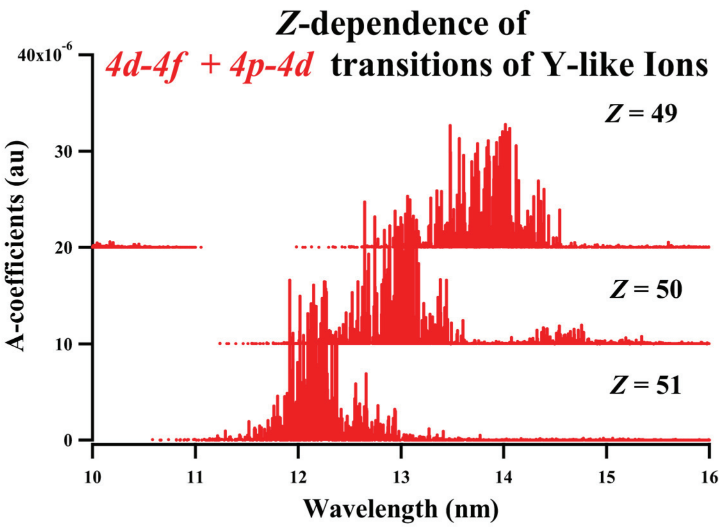

Figure 3. Atomic number Z dependence of A-factors for $4d - 4f + 4p - 4d$ transitions of Y-like ions. The interference effects of $4d - 4f$ and $4p - 4d$ transitions are taken into account by configuration interaction calculations.

Although the figures are not illustrated in the present paper, we have observed quite a similar interference effect in transitions for wide range of atomic numbers, say, for the range $Z = 48$ to 56, and also for wide range of occupation numbers of N shells.

3. Discussion

The precise and acculate theoretical data of the atomic structures and dynamics that includes the information about the relativistic effect and the electron-electron correlation effects provide us with a good base for precision plasma analysis. Owing to the general nature of many electron atoms or atomic ions, the inclusion of the effect of configuration interactions among virtually excited states is indispensable to obtain physically realistic atomic state wavefunctions. Especially, it is important to take into account the modification of the atomic state wavefunctions due to the interactions among various many-electron configurations, which can be evaluated by only an SCF iterations in MCDF calculations.

As seen in Fig.1 and Tables 1 and 2, we have obtained the A-factors in $4d - 5p$ transitions of Xe^{10+} ions. However, due to the heavy mess of transition lines, the line by line comparison with experiment has not yet been accomplished and has been rendered to the forthcoming sophicticated works.

We have pointed out also that the spectral shift and narrowing should be the effects which are quite common to the $4d$ open shell atomic ion species with moderate atomic numbers.

Acknowledgement

This work is partly supported by the Leading Project for advanced semiconductor technology of MEXT. This work was partly supported by the JSPS-CAS Core-University Program in the field of Plasma and Nuclear Fusion.

References

[1] Gillaspy J D 2006 *EUV Sources for Lithography Edited by V. Bakshi, SPIE Press Bellingham, Washinton, USA* 47
[2] Tolstikhina Yu et al 2006 *EUV Sources for Lithography Edited by V. Bakshi, SPIE Press Bellingham, Washinton, USA* 113
[3] G. OSullivan G et al 2006 *EUV Sources for Lithography Edited by V. Bakshi, SPIE Press Bellingham, Washinton, USA* 149
[4] Saloman E B 2004 *J. Phys. Chem. Ref. Data* **33** 921
[5] Sasaki A et al 2006 *Proc. of SPIE* **6151** 61513W.
[6] Tanuma H et al 2005 *Nucl. Instr. Meth.* **B235** 331
[7] Tanuma H et al 2007 *J. Phys. Conf. Ser.* **58** 231
[8] Ohashi H et al 2007 *J. Phys. Conf. Ser.* **58** 235
[9] Parpia F A, Fischer C F and Grant I P 1996 *Commpt. Phys. Commun.* **94** 249
[10] Fritzsche S 2001 *J. Elec. Spec. Rel. Phenom.* **114-116** 1155
[11] Koike F, Fritzsche S 2007 *J. Phys. Conf. Ser.* **58** 157.
[12] O'Sullivan G, Faukner R 1994 *Opt. Eng.* **33**, 3978.

DYNAMIC BEHAVIOR FOR VALENCE SHELL EXCITATION PROCESSES OF NOBLE ATOMS STUDIED BY FAST ELECTRON IMPACT

Lin-Fan Zhu and Ke-Zun Xu
Hefei National Laboratory for Physical Sciences at Microscale, Department of Modern Physics, University of Science and Technology of China, Hefei, Anhui 230026, China
e-mail: lfzhu@ustc.edu.cn

Abstract

The generalized oscillator strengths for the valence shell excitations of noble atoms were measured at an incident electron energy of 2500 eV, and the parallel character of the generalized oscillator strength curves for the pair of transitions of $(n-1)p^5ns[3/2]_1$ and $(n-1)p^5ns'[1/2]_1$ of Ne (n=3), Ar (n=4), and Kr (n=5) was observed. This phenomena is elucidated by analyzing the experimental results and the calculated intermediate coupling coefficients: the *LS* coupling singlet nature of the ground state selects the *LS* coupling singlet components from the intermediate coupling wave functions of the excited states, and the contributions from excitations to singlet components dominate the generalized oscillator strength for fast electron impact. Similar behavior was also observed for the inner shell excitation process of lithium.

Keywords: Generalized oscillator strength, differential cross section, *LS* coupling, intermediate coupling, fast electron excitation

1.Introduction

Because of the enhancement of the relativistic effect, *LS* coupling would be transferred to intermediate coupling to describe the energy levels as noble atoms get heavier. Considering the *LS* coupling nature of the ground states and the intermediate coupling nature of the excited states of noble atoms, it is very important and fundamental to explore the valence shell excitation behaviors of heavy noble atoms for fast electron impact [1]. Compared with slow electron impact in which the incident particle and the target are considered as a combined system and both of them lost their mechanical individuality, the fast electron impact can be regarded as a sudden and small external perturbation to an atom or molecule, and the exchange effect is negligibly small. Therefore, the cross section can be factorized into two factors: one dealing with the incident particle and the other (generalized oscillator strength, GOS) dealing with the target [2]. So the GOS may provide new insight into the atomic excitation process. In addition, the electron impact excitation mechanism for noble atoms has been extensively used in producing x-ray laser [3, 4].

Using the angle-resolved fast electron-energy-loss spectrometer, we measured the GOS's for valence shell excitations of neon, argon and krypton at an impact energy of 2500 eV. Then the dynamic behavior, i.e., the parallel character of the GOS's for the pair of transitions of $(n-1)p^5ns[3/2]_1$ and $(n-1)p^5ns'[1/2]_1$ of Ne (n=3), Ar (n=4), and Kr (n=5), is analyzed and elucidated with the help of our calculated intermediate coupling coefficients.

2. Experimental method

The experimental methods have been described in detail in our recent works [1, 5, 6, 7, 8]. Briefly, an angle-resolved electron-energy-loss spectrometer were used in the present measurement, and the impact energy was set at 2500 eV. The energy resolution was less than 75 meV [full width at half maximum (FWHM)], while the angular resolution was about 0.8° (FWHM). After the electron energy loss spectra at different scattering angles and different pressures were measured, the corrections of the pressure effect and angular resolution were made. Then the absolute GOS's for the valence shell excitations of noble atoms were obtained by normalized the relative ones to the corresponding optical oscillator strengths at the optical limit.

3. Results and discussions

Figure 1 shows the measured GOS's for the pair of transitions of $(n-1)p^5ns[3/2]_1$ and $(n-1)p^5ns'[1/2]_1$ of Ne (n=3), Ar (n=4), and Kr (n=5). It can be seen clearly that the GOS curves of $(n-1)p^5ns[3/2]_1$ and $(n-1)p^5ns'[1/2]_1$ are nearly parallel. This phenomena is strange because the wave functions for the two excited states of every atom are different although its wave function for the ground state is same. In order to explain the phenomena, we calculated the intermediate coupling coefficients for relevant levels of Ne, Ar, and Kr using Cowan code [9]. Then the intermediate coupling wave functions for the excited states of intermediate coupling can be expanded by the linear combination of the basis of the *LS* coupling wave function:

$$\Psi_{ns[3/2]_1} = \alpha_n \Psi_{ns^3P_1} + \beta_n \Psi_{ns^1P_1} \tag{1}$$

$$\Psi_{ns'[1/2]_1} = -\beta_n \Psi_{ns^3P_1} + \alpha_n \Psi_{ns^1P_1}. \tag{2}$$

Here $\Psi_{ns[3/2]_1}$ and $\Psi_{ns'[1/2]_1}$ are the wave functions of the states of $ns[3/2]_1$ and $ns'[1/2]_1$

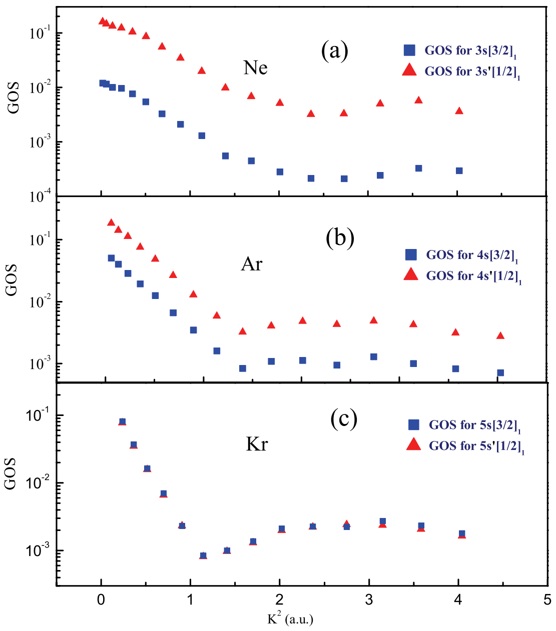

Figure 1: The generalized oscillator strengths for the pair of transitions of $(n-1)p^5ns[3/2]_1$ and $(n-1)p^5ns'[1/2]_1$ of (a) Ne (n=3); (b) Ar (n=4); and (c) Kr (n=5).

in the intermediate coupling scheme, and $\Psi_{ns^3P_1}$ and $\Psi_{ns^1P_1}$ are the wave function basis in the LS coupling scheme while α_n and β_n are the corresponding intermediate coupling coefficients. Now we can obtain the GOS ratio δ according to the definition of GOS:

$$\begin{aligned}
\delta &= \frac{f(ns[3/2]_1)}{f(ns'[1/2]_1)} \\
&= \frac{E_1}{E_2}\frac{K_2^2}{K_1^2}\frac{|<\Psi_{ns[3/2]_1}|\sum_{j=1}^{N} exp(i\mathbf{K_1}\cdot\mathbf{r_j})|\Psi_{(n-1)p^6{}^1S_0}>|^2}{|<\Psi_{ns'[1/2]_1}|\sum_{j=1}^{N} exp(i\mathbf{K_2}\cdot\mathbf{r_j})|\Psi_{(n-1)p^6{}^1S_0}>|^2} \\
&= \frac{E_1}{E_2}\frac{K_2^2}{K_1^2}\frac{|<\alpha_n\Psi_{ns^3P_1}+\beta_n\Psi_{ns^1P_1}|\sum_{j=1}^{N} exp(i\mathbf{K_1}\cdot\mathbf{r_j})|\Psi_{(n-1)p^6{}^1S_0}>|^2}{|<-\beta_n\Psi_{ns^3P_1}+\alpha_n\Psi_{ns^1P_1}|\sum_{j=1}^{N} exp(i\mathbf{K_2}\cdot\mathbf{r_j})|\Psi_{(n-1)p^6{}^1S_0}>|^2} \\
&= \frac{E_1}{E_2}\frac{K_2^2}{K_1^2}\frac{|<\beta_n\Psi_{ns^1P_1}|\sum_{j=1}^{N} exp(i\mathbf{K_1}\cdot\mathbf{r_j})|\Psi_{(n-1)p^6{}^1S_0}>|^2}{|<\alpha_n\Psi_{ns^1P_1}|\sum_{j=1}^{N} exp(i\mathbf{K_2}\cdot\mathbf{r_j})|\Psi_{(n-1)p^6{}^1S_0}>|^2} \\
&\simeq \frac{E_1}{E_2}\frac{\beta_n^2}{\alpha_n^2},
\end{aligned} \tag{3}$$

where $f(ns[3/2]_1)$, E_1 and K_1 are the GOS, excitation energy and momentum transfer

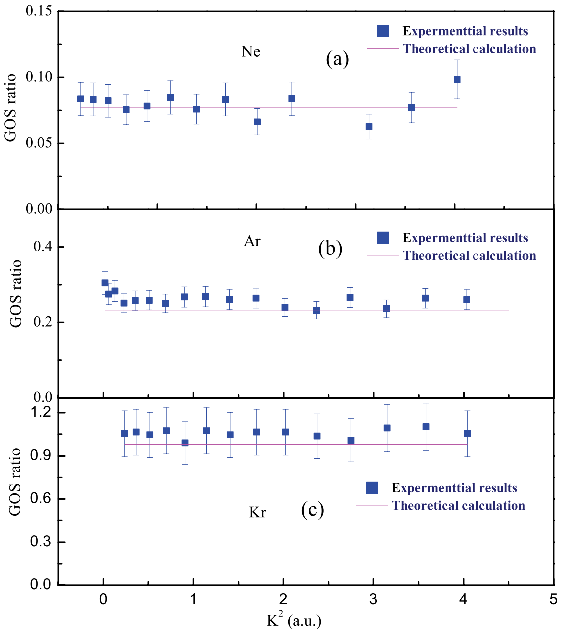

Figure 2: The experimental and calculated generalized oscillator strenght ratios between the transitions of $(n-1)p^5ns[3/2]_1$ and $(n-1)p^5ns'[1/2]_1$ of (a) Ne (n=3); (b) Ar (n=4); and (c) Kr (n=5).

of $ns[3/2]_1$, while $f(ns'[1/2]_1)$, E_2 and K_2 are the corresponding quantites of $ns[3/2]_1$, respectively. Herein $\mathbf{r_j}$ is the position vector of the jth electron, and $\mathbf{K_1} \simeq \mathbf{K_2}$ for the same scattering angle. Since the spin-forbidden transition is negligibly small for fast electron impact [2] and the initial ground state is singlet, the contribution of excitation to triplet component to GOS is neglected in equation (3).

From equation (3) we can obtain the conclusion that the GOS ratio for the pair of transitions, which are formed by the same electronic configuration through the intra-channel interaction, should be a constant. Now the parallel character of the GOS's of $(n-1)p^5ns[3/2]_1$ and $(n-1)p^5ns'[1/2]_1$ of Ne (n=3), Ar (n=4), and Kr (n=5) shown in figure 1 can be easily elucidated: the *LS* coupling singlet nature of the ground states of noble atoms selects the *LS* coupling singlet components from the intermediate coupling wave functions of the excited states, and the *LS* coupling singlet components are enough to describe the excitation process from the ground state for fast electron impact. Furthermore, since the photoexcitation and photoionization are the electric dipole processes, which correspond to the excitation and ionization for fast electron impact at optical limit ($K^2 \to 0$), the 4-parameter model suggested by Snell *et al.* [10] is sufficient to describe the Xe 4d photoionization process. Now we will see the quantitative information of GOS ratios. Figure 2 shows the GOS ratios for $(n-1)p^5ns[3/2]_1$ and $(n-1)p^5ns'[1/2]_1$ of Ne (n=3), Ar (n=4), and Kr (n=5), and it can be seen that the agreement between the

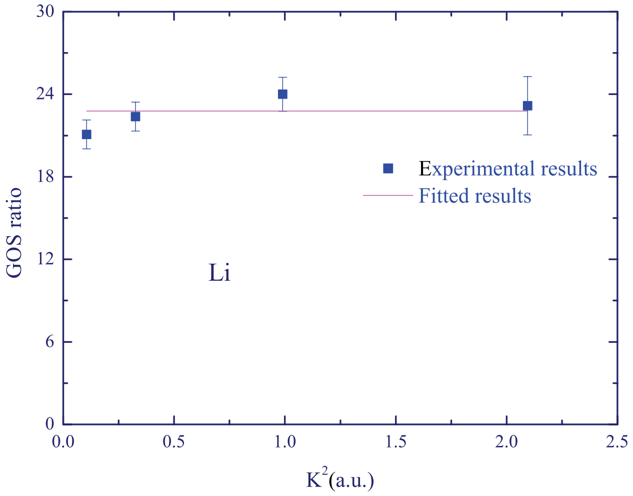

Figure 3: The experimental generalized oscillator strenght ratios between the excitations of $1s2s(^3S_1)2p\ ^2P$ and $1s2s(^1S_0)2p\ ^2P$ of lithium.

experimental results and the theoretical ones are satisfactory.

Recently, we have measured the electron energy loss spectra of the inner shell excitations of $1s$ electrons of lithium. Then the GOS ratio between the excitations of $1s2s(^3S_1)2p\ ^2P$ and $1s2s(^1S_0)2p\ ^2P$ of lithium was also determined and shown in figure 3. It can be seen clearly that the GOS ratio is a constant and it is independent of the momentum transfer. The present results shows that the above elucidation is still valid for the excitation process of inner shell of lithium..

3. Conclusion

From the measured GOS curves of $(n-1)p^5ns[3/2]_1$ and $(n-1)p^5ns'[1/2]_1$ of Ne (n=3), Ar (n=4), and Kr (n=5), the parallel character of the pair transitions was observed. With the help of the calculated intermediate coupling coefficients, the dynamic behavior is elucidated: the LS coupling singlet nature of the ground state selects the LS coupling singlet components from the excited wave function, i.e., the contributions from excitations to singlet components are dominant the GOS's. Furthermore, similar dynamic behavior was observed from the measured GOS ratio between the inner shell excitations of $1s2s(^3S_1)2p\ ^2P$ and $1s2s(^1S_0)2p\ ^2P$ of lithium.

Acknowledgement

Supports of this work by the National Nature Science Foundation of China (Grants No.

10474089 and No. 10734040) are gratefully acknowledged.

References

[1] H. D. Cheng et al., Phys. Rev. A **71**, 032714 (2005).

[2] M. Inokuti, Rev. Mod. Phys. **43**, 297 (1971).

[3] D. L. Matthews et al., Phys. Rev. Lett. **54**, 110 (1985).

[4] G. J. Tallents, J. Phys. D. **36**, R259 (2003).

[5] W. B. Li et al., Phys. Rev. A **67**, 062708 (2003).

[6] H. D. Cheng et al., Phys. Rev. A **72**, 012715(2005).

[7] L. F. Zhu et al., Phys. Rev. A**73**, 042703 (2006).

[8] L. F. Zhu et al.,Phys. Rev. A**75**, 032701(2007).

[9] R. D. Cowan, *The theory of Atomic Structure and Spectra* (University of California Press, Berkeley, CA, 1981).

[10] G. Snell, M. Drescher, N. Müller, U. Heinzmann, U. Hergenhahn, J. Viefhaus, F. Heiser, U. Becker, and N. B. Brookes, Phys. Rev. Lett. **76**, 3923 (1996).

Non-equilibrium and Anisotropic K-shell Radiation in Ultra-intense Laser-produced Plasmas

KAWAMURA Tohru, KAI Takeshi[1], KOIKE Fumihiro[2],
NAKAZAKI Shinobu[3], INUBUSHI Yuichi[1], OKANO Yasuaki[1],
FUJIOKA Shinsuke[1], NISHIMURA Hiroaki[1], NAKAMURA Tatsufumi[1],
JOHZAKI Tomoyuki[1], NAGATOMO Hideo[1], and MIMA Kunioki[1]
Department of Energy Sciences, Tokyo Institute of Technology, Nagatsuta-cho 4259, Midori-ku, Yokohama, Kanagawa, 226-8502 Japan
1) Institute of Laser Engineering, Osaka University, Yamada-oka 2-6, Suita, Osaka, 565-0871, Japan
2) Physics Laboratory, School of Medicine, Kitasato University, Kitasato 1-15-1, Sagamihara, Kanagawa, 228-8555 Japan
3) Department of Applied Physics, University of Miyazaki, Gakuen Kibanadai-nishi 1-1, Miyazaki, 889-2129, Japan
e-mail: kawamura@es.titech.ac.jp

Abstract

Numerical and experimental studies were carried out to gain insight into fast electron transport relevant to fast ignition. Atomic-population kinetics codes associated with K-shell radiation have been developed for quantitative and/or qualitative understanding of the energy deposition process by fast electrons. In the experiments, the Kα lines from partially ionized chlorine were diagnosed as a function of the thickness of an over-layered target, and a dramatic decrease in the radiation yield was found with an increase in the overcoat-thickness of the target at laser intensity of about 10^{17} W/cm^2. The experimental results were analyzed with the use of the numerical calculation codes, resulting in a plasma bulk-electron temperature of ~ 150 eV. With the spectroscopy of polarized Heα radiation, the velocity distribution function of fast electrons can be deduced and high polarization was experimentally obtained in low density plasma region ($\leq$ 10 times the critical density). It is inferred that collimated fast electrons are generated, and show large anisotropy along the propagation direction.

Keywords: fast ignition, fast electron transport, Kα radiation, polarization

1.Introduction

In fast ignition research, the efficient energy transfer from fast electrons generated by ultra-intense laser pulses is one of the critical issues [1]. A new x-ray spectroscopic method providing time- and space-resolved information has been expected to get quantitative and/or qualitative understanding of the energy transport in fast igniter plasmas. We propose the observation of Kα lines from partially ionized materials seeded in a target for the purpose. In fast ignition plasmas, free electrons can be approximated into two components, namely cold bulk electrons and fast electrons. The fast electrons are generated through collective processes with intense laser pulses [2] and are mainly responsible for the K-shell ionization (inner-shell ionization), while the cold bulk electrons are responsible for the outer-shell ionization. With the Kα radiation from partially ionized materials, this approximation thus work well to derive the bulk electron temperature heated by fast electrons [3]. In the study, a collisional-radiative equilibrium (CRE) code was developed to study the Kα radiation of dopant chlorine experimentally observed [4], and the plasma creation of about 100 eV was obtained [3].

In addition, direct observation of the fast electron properties is also indispensable to understand the energy deposition processes by fast electrons accompanied with electromagnetic instability in the over dense plasma. The fast electrons generated by ultra-intense laser pulses show anisotropic distribution along the propagation axis and the surrounding cold bulk electrons form return current to compensate for the neutrality with fast electrons. Optically allowed transition radiation was used to diagnose the velocity distribution function (VDF) of fast electrons [5]. However, the fast electrons were measured at the rear-side of an irradiated target, and the original features of the fast electrons may be lost for the sake of the long propagation in a target. To gain insight into the fast electron transport, polarized Heα radiation ($1s^2\,{}^1\mathrm{S}_0$ - $1s2p\,{}^1\mathrm{P}_1$) has been proposed as a useful diagnostic tool [6,7]. Polarized x-rays are generated due to anisotropic electron impacts by fast electrons, and the creation of population alignment associated with magnetic atomic sublevels is essential.

In this paper, the studies of Kα radiation associated with fast electrons transport relevant to fast ignition scheme are surveyed, and the anisotropic features of the generated fast electrons are discussed with the polarized Heα radiation, which is the latest progress of our study.

2. Kα Transitions from Partially Ionized Chlorine

The emission energies and oscillator strengths of Kα transitions were calculated by a multi-configuration Dirac-Fock (MCDF) atomic code GRASP [8]. Figure 1 shows the resultant radiative decay rates for various ionization states of chlorine. For the clarity of illustration, the transitions of the single 1s-vacant states are given; they are Cl^{1+} $1s2s^22p^63s^23p^5 \longrightarrow 1s^22s^22p^53s^23p^5$, ... Cl^{13+} $1s2s^22p^1 \longrightarrow 1s^22s^2$. For Cl^{14+}, the atomic transitions associated with all $1s2lnl'$ $(n = 2 \sim 3)$ state are shown. The energy differences from the primary Kα lines (Cl^{1+}) can distinguish the respective charge states. This feature is essential that the line radiation is useful for plasma diagnostics.

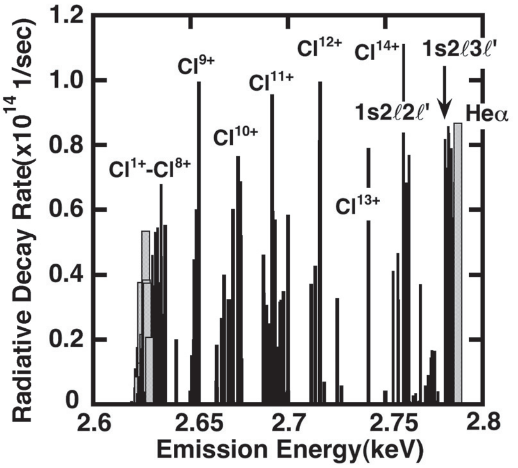

Figure 1: Radiative decay rates of Kα lines from partially ionized chlorine. The gray bars at the left-side show the Cl^{1+} Kα, and that at the right-side is the Heα.

In this study, the single 1s-vacant states with a highly excited spectator electron are considered; $1s2s^22p^Nnl(N = 1 \sim 5, n = 3 \sim 4)$ (Cl^{8+} $\sim$ Cl^{12+}) are included. The Kα transition energies from these states overlap significantly with those from $1s2s^22p^N(N = 1 \sim 5)$ (Cl^{9+} $\sim$ Cl^{13+}) [9].

To estimate the net intensity of the Kα radiation, Auger transitions are indispensable since Kα radiation is affected by the competition between radiative and Auger processes. Calculation of the Auger rates was performed with the use of a code developed by Fritzsche *et al.* [10]. The KLL-Auger is the predominant and the fluorescence yield is at most ~ 0.1.

3. Description of The Atomic Kinetics Model

The free electron distribution is assumed to be bi-Maxwellian consisting of cold bulk and fast electrons. In the framework of a bi-Maxwellian distribution, effective rate coefficients $Rate_{\rm eff}$ can be obtained as follows:

$$Rate_{\rm eff} \quad = \quad (1-h)\cdot Rate_{\rm Bulk} + h\cdot Rate_{\rm Fast}\ \ (1/\text{sec}), \tag{1}$$

where h stands for a fractional number of fast electrons, namely, $h = \frac{N_{\rm eFast}}{N_{\rm eFast}+N_{\rm eBulk}}$, $N_{\rm eFast}$ is the density of fast electrons, and $N_{\rm eBulk}$ is the density of the cold bulk electrons. In the case of three-body recombination $R_{\text{eff}}^{\text{3b}}$, however, two free-electrons have to be taken into consideration [3].

On polarization calculation, atomic cross-sections with magnetic sublevels for helium-like atoms were obtained using the Breit-Pauli R-matrix method [11]. The details of the calculations are described in the study by Kai *et al.* [12]. Radiative decay rates associated with LSJ-states were also obtained using the GRASP code, and the optical allowed transitions between JM-states were estimated using the Wigner-Eckert theorem. The calculation scheme to solve the population kinetics and the polarization of Heα radiation are given in Refs.[13,14]. π-light is defined as the x-ray component of which electric field is parallel to the direction of electron motion, and the light arises from the atomic transition $1s2p\,^1\mathrm{P}_1 \rightarrow 1s^2\,^1\mathrm{S}_0 + h\nu$ with $\Delta M = 0$. σ-light is the component perpendicular to the electron motion for which $\Delta M = \pm 1$. A quantization axis can be defined as perpendicular to an irradiated target surface, and the polarization P can be defined as $P = \frac{I_{\parallel} - I_{\perp}}{I_{\parallel} + I_{\perp}}$, where $I_{\parallel}$ and $I_{\perp}$ are respectively the intensity of Heα radiation of which electric fields are parallel and perpendicular to the axis. In the calculation, the VDF of the fast electrons is characterized by $T_{\text{Fast}-\text{z}}$ and $T_{\text{Fast}-\text{r}}$, where $T_{\text{Fast}-\text{z}}$ denotes the fast electron temperature along the quantization axis, and $T_{\text{Fast}-\text{r}}$ is that perpendicular to the axis.

4. Study on Kα Radiation from Partially Ionized Chlorine

An experiment [4] was carried out using a Ti:sapphire laser system, yielding average laser intensity of $1 \sim 2 \times 10^{17}\,\mathrm{W/cm^2}$.

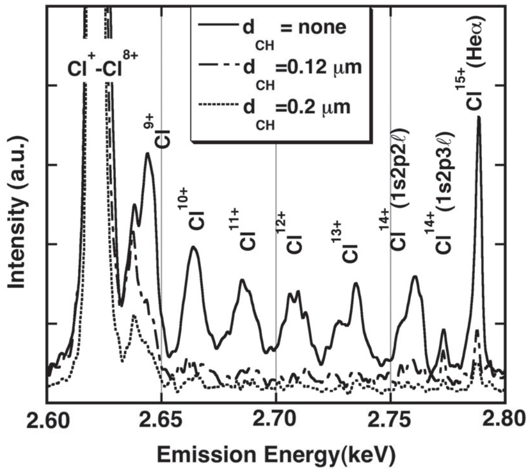

Figure 2: Time- and space-integrated Kα spectra experimentally obtained with the use of a Ti:sapphire laser system.

In the experiment, the fast electron temperature at the rear-side of an irradiated target was about 50 keV. A target was a 200 mm-thick polyvinylchloride (C_2H_3Cl) sheet coated with a parylene layer (CH) of which overcoat thickness d_{CH} was varied from $0 \sim 2.2$ mm. Figure 2 is a typical time- and space integrated spectrum, and the Kα radiation dramatically becomes weak with increase in the thickness of the CH-overcoat.

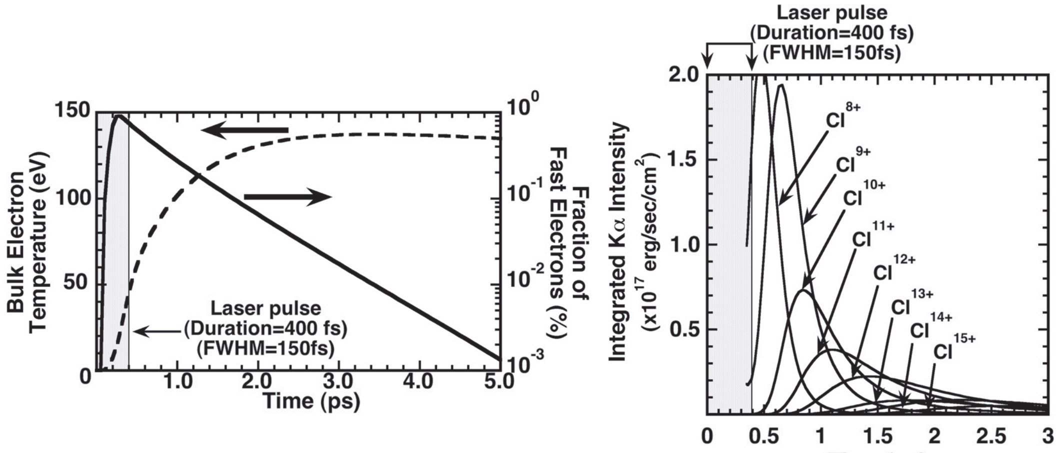

(a)

(b)

Figure 3: (a) Time evolution of bulk electron temperature and fractional fast electrons. (b) Time evolution of Kα radiation in the framework of a postprocess. The plasma density is assumed to be solid density of a target.

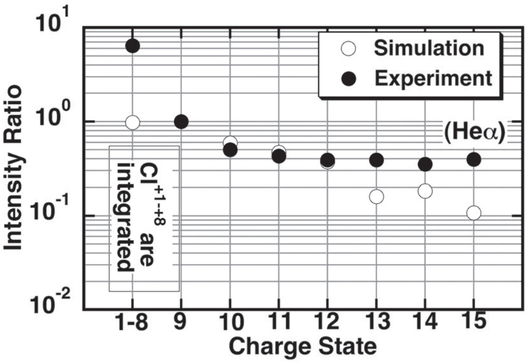

Figure 4: Intensity Ratio with respect to the Cl^{9+} Kα emission.

To estimate the time dependent Kα radiation, fast electron transport was calculated by a one-dimensional relativistic Fokker-Planck code [15]. The result is presented in Fig.3(a). After the irradiation of a laser pulse, the number of fast electrons decreases in time, dissipating their energy to the surrounding cold bulk electrons and the temperature rises up to about 140 eV. The temporal evolutions of the Kα radiation from each charge state are shown in Fig.3(b). They are integrated with respect to the time and the comparison was made between the numerical and the experimental results. In the comparison, the experimental data without the overcoat was used. In Fig.4, a reasonable agreement can be obtained.

5. Study on Polarized Heα Radiation

At the same laser intensity as in the above experiment, the polarization spectroscopy of Heα radiation from a C_8H_7Cl plasma was carried out [6,7]. Since the bulk electron temperature is low ($100 \sim 200$ eV) in the experiment, the K-shell atomic transitions are attributed to electron impacts by fast electrons. In the calculation, all the magnetic sublevels from the helium-like ground-state $1s^2\,{}^1S_0$ up to the $1s3d\,{}^3D_{3,2,1},{}^1D_2$ are considered.

For instance, Fig.5 shows the collisional excitation cross-sections by an electron impact for $1s^2\,{}^1S_0\,(M=0) \rightarrow 1s2p\,{}^1P_1\,(M=0,1)$. With the increase in the incident kinetic energy of a colliding electron, difference between the $M=0 \rightarrow M=0$ and the $M=0 \rightarrow M=1$ becomes small, and polarization shows negative if the electrons have an energy of above 50 keV, while those with the energies of below 50 keV have a contribution to positive polarization.

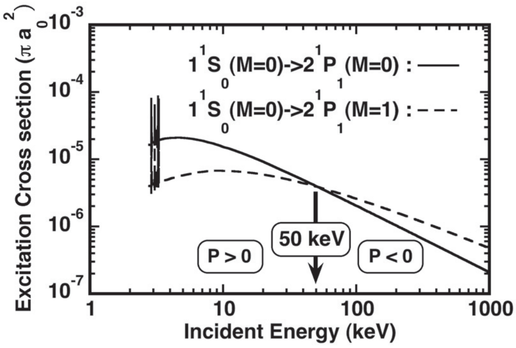

Figure 5: Collisional excitation cross-sections by an electron impact for $1s^2\,{}^1S_0\,(M=0) \rightarrow 1s2p\,{}^1P_1\,(M=0,1)$. a_0 stands for the Bohr radius.

To determine a time-history of background bulk electrons, the stopping range described by Batani [16] was adopted. The temporal evolution profile of fast electrons is assumed to be Gaussian with a full-width at half-maximum (FWHM) of 0.5 ps. The peak of fraction of fast electrons is the critical density for the laser wavelength of $\lambda = 800$ nm used in the experiments. In the study of Kawamura *et al.* [14], highly polarized Heα radiation can be observed only at low density plasma, while there is no polarization at solid density due to the frequent elastic collisions by the surrounding low temperature bulk electrons. In this study, the polarizations of above 10% can be expected at $N_\mathrm{i} = 4.5 \times 10^{21}\,\mathrm{cm}^{-3}$ ($\approx 0.05\rho_\mathrm{s}$, which corresponds to about $10n_\mathrm{c}$, where ρ_s, n_c are respectively the solid density and the critical density.), $T_\mathrm{Fast-z} = 10 \sim 50$keV and $T_\mathrm{Fast-r} = 1$ keV. In the experiment, because the resultant polarizations of time- and space-integrated Heα radiation are $10 \sim 30\%$, the plasma density from which the polarized Heα radiation arises may be less than the number density.

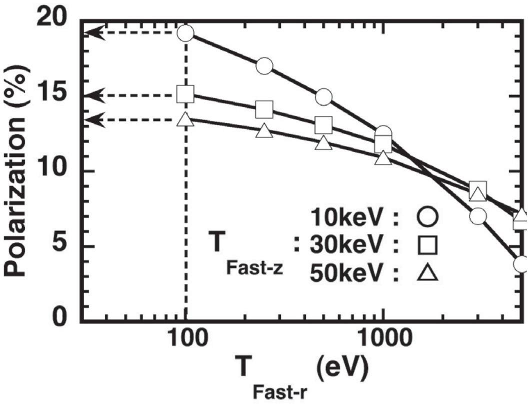

Figure 6: Dependence of polarization on $T_\mathrm{Fast-r}$ for $T_\mathrm{Fast-z} = 10$, 30, 50 keV, and total ion density $N_\mathrm{i} = 4.5 \times 10^{21}\,\mathrm{cm}^{-3}$.

In Fig.6, the calculations with $T_\mathrm{Fast-r} \leq 5$ keV are presented to demonstrate the effect of the narrow transverse thermal spread of the fast electron beam. The calculation results show that the polarization may reach up to $\sim 20\%$ at $T_\mathrm{Fast-r} \sim 100$ eV, $T_\mathrm{Fast-z} = 10$ keV. Since the fast electrons with a large transverse velocity component are captured by the locally generated magnetic field due to filamentation instability, the anisotropy of the VDF of the fast electrons is enhanced and so is the polarization at a plasma density of $\sim 4n_\mathrm{c}$ [17]. Due to an increase in the number of elastic collisions in the dense region of greater than $10n_\mathrm{c}$, the alignment can be broken, reducing the polarization.

6. Conclusions

In conclusion, the present status of the study on fast electron transport relevant to fast ignition plasmas in the framework of x-ray spectroscopy was presented. In this study, population kinetics codes associated with the 1s-vacant atomic states for Kα spectroscopy, and the alignment creation among magnetic atomic sublevels for polarization spectroscopy were developed. This study provides quantitative and/or qualitative understanding of x-ray generation from hot dense plasmas, and it also demonstrates the promising potential of x-ray spectroscopy to gain insight into fast electron transport in the fast ignition plasmas.

7. Acknowledgments

This work was partly supported by the JSPS-CAS Core-University Program in the field of “Plasma and Nuclear Fusion”.

References

[1] M. Tabak *et al.*, Phys. Plasmas **1**, 1626 (1994).
[2] S. C. Wilks and W. L. Kruer, J. Quant. Electron **33**, 1954 (1997)
[3] T. Kawamura *et al.*, Phys. Rev. E **66**, 016402 (2002).
[4] H. Nishimura *et al.*, J. Quant. Spectrosc. Radiat. Transfer **81**, 327 (2003), *ibid.* **87**, 211 (2004).
[5] J. Zheng *et al.*, Phys. Rev. Lett. **92**, 165001 (2004).
[6] Y. Inubushi *et al.*, J. Quant. Spectrosc. Radiat. Transfer **99**, 305 (2006), *ibid.* **101**, 191 (2006).
[7] H. Nishimura *et al.*, Plasma Phys. Control. Fusion **47**, B823 (2005).
[8] K. G. Dyall *et al.*, Comput. Phys. Commun. **55**, 425 (1989).
[9] T. Kawamura *et al.*, J. Quant. Spectrosc. Radiat. Transfer **81**, 237 (2003); *Proceedings of the 3rd IFSA*, 1022 (2003) (American Nuclear Society, Illinois, 2004).
[10] S. Fritzsche, and B. Fricke, Phys. Scripta **T41**, 45 (1992).
[11] K. A. Berrington *et al.*, Comput. Phys. Commum. **92**, 290 (1995).
[12] T. Kai *et al.*, Phys. Rev. A **75**, 012703 (2007).
[13] P. Hakel *et al.*, Phys. Rev. E **69**, 056405 (2004).
[14] T. Kawamura *et al.*, Phys. Rev. Lett. **99**, 115003 (2007).
[15] T. Johzaki, *et al.*, Fusion Sci. Technol. **43**, 428 (2003).
[16] D. Batani, Laser Part. Beams **20**, 321 (2002).
[17] Y. Inubushi *et al.*, Phys. Rev. E **75**, 026401 (2007).

Analysis and Simulation of XUV/EUV Spectra of Laser-produced Gold, Iodine and Tin Plasmas

Maogen Su[1], Chenzhong Dong[1, 2, †], N Murphy [3], P Hayden[3] and G O'Sullivan[3]

1) College of Physics and Electronics Engineering, Northwest Normal University, Lanzhou, 730070, China
2) National Laboratory of Heavy–Ion Accelerator of Lanzhou, Lanzhou, 730000, China
3) School of Physics, University College Dublin, Belfield, Dublin 4, Ireland

†*e-mail: dongcz@nwnu.edu.cn*

Abstract

The photoabsorption spectra of gold and iodine ions have been recorded using the Dual Laser-produced Plasma (DLP) technique in the 65 to 125 eV region, and the EUV emission spectra of tin ions have also been observed. With the aid of multiconfiguration Hartree-Fock calculations, the measured spectra have been identified. The dominant features in the gold spectra are $4f-5d, 6d$ and $5p-5d$ transitions arrays, while the iodine spectra arise from $4d-nf$ excitation, which evolves from $4d-\varepsilon f$ shape resonance. The EUV spectra of tin plasma have also been simulated by combining the calculations of atomic data using the cowan code and a steady-state collisional radiative (CR) model.

Keywords: photoabsorption, the Dual Laser-produced Plasma (DLP), emission spectra, EUV, shape resonance, collisional radiative (CR) model

1.Introduction

In recent years, there has been an ongoing interest to study the Laser Produced Plasma (LPP) when solid targets are subjected to high energy or high power laser radiation. In order to test theoretical models and explain the experimentally associated phenomena in the laser produced plasma, it is necessary to obtain detailed information on the positions and intensities of lines from each stage.

In the present work, the photoabsorption spectra of gold and iodine ions have been recorded using the dual laser-produced plasma (DLP) technique in the 65 to 125 eV region, and the EUV emission spectra of tin ions have also been observed. To identify the measured spectra, a series of theoretical calculations are performed with the RCN/RCN2/RCG suite of Hartree-Fock codes [1].

2. Photoabsorption spectra of Au^{2+}, Au^{3+} and Au^{4+}

Gold is the last member of the 5d transition metal series which has a filled 5d subshell. In the $5d^n6s^2, 5d^{n+1}6s$ and $5d^{n+2}$ configurations of the 5d transition metal series, $5d$ and

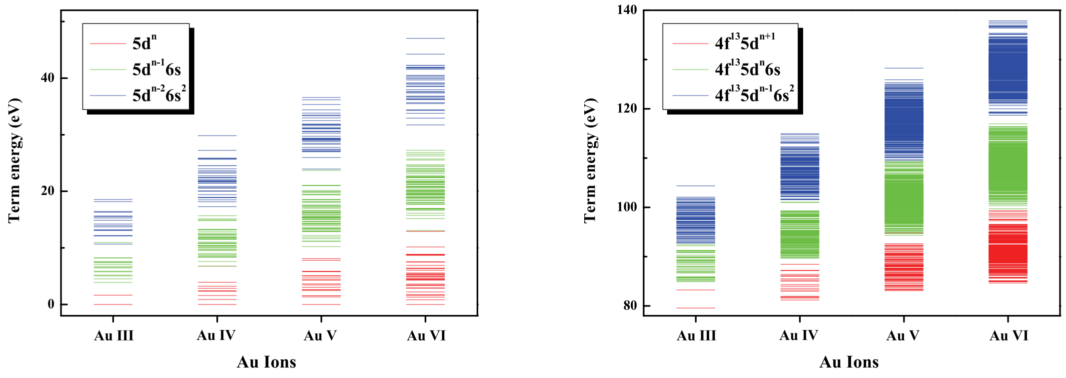

Figure 1: Energy level diagram from Au^{2+} to Au^{5+}.

$6s$ electrons have similar binding energies, the configuration interactions among them are generally important. The ground state of gold ions from Au^{2+} to Au^{4+} possess open $5d$ subshell, and the excited states contain open $4f, 5p, 5d, 6s$ and $6d$ sub-shells, so the resulting configurations contain a large number of near degenerate energy levels, as it is indicated in Figure 1. Meanwhile, because the $5p-5d$ and $4f-5d$ excitations are strongly coupled to the same $5d-\varepsilon f$ continuum, the autoionization widths must be calculated by summing the contributions from the allowed non-radiative decay processes. So the spectrum of gold ions are very complicated.

Figure 2 shows the $4f-md$ and $5p-md$ (m= 5, 6, 7 and 8) transition arrays of Au^{2+}, respectively. If their autoionization width are larger than the Gauss instrument width, all the transition lines are convolved with their autoionization width, otherwise they are convolved with a Gaussian profile (FWHM=0.05 eV). From the left figure, we found that the $4f-5d$ transition arrays mainly lie at about 82 eV, which close together. However, for the $4f-6d, 7d, 8d$ transition arrays, each transition array consists of four broader peaks of the different magnitude and the interval between peaks is about 4 eV, and with increasing m, they shift to the higher energy side and overlap with each other. In the right figure, it shows the $5p-md$ transition arrays. Seen from this figure, the contribution of the $5p-5d$ transition arrays mainly lie at the lower energy side, it consists of two more broader continuum band than the $4f-5d$ transition arrays, the center of one band lie at near 57 eV and the other is about 72 eV. With increasing m, the cross section of other transition arrays decrease rapidly, the band also shifted to the higher energy side, and overlap with each other.

In Figure 3, the calculated and experimental spectrum of Au^{2+}, Au^{3+} and Au^{4+} are

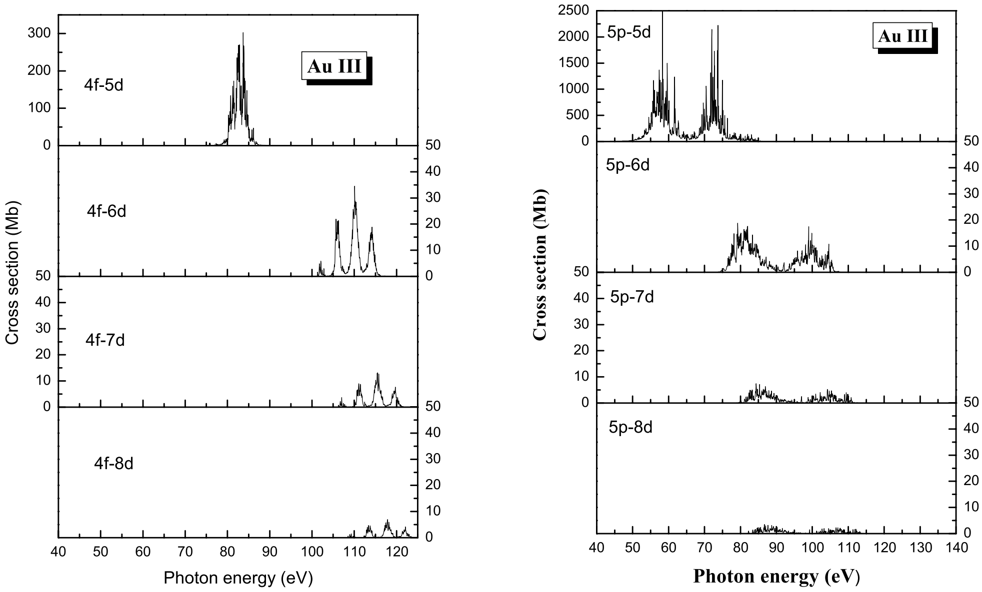

Figure 2: $4f, 5p - md(m = 5, 6, 7, 8)$ transition arrays of Au^{2+}.

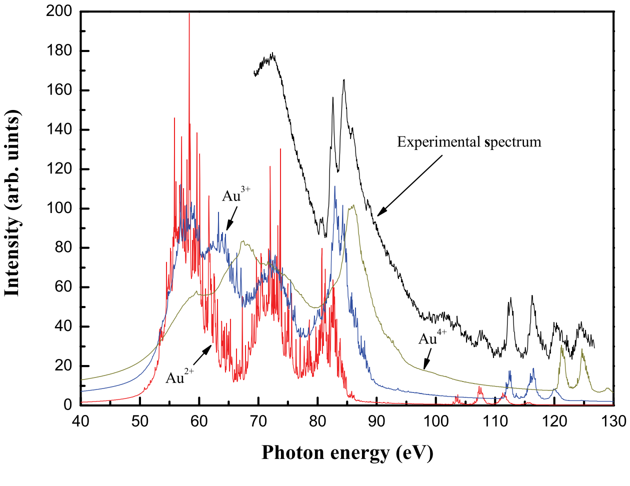

Figure 3: Comparison between theoretical and experimental spectra .

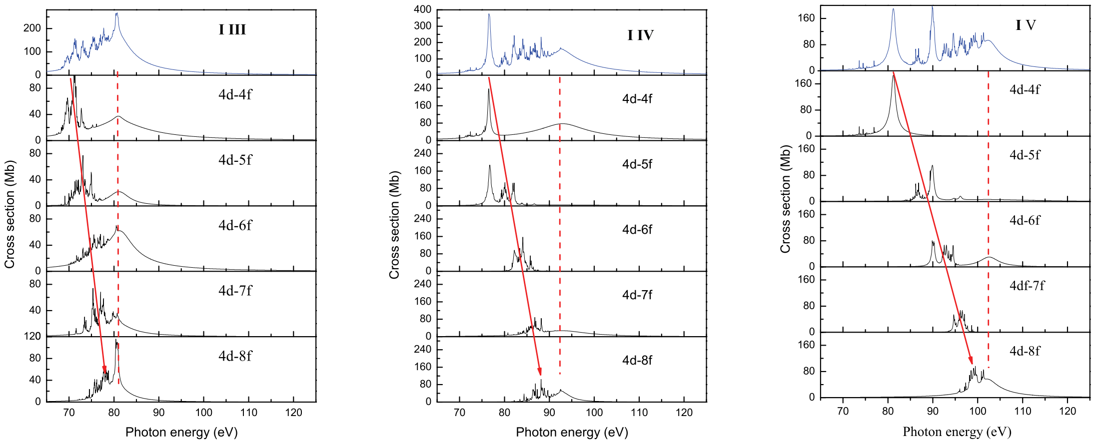

Figure 4: Cross section of $4d-mf$ transition array from I^{2+}, I^{3+} and I^{4+}.

shown. It can be clearly seen that experimental spectrum of gold ions in the XUV range do not consist of sharp and well separated features. By comparing the $4f-5d$ and $5p-5d$ transition spectra of the different gold ions, it is found that the transitions tend to overlap for different ionization stages, the $5p-5d$ transition cover a very wide energy range from 40 to 110 eV, while the contribution of the $4f-5d$ mainly lies in the 79 to 90 eV energy region which overlaps with the $5p-5d$ transitions in Au^{3+} and Au^{4+}, the transition features have the sharp asymmetric structure which is quite similar with the structure of Pt I observed by J. T. Costello, *et al.* [2,3]. The $4f-6d$ arrays are well separated at the higher energy side, which makes identification of different ions from an experimental spectrum possible.

3. Photoabsorption spectra of I^{2+}, I^{3+} and I^{4+}

The $4d$ absorption spectra of I, I^{+} and I^{2+} have been observed by G. O'Sullivan, *et al.* [4] using the dual laser-produced plasma technique. They found that the dominant feature in each spectrum arises from $4d-mf$ excitation, and which evolves from a $4d-\varepsilon f$ shape resonance in neutral iodine to a feature containing discrete $4d-mf$ transitions in I^{2+}. They think that the gradual collapse of the 4f wave function causes the 4d-f oscillator strength to shift slowly from a shape resonance in the neutral to the discrete spectrum in the ions.

In this work we revisit the I^{2+} spectrum and investigate the situation in I^{3+}, I^{4+} and I^{5+} ions. The photoabsorption spectra of iodine ions were recorded in UCD using the DLP technique. Figure 4 shows the cross sections of $4d-mf$ transition arrays of I^{2+}, I^{3+}

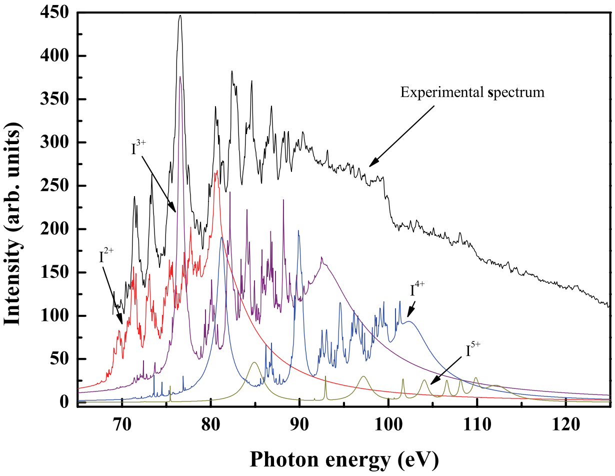

Figure 5: Comparison between theoretical and experimental spectrum.

and I^{4+}, respectively. Compared with the $4d-4f$ transition arrays of these three ions, we found, with increasing ionization, the shape resonance of $4d-4f$ not only relatively away from the discrete structure but also disappear when in I^{4+}. This reflects the $4f$ wavefunction contraction into the inner well region, with increasing ionization, the inner potential well becomes deeper and narrower, then the barrier disappears. In addition to, we can find that the center of the shape resonant part is not changed. The discrete structures of the left side, with increasing m, shifted to the centre of the shape resonant.

Figure 5 shows the comparison between theoretical and experimental spectra of I^{2+}, I^{3+}, I^{4+} and I^{5+}, respectively. It can be clearly seen that the spectrum is dominated by a broad $4d-f$ resonance while discrete transition arise from $4d-nf$ excitation. And with increasing ionization, the shape resonance disappears and the discrete structures become dominant. And we also find when the time delay is longer, the contributions from I^{2+} and I^{3+} are more important than those from higher charged I^{4+} and I^{5+} ions. But for the shorter time delay, the contributions from higher charged ions become more important.

4. EUV spectra in laser-produced Sn plasmas

Laser-produced tin plasmas have been selected as a promising light source for the next-generation extreme ultraviolet (EUV) lithography process in semiconductor device fabrication [5-7]. For the pure tin plasmas, it is optically thick to 13.5 nm EUV light because the properties of Sn plasma depend strongly on the parameters of the laser pulse

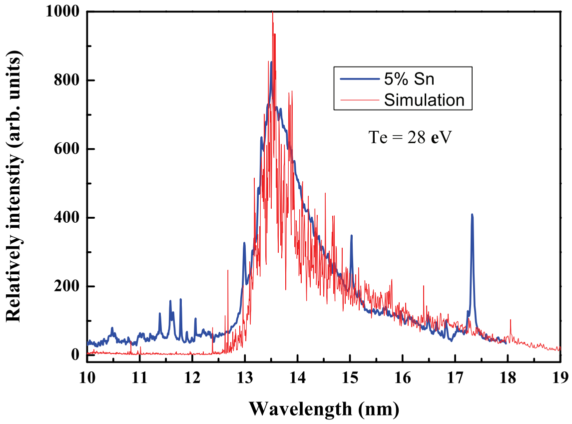

Figure 6: Comparison between simulated and experimental spectra.

and target concentration, such as wavelength, pulse width, and focal spot size. Whats more, when the focal spot is large, the EUV emission must pass through a longer plasma with higher density, and exist stronger reabsorption [8].

To reduce reabsorption, one of the techniques is by using 5% tin doped target to reduce the number of tin ions presented in the plasma. Figure 6 shows the emission spectrum from 5% tin doped target. In the present calculations, the configurations of tin ions are $4d^n$ for the ground state, $4d^{n-1}ml$ and $4p^5 4d^{n+1}$ (n=1-8, m=5,6) for the excited states. The transitions between these configurations relate to open 4p and 4d subshells, so there exits a large number of near-degenerate energy levels when they couple with the electrons of other subshells. As a result, the transitions between these levels are extremely complex and overlap with each other, and form an unresolved transition array (UTA). In order to simulate the experimental spectra, a steady state collisional-radiative (CR) model of Colombant and Tonon [9] is used to caculate the populations of each ion, where the electron temperature is taken as 28 eV and the electron density is $1 \times 10^{20} cm^{-3}$. A comparison with the experimental spectra is presented in Figure 6. Good agreement between the theory and the experiment can be found.

5. Conclusions

The spectra of gold, iodine and tin ions have been observed and analyzed in the XUV/EUV spectral region. Calculations with the Cowan suite of programs are successful in accounting for all of the observed spectra structure. And the spectra clearly display the effects of the 4f wavefunction contraction.

Acknowledgements

This work was supported by the SFI/RIA China-Ireland Research Collaboration Fund(CI-2004-07), the National Natural Science Foundation of China (Grant No.10434100, 10774122), the Core-University Program between Japanese Society of Promotion of Science and Chinese Academy of Sciences, the Specialized Research Fund for the Doctoral Program of Higher Education of China (Grant No. 20070736001), the Foundation of Center of theoretical Nuclear Physics of National Laboratory of Heavy Ion Accelerrator of Lanzhou, and the Foundation of Northwest Normal University(NWNU-KJCXGC-03-21).

References

[1] R. D. Cowan, The Theoretical of Atomic Structure and Spectra(University of California Press, Berkely, 1981)
[2] J. T. Costello, E. T. Kennedy, B. F. Sonntag, et al, J. Phys. B: At. Mot. Opt. Phys., **24**, 5063(1991).
[3] U. Köble, J. T. Costello, J. P. Mosnier, et al, J. Phys. B: At. Mot. Opt. Phys, **28**, 181(1995)
[4] G. O'Sullivan, C. McGuinness, J. T. Costello, et al, Phys. Rev. A, **53**, 3211(1996).
[5] D. Attwood, J. Phys. D: Appl. Phys., **37**(2004).
[6] C. Gwyn, D. Attwood and D. Sweeney, J. Van. Sci. Technol. B, **16**,3142(1998).
[7] A. Sasaki, A. Sasaki, K. Nishihara, et al, IEEE J. Quan. Elec., **10**,1307(2004).
[8] Y. Tao, S. S. Harilal, M. S. Tillack, et al, Optic. Lett., **31**, 2492(2006).
[9] D. Colombant, G. F. Tonon, J. Appl. Phys., **44**, 3524(1973).

ATOMIC STRUCTURE CALCULATIONS UNDER EXTERNAL CONFINEMENT

B. Fricke*, J. Anton*, S. Fritzsche* and P. K. Mukherjee†

* Institut für Physik, Universität Kassel, D-34109 Kassel, Germany
† Department of Spectroscopy, Indian Association for the Cultivation of Science,
Jadavpur, Kolkata 700032, India

Abstract

We present a brief overview of the various types of plasmas as well as the state of the art of the description of atomic data under external confinement. The Debye screening method and the Ion sphere model are described shortly. Using the inherent parameters of these models one is able to describe the shifts of atomic spectral data in a plasma. Newest results of fully self-consistent relativistic ab-initio DF-calculations are presented for the resonance line shifts of Na, Rb, and Cs in fluid helium.

1 Introduction

In addition to the three normal states of matter: solid, fluid and gaseous one often adds the plasma state, because the dominant part of the matter in the world exists in this form. Of course all matter consists of atoms or ions, but the complexity of their description is very different. As we all know, already single atoms are quite complicated to describe. This becomes even more complex in a gas under pressure and even more in a plasma, where the gas is ionized so that the ions are in a bath of electrons.

In this contribution we would like to summarize the theoretical descriptions of this state of matter where we call the influence of the other atoms on an atom as "under external confinement".
Which atomic physical quantities are expected to change with respect to the free atom? These are: energy levels, polarizabilities, oscillator strengths, transition probabilities etc.

In order to describe these quantitites one adopts models based on surrounding weakly and strongly-coupled plasmas which are described by a parameter called "coupling strength". The plasma strength (Γ) is expressed as the ratio of the average Coulomb energy to the kinetic energy of the plasma particles. One has a weakly coupled plasma with a coupling strength $<< 1$ for

- gaseous discharge plasma with $T \sim 10^4$ K and $n \sim 10^{11}$/c.c.
- plasma in controlled thermonuclear reaction at $T \sim 10^8$ K and $n \sim 10^{16}$/c.c.
- solar coronal plasma $T \sim 10^6 - 10^7$ K and $n \sim 10^6 - 10^{10}$/c.c.
- Tokomak plasma $T \sim 10^5 - 10^7$ K and $n \sim 10^8 - 10^{16}$/c.c.

and a strongly coupled plasma with a coupling strength ≥ 1 and sometimes $>> 1$

- highly evolved stars in high density states
- interior of Jovian planets
- plasma in explosive shock tubes
- two-dimensional states of electrons trapped in surface states of liquid helium
- laser-produced plasmas.

The temperature varies and the typical densities are $> 10^{23}$/c.c.

Plasma embedded calculations are important because

- plasma polarisation shifts are used for spectroscopic diagnostics and X-ray laser design,
- the deformation of the ionic field by plasma results in the interesting phenomena of pressure ionization and line merging,
- spectral line shifts determine the magnitude of the plasma coupling strength and suggests possible ways to obtain plasma parameters.

In effect one can say that each different type of calculation can be of importance in the understanding of the plasma under consideration.

2 Models

Several atomic and ionic species of one- and two-electron systems have been investigated using the weak coupling model of the plasma which usually is described by the *Debye screening model* [1].

Several ionic species of one-and two-electron systems have been investigated using the strong coupling model of the plasma which often is described by the *Ion sphere model* [2].

In addition the effect of weakly coupled plasma on exotic systems like $p^+\mu^-$, $\mu^+\mu^-$, $e^+e^-e^-$, H_2^+, $\mu^+e^-e^-$, $\mu^+\mu^-\mu^-$, $\pi^+\mu^-\mu^-$, $p^+p^+\mu^-$, $d^+d^+\mu^-$, $t^+t^+\mu^-$ etc. have been analyzed in detail and their stability under Debye plasma has been investigated [3]. These systems can also be considered "under external confinement" because the systems are created in a neutral environment when particles are slowed down in matter and as such we may consider it as a plasma sourrounding the exotic systems.

Both models depend on parameters. The *Debye screening model* depends on the Debye screening parameter μ which is dependent on the temperature and number density of the surrounding plasma. The *Ion sphere model* depends on the size of an inpenetrable spherical box surrounding the system. This gives additional restriction due to the altered boundary conditions applied to the wave functions, and the subsequent conditions of the pressure generated due to that confinement. In both models one solves the many-electron Schrödinger equation, but with different effective potentials. The Hamiltonian can be written as

$$H_0 = \sum_{i=1}^{n} \left[-\frac{1}{2}\nabla_i^2 + V_{\mathrm{eff}}(r_i) \right] + \sum_{i<j} \frac{1}{r_{ij}}. \tag{1}$$

The effective potentials are defined as

$$V_{\mathrm{eff}} = \frac{Z\, e^{-\mu r_i}}{r_i} \quad \text{and the two} - \text{body interaction} \quad \frac{e^{-\mu r_{ij}}}{r_{ij}} \tag{2}$$

for the *Debye plasma model* [1] and

$$V_{\mathrm{eff}} = -\frac{Z}{r_i} + \frac{Z-N}{2\,R} \left\{ 3 - \left(\frac{r_i}{R} \right)^2 \right\} \tag{3}$$

for the *strongly coupled model* [2].

The effective potentials are functions of the plasma parameters. For a Debye plasma one uses the Debye screening parameter [1]

$$\mu = \left[\frac{4\,\pi\,(1+Z)\,n}{k\,T} \right]^{1/2} \tag{4}$$

where k is the Boltzman constant. A wide variety of plasma conditions can be simulated by altering the value of μ. The quantity $r_d = 1/\mu$ is called the Debye shielding length.

For a strongly coupled plasma one uses the Wigner-Seitz radius [2]

$$R = \left(\frac{Z-N}{\frac{4}{3}\,\pi\,n} \right)^{1/3} \tag{5}$$

which is a function of the plasma density n. In this strongly coupled plasma model one assumes that no electron current goes through the boundary surface and the wave function must vanish at the Wigner-Seitz radius.

Using these procedures one yields results on: spectral frequencies, excited state wave functions, response properties like the dynamic polarizabilities, oscillator strengths and transition probabilities as well as ionization potentials under confinement. Particularly valuable are the shifts of spectral lines which might give an idea about the order of magnitude of the plasma parameters.

In the case of three-body exotic systems one also solves the Schrödinger equation with a Hamiltonian where each of the 3 particles is described by the single-particle kinetic energy $\nabla^2/2\,m$ and a potential term $\exp\left(-\mu\, r\right)/r)$ with reference to a coordinate system associated with a triangle the corners of which represent the positions of the three particles and the sides, their distances. Such a description favours correlated wave functions of Hylleraas type and one obtains accurate results. The details can be found in [3].

One of the many examples is given in Tab. 1 where the energy shifts in eV of the Lyman-α-line of Al^{+12} in a strongly coupled plasma are listed for different electron densities. A comparison with the experimental shifts might give an idea about the parameters in the observed system.

Electron density (n)	non-relativistic	relativistic
$2 \cdot 10^{24}$	2.72	2.69
$2.5 \cdot 10^{24}$	3.41	3.37
$3 \cdot 10^{24}$	4.10	4.06

Table 1: Line shifts in eV of the Ly_α line of Al^{+12} in a strongly coupled plasma as function of the electron density

The experimental shift is 3.7 ± 0.7 eV at $T = 300$ eV and $n \approx 8 \cdot 10^{23}$/c.c. [4]. The quantum mechanical impact theory [5] produces a red shift of 3.5 eV at $T = 300$ eV and $8 \cdot 10^{23}$/c.c.

Besides these parameter-dependent models the theoretical description tries to be more and more ab-initio. The state of the art for the spectral line shifts in atoms in a He matrix is described below.

3 Shifts of spectra of guest atoms in a He matrix

Experiments involving optical investigations on the spectra of foreign atoms in liquid helium were done by a number of groups over many years [6, 7, 8, 9]. Liquid helium is especially interesting because the constituents are small, the interaction between them is weak, there is no solidification under saturated vapour pressure, the quantum effects are manifested under superfluid conditions, the motion is highly correlated and the surface conditions are clean and undisturbed.

Observations are as follows [6]: spectral lines shifts compared to free systems, change in the line shape and profile, a broadening and splitting of adsorption lines, a reduction of the ionization potential, absence of resonant radiation in light alkali atoms (between 200 and 800 nm) and the presence of forbidden lines.

Due to the complexity of the problem ab-initio calculations are difficult and up to now has been applied only to the principal excitation lines of alkali atoms Na, Rb and Cs embedded in liquid helium where the line shifts are expected to be relatively large due to their loosely bound valence electron. Such an attempt has been made for the system Na in liquid helium by Ludwig et al. [10] using Monte-Carlo simulations followed by quantum chemical calculations. The liquid configuration was generated by computer simulation using the Metropolis technique in which Lennard-Jones pair potential was used for the Na-He interaction. The He-He pair potential was generated from quantum chemical calculation. Using this method a large number of He atoms (up to 1000) were included at 2 K and 1 atm. In the full quantum chemical calculation using TDDFT 42 atoms in the first solvation shell were used. This method yielded a shift between 14.7 and 18.9 nm with a FWHM of about 6 to 7 nm depending of the density functional choosen in the calculation [10].

We have adopted here a different approach. We perform fully relativistic density functional calculations (RLDA) [11] of a cluster where we included the central atom together with 14 He atoms which build up a first layer of surrounding He atoms with a reasonable spherical symmetry. The He-He pair distances are compatible with that in the pure liquid phase. In this method the distance R between the central and the He atoms is not a free parameter anymore; instead we calculate the total energy of the system as function of the distance R. The result is shown in Fig. 1 for the three systems NaHe$_{14}$, RbHe$_{14}$ and CsHe$_{14}$. All three potential curves show clear minima. At these distances we then have calculated the shift of the resonance lines s to $p_{1/2}$ and s to $p_{3/2}$. The result is presented in Tab. 2 where we also have included the results of other theoretical calculations as well as the experimental ones. Unfortunately experimental results are available only for the Rb and Cs system. For both systems the values agree very well. The main discrepancy exists between our result and other theoretical values for the Na system. But one has to have in mind that no experimental results are available for this system yet.

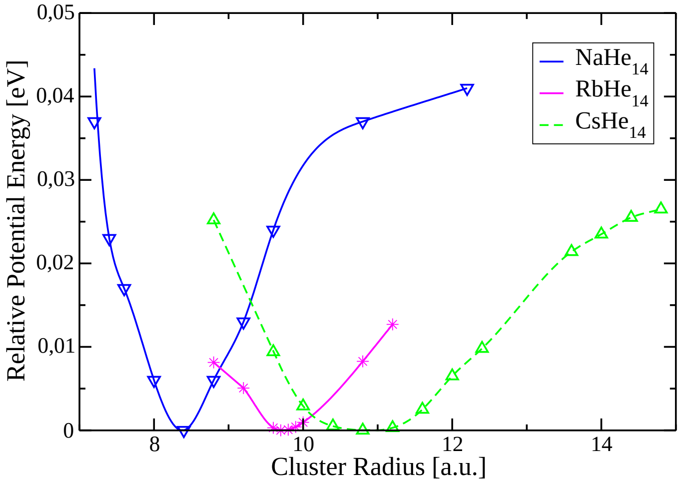

Figure 1: Ab-initio potential energy curves for the three systems NaHe$_{14}$, RbHe$_{14}$ and CsHe$_{14}$.

Transition	Shift		Av. Shift	
	Present	Other	Present	Other
Na				
$s_{1/2} \to p_{1/2}$	-22.90		-22.81	-16.70^a
$s_{1/2} \to p_{3/2}$	-22.72			-15.00^b
				-18.6∼-18.9^c
Rb				
$s_{1/2} \to p_{1/2}$	-14.02	-16.8±0.5^d	-15.415	-16.4^d
$s_{1/2} \to p_{3/2}$	-16.81	-16.0±0.5^d		
Cs				
$s_{1/2} \to p_{1/2}$	-15.52	-18.4±0.5^d	-16.675	-18.25^d
		-26^b		-26.5^b
$s_{1/2} \to p_{3/2}$	-17.83	-18.1±0.5^d		
		-27^b		

^{a}: Ref.[12], ^{b}: Ref.[13], ^{c}: Ref.[10], ^{d}: Ref.[14]

Table 2: Spectral line shifts (nm) in alkali-Helium cluster by the RLDA method

4 Conclusion

We have tried to illustrate the various possibilities to describe the change of atomic spectral parameters when the atoms are embedded in a plasma. The two methods, the *Debye screening method* for the weakly coupled plasma and the *Ion sphere model* for the strong coupling plasma are very valuable to describe such systems. The disadvantage of course is that their results depend on parameters: for the *Debye screening model* on the Debye screening parameter and for the *Ion sphere model* on the Wigner-Seitz radius which defines the confinement of an atom in a box with this radius.

Both methods help to "understand" the behaviour of such systems. In the ab-initio methods one calculates parts of the plasma and includes the influence of the external confinement. This means that the other surrounding atoms are included in the calculation on the same level as a whole in a quantum-chemical fashion. This is a big step in the direction to overcome the parameters used in the old methods up to now. In the case of the systems of Na, Rb and Cs in liquid helium we have made the first step in this direction. The agreement with experimental values speaks for this method. Of course one has to be aware that such a method is very eleborate and time consuming.

5 Acknowledgement

J.A. and S.F. would like to acknowledge the support by the DFG and P.K.M to the AvH Foundation.

References

[1] A. I. Akhiezer, I. A. Akhiezer, R. A. Polovin, A. G. Sitenko, K. N. Stepanov, Plasma Electrodynamics, Linear Response Theory, Vol. 1, Oxford: Pergamon Press (1975)

[2] S.Ichimaru, Rev. Mod. Phys. **54**, 1017 (1984)

[3] A. N. Sil, M. Pawlak, P. K. Mukherjee, M. Bylicki, J.Q.S.R.T., **109**, 873 (2008) (available online) and references therein.

[4] A. Saemann, K. Eidmann, I. E. Golovkin, R. C. Mancini, E. Andersson, E. Förster, K. Witte, Phys. Rev. Lett. **82**, 4843 (1999)

[5] H. Nguyen, M. Koenig, D. Benredjem, M. Caby, G. Coulaud, Phys. Rev. A **33**, 1279 (1986)

[6] B. Tabbert, H. Günther, G. zu Putlitz, J. Low Temp. Phys. **109**, 653 (1997)

[7] B. Tabbert, M. Beau, M. Foerste, H. Günther, C.Hönninger, H. Hust, K. Layer, G. zu Putlitz, T. Schumacher, Z. Phys. B **98**, 399 (1995)

[8] T. Yabuzaki, T. Kinoshita, K. Fukuda, Y. Takahashi, Z. Phys. B **98**, 367 (1995)

[9] Q. Hui, J. L. Persson, J. H. M. Beijersbergen, M. Takami, Z. Phys. B **98**, 353 (1995)

[10] V. Ludwig, P. K. Mukherjee, K. Coutinho, S. Canuto; Phys. Rev. A **72**, 062714 (2005)

[11] J. Anton, P. K. Mukherjee, B. Fricke, S. Fritzsche, J. Phys. B **40**, 2453 (2007)

[12] M. Beau, H. Günther, G. zu Putlitz, B. Tabbert; Z. Phys. B **101**, 253 (1996)

[13] G. De Toffol, F. Ancillito, F. Toigo; J. Low Temp. Phys. **102**, 381 (1996)

[14] Y. Takahashi, K. Sano, T. Kinoshita, T. Yabuzaki; Phys. Rev. Lett. **71**, 1035 (1993)

Spectroscopy of Highly Charged Ion with an EBIT

H.A.Sakaue, H.Kikuchi[A], N.Nakamura[A], S.Ohtani[A], H.Tanuma[B], N.Yamamoto, D.Kato, T.Kato, H.Hara[C] and T.Watanabe[C]

NIFS, ILS/UEC[A], TMU[B], NAOJ[C]

Abstract

The spectroscopic investigation extreme ultraviolet (EUV) radiation is very important for determination of properties and mechanism of astrophysical and laboratory fusion plasma, such as density, temperature, charge distribution, heating and cooling etc. The EUV wavelength range contains emission line of the L-shells of highly charged ion of low- and medium-Z elements as well as of the M-shells of HCI for high-Z elements. We measured the EUV spectra (100-300Å) of highly charged iron ion with flat-field grazing-incidence (3°) grating (1200/mm) spectrometer mounted at the Tokyo-EBIT. The electron energy ranges are from 2.2keV to 300eV. We compared this EBIT spectrum with LHD spectrum and found a difference.

Keywords: EUV, highly charged ion, HCI's, EBIT, electron-ion collision,

1. Introduction

As for the diagnostics of LHD plasma and the heating mechanism of the corona of the sun, it pays attention to the spectrum of the highly charged Na, Mg, Al-like iron ion, recently [1]. At present, in our National Institute for Fusion Science (LHD) and National Astronomical Observatory of Japan (Solar-B), we proceed with the joint research of "The research of the non-equilibrium plasma"[2]. The Solar-B is a highly sophisticated observational satellite. This satellite is equipped with three advanced solar telescopes. These are visible light, extreme ultraviolet (EUV) and X-ray spectrometers. It was launched on 22 September 2006. The diagnostics for the Solar corona through EUV spectroscopy would reveal the heating mechanism and dynamics of the active solar corona. Highly charged ions (HCI's) of Fe with moderate charge states (q~10) are observed [3,4]. On the other hand, the high temperature and density plasma which can be controlled is diagnosed in LHD. From the comparison of two kind of plasma, we purpose to construct the non-equilibrium plasma model. And EBIT (Electron Beam Ion Trap) provides the fundamental data on the electron-HCI collision process in such a non-equilibrium plasma.

2. Experiments

We explain about EBIT. The performance of the highly charged ion source is very important when the highly charged ion research is done. Our joint research group succeeded in the development of the superconductive EBIT [5], and it had given many research results. The experimental set up of the Tokyo-EBIT is shown in figure 1. This EBIT is composed of ion trap and high density and high energy electron beam. The emitted electrons from the cathode are compressed by the superconductive magnet (4.5T) and become high density beam. The ionized ion by the electron beam is trapped by an electrostatic well potential field at axial direction and the electron space charge at radial direction. The trapped ions are ionized sequentially. Then we observed the emitted photon from the trapped HCI. Maximum electron energy is 200keV and electron current is 330mA.

As for this EBIT, it is possible that almost atoms are made a naked ion. But the Solar corona is diagnosed through EUV spectroscopy of highly charged Fe ions with moderate charge states (q~10). Therefore low electron energy (less than 1keV) is needed. In this experiment, electron energy is from 3 to 0.3 keV and electron current is about 10mA.

In this experiment, we used the flat filed grazing incidence spectrometer. This grating is the holographic grating (1200 grooves/mm) of the shimadzu corporation. And detector is the back-illuminated CCD of the hamamatu corporation. Fe atoms were injected to this EBIT from an effusion cell. The effusion cell is oven. The operation temperature is about 1300℃.

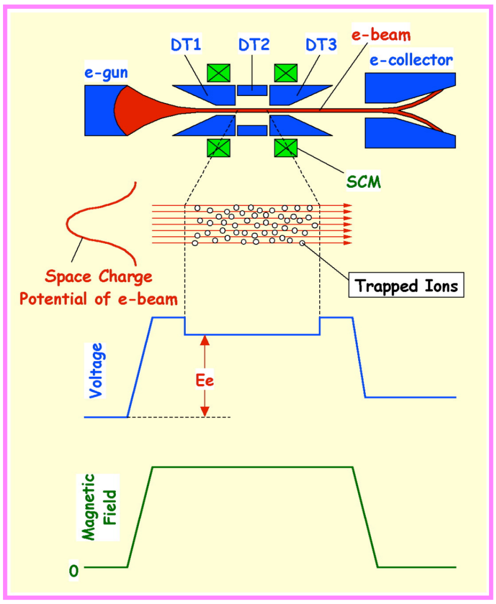

Fig.1 The experimental set up of the Tokyo-EBIT.

3. Results and Discussion

Fig.2 is the electron energy dependence of the emission EUV spectrum from highly charged iron ion. The wavelength of spectrum is from 100 to 300Å and the electron energy is from 2.2keV to 0.3keV respectively. It is possible that the HCI's which are from Be-like to Ar-like are produced by this electron energy range in EBIT. But there is the electron energy limit at 300eV. Because the electron current decreases from 30 to 3mA as electron energy lowers. And the photon emission signal decreases as the

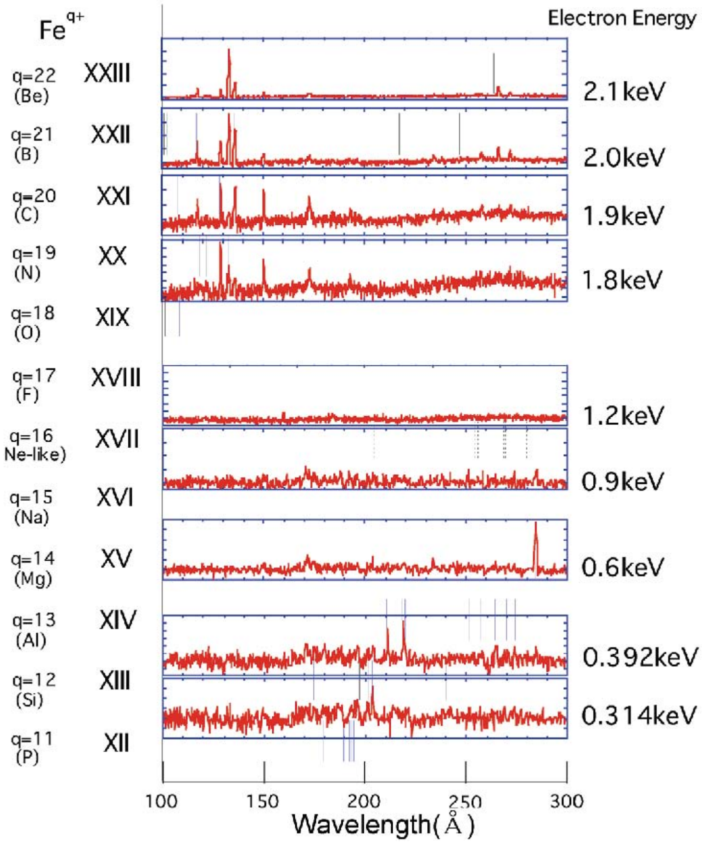

Fig.2 The EUV spectrum of highly charged iron ion.

product HCI decreases.

In Fig.3, we show the characteristic spectrum of LHD plasma [6] in comparison with the EBIT spectrum of 2.2keV. The LHD plasma parameters are following:

B=2.5T

Neutral Beam Energy: 100keV

Beam Power: 3MW

Exposure time: 0.2 sec

The central electron temperature: 2.2keV (by Thomson scattering).

The EBIT spectrum of 2.2keV agree with this LHD spectrum. The observed lines with EBIT and LHD are following:

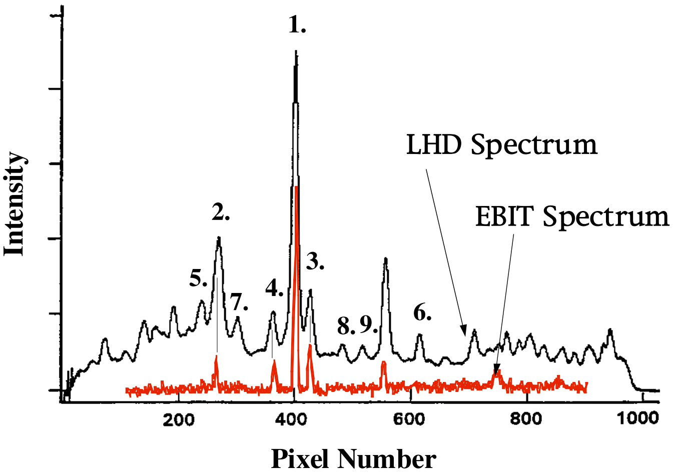

Fig.3 The characteristic spectrum of LHD plasma in comparison with the EBIT spectrum.

1. Fe^{22+} XXIII $1s^2 2s^2\ {}^1S_0$ - $1s^2 2s2p\ {}^1P_1$ (135.87Å)
2. Fe^{21+} XXII $2s^2 2p\ {}^2P_{1/2}$ - $2s2p^2\ {}^2P_{1/2}$ (117.17Å)
3. Fe^{21+} XXII $2s^2 2p\ {}^2P_{1/2}$ - $2s2p^2\ {}^2D_{3/2}$ (135.78Å)
4. Fe^{20+} XXI $2s^2 2p^2\ {}^3P_0$ - $2s2p^3\ {}^3D_1$ (128.73Å) .

On the other hand, there are several lines which are not observed in EBIT but observed in LHD plasma. These are following:

5. Fe^{21+} XXII $2s^2 2p\ {}^2P_{3/2}$ - $2s2p^2\ {}^2P_{3/2}$ (114.41Å)
6. Fe^{21+} XXII $2s^2 2p\ {}^2P_{3/2}$ - $2s2p^2\ {}^2D_{5/2}$ (156.02Å)
7. Fe^{20+} XXI $2s^2 2p^2\ {}^3P_2$ - $2s2p^3\ {}^3P_2$ (121.21Å)
8. Fe^{20+} XXI $2s^2 2p^2\ {}^3P_1$ - $2s2p^3\ {}^3D_{1,2}$ (142.16, 142.27Å)
9. Fe^{20+} XXI $2s^2 2p^2\ {}^3P_2$ - $2s2p^3\ {}^3D_3$ (145.79Å) .

The final states of both transitions are ground state. However, the quantum number J of final state is not the same. The J states of the non-observed lines in EBIT are 3/2, 2, or 1. It is the high energy state of J. On the other hand, the J states of the observed lines are 1/2 or 0. It is the low energy state of J. That is to say, in EBIT, the HCIs emit only photon by a transition to the ground state of low J. We expect that the cause is the high electron density, ion-ion collision and the low energy electron collision. There are enough the ground states of the high level J in the plasma. At present, we proceed with the detailed analysis of this spectrum.

In Fig.2, the many lines are observed at the low electron energy collisions (~0.3keV, q=11~13). But the resolution is not good and the photon emission intensity is very low. At the spectroscopy of the corona, the necessary number of HCI charge is about from 16 to 10. It is moderate charge state ions. Therefore, we decided to construct of a low energy compact EBIT for spectroscopy of moderate charge state ions. In fig.4, we show the experimental apparatus of the compact EBIT.
The compact EBIT is composed by four parts.

1. Electron gun, 2.drift tube, 3. Helmholtz coil and Lq.N_2 reservoir, 4.Collector.
All parts are cooled down by Lq. N_2. The compact EBIT operation parametesr are following:

Electron energy: 200~1000eV

Electron current: ~10mA

B-field: 0.2T

Pressure: 7×10^{-8}Pa

Transmittance: 97% from cathode to collector.

There are merits of the compact EBIT compared with the Toky-EBIT.

1. The running cost is very low because Lq. He is not used.
2. Because the distance from the trap to the port is short, the view is wide.
3. The electron beam position easily move. The alignment is easy.
4. The optical mirror can be installed around the trap. The high efficiency visible spectroscopy is possible.

At present, this compact EBIT has started run, and we advance visible and EUV spectroscopy.

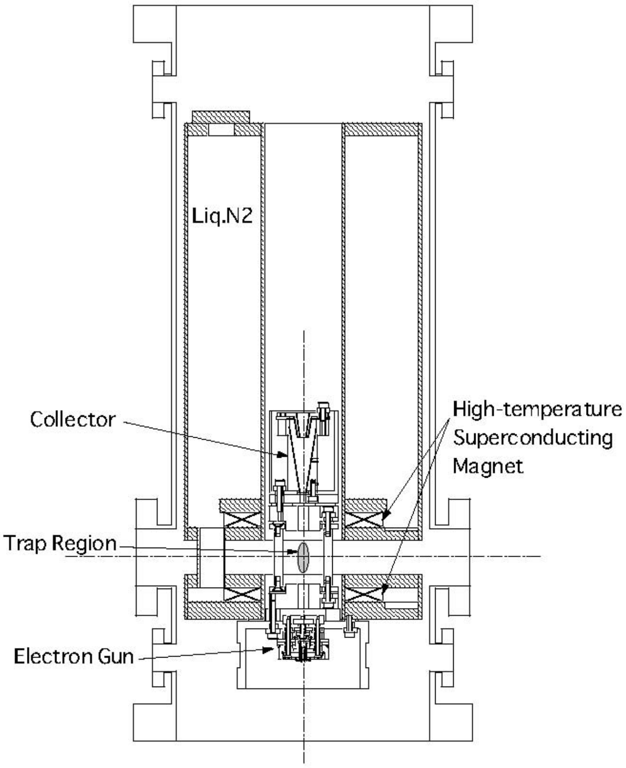

Fig.4 The experimental apparatus. (CoBIT)

Acknowledgement

This work was partly supported by the JSPS-CAS Core-University Program in the field of “Plasma and Nuclear Fusion”

References

[1] I. Murakami et al, J. Phys. B39, 2917 (2006)

[2] T. Watanabe, “Solar and LHD Plasma Diagnostics,” 2007, Atomic andMolecular Data and Their Applications, AIP Conf. Proc., 901, pp.215 – 220.

[3] T. Watanabe, H. Hara, J. L. Culhane,, L. K. Harra, G. A. Doschek, J. T. Mariska, P. R. Young, “Temperatures and Density Structures of Corona – A Test of Iron Line Capability of EIS Instrument on Board Hinode, 2007, “PASJ, 59 in press.

[4] H. Hara, T. Watanabe, K. Matsuzaki, J. L. Culhane, L. K. Harra, P. Cargill, J. T. Mariska, G. A. Doschek, “2006 Dec 17 Long Duration Flare Observed with the Hinode EUV Imaging Spectrometer,” 2008, PASJ, 60, in press.

[5] N.Nakamura et al, Phys. Scr. T73 (1997) 362-364

[6] Sato,K., Kobuchi, T.,m Funaba, H. “Characterristics of the VUV Emissions during NBI Experiment”, NIFS Ann. Rep. (1999), 7

Electron Stereodynamics in Coulomb Explosion of Molecules by Slow Highly Charged Ions

Atsushi ICHIMURA and Tomoko OHYAMA-YAMAGUCHI*

Institute of Space and Astronautical Science, JAXA, Sagamihara 229-8510, Japan
**Tokyo Metropolitan College of Industrial Technology, Shinagawa 140-0011, Japan*

e-mail: ichimura@isas.jaxa.jp

Abstract

The three-center Coulombic over-the-barrier model is developed for Coulomb explosion of a homonuclear diatomic molecule in collisions with a slow ($\sim$ 10 eV/amu) highly charged ion. A conventional two-step picture of multiple electron transfer *followed by* Coulomb explosion is far from appropriate because the molecule sets out to dissociate before the incident ion approaches the closest distance. We treat the formation of a quasi-molecule and its decay into the three moving atomic ions. Charge-asymmetric population between fragment ions observed in a triple-coincidence measurement is suggested to reflect the bond elongation during a collision. Collisions of $\mathrm{Kr}^{8+} + \mathrm{N}_2$ are analyzed.

Keywords: *highly charged ion, slow collision, multiple electron transfer, Coulomb explosion of diatomic molecule, over-the-barrier model, three-center quasi-molecule, charge asymmetry, bond elongation*

1. Introduction

Much attention has been called to the Coulomb explosion of molecules in a variety of collision processes on the basis of the momentum imaging technique. In particular, Kaneyasu and coworkers [1, 2] have made a triple coincidence measurement in a coplanar geometry for N_2 molecules colliding with slow (10 — 100 eV/amu) Kr^{8+} ions. They employ an experimental setup where the fragment ion pair $(\mathrm{N}^{Q+}, \mathrm{N}^{Q'+})$ is detected 'back-to-back' in transverse to the beam axis and in coincidence with the scattered ion. The most remarkable aspect in their measurement is unequal strengths of charge-asymmetric $(Q \neq Q')$ fragmentation between the *near* and *far* sites relative to the point of closest approach on a projectile trajectory [1, 2]. For a given charge pair $(Q,\ Q')$, the asymmetry parameter $A = (P_> - P_<)/(P_> + P_<)$ is obtained through the measurement of coincidence populations, $P_> \equiv P[Q_{\mathrm{far}} > Q_{\mathrm{near}}]$ and $P_< \equiv P[Q_{\mathrm{far}} < Q_{\mathrm{near}}]$. The experiment indicates a positive asymmetry $A > 0$; the far site is populated more by the higher charge than by the lower charge. This asymmetry was interpreted [1] as coming from electron polarization by the projectile in the course of dissociation, and qualitatively supported by a microscopic calculation [1] with the time-dependent density functional theory.

In a former paper [3], we made an analysis to get insight into the charge-asymmetric fragmentation observed, by applying the three-center Coulombic over-the-barrier model [4]. We took for simplicity a conventional but questionable two-step picture of the electron removal followed by the Coulomb explosion. In this picture, the charge asymmetry is only caused by residual electrons in the target, which are localized into two atomic sites on the way of fragmentation. Although leading to a correct sign of A, this effect is too small to account for the observations.

In this contribution, we further examine the electron stereodynamics in the charge-asymmetric fragmentation without taking the two-step picture but by treating the formation of a three-center quasi-molecule and its decay into three atomic ions [5].

2. Three-center Coulombic over-the-barrier model

We modify the three-center Coulombic over-the-barrier model so as to describe an inseparable process of electron transfer and Coulomb explosion, and so as to take full account of the three-center nature in the electron localization among three moving (one scattered and two dissociating) atomic ions.

We address collisions of a slow ($v \ll 1$ au) highly charged ion A^{q+} with a homonuclear diatomic molecule BC. The collision dynamics is treated as formation and decay of a triatomic quasi-molecule ABC^{q+},

$$\mathrm{A}^{q+} + \mathrm{BC} \quad \rightarrow \quad \mathrm{ABC}^{q+} \quad \rightarrow \quad \mathrm{A}^{(q-r)+} + \mathrm{B}^{r_\mathrm{B}+} + \mathrm{C}^{r_\mathrm{C}+},$$

where $r = r_\mathrm{B} + r_\mathrm{C}$ is the number of removal electrons from the molecule. According to the model by Niehaus [6], many-electron dynamics is described by a sequence of quasi-molecule formations of respective electrons in numerical order of 'rank' t $(= 1, 2, \ldots)$ in the way in of a collision, and by a sequence of their decays in the reverse order in the way out. The t-th electron is assumed to be initially bound in the molecule with its t-th ionization potential. One electron dynamics in respective steps is described with a three-center Coulomb potential determined by ion core charges q_A, q_B, and q_C. The three-center potential has two saddle points, higher one U_high and lower one U_low, in contrast with the two-center potential (see Fig. 1) .

A critical distance of the quasi-molecule formation is determined for each electron by a classical *over-the-barrier* criterion, $E = U_\mathrm{high}$, with the electron diabatic energy E and the barrier height U_high. The intramolecular bond length is not fixed to be the equilibrium one but allowed to be elongated during a collision due to the Coulomb repulsion between dissociating ions with charges $q_B = q_C = t/2$ after passing the t-th critical distance.

As indicated in the right panel of Fig. 1, the electron localization may occur in general via three processes according to the nuclear configuration formed by three ion cores A, B, and C. Note that, relating to the three processes (labeled by I, II, and III), the nuclear configuration space is divided into three domains labeled by $\mathcal{D}_{\mathrm{A-BC}}$, $\mathcal{D}_{\mathrm{C-AB}}$, and $\mathcal{D}_{\mathrm{B-CA}}$ in view of classical electron motion when $U_{\mathrm{high}} > E > U_{\mathrm{low}}$. In the respective decay processes, the branching probabilities are calculated with classically available phase-space volumes at $E = U_{\mathrm{high}}$ and $E = U_{\mathrm{low}}$ along a nuclear (scattering and dissociating) trajectory.

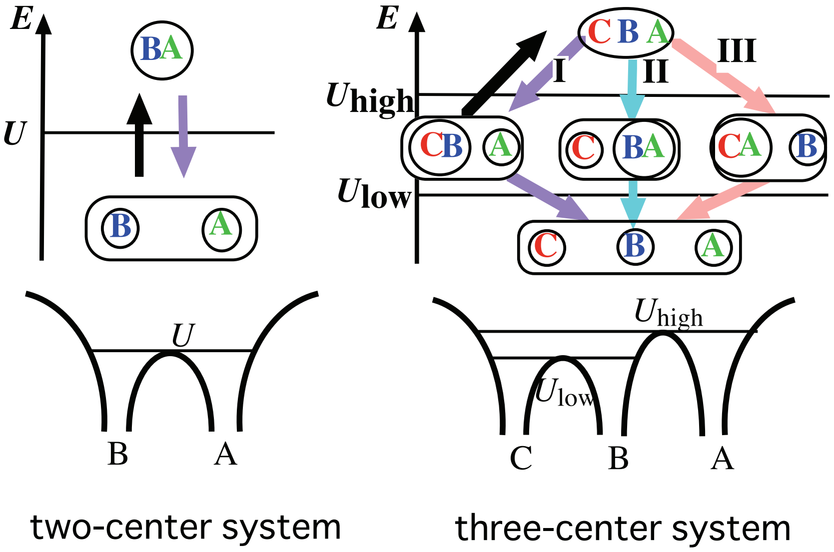

Figure 1: Formation (upward arrows) and decay (downward arrows) of a quasi-molecule. In the decay of a three-center quasi-molecule, the electron is localized into three atomic ions via two steps associated with higher (U_{high}) and lower (U_{low}) saddle points generated by a three-center Coulombic potential.

3. Results and Discussion

We apply the present model to collisions of $\mathrm{Kr}^{8+} + \mathrm{N}_2$ at velocities of $v = 0.01$ — 0.08 atomic unit (*i.e.*, 2.5 — 160 eV/amu) and consider 10 covalent electrons in the N_2 molecule. We assume a linear trajectory of incidence with the impact parameter of $b = 3$, together with a dissociation trajectory retaining the initial orientation taken in perpendicular to the beam axis.

Time τ evolution of half the bond length d is calculated and shown in Fig. 2, where the horizontal scale is taken $v\tau$, representing the projectile position along the incident linear trajectory. Also plotted is a boundary between nuclear domains $\mathcal{D}_{\mathrm{A-BC}}$ and $\mathcal{D}_{\mathrm{C-AB}}$ for the 6-th electron. Note that the nucleus B (C) is defined to belong to the near (far) site relative to the trajectory of incident ion A.

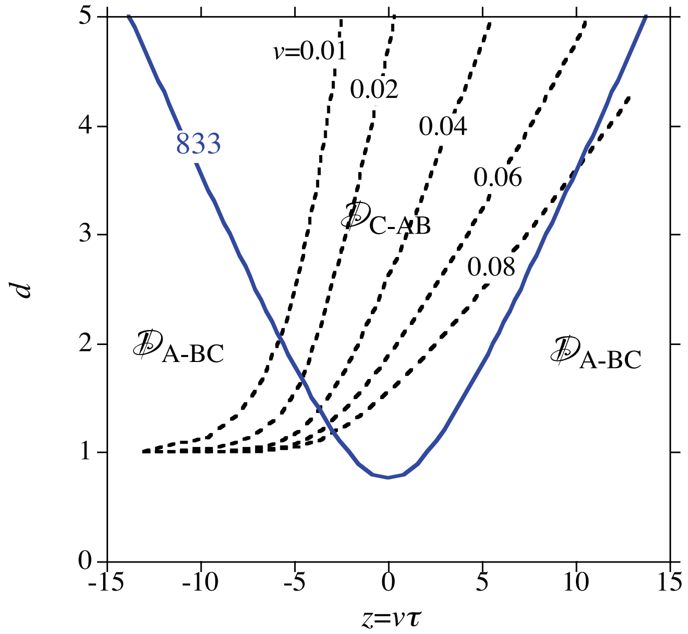

Figure 2: Time τ evolution of half the bond length d for collision velocities of $v = 0.01$, 0.02, 0.04, 0.08 (dashed lines). Also shown (solid line) is a boundary between nuclear domains $\mathcal{D}_{\mathrm{A-BC}}$ and $\mathcal{D}_{\mathrm{C-AB}}$ for an electron of rank $t = 6$ by effective charges $(q_{\mathrm{A}}, q_{\mathrm{B}}, q_{\mathrm{C}}) = (8, 3, 3)$ of ion cores.

It is seen from Fig. 2 that the nuclear configurations asymptotically belong to $\mathcal{D}_{\mathrm{A-BC}}$ on the way in ($\tau < 0$) regardless of the velocities. On the way out ($\tau > 0$), however, relevant domains depend on the velocity; both $\mathcal{D}_{\mathrm{A-BC}}$ and $\mathcal{D}_{\mathrm{C-AB}}$ are competing at $v = 0.08$, while only $\mathcal{D}_{\mathrm{C-AB}}$ is involved for $v \leq 0.04$. At the lower velocities, therefor, the near site B is populated exclusively via two steps as ABC → AB → B, while the far site C via one step as ABC → C. This mechanism is due to nuclear trajectories such that the molecule sets out to dissociate before the projectile recedes from it.

Using nuclear trajectories shown in Fig. 2, one-electron branching probabilities in the decay scheme above have been calculated for ion core charges of $(q_{\mathrm{A}}, q_{\mathrm{B}}, q_{\mathrm{C}}) = (8, t/2, t/2)$ ($t = 2$, 4, and 6) and shown in Fig. 3. It is found that the probability of ABC → AB

(ABC $\rightarrow$ C) at $E = U_{\mathrm{high}}$ is almost one (vanishing), while the probability of AB $\rightarrow$ B at $E = U_{\mathrm{low}}$ is $0.1 \sim 0.2$. This result qualitatively supports the observation [1, 2] that the near (B) site is more populated than the far (C) site.

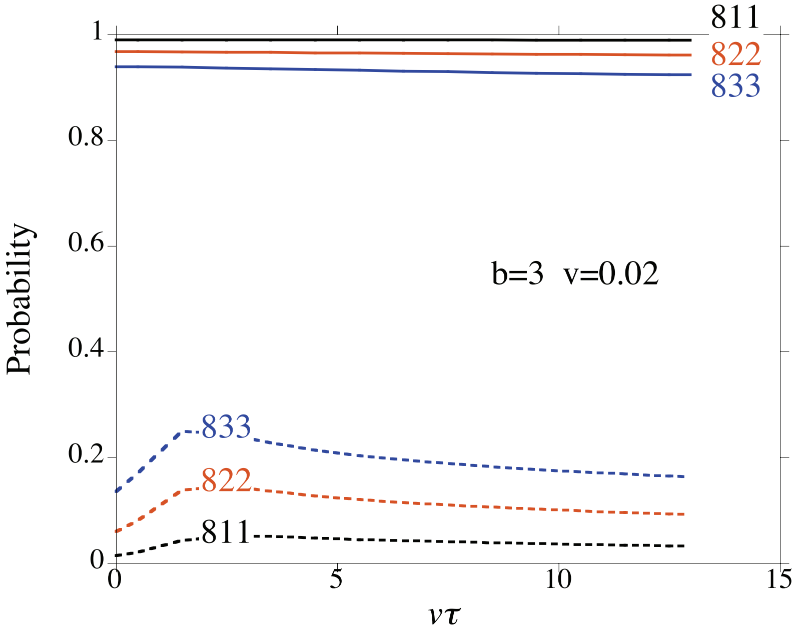

Figure 3: One-electron branching probabilities of ABC $\rightarrow$ AB at $E = U_{\mathrm{high}}$ (solid lines) and of AB $\rightarrow$ B at $E = U_{\mathrm{low}}$ (dashed lines) with ion core charges of $(q_{\mathrm{A}}, q_{\mathrm{B}}, q_{\mathrm{C}}) = (8, 1, 1)$, (8,2,2), and (8,3,3).

4. Concluding Remarks

The contribution from a nuclear domain $\mathcal{D}_{\mathrm{C-AB}}$ is expected to account for the sign $(A > 0)$ of charge asymmetry observed and also for the larger asymmetry in the slower collisions [1, 2]. This means that the large charge asymmetry reflects the nuclear dynamics of molecular bond elongation during a collision and also the electron stereodynamics associated with three-moving centers (*i.e.*, the scattered ion and the two dissociating fragment ions).

Further systematic calculations are in progress for the charge-asymmetry parameter A, taking account of all covalent electrons of a target molecule.

Acknowledgement

This work is partly supported by the JSPS-CAS Core-University Program in the field of 'Plasma and Nuclear Fusion'.

References

[1] M. Ehrich, U. Werner, H.O. Lutz, T. Kaneyasu, K. Ishii, K. Okuno, and U. Saalmann, *Phys. Rev.* A **65**, 030702(R) (2002).

[2] T. Kaneyasu, T. Azuma and K. Okuno, *J. Phys. B: At. Mol. Opt. Phys.* **38**, 1341 (2005).

[3] T. Ohyama-Yamaguchi and A. Ichimura, *Nucl. Instr. and Meth.* B **235**, 382 (2005).

[4] A. Ichimura and T. Ohyama-Yamaguchi, *Physica Scripta* T **80**, 190 (1999); *ibid.* T **92**, 162 (2001).

[5] T. Ohyama-Yamaguchi and A. Ichimura, J. Phys.: Conference Series **58**, 247 (2007).

[6] A. Niehaus, *J. Phys. B: At. Mol. Opt. Phys.* **19**, 2925 (1986).

Analysis of $D_\alpha(H_\alpha)$ spectrum emitted in front of the limiter in HT-7

J. Huang[1], B.N. Wan[1], D.P. Stotler[2], B.J. Xiao[1], Z.W. Wu[1], and the HT-7 Team[1]
[1] *Institute of Plasma Physics, Chinese Academy of Sciences, P.O.Box 1126, Hefei, Anhui 230031, People's Republic of China*
[2] *Princeton Plasma Physics Laboratory, Princeton University, Princeton, New Jersey 08543*
e-mail: janejoy@ipp.ac.cn

Abstract

The tokamak is one of the magnetic confinement fusion experimental devices and is most promising. In order to understand the recycling and emission processes of hydrogen atoms in the HT-7 tokamak, spectral profiles of the $D_\alpha(H_\alpha)$ line emitted in front of the limiter have been observed with a high-resolution spectrometer and simulated by the neutral particle transport code DEGAS 2. The results show that four processes are necessary to interpret the $D_\alpha(H_\alpha)$ line shape: 1) atom desorption, 2) molecular dissociation, 3) particle reflection, and 4) charge-exchange. The products of the first two processes are cold atoms which emit photons near the peak of $D_\alpha(H_\alpha)$ line shape, and those from the last two are warm atoms contributing to the blue side of the spectrum.

Keywords: tokamak, atomic and molecular processes, edge recycling

1. Introduction

The ever increasing demand of mankind for controllable energy sources is perhaps the most important and difficult problem faced by the world today. Energy from the thermonuclear fusion of light elements is the most promising long term alternative source. The most intense international effort has concentrated upon the Tokamak concept, in which a high temperature plasma is contained by strong magnetic fields in a toroidal configuration. To characterize the plasma, the experimental diagnostics are very important. For the spectroscopic diagnostics, it can identify impurity species, monitor the impurity behaviors. It can also study particle confinement, impurity transport in plasmas, edge recycling, plasma and wall interaction, and so on. This paper will be focused on the study of edge recycling.

For extrapolation to future fusion reactor devices, an understanding of the edge plasma in present tokamaks is necessary. The transport of neutrals, atomic processes, and plasma-wall interactions play key roles in edge plasma physics. To study basic recycling processes [1], the spectral profile of the D_α line emitted from the divertor region of JT-60U

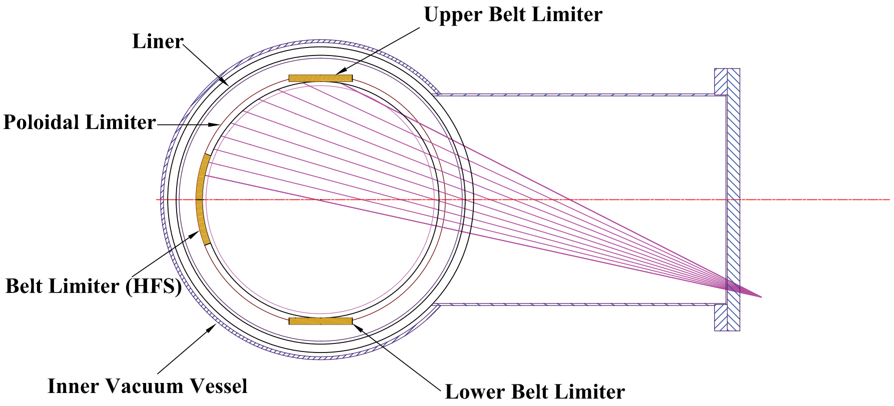

Figure 1: Schematic diagram in the poloidal cross-section of HT-7 tokamak.

was measured and simulated. In TFTR, Monte Carlo neutral transport simulations of hydrogen velocities using DEGAS were compared with experiment using Balmer-α spectral line profile [2]. In TEXTOR, the profiles of the $D_\alpha(H_\alpha)$ lines emitted in front of limiters were observed with high-resolution spectrometers and analyzed by Monte Carlo calculations [3]. H_α line shape tokamak was once analyzed by multi-Gaussian fitting [4] in front of the limiter in the HT-6M. The spectral profile of the H_α line contains abundant information on the velocity distribution of hydrogen atoms which determines their penetration depth into plasmas and their basic recycling processes. Understanding the behaviour of hydrogen atoms in the edge region is necessary to control fuelling and pumping in fusion plasmas.

For the HT-7 tokamak in a limiter configuration, recycling particles contribute more than 90% of the total fueling to sustain particle balance during the plateau of a discharge [5]. The limiter plays an important role in edge recycling, so the study of recycling from the limiter is the focus of this paper. To investigate the recycling mechanism in detail, the $D_\alpha(H_\alpha)$ line shape was simulated by DEGAS 2 [6].

The paper is organized as follows. In section 2, a description of relevant diagnostics

Table 1: Atomic and molecular processes considered in DEGAS 2 (A-J); plasma and surface interactions (K: reflection, L: desorption)

Label	Processes
A	$H_2 + e \rightarrow H(1s) + H(1s) + e$
B	$H_2 + e \rightarrow H^*(n = 3) + H(1s) + e$
C	$H_2 + e \rightarrow e + H_2^+ + e$
D	$H_2 + e \rightarrow H(1s) + H^+ + 2e$
E	$H_2^+ + e \rightarrow e + H^+ + H^+ + e$
F	$H_2^+ + e \rightarrow H(1s) + H^+ + e$
G	$H_2^+ + e \rightarrow H^*(n = 3) + H^+ + e$
H	$H_2^+ + e \rightarrow H^*(n = 3) + H(1s)$
I	$H + e \rightarrow e + H^+ + e$
J	$H + H^+ \rightarrow H^+ + H$
K	$H + C \rightarrow H$ (Reflection)
L	$H + C \rightarrow H + H_2$ (Desorption)

is given. A brief description of DEGAS 2 code and the simulation method for HT-7 are presented in section 3. In section 4, the basic recycling processes of deuterium atoms are discussed by comparison of the observation and simulation of the $D_\alpha(H_\alpha)$ spectral profile. Finally, section 5 is a short summary.

2. Experimental measurement

HT-7 is a medium-sized iron core superconducting tokamak. The main parameters are: major radius $R = 1.22$ m, minor radius $a = 0.27$ m; the working gas is deuterium. It is equipped with active water-cooled up-down symmetric toroidal limiter and belt limiters located on the high-field side, shown in Fig.1. A new form of doped graphite with a SiC gradient coating is chosen as the plasma facing material. Edge electron density and temperature profiels from 25 cm of raidal radius to 30 cm were measured by a Langmuir probe located on the top of the tokamak along the central line [7]. Plasma electron density profile from 0 cm to 25 cm was measured by a vertical 5-channel far-infrared hydrogen cyanide (HCN) laser interferometer [8]. The electron temperature profile is estimated from the soft x-ray pulse height analyzer (PHA) [9]. The center ion temperature was measured with the neutral particle analyzer (NPA) [10].

The $D_\alpha(H_\alpha)$ spectral profile is measured by an optical multi-channel analysis (OMA) system. It is equipped with a high-resoulution Acton Research Spectrometer (SP-750) and ICCD (EEV 384 × 578 pixels) cooled by a multistage Peltier element. The 2400 gr

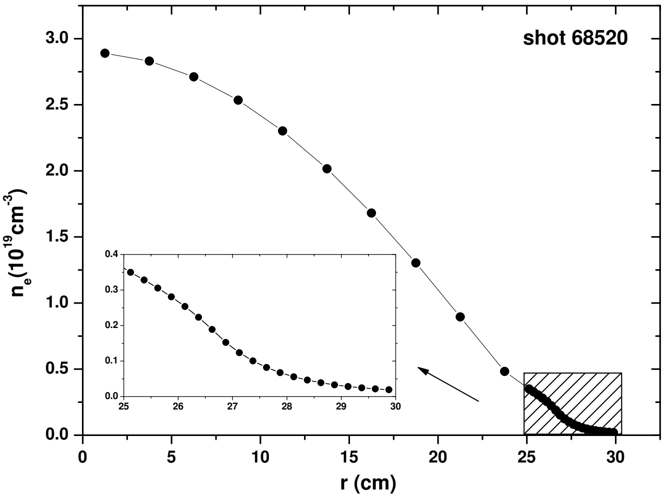

Figure 2: Radial distribution of electron density $n_\mathrm{e}(r)$ for a ohmic discharge shot 68520.

mm^{-1} grating is used with a spectral resolution 0.01 nm. Ten lines of sight shown in Fig.1 go through the upper-midplane plasma region. The lowest chord of these sights, used for this analysis, passes through the plasma center facing the belt limiter located on the high field side. Thus, the photons from particles moving towards the centre are Doppler shifted to shorter wavelengths and wavelength shift due to plasma rotation is avoided. The measured $\mathrm{D}_\alpha(\mathrm{H}_\alpha)$ line shape is determined by the convolution of a number of effects: the instrument function, the geometry of observation, the geometry of the source, the effects of plasma profiles, atomic and molecular processes, etc. Because of the strong toroidal magnetic field perpendicular to the plane of observation, the $\mathrm{D}_\alpha(\mathrm{H}_\alpha)$ spectral line is split into three Zeeman components. The two σ components can be eliminated by the use of a suitably orientated polarizer, and the measurements refer to the unshifted single π component. The instrument function is taken as the measured shape of 6328 Å He-Ne laser line and can be deconvolved. Corresponding to the 2400 gr mm^{-1} grating with the slit width 50 μm, the measured instrumental width is about 0.03 nm. Electric fields in the plasma also affect the energy level structure of hydrogenic ions through the Stark effect; however, the ambipolar fields and ion mircrofields are generally too small to influence spectral line widths. So, the Doppler Effect is dominant.

3. Simulation

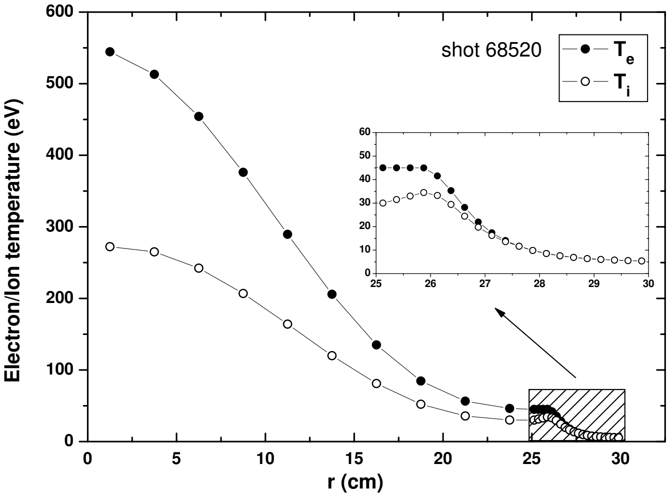

Figure 3: Raidal distribution of electron and ion temperature (shot 68520).

In this work, the simulation of $D_\alpha(H_\alpha)$ line shape was performed using the three-dimensional neutral gas transport code DEGAS 2 in which toroidal symmetry is assumed. For a given geometry and plasma parameters, neutral atoms and molecules are tracked using the Monte Carlo technique as they undergo ionization, charge exchange, dissociation, and interactions with surfaces. The result is effectively a numerical solution of the Boltzmann equation for the neutral distribution function.

As shown in Fig.1, the magnetic geometry of HT-7 is assumed to be a circular configuration. Four regions are set: core plasma (0-25 cm), cold plasma (25-27 cm), SOL plasma (27-30 cm), and vacuum (30-33 cm).

In the simulation, it is assumed that the hydrogen ions arriving at the limiter are either reflected as atoms or desorbed as atoms and molecules. The H^+ flux or current to the surface is input to DEGAS 2. In computing the neutral profile associated with that source, DEGAS 2 begins by sampling an ion from that flux using the ion temperature and velocity near that surface. The local sheath potential is evaluated using the electron temperature there and used to accelerate the ion to the target. This gives the energy with which it will strike the plate. It is assumed that it hits at normal incidence. The ion is assumed to be neutralized by the cloud of electrons at the surface, and thus interacts with the material as an atom. This allows us to use the same set of particle-material interactions to describe incoming ions and atoms. Some are reflected as atoms ($H+C \rightarrow H$

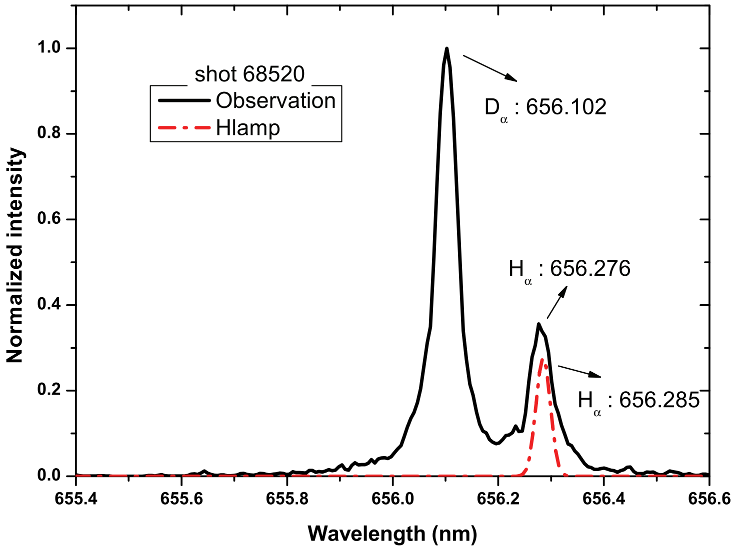

Figure 4: Comparison of D_α/H_α observed spectrum(black line) in a typical ohmic discharge (shot 68520) and H_α line shape (dashed) from a hydrogen lamp.

shown label K in Tab. 1). The reflected atoms from the ion incidence on the limiter have the energies $E_{\mathrm{refl}} = R_{\mathrm{E}}(E_{\mathrm{i}} + \Phi_{\mathrm{sh}})$, where R_{E} is the fraction of the incident energy retained by the reflected atoms, which is dependent on the incident angle, energy and the target material, E_{i} is the ion energy before the sheath, Φ_{sh} is the sheath potential, taken to be $3T_{\mathrm{e}}$. The dependence of reflection yield and energy reflection coefficient on the incidence energy used is from 'refl.dat' in DEGAS 2 which is calculated by VFTRIM code [11]. Reflected particles are assumed to have a cosine angular distribution. In low incident energy of carbon or deuterium, the sputtering yields of deuterium are less than the reflection probability [2]. So, in our case the sputtering of hydrogen isotopes from the graphite limiter can be neglected. Deuterium ions that are not reflected are assumed to be desorbed as atoms or molecules with an energy of the surface temperature of the limiter. In [12], it is observed that at the limiter temperature $T_{\mathrm{TL}} \geq 1100$ K the direct atomic release is dominant, whereas at low temperature (550 K< $T_{\mathrm{TL}} < 1100$ K) the ratio of molecules to atoms is unknown. Thus, desorption process is set as $\mathrm{H+C \rightarrow H+H_2}$ (label L in Tab. 1). Molecular hydrogen entering the plasma will be ionized and/or dissociated by electron collisions. Tab. 1 lists all atomic and molecular reactions considered in our simulation. The energy of the hydrogen product atoms depends on the particular dissociation pathway

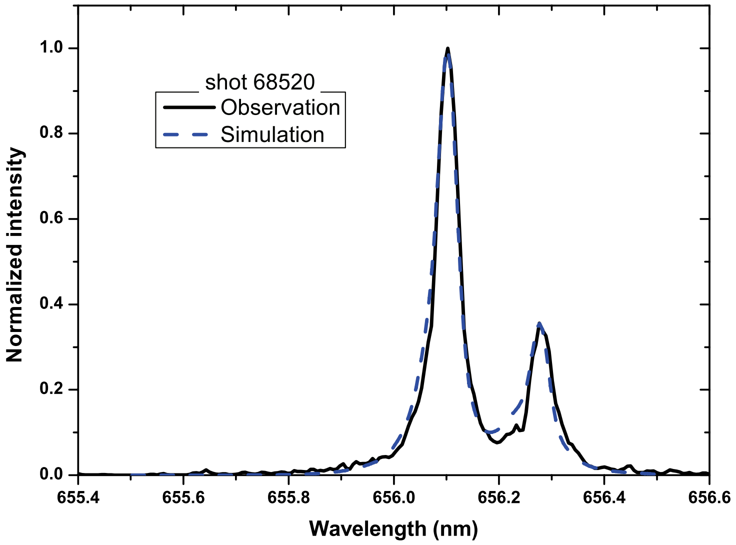

Figure 5: Observed (black line) and simulated (dashed) $D_\alpha(H_\alpha)$ spectra of shot 68520.

and the energy transferred from the electron [8].

4. Results and discussion

The plasma electron density n_e and electron (ion) temperature $T_\mathrm{e}(T_\mathrm{i})$ of a typical ohmic discharge 68520 are shown in Fig.2 and Fig.3, respectively, which are fitting chart according to repetitious measured raw data. The ion temperature profiles are not available and are treated as an adjustable parameter.

The spectral profiles for the present study were measured in the plateau state of this discharge with an integration time of 0.1 s. Fig. 4 shows the observed $D_\alpha(H_\alpha)$ line shape and the H_α spectral profile from a hydrogen lamp as a comparison. The working gas was deuterium; hydrogen came from the wall and limiter surfaces. The rest wavelength of H_α is 656.285 nm (D_α: 656.104 nm), and the center wavelengths of observed D_α and H_α line shape were 656.102 and 656.276 nm, respectively. It is shown that compared with standard H_α shape, the spectrum differs strongly from the Gaussian profile and is clearly asymmetric with a slight but significant blue shift of the peak.

Observed and simulated $D_\alpha(H_\alpha)$ spectra are shown in Fig.5. The simulated line profile agrees reasonably well with that observed. The isotopic mix of incident hydrogen ions

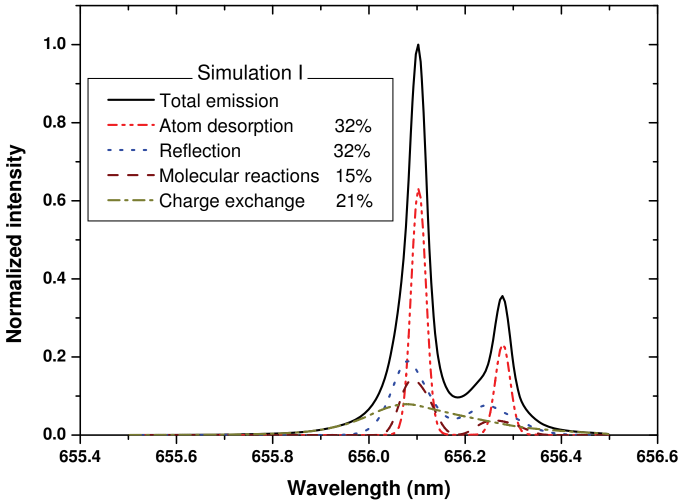

Figure 6: Composition of the simulated $D_\alpha(H_\alpha)$ spectrum with four processes: 1) atom desorption (32%), 2) molecular dissociation (15%), 3) particle reflection (32%), and 4) charge-exchange (21%).

is adjusted to match that experimentally observed in the Balmer-α spectral profile. According to the area of the shape of the $D_\alpha(H_\alpha)$ spectra, the ratio of H/(H+D) is about 30%.

Fig. 6 shows that four processes are necessary to interpret $D_\alpha(H_\alpha)$ line shape: 1) atom desorption, 2) molecular reactions, 3) particle reflection, and 4) charge-exchange. The products from the first two processes are cold atoms which emit photons near the peak $D_\alpha(H_\alpha)$ line shape, and those from the last two are warm atoms contributing to the blue side of the spectrum. These components have the proportions 32%, 15%, 32% and 21%, respectively. Atom desorption and reflection are the two dominant processes in edge recycling. Although charge-exchange does not contribute to particle recycling directly, it can transfer energy from plasma ions to atoms produced by dissociated, increasing their penetration into the plasma.

Since the edge density is insufficient to thermalize the velocity distribution, the contributions of the various reaction pathways that generate hydrogen atoms may be associated with different wavelength regions (velocities) in the spectral profile. For atom desorption, the position of its simulated peak is at 656.102 nm. According to Doppler shift, a mean energy of an atom is about 0.05 eV which corresponds to 600 K of the limiter temperature. The limiter temperature used in DEGAS 2 was based on measurements. This leads to a

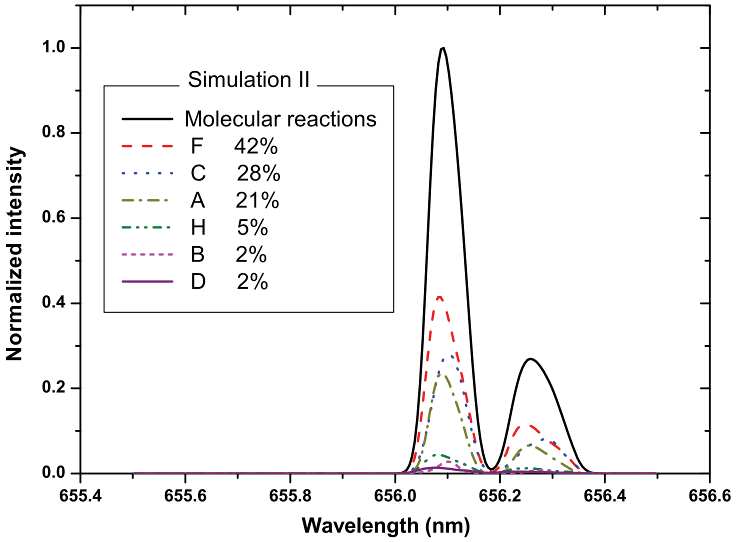

Figure 7: Detailed composition of the molecular reaction component (each label shown in Tab. 1).

slight shift in the peak of the emission from desorbed atoms which seems consistent with observations. The peak of the reflection component is 656.082 nm, corresponding to an energy of 12 eV. The models used in the code imply a shift in the emission from reflected atoms. The resulting emissions are consistent with observations given the overall agreement of the observed and simulated spectra. Those atoms from molecular reactions have a mean energy of 3.7 eV. The detailed composition of the molecular reactions is shown in Fig.7. There are two principal breakup reactions, dissociation into two ground state atoms (A in Tab. 1) and ionization (C in Tab. 1) followed by dissociation (F in Tab. 1). In molecular reactions, F contributes 42% to Balmer-α emission, and A about 21%. The edge electron temperature of this shot from 25-27 cm is about 40-15 eV shown in Fig.3. Under these conditions, molecular ion dissociation and molecular ionization are the two principal breakup reactions.

To understand the phenomena observed in the $D_\alpha(H_\alpha)$ line shape, the characteristics of edge plasma must be examined more closely. The deuterium ionization length can be expressed as $\lambda_\mathrm{i} = v_\mathrm{D}/(n_\mathrm{e}\langle\sigma v_\mathrm{i}\rangle)$. The reaction rates for the most important neutral processes are given in [13]. As can be seen in [1] for temperatures lower than 15 eV, Franck-Condon (F-C) breakup of D_2 into atoms is important, while above 15 eV, direct ionization dominates. In a typical HT-7 ohmic discharge plasma, edge parameters are $n_e(a) \simeq 2 \times 10^{18}$ m^{-3} and $T_e(a) \simeq 20$ eV. First, for thermal D_2 particles, $v_D \simeq 1.7 \times 10^5$ cm/s, $\langle \sigma v_i \rangle \simeq 2 \times 10^{-8}$ cm^3/s, then $\lambda_i \simeq 4$ cm, which shows that recycing molecules can only exist near the limiter region. Secondly, D_2 ionization by electron impact predominates, producing F-C atoms with an average energy of 4.3 eV corresponding to $v_D \simeq 2 \times 10^6$ cm/s, $\langle \sigma v_i \rangle \simeq 1.5 \times 10^{-8}$ cm^3/s, and $\lambda_i \simeq 60$ cm. Thus, not only charge-exchange atoms but also FC atoms can reach into the core plasma. During ionization, ion molecules D_2^+ can also be formed, $v_D \simeq 1 \times 10^5$ cm/s, $\langle \sigma v_i \rangle \simeq 2 \times 10^{-7}$ cm^3/s, $\lambda_i \simeq 0.25$ cm, that means once D_2^+ is formed, it will be dissociated as soon as possible.

5. Summary

To investigate the recycling mechanism in HT-7, spectral profiles of $D_\alpha(H_\alpha)$ emitted from the limiter have been observed and simulated. The results show that four processes are necessary to interpret the $D_\alpha(H_\alpha)$ line shape: 1) atom desorption, 2) molecular dissociation, 3) particle reflection, and 4) charge-exchange. For a typical ohmic discharge shot 68520 ($n_e(0) \sim 3 \times 10^{19}$ m^{-3}), these components have the proportions 32%, 15%, 32% and 21%, respectively. Atom desorption and particle reflection are the two dominant processes in edge recycling.

References

[1] Kubo H. et al, *Plasma Phys. Control. Fusion* **40**, 1115–1126 (1998).

[2] Stotler D.P. et al, *Phys. Plasmas* **3**, 4084–4094 (1996).

[3] Samm U. et al, *J. Nucl. Mater.* **162-164**, 24–37 (1989).

[4] Wan B.N. et al, *Nucl. Fusion* **39**, 1895–1899 (1999).

[5] Huang J. et al, *Nucl. Fusion* **46**, 262–271 (2006).

[6] Stotler D.P., Karney C.F., *Contrib. Plasma Phys.* **34**, 392–397 (1994).

[7] Xu G.S. et al, *J. Nucl. Mater* **313-316**, 259–262 (2003).

[8] Jie Y.X. et al, *Plasma Sci. Technol.* **2**, 105–109 (2000).

[9] Shi Y.J. et al, *Rev. Sci. Instrum* **75**, 4930–4933 (2004).

[10] Liu S.X. et al, *Fusion Eng. Des.* **60**, 211–216 (2002).

[11] David N.Ruzic. et al, *Nucl. Instrum. Methods Phys. Res. B* **47**, 118–25 (1990).

[12] Brezinsek S. et al, *Plasma Phys. Control. Fusion* **47**, 615–634 (2005).

[13] Janev R.K. et al, *Springer Series on Atoms and Plasmas* **4**, (Berlin and New York: Springer-Verlag), ISSN: 0-387-17588-1 (1987).

Correlated relativistic dynamics and nuclear effects in dielectronic and visible spectra of highly charged ions

Z. Harman[1], A.N. Artemyev[1,2], J.R. Crespo López-Urrutia[1], A.J. González Martínez[1], U.D. Jentschura[1], C.H. Keitel[1], V. Mäckel[1], R. Soria Orts[1], H. Tawara[1], I.I. Tupitsyn[1,2], J. Ullrich[1], A. Volotka[1,2]

[1]*Max Planck Institute for Nuclear Physics, Saupfercheckweg 1, 69117 Heidelberg, Germany*

[2]*St. Petersburg State University, Oulianovskaya 1, St. Petersburg 198504, Russia*

e-mail: harman@mpi-hd.mpg.de

Abstract

Dielectronic recombination and visible emission spectra are investigated theoretically and experimentally. Spectra of x-rays emitted from electron beam ion trap plasmas allow the study of correlation and quantum electrodynamic effects in relativistic few-body systems. In the visible range, exploring the forbidden M1 transitions in Be- and B-like argon ions provides one new insights into the relativistic modelling of isotope shift effects and extend the scope of bound-electron g factor measurements to few-electron ions.

Keywords: dielectronic recombination, relativistic theory, highly charged ions, relativistic nuclear recoil, bound-electron g factors, electron beam ion traps

1. Introduction

One of the dominant atomic processes occurring in astrophysical and nuclear fusion plasmas is dielectronic recombination (DR). Spectra of x-rays emitted during this resonant process yield indispensable information on a range of plasma properties. Furthermore, studies of DR processes with highly charged few-electron ions provide unique possibilities for investigating correlation, quantum electrodynamic (QED), and nuclear effects in many-body systems bound by strong Coulomb fields [1,2].

At medium charge numbers Z, e.g., in the case of Ar (Z=18), relativistic and nuclear effects are intertwined with large electron correlation contributions. Because of this complex interplay, increasingly accurate measurements of transition energies and excited-state lifetimes characterizing the visible emission spectra of electron beam ion trap (EBIT) plasmas represent a challenge to theory. We have performed extensive studies [3] of the ground-state forbidden M1 transition in Be- and B-like argon ions. The mass isotope shift [4], the radiative lifetime [5] and the bound electron gyromagnetic (g) factors [6]

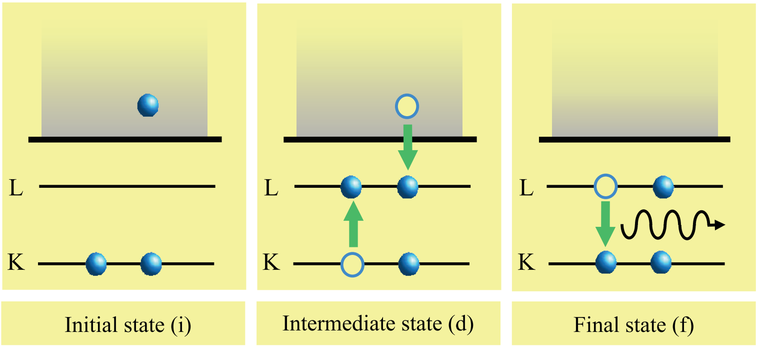

Figure 1: Scheme of KLL dielectronic recombination into He-like ions.

associated with this line have been determined with high accuracy using the Heidelberg electron beam ion trap.

2. KLL dielectronic recombination with heavy few-electron ions

We study the dynamical process of dielectronic recombination (DR) as a means of generating and studying excited ions in an electron beam ion trap. In the first step of DR, a free electron is captured into an ion by the simultaneous excitation of a bound electron (see Fig. 1). The designation KLL refers to the shell structure of the bound electronic states actively involved in the process. The resolving power of the experiment allows us to separate peaks corresponding to different charge states and electronic states.

We calculate resonance features of dielectronic recombination into He-, Li-, Be- and B-like heavy ions in the KLL energy range, applying the multiconfiguration Dirac-Fock and the configuration interaction Dirac–Fock–Sturmian methods, and quantum electrodynamic many-body theory [1]. Table 1 shows a breakdown of physical contributions for specific resonances in the case of recombination into Li-like W ions.

Theory results are compared to our experimental spectra explored with the Heidelberg EBIT [2]. This comparison illustrates the significance of relativistic electron correlation effects and QED corrections. Few unexplained discrepancies found in specific recombination resonances for initially Li-like Hg ions led us to further studies along these isoelectronic sequences.

3. Relativistic nuclear recoil effect in B- and Be-like Ar ions

Isotope shifts arise from the combined effect of the finite nuclear mass and volume on the electronic binding energy. The mass-dependent, or recoil part, is usually divided into the normal mass shift and the specific mass shift (also known as mass polarization).

Table 1: Theoretical contributions to the energy of specific dielectronic resonances in the case of initially Li-like W^{71+}. The resonance energy E_{res} is given as the difference of the level energy E_d of the intermediate autoionizing state and the level energy E_i of the initial ionic ground state. DF: Dirac-Hartree-Fock energy; rel. correlation: relativistic electron correlation contribution (beyond the DF approximation); FS: field shift in the one- or many-electron case; NMS, SMS: normal- or specific mass shift; Breit: Breit interaction contribution; VP and SE: vacuum polarization and self-energy correction in the one-electron approximation; VP and SE screening: electron screening correction of the QED effects.

	$E_i : 1s^2 2s$ [eV]	$E_d : \mathrm{Li}_2$ [eV]	$E_{\mathrm{res}} : \mathrm{Li}_2$ [eV]	$E_d : \mathrm{Li}_3$ [eV]	$E_{\mathrm{res}} : \mathrm{Li}_3$ [eV]
Dirac	-182401.6	-141143.6	41258.0	-141143.6	41258.0
DF correction	2338.2	2553.6	215.4	2592.4	254.1
rel. correlation	-1.3	-1.5	-0.2	-2.2	-0.9
FS, one-el.	63.7	34.6	-29.1	34.6	-29.1
FS, many-el.	62.8	34.4	-28.4	34.3	-28.5
NMS	0.6	0.5	-0.2	0.5	-0.2
SMS	0.0	-0.0	-0.0	-0.0	-0.0
Breit	172.5	24.3	-148.2	29.6	-142.9
VP	-63.6	-34.7	29.0	-34.7	29.0
VP Screening	0.9	0.4	-0.5	0.3	-0.6
SE	335.5	185.6	-149.9	185.6	-149.9
SE Screening	-5.7	-3.0	2.7	-2.7	2.9
Total	-179624.1	-138418.6	41205.5	-138374.6	41249.5

In highly charged ions, large relativistic nuclear recoil contributions must be included. The volume effect, also called the field shift (FS), is caused by the penetration of the electronic wave function into the nucleus. In our systems, the mass shift terms strongly dominate over the FS.

The many-body relativistic recoil operator for a general atomic system of electrons with indices i, j, reads (see Ref. [7], in relativistic units, $\hbar = c = \epsilon_0 = 1$)

$$R_{ij} = \frac{\vec{p}_i \cdot \vec{p}_j}{2M} - \frac{Z\alpha}{2Mr_i}\left(\vec{\alpha}_i + \frac{(\vec{\alpha}_i \cdot \vec{r}_i)\vec{r}_i}{r_i^2}\right) \cdot \vec{p}_j \, . \tag{1}$$

Here, $\vec{r}_i$ and $\vec{p}_i$ are the position vector and the momentum operator of the ith electron, respectively, and $\vec{\alpha}_i$ is the vector of Dirac matrices acting on its bispinor wave function. The nuclear mass is denoted by M and α is the fine-structure constant. The normal mass shift correction to a given atomic state is obtained as the expectation value $\langle \sum_i R_{ii} \rangle$, whereas the specific mass shift term is given by $\langle \sum_{i \neq j} R_{ij} \rangle$. The first term in Eq. (1)

corresponds to the mass shift operator also known in the nonrelativistic theory.

The wavelengths of the $1s^22s^22p\ ^2P_{3/2}$ - $^2P_{1/2}$ forbidden M1 transition in B-like Ar^{13+} and the $1s^22s2p\ ^3P_1 - {}^3P_2$ M1 transition in Be-like Ar^{14+} measured at the Heidelberg EBIT were compared for the isotopes ^{36}Ar and ^{40}Ar as described in Ref. [4]. Table 2 summarizes the results and compares experimental values to theoretical predictions. The observed isotope shift has confirmed the relativistic theory of nuclear recoil effects in many-body systems. Our calculations, based on the fully relativistic recoil operator (1), are in excellent agreement with the measured results. A calculation applying the nonrelativistic part of the operator only would yield values for the isotope shift which are smaller than the experimental result by a factor of roughly three.

Table 2: Transition wavelengths for $^{40}\mathrm{Ar}^{13+,14+}$ and isotope shifts (^{36}Ar – ^{40}Ar) (in nm, air). The π- and σ-components are marked accordingly, and their average is denoted by the superscript av. See text for further explanations.

	Wavelength (^{40}Ar)		Isotope shift (^{36}Ar – ^{40}Ar)	
Ion	Theory	Experiment	Theory	Experiment
Ar^{13+}	441.16(27)	441.2556(1)	0.00123(5)	$0.00120(10)^{\pi}$ $0.00125(7)^{\sigma}$ $0.00123(6)^{\mathrm{av}}$
Ar^{14+}	594.24(30)	594.3879(2)	0.00122(5)	0.00120(10)

4. Zeeman splitting and g factor of the ground-state levels in B-like Ar

The Zeeman line components of the magnetic-dipole ($M1$) $1s^22s^22p\ ^2P_{3/2}$-$^2P_{1/2}$ transition in B-like Ar^{13+} were experimentally resolved by high-precision emission spectroscopy using the Heidelberg EBIT. A typical Zeeman spectrum is shown on Fig. 2.

We determined the gyromagnetic (g) factors of the ground and first-excited states through measurements of the transition wavelengths of the magnetic dipole $M1$ transitions between the levels. The results for the $J = 1/2$ and $J = 3/2$ state are $g_{1/2}$=0.663(7) and $g_{3/2}$=1.333(2), respectively. This corresponds to a measurement of the g factor of a relativistic electron in a bound non-S state of a multielectron ion with a 1.5 per mil accuracy. In Table 3, the results are compared to theoretical calculations by means of relativistic multiconfiguration methods including electron correlation effects and additional quantum electrodynamic corrections.

Our measurements show that the classical Landé g factor formula is sufficiently accurate to the present level of accuracy in few-electron ions of medium nuclear charge number Z. To the best of our knowledge, the achieved 1.5 per mil accuracy of determining the g factor

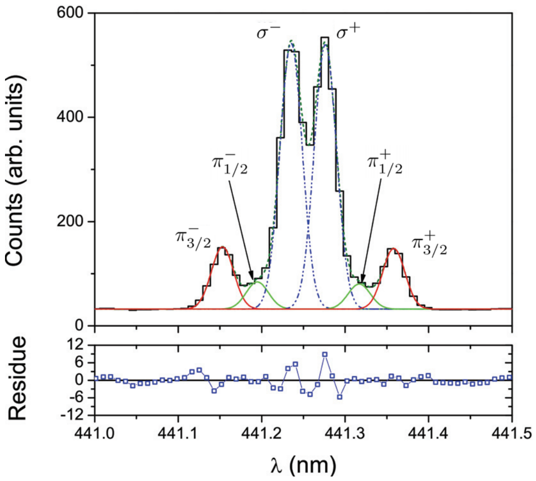

Figure 2: Emission spectrum of the $^2P_{3/2}$ $-$ $^2P_{1/2}$ line in Ar^{13+}. The six dashed curves are fits to the Zeeman components. The lower plot shows the fitting residue. See text for further details.

of a bound electron in a *P* state of a few-electron highly charged ion is unprecedented.

References

[1] Z. Harman, I. I. Tupitsyn, A. N. Artemyev, *et al.*, Phys. Rev. A **73**, 052711 (2006).

[2] A. J. González Martínez, *et al.*, Phys. Rev. A **73**, 052710 (2006).

[3] Z. Harman, U. D. Jentschura, C. H. Keitel, *et al.*, J. Phys.: Conf. Ser., **58**, 133 (2007).

[4] R. Soria Orts, Z. Harman, *et al.*, Phys. Rev. Lett. **97**, 103002 (2006).

[5] A. Lapierre, U. D. Jentschura, *et al.*, Phys. Rev. Lett. **95**, 183001 (2005).

[6] R. Soria Orts, J. R. Crespo López-Urrutia, *et al.*, Phys. Rev. A **76**, 052501 (2007).

[7] See V.M. Shabaev, Yad. Fiz. **47**, 107 (1988) and references therein.

Table 3: Theoretical contributions to the g factor g_{total} in comparison with the experimental result g_{exp}. The symbol g_{nr} stands for the nonrelativistic Landé g factor, g_{D} is the relativistic Dirac value, Δg_{corr} represents the electron correlation correction, Δg_{neg} is the contribution of the negative part of the continuous spectrum, and Δg_{QED} denotes QED corrections to the g factor. See text for further details.

Level	g_{nr}	g_{D}	Δg_{corr}	Δg_{neg}	Δg_{QED}	g_{total}	g_{exp}
$^2P_{1/2}$	0.6666667	0.6637754	0.0006943	-0.0000425	-0.00078	0.66365	0.663(7)
$^2P_{3/2}$	1.3333333	1.3310304	0.0005443	-0.0000613	0.00077	1.33228	1.333(2)

Atomic Properties from High-Resolution Laser Spectroscopy

Wei-Guo Jin, Masayuki Kawamura, Tatsuya Minowa and Hidetsugu Katsuragawa

Department of Physics, Faculty of Science, Toho University
Miyama 2-2-1, Funabashi, Chiba 274-8510, Japan

Abstract

High-resolution UV laser spectroscopy has been performed by frequency doubling of the diode-laser beam together with the collimated atomic beam. Spectroscopic data on hyperfine structure, isotope shift and atomic configuration have been obtained for high-lying atomic levels. High-resolution spectroscopy has also been used to measure the Stark effect of alkali atoms. Results on the Rb Stark shift produced by strong electric field are reported and scalar and tensor polarizabilities are discussed.

Keyword: high-resolution laser spectroscopy, isotope shift, hyperfine structure, Stark effect

1. Introduction

High-resolution laser spectroscopy has been proved to be a powerful method to measure atomic hyperfine structure (HFS) and isotope shift (IS). From such measurements, one can obtain atomic properties such as atomic configuration, electron density and HFS constants as well as nuclear properties such as nuclear moments and charge distribution. These spectroscopic data are indispensable information to deepen understanding of atomic and nuclear structures [1].

Up to now, extensive studies have been performed in the visible region that is related to the atomic level of about 16000 cm^{-1}[2]. Measurements in the ultraviolet (UV) region, corresponding to the atomic level of 26000 cm^{-1}, have been scarcely reported. Atomic properties such as hfs, IS, even atomic configuration, are not yet well known for high-lying levels. Strong configuration mixing is expected for such a highly excited level that provides a critical check of theoretical calculation.

Recently, study of parity nonconservation and search for permanent electric dipole moment of atoms are performed and these experiments provide sensitive tests of the standard model [3]. Such studies are related to the Stark effect. The Stark effect of alkali atoms is suitable for study of the atomic core contribution and relativistic effect. Recently, precise calculation, up to several %, is possible [4]. Therefore, precise experimental data are needed to check such theoretical calculation.

The Stark effect is less investigated even for alkali atoms compared with the HFS and Zeeman effect. Strong electric field is necessary to get observable shift and splitting, particularly for light elements. However, it is difficult to produce strong electric field experimentally.

Using the diode laser together with a highly collimated atomic beam, we developed a high-resolution atomic-beam diode-laser spectroscopic system, which enabled us to make systematic studies of HFS and IS as well as the Stark effect. Spectroscopic measurements were performed not only for the red and near-infrared regions but the UV region by the frequency doubling of laser beam. In this paper, we report the high-resolution HFS and IS measurements in the UV region for the rare-earth elements as well as measurements on the Stark effect of Rb atom.

2. Experiment

The present experiment was performed by high-resolution atomic-beam laser spectroscopy. For the rare-earth elements, an electron-bombardment heating method was used to produce an atomic beam. The atomic beam was ejected from a molybdenum oven heated to approximately 1500 °C for Gd, Dy and Er. For alkali atoms such as Rb, the sample was heated to about 200 °C and the atomic beam was collimated by a slit set at about 1.5 m far away from the oven in order to achieve (Doppler-free) high resolution. A commercial tunable diode laser (Newport 2010) with an external cavity was used to produce a laser beam with a wavelength of 780 – 810 nm. The UV beam with a wavelength of 390 – 405 nm was obtained by the frequency doubling of a laser beam using a cw frequency doubler (Spectra-Physics, WAVETRAIN).

To study the Stark effect, the electric field was produced in the interaction region between the laser and atomic beams by two transparent electrodes, which were BK7 glasses coated with $InSnO_2$. We developed two types of electrode systems and the electric field, up to 82 kV/cm, could be applied. Great attention was paid to large background produced by scattering of the incident laser beam from the electrodes.

To reduce Doppler broadening, the laser beam was collimated and allowed to cross the atomic beam perpendicularly. Laser-induced fluorescence was collected with a spherical mirror and detected with a cooled photon-counting photomultiplier (Hamamatu R2257P). For relative frequency calibration, the intensity of the laser light transmitted through a confocal Fabry-Perot interferometer with a free spectral range of 300 MHz was measured simultaneously with the fluorescence from the atomic beam. The experimental setup has been described elsewhere [5].

3. Results and Discussion

3.1 Hyperfine Structure and Isotope Shift

High-resolution diode-laser spectroscopy was performed in the red and near-infrared regions as well as the UV region for the rare-earth elements. Figure 1 shows a typical observed HFS spectrum of the $4f^7 5d6s^2\ {}^9D_2 - 4f^7 6p6s^2\ {}^7D_1$ transition at 394.3 nm in Gd I. Peaks of the even-mass isotopes, including the lowest abundance one ^{152}Gd, are labeled with the atomic symbol, and other peaks are HFS peaks of the odd-mass isotopes ^{155}Gd and ^{157}Gd. The full width at half maximum (FWHM) of peaks is about 30 MHz and is considered to be mainly from the natural width of the upper level of the transition and the residual Doppler broadening of the atomic beam.

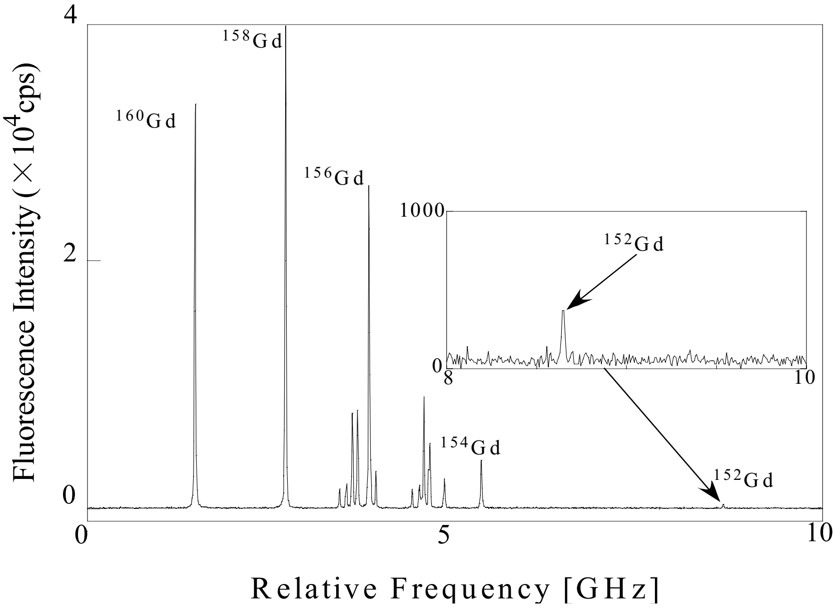

Fig. 1. Observed HFS spectrum of the $4f^7 5d6s^2\ {}^9D_2 - 4f^7 6p6s^2\ {}^7D_1$ transition at 394.3 nm in Gd I

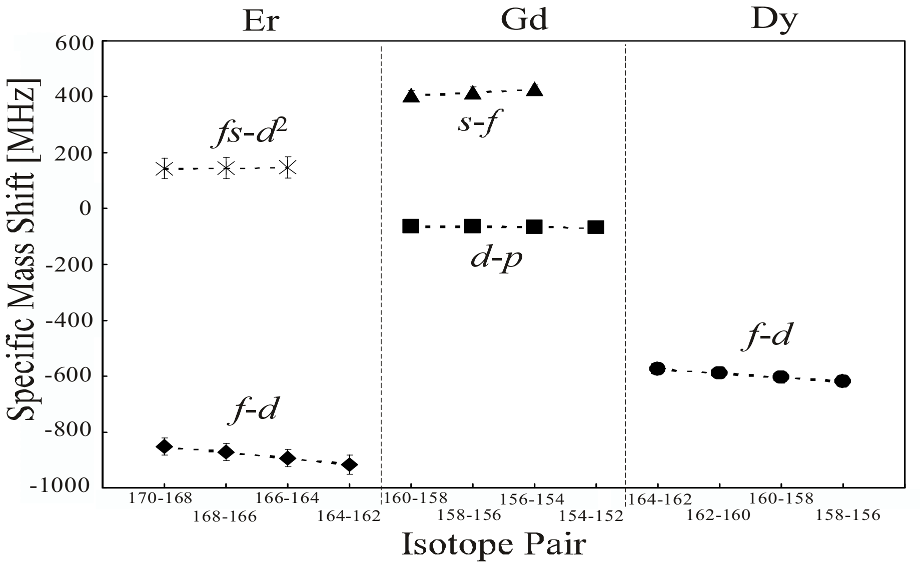

Fig. 2. Specific mass shift for different transitions in Er, Gd and Dy

The IS is the sum of the normal mass shift (NMS), the specific mass shift (SMS) and the field shift (FS) [6,7]. Since the NMS can be calculated easily, the SMS and FS can be derived from the observed IS by the King plot [6,7]. The derived SMSs are shown in Fig. 2 for different atomic transitions of Er, Gd and Dy. It can be seen that the SMSs have quite different values for the different transitions: the SMS of the $f - d$ transition is several times larger than that of the $d - p$ transition. This shows that the SMS strongly depends on the orbital angular momentum of electrons. The SMS is related the correlation between electrons which is important effect particularly for many-electron atoms such as the rare-earth elements. The present experimental data are useful to check theoretical many-electron atomic calculation; as the SMS provides the challenge task for such calculation.

From the FS, the 6*s*-electron charge density at the nucleus [8] $D_{6s} = 4\pi|\Psi(0)|^2$ was derived. We also performed the non-relativistic Hartree-Fock calculation for D_{6s} using the computer code written by Fischer [9]. The experimental and calculated 6*s*-electron densities at the nucleus are shown in Fig. 3 as a function of the atomic number. It is seen that the experimental and calculated values have a same tendency of increasing with the increase of the atomic number. However, the calculated values are smaller than the experimental ones by 30 %. This can be attributed to the configuration interaction and core polarization, which were neglected in the Hartree-Fock approximation.

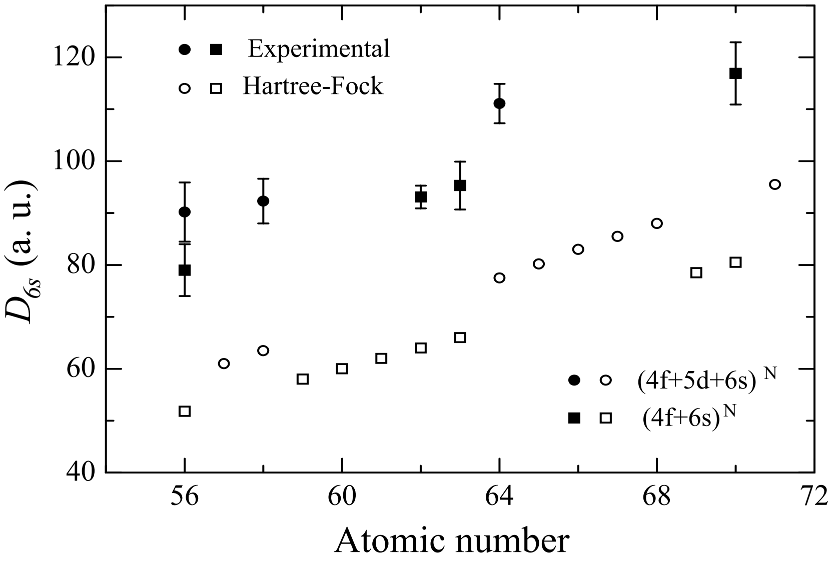

Fig. 3. Experimental and calculated (Hartree-Fock) 6*s*-electron density at the nucleus as a function of the atomic number

From measured IS, atomic configuration can be determined for the unknown levels. For the 397.4 nm transition in Er I, atomic configuration of the upper level at 25159 cm^{-1} is not yet known. The IS of this transition was measured to be 966.15(61) MHz for $^{170\text{-}168}$Er. The ISs of other transitions for $^{170\text{-}168}$Er were also measured to be 918.42(72) MHz for the $4f^{12}6s^2$ – $4f^{11}5d6s^2$ transition and -496.32(80) MHz for the $4f^{12}6s^2$ – $4f^{11}5d^26s$ transition. Comparing these results, we determined the atomic configuration of the upper level at 25159 cm^{-1} for the 397.4 nm transition as $4f^{11}5d6s^2$.

3.2 The Stark Effect

The Stark effect for alkali atoms of Rb and Cs was investigated by high-resolution laser spectroscopy. For Rb, we used transitions of $5s\ ^2S_{1/2} - 5p\ ^2P_{1/2}$ (D1) at 794.8 nm and $5s\ ^2S_{1/2} - 5p\ ^2P_{3/2}$ (D2) at 780.0 nm. Highly collimated atomic beam was used in this experiment. All HFS peaks at zero electric field were clearly resolved and the FWHM of observed spectra is about 16 MHz for

Rb D1 and D2 transitions. This width is considered to be from the natural width of the upper level of the transition and the residual Doppler broadening of the atomic beam is negligible.

Figure 4 shows typical Stark spectra of ^{87}Rb 5*s* $^2S_{1/2}$ (F=2) – 5*p* $^2P_{3/2}$ (F=3) transition measured at different electric field. It can be seen that spectra are shifted to the lower frequency by the electric field. Not only the shifts but splittings are observed and become larger as the electric field rises. The F=2 ($^2S_{1/2}$) – F=3 ($^2P_{3/2}$) transition, corresponding to the right peak at 0 kV/cm in Fig. 4, is expected to split into four peaks owing to the splitting of the upper level by the Stark effect according to the theoretical prediction. These four peaks are all clearly resolved at the electric field of 80.6 kV/cm, as shown in Fig. 4.

By carefully changing the electric field, dependence of shifts and splittings on the electric field was measured. A linear relation between the shift (splitting) and the square of the electric field was confirmed, which agrees with the theoretical prediction calculated by the second-order perturbation. From these measurements, we deduced scalar and tensor polarizabilities, which measure the atomic electric dipole moments induced by the electric field [10]. For Rb D2 transition, the scalar polarizability was derived to be 110.6(9) kHz/(kV/cm)^2 and the tensor polarizability –54.0(31) kHz/(kV/cm)^2, which can be compared with the previously reported values [11] of 146(32) kHz/(kV/cm)^2 and –40(6) kHz/(kV/cm)^2. The precision of the present values is improved considerably compared with the reported values, where HFS was not resolved. The present obtained scalar and tensor polarizabilities are related to the atomic wave function and are the fundamental properties for atomic physics.

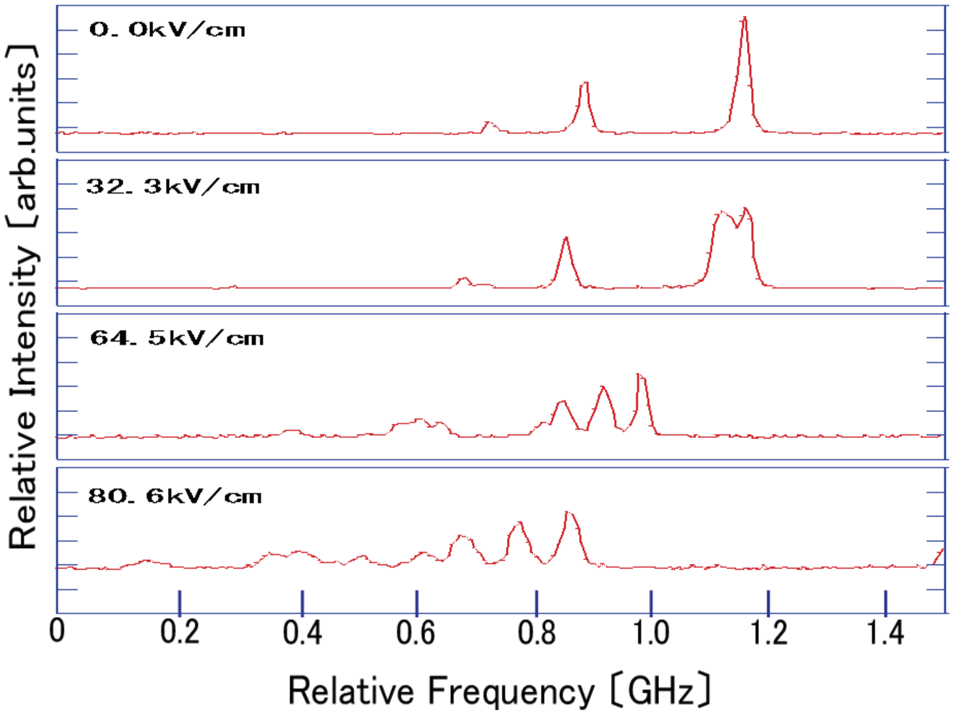

Fig.4. Stark spectra of ^{87}Rb 5*s* $^2S_{1/2}$ (F=2) – 5*p* $^2P_{3/2}$ (F=3) transition measured at different electric field

4. Summary

High-resolution atomic-beam diode-laser spectroscopy has been performed. ISs and HFSs have been measured for the rare-earth elements in the UV region as well as the red and near-infrared regions. Atomic property such as the configuration has been determined for the high-lying atomic level of Er. From IS measurements, the SMSs have been derived for different atomic configurations and found to strongly depend on the orbital angular momentum of electrons. The 6*s*-electron densities at the nucleus, related to the 6*s*-electron wave function, have been derived and compared with the Hartree-Fock calculation. Results show that the electron-correlation effects, such as the configuration interaction, core polarization, play an important role for the atomic structure.

The Stark effect of Rb atom has been investigated by high-resolution laser spectroscopy. Strong electric field, up to 82 kV/cm, has been successfully produced and the Stark shift and splitting have been observed for the Rb D1 and D2 transitions. Dependence of the shift and splitting on the electric field has been carefully examined. The scalar and tensor polarizabilities have been obtained for the Rb D1 and D2 transitions. Further experiments on other atoms are now performing.

The authors thank Y. Nemoto, H. Nakai and K. Nagami for assistance in this study. This work was partly supported by the JSPS-CAS Core-University Program in the field of “Plasma and Nuclear Fusion”.

Reference

[1] E.W. Otten, in: *Treatise on Heavy-Ion Science*, Vol. 8, ed. D. A. Bromly (Plenum, New York, 1989) p. 517.

[2] W. C. Martin, R. Zalubas and L. Hagan: *Atomic Energy Levels - The Rare-Earth Elements*, NSRDS - NBS60 (U.S. GPO, Washington D.C., 1978).

[3] C. S. Wood, S. C. Bennett, D. Cho, B. P. Masterson, J. C. Roberts, C. E. Tanner, C. E. Wieman: Science **275** (1997) 1759.

[4] J. M. Amini and H. Gould: Phys. Rev. Lett. **91** (2003) 153001.

[5] T. Wakui, W. G. Jin, K. Hasegawa, H. Uematsu, T. Minowa, H. Katsuragawa and M. Wakasugi: Jpn. J. Appl. Phys. **37** (1998) 4188; H. Nakai, W. G. Jin, M. Kawamura, T. Minowa, H. Katsuragawa and H. Uematsu: Jpn. J. Appl. Phys. **46** (2007) 815.

[6] K. Heilig and A. Steudel: At. Data Nucl. Data Tables **14** (1974) 613.

[7] W. G. Jin, T. Wakui, T. Endo, H. Uematsu, T. Minowa and H. Katsuragawa: J. Phys. Soc. Jpn. **70** (2001) 2316.

[8] For example, P. Aufmuth: J. Phys. B **15** (1982) 3127; J. Phys. B **18** (1985) 4007.

[9] C. F. Fischer: Comput. Phys. Commun. **43** (1987) 355.

[10] J. R. P. Angel and P. G. H. Sandars: Proc. Roy. Soc. A **305** (1968) 125.

[11] R. W. Schmieder, A. Lurio and W. Happer: Phys. Rev. A **3** (1971) 1209.

Theoretical Investigation on Dielectronic Recombination of High-Z Few-Electron Ions

Yinglong Shi[1], Chenzhong Dong[1, 2†], Denghong Zhang[1], and Yanbiao Fu[1]

[1]) College of Physics and Electronics Engineering, Northwest Normal University, Lanzhou 730070, China
[2]) Center of Theoretical Nuclear Physics, National Laboratory of Heavy Ion Accelerator of Lanzhou, Lanzhou 730000, China

† *e-mail: dongcz@nwnu.edu.cn*

Abstract

With a developed program for studying dielectronic recombination (DR) process, which is based on Multi-configuration Dirac-Fock (MCDF) method, the *KLL* DR processes for highly charged He-like to C-like iodine ions have been investigated systematically. The contributions from quantum electrodynamic (QED) effect and Breit interaction to the DR processes have been discussed. The *KLL* DR resonant energies and corresponding resonant strengths have been calculated. The theoretical DR spectra for different charged iodine ion are obtained in the *KLL* region. Comparison has been made between the present calculations and the experiments in Tokyo-EBIT.

Keywords: DR spectra, resonant strength, MCDF, *KLL* resonance, iodine

1. Introduction

Dielectronic recombination (DR) is a two-step resonant electron capture process. In the first step, a free electron is captured radiationlessly by the simultaneous excitation of a bound electron, and in the second step, the doubly excited state decays radiatively to a bound final state. The DR resonances are normally labeled by analogy with the nomenclature used for Auger process [1], such as *KLL*, *KLM*, *KLN*, etc. The case of *KLL* DR for initially He-like ions involves a continuum electron being captured to the *L* shell and a bound electron promoted from the *K* shell to the *L* shell.

The DR process is important in high-temperature plasmas, where it strongly affects both the charged state distribution and the emitted x-ray spectrum [2-7]. Accurate knowledge of DR cross sections is extensively needed in models of astrophysical and fusion plasmas [2]. Indeed, the understanding of the DR process is considered very important nowadays in plasma research. For example, it is well known that the ions of heavy elements such as tungsten can exist in fusion plasmas due to sputtering of the wall materials of the vessel [3]. The DR of such heavy ions is one of the primary sources of radiative energy loss from fusion plasmas and can lead to plasma cooling. The understanding of DR process is important for controlling such energy-loss.

Over the last two decades, the theoretical and experimental progress in investigations of the DR process of highly charged ions has opened perspectives for probing relativistic, quantum electrodynamic (QED), electron interaction, and nuclear effects in strong Coulomb fields (for review article see, e.g., Ref.[8-10]). Recently, Watanabe et al. [3] studied the DR processes of open-shell highly charged He-like to C-like iodine (Z=53) ions using the Tokyo-EBIT for the first time, where the different charge states were clearly separated. However, there are no available theoretical calculations to confirm the experimental resonant strengths and resonant energies for the highly charged iodine ions so far. In the present work, based on our previous computational experience, which has obtained success on the *KLL* DR processes of highly charged He-like to B-like mercury and uranium ions [11], a systematical study on the *KLL* DR processes of He-like to C-like iodine ions was performed.

2. Theoretical method

The DR cross section for an individual resonance, involving excitation from an initial state i, via a doubly excited state j, to a final state k, can be given by the following equation in atomic units in the framework of the isolated resonance approximation:

$$\sigma_{DR}(i,j,k) = \sigma^{c}_{i,j} B^{r}_{j,k}, \tag{1}$$

where $\sigma^{c}_{i,j}$ is the cross section for the resonance capture process from i to j, and $B^{r}_{i,j}$ is the radiative branching ratio for the process from j to k. The quantities $\sigma^{c}_{i,j}$ and $B^{r}_{i,j}$ can be written by [12]

$$\sigma^{c}_{i,j} = \frac{\pi^2\hbar^3}{m_e\varepsilon_j}\frac{g_j}{2g_i}A^{a}_{ji}\delta(\varepsilon-\varepsilon_j), \tag{2}$$

and

$$B^{r}_{j,k} = \frac{A^{r}_{jk}}{\sum_{k'} A^{r}_{jk'} + \sum_{i'} A^{a}_{ji'}}, \tag{3}$$

where g_i and g_j are the statistical weights of the state i and j, respectively. The summation $i^{'}$ runs over all the possible Auger final states, and the summation $k^{'}$ runs over all possible radiative final states. $\delta(\varepsilon$-$\varepsilon_j)$ is a delta function that requires the matching of the free electron energy ε to the resonance energy ε_j. The DR strength S_{ijk} is obtained by integrating the DR cross section $\sigma_{DR}(i,j,k)$ in Eq.(1) over the energy ε in the vicinity of the resonant energy ε_j. Substituting Eq.(2) and (3) into Eq.(1), we can obtain [5]

$$S_{ijk}(\varepsilon_j) = \frac{\pi^2\hbar^3}{m_e\varepsilon_j}\frac{g_j}{2g_i}A^{a}_{ji}\frac{A^{r}_{jk}}{\sum_{k'} A^{r}_{jk'} + \sum_{i'} A^{a}_{ji'}}, \tag{4}$$

Then, the total DR strengths may be obtained by a sum of S_{ijk} over all possible intermediate states j and the final states k. In order to compare with experimental results, the calculated cross section should be convoluted with a Gaussian distribution with an energy resolution Γ. The convoluted cross section is given by [12]

$$\sigma_t^{DR}(\varepsilon) = \sum_{j,k} \frac{S_{ijk}(\varepsilon_j)}{\sqrt{2\pi}\Gamma} \exp\left[-\frac{(\varepsilon - \varepsilon_j)^2}{2\Gamma^2} \right], \tag{5}$$

Here, an experimental resolution of $36\,eV$ (FWHM) [13] is adopted in the present calculations.

In this study, energies and wavefunctions have been generated by the widely used atomic structure package GRASP92 [14], which is an implementation of the MCDF method. Where, an atomic state wavefunction (ASF) is approximated by a linear combinations of the configuration state wavefunctions (CSFs) of the same symmetry. In the standard computations, the CSFs are linear combinations of the antisymmetrized products of a common set of orthonormal orbitals, which are optimized on the basis of the Dirac-Coulomb Hamitonian. In order to accounting for electron correlation effects, the active space method has been applied. In our calculations, the active space of CSFs includes all single and double excitations from the reference configurations up to one-particle orbitals in the $n = 3$ shell. Further relativistic contributions to the atomic states owing to (transverse) Breit interactions were also added by diagonalizing the Dirac-Coulomb-Breit Hamiltonian matrix. In addition, the dominant QED contributions (i.e. self-energy and vacuum polarization effects) to energy levels are estimated in the computations as a perturbation. The radiative decay rates and the Auger decay rates are calculated using the programs REOS99 [15] and AUGER [16], respectively.

3. Results and discussions

The contributions from the QED and Breit effects to the energy levels of the ground states and doubly excited states involved in the DR processes of He-like to C-like iodine ions are given in Fig.1(a) and (b), respectively. As shown in Fig.1, the QED and Breit contributions to the ground states are greater than that to the doubly excited states. For the Li-like iodine ion, for instance, the present QED and Breit contribution to the ground state Li_0 $[1s^2 2s]_{1/2}$ is $85.50\,eV$ and $60.83\,eV$, respectively, while to the doubly excited state Li_1 $[1s2s^2 2p_{1/2}]_1$ is $50.84\,eV$ and $8.85\,eV$ respectively. It is obviously that the QED and Breit effects are very sensitive to the inner-shell excitations. The reason is that following the transfer of the inner $1s$ electron to a higher orbital, the strong orbital relaxation happened, which is consistent with our previous study for high-Z ions [17].

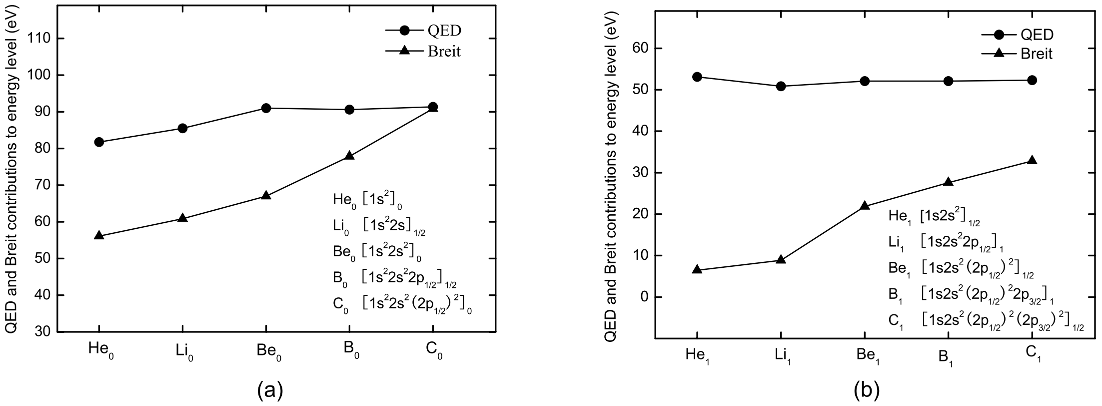

Figure 1: Contributions from QED and Breit effects to the energy levels of the ground states (a) and doubly excited states (b) as functions of different charged iodine ions. The labels of the energy levels are similar to that used by González Martínez et al. [10].

Table 1 listed the present results of the total strengths for *KLL* DR processes of He-like to C-like iodine ions. As a comparison, the newly experimental results measured in Tokyo-EBIT by Watanabe et al. [3] are also presented. It can be found that the total resonant strengths increased gradually with increasing charge state. This increase mainly comes from the increased number of *L* shell vacancies, since which causes the number of the intermediate doubly excited states increasing. Compared with the experimental results, we can found that the present total *KLL* strengths for different charged iodine ion are smaller than that of experiments by around 20 % .

Table 1: Comparison between the present theoretical and the experimental total resonant strengths (in 10^{-19} cm^2 eV) for He-, Li-, Be-, B-, and C-like iodine ions.

	Resonant strengths	
Iodine ions	This work	Experiment[3]
He-like	3.411	4.27(39)
Li-like	2.316	2.91(26)
Be-like	1.856	2.39(22)
B-like	1.178	1.49(14)
C-like	0.593	0.764(76)

In order to further investigate the discrepancy between the present calculated and the measured DR strengths, the behavior of the resonant strengths with atomic number Z are analyzed for He-like ions in detail. The *KLL* resonant strengths for He-like ions, which have been widely studied [2, 3, 7, 11, 18-21], are summarized in Fig.2 together with the present result for iodine ion. Although we found that the present resonant strength for He-like iodine ion is less than the experimental result [3], it is in better agreement with other theoretical calculations for He-like ions. As shown in Fig.2, for elements heavier than Ar, the resonant strengths become smaller with increasing Z since electron capture into doubly excited states becomes more difficult as Z increases. However, for lower Z elements Auger processes which compete with radiative processes become significant which tends to decrease the resonant strength. In the high-Z region, no experimental resonant strength has been reported apart from the recent result for iodine ion. So, the present and previous [11] results can give important theoretical guide for further DR experiment of high-Z ions. Also, more benchmarked measurements over a wide range of atomic numbers are needed to validate the behavior of the *KLL* resonant strengths for He-like ions.

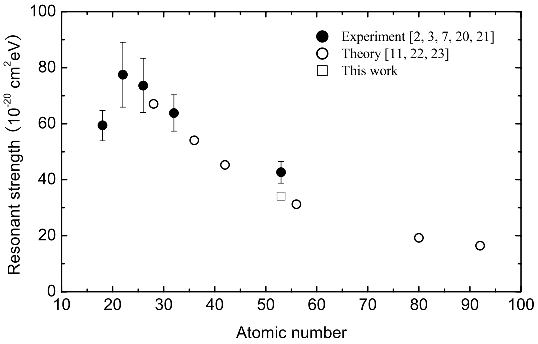

Figure 2: The *KLL* DR resonant strength of He-like ions. The solid circles are experimental values, while the open circles are theoretical values. The open square is present result (I^{51+}). The other data are Ar^{16+} [18], Ti^{20+} [2], Fe^{24+} [19], Ni^{26+}, Mo^{40+}, and Ba^{54+} [20], Ge^{30+} [7], Kr^{34+} [21], I^{51+} [3], Hg^{78+} and U^{90+} [11].

The theoretical DR spectra for each ion species can be obtained through convoluting the resonant strengths using a Gaussian distribution with the experimental energy resolution of $36\,eV$ [13]. In Fig.3, it present the our theoretical DR spectra and the experimental spectra by Watanabe et al. [3]. In order to match with the experimental results, the calculated DR resonant positions have been shifted by 420 eV around toward high electron energy. The comparisons with the experimental results are made, which shows very good agreement for both the amplitudes of the cross section and the line shapes. At present, the reasons for the discrepancy between theoretical and experimental resonant energies (i.e. peak positions) are still not very clear and should be the subject of future investigations.

4. Conclusions

Based on the systematical calculations of DR resonant strengths and cross sections related with the *KLL* DR processes of highly charged He-like to C-like iodine ions, the contributions from QED and Breit effects to the DR processes have been discussed. The *KLL* DR resonant energies and corresponding resonant strengths have been obtained, which are necessary for further identify the experimental DR spectra in detail. Finally, the theoretical DR spectra for each highly charged ion species are gained through convo-

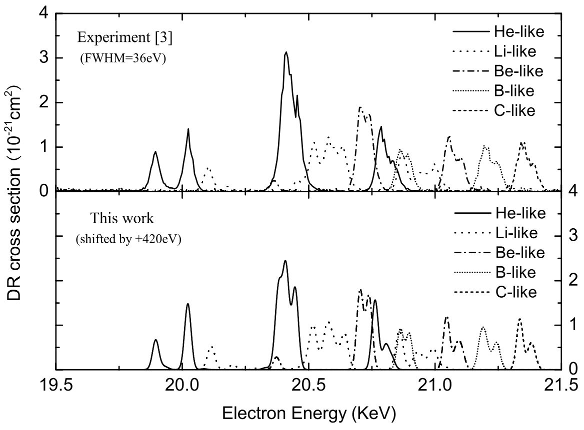

Figure 3: The *KLL* DR spectra of He-like to C-like iodine ions.

luting the resonant strengths using a Gaussian distribution with the experimental energy resolution of $36\,eV$. Good agreement has been found between the present calculations and the recent experiments.

Acknowledgements

The authors would like to thank Dr.Hirofumi Watanabe at UEC Tokyo for useful and stimulating discussions. This work was supported by the SFI/RIA China-Ireland Research Collaboration Fund(CI-2004-07), the National Natural Science Foundation of China (Grant No.10434100, 10774122), the Core-University Program between Japanese Society of Promotion of Science and Chinese Academy of Sciences, the Specialized Research Fund for the Doctoral Program of Higher Education of China (Grant No. 20070736001), the Foundation of Center of theoretical Nuclear Physics of National Laboratory of Heavy Ion Accelerrator of Lanzhou, and the Foundation of Northwest Normal University(NWNU-KJCXGC-03-21).

References

[1] D.A. Knapp, P. Beiersdorfer, M.H. Chen, et al., Phys. Rev. Lett., **74**, 54 (1995).
[2] B.E. O'Rourke, H. Kuramoto, Y.M. Li, et al., J. Phys. B, **37**, 2343 (2004).
[3] H. Watanabe, H. Tobiyama, A.P. Kavanagh, et al., Phys. Rev. A, **75**, 012702 (2007).
[4] D.H. Zhang, C.Z. Dong, L.Y. Xie, et al., Acta Phys. Sin., **55**, 0112 (2006).
[5] Y.B. Fu, C.Z. Dong, D.H. Zhang, et al., Chin. Phys., **15**, 2583 (2006).
[6] H. Watanabe, F.J. Currell, H. Kuramoto, et al., J. Phys. B, **34**, 5095 (2001).
[7] X. Zhang, J.R. Crespo López-Urrutia, P. Guo, et al., J. Phys. B, **37**, 2277 (2004).
[8] H.F. Beyer, V.P. Shevelko, Introduction to the physics of highly charged ions, Institute of Physics, Bristol, 2002.
[9] Z. Harman, I.I. Tupitsyn, A.N. Artemyev, et al., Phys. Rev. A, **73**, 052711 (2006).
[10] A.J. González Martínez, J.R. Crespo López-Urrutia, J. Braun, et al., Phys. Rev. A, **73**, 052710 (2006).
[11] Y.L. Shi, C.Z. Dong, D.H. Zhang, et al., Acta Phys. Sin., **57**, 0088 (2008).
[12] J.G. Wang, T.Q. Chang, C.Z. Dong, et al., Eur. Phys. J. D, **5**, 167 (1999).
[13] H. Watanabe, Private communication (2007).
[14] F.A. Parpia, C. Froese Fischer, I.P. Grant, Comput. Phys. Commun., **94**, 249 (1996).
[15] S. Fritzsche, C. Froese Fischer, C.Z. Dong, Comput. Phys. Commun., **124**, 340 (2000).

[16] S. Fritzsche, H. Aksela, C.Z. Dong, et al., Nucl. Instrum. Methods B, **205**, 93 (2003).
[17] C.Z. Dong, D.H. Zhang, Th. Stöhlker, et al., J. Phys. B, **39**, 3121 (2006).
[18] R. Ali, C.P. Bhalla, C.L. Cocke, et al., Phys. Rev. A, **44**, 223 (1991).
[19] P. Beiersdorfer, T.W. Phillips, K.L. Wong, et al., Phys. Rev. A, **46**, 3812 (1992).
[20] D.A. Knapp, R.E. Marrs, M.B. Schneider, et al., Phys. Rev. A, **47**, 2039 (1993).
[21] T. Fuchs, C. Biedermann, R. Radtke, et al., Phys. Rev. A, **58**, 4518 (1998).

Storage and Cooling of Ions in an Electrostatic Ring

TANUMA Hajime[1], JINNO Satoshi[1], TAKAO Tomoharu[1], HANADA Katsuhiko[1],
OSHIKIRI Kohki[1], GOTO Motoshi[2], TOGAWA Mami[2], MATSUMOTO Jun[2],
OKUNO Kazuhiko[1], AZUMA Toshiyuki[1], and SHIROMARU Haruo[2]
1) Department of Physics, Tokyo Metropolitan University,
1-1 Minami-Ohsawa, Hachioji, Tokyo 192-0397, Japan
2) Department of Chemistry, Tokyo Metropolitan University,
1-1 Minami-Ohsawa, Hachioji, Tokyo 192-0397, Japan
e-mail: tanuma@phys.metro-u.ac.jp

Abstract

Keywords: electrostatic ion storage ring, molecular ion, meta-stable state, life time

1. Introduction

An electrostatic ion storage rings is a suitable device to investigate slow dynamic processes and spectroscopic properties of ions. As compared to a magnetic storage ring, this has several advantages, i.e. the absence of magnetic field, no hysteresis, the smaller size, and, in particular, no restriction on the mass of the stored ion.

After the construction of the first electrostatic ion storage ring, ELISA, at University of Aarhus, Denmark in 1997 [1] and that of the second one at KEK (High Energy Accelerator Research Organization in Tsukuba, Japan) in 2002 [2], we have developed the third ring at Tokyo Metropolitan University in 2003 [3].

2. Experimental setup

Figure 1 shows a layout of our electrostatic ion storage ring, named TMU E-ring. It was basically designed with a common concept to the preceding rings, and it has a race-track-type shape of about 7.7 m in circumference. However, we specially designed it to be kept all electrodes at very low temperature with a cooling system by using liquid nitrogen for the reduction of the black-body radiation which is irradiated on the stored ions.

Two neutral particle detecters were equipped to the ring in order to observe the intensity and profile of the neutrals produced by fragmentation or neutralization of primary ions. Each detector consists of a chevron type microchannel plate (MCP) and a phosphor screen with a diameter of 45 mm.

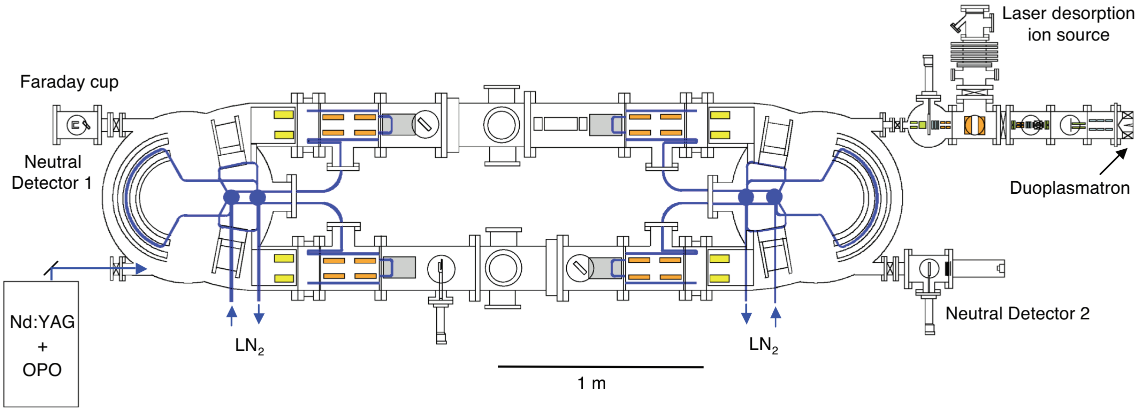

Figure 1: Schematic diagram of the TMU E-ring with two different ion sources and a Nd:YAG and OPO lasers.

In this ring, three different-type ion sources has been installed for injections of various kinds of ions, i.e. a duoplasmatron for positive atomic and small molecular ions, a cesium sputter ion source for negative atomic and small cluster ions, and a laser desorption ion source for positive and negative large molecular and cluster ions. As the typical injection energy for the ring is 20 keV, the circulation time is about 4 μs for the lightest ion, H^+, and about 0.1 ms for a heavy fullerene ion as C_{60}^+. The typical storage lifetime, which depends on the background pressure in the ring, is about 10 s for heavy ions under vacuum conditions of several 10^{-9} Pa. Therefore, the relatively slow processes having the reaction rates from ms to a few seconds are feasible to be investigated with this apparatus.

Since the construction of TMU E-ring, several kinds of ions have been stored in it, and the following physical experiments have been performed: 1) lifetime measurements for metastable states of CO^{2+} [4], 2) laser spectroscopy of metastable O_2^+ ions, 3) photodetachment of porphyrin (H_2TPP) anions [5], 4) collisional detachment cross sections of C^- with rare gases [6], 5) observation of weakly bound excited states of C_n^- ($1 \leq n \leq 8$) [6]. In this report, we describe the some results on these topic very briefly.

3. Lifetime measurements for metastable states of CO^{2+}

Generally speaking, doubly charged diatomic molecular ions are thermodynamically unstable due to the Coulombic repulsion. These ions occasionally survive for a certain period, however, due to the shallowness of their potential well and the corresponding thickness of the potential barrier. Eventually the ions dissociate by tunneling through the barrier. Since the tunneling rate is very sensitive to the thickness of the potential barrier, the lifetime of such doubly charged ions also depends on their vibrational states in the

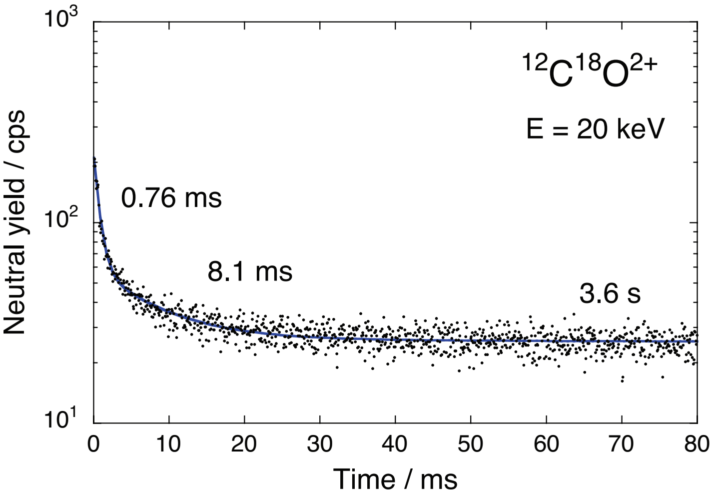

Figure 2: Neutral particle yield for the 20 keV $^{12}C^{18}O^{2+}$ beam as a function of time after injection into the ring. The solid line shows the fitted decay curve, obtained as the sum of three exponential functions with the lifetimes of 0.76 ms, 8.1 ms, and 3.6 s.

shallow potential well. When a repulsive potential curve crosses the potential well, these vibrational states often decay immediately.

When spontaneous dissociation of metastable CO^{2+} occurs, two charged fragments are produced :

$$CO^{2+} \rightarrow C^+ + O^+, \tag{1}$$

where the pair of fragment ions is either $C^+(^2P) + O^+(^4S)$ or $C^+(^2P) + O^+(^2D)$. Though these fragment ions cannot be detected in this apparatus, we measured the neutral particles which originate from the fragmentation through charge exchange reactions between the CO^{2+} ions and the residual gas (R) :

$$\begin{aligned} CO^{2+} + R &\rightarrow C + O^+ + R^+ \quad (2) \\ &\rightarrow C^+ + O + R^+. \quad (3) \end{aligned}$$

The two fragmentation paths of CO^{2+} are both accompanied by a neutral product created by collisions with the residual gas.

We used the duoplasmatron ion source in electron impact mode to prepare CO^{2+} ions. In this experiment, a CO gas consisting of isotopic ^{18}O was used to separate CO^{2+} from ^{14}N and $^{14}N_2^{2+}$. The $^{12}C^{18}O$ ions were injected into the ring with the kinetic energy of 20 keV at a beam current between 100 and 600 pA.

Figure 2 shows the decay curve of the neutral yield from stored CO^{2+} ions measured by the neutral detector 1, which clearly consists of multiple components. This decay

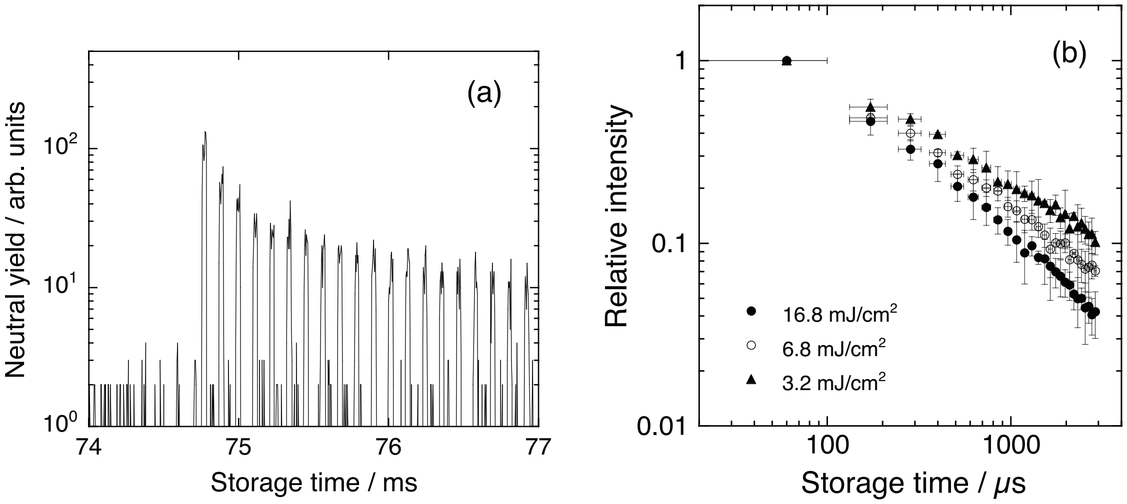

Figure 3: The neutral particle yield for the H_2TPP anions. (a) Yield of the delayed detachment by the laser irradiation as a function of the storage time; (b) Log-log plot of the relative neutral yield, normalized using the first peak, versus the time after excitation with various laser fluence.

curve was reasonably fitted by the sum of three exponential components with lifetimes of 0.76 ms, 8.1 ms, and 3.6 s. The longest lifetime is not relate to the spontaneous dissociation of metastable CO^{2+} ions, and is likely to be governed by the storage lifetime for population decaying only by collisions with the residual gas. The shorter lifetimes corresponding to the inherent lifetimes. The results obtained by our ring agree well with results obtained by the magnetic ring ASTRID [7].

4. Photo-detachment of porphyrin (H_2TPP) anions

A laser desorption ion source equipped with the ring can be used to produce positive and negative large molecular ions. Powder of a typical metal-free porphyrin molecule, 5,10,15,30-tetraphenyl-21H,23H-porphyrin (hereafter H_2TPP), was dissolved in $CHCl_3$, and the solution was put in a sample holder. An H_2TPP cast film prepared in this way was desorbed by the fourth harmonic output of an Nd:YAG laser. The produced H_2TPP anions were extracted and injected into the ring with the kinetic energy of 15 keV.

Generally speaking, the large molecular ions produced by the laser desorption are extremely hot, and the radiative cooling of the ions with emissions of infrared photons continues during the circulation in the ring. This cooling process of H_2TTP anions has been investigated with measurements of the neutral yield by the laser merging of various wavelengths and fluences at different storage times.

The signals of the neutral particles measured by the neutral detector 2 with the laser merging at the storage time of 75 ms is shown in Figure 3(a). The delayed components, which are observed several revolutions after irradiation, are clearly seen in this figure. The log-log plots of the integrated intensity of each peak against the time after irradiation with the 600 nm laser, obtained for various laser fluences, are shown in Figure 3(b). As reported by the ELISA group, a broad distribution of the initial internal energy gives the delay process being fitted to a t^{-1} function [8]. The data in Figure 3(b) can be fitted with straight lines, indicating that the power law is also valid in these cases. However, the slope deviates considerably from -1, depending systematically on the laser fluence. That is, lowing the fluenece produces a gentle slope, which is about -0.5 at a low fluenece. This indicates that the super-excited anions do not populate various internal energies uniformly, at least if the contribution of multiphoton excitation is small.

5. Collisional detachment cross sections of C^- with rare gases

The negative carbon atomic ions, C^-, were produced by using a cesium sputter ion source and injected into the ring after the accelerate by the electric potential of 20 kV. The neutral carbon atom produced by the collision with the residual gas can be observed by the neutral particle detectors. When the target gas was introduced in the ring with the very small pressure, we can observe the enhance of the neutral intensity. The decay curve of the neutral yield from stored C^- ions with the velocity v measured by the neutral detector 2 can be given by the following equation :

$$I(t) = I(t_0) \exp\left[-\left(\sigma_{\mathrm{R}} n_{\mathrm{R}} + \sigma_{\mathrm{T}} n_{\mathrm{T}}\right) vt\right] \tag{4}$$

where σ_{R} and σ_{T} are the detachment cross sections by the residual and target gases, and n_{R} and n_{T} are the densities of the residual and target gases, respectively. From the decay curves measured with the different target gas pressures of various target gases, we have obtained the detachment cross sections of the C^- ion with the rare gases, namely He, Ne, Ar, Kr, and Xe.

Figure 4 shows the detachment cross sections as a function of the scattering length of s-wave electron. The cross section of the elastic collision of an electron with a neutral gas is given by

$$\sigma = \frac{4\pi L^2}{1 + L^2 K^2} \tag{5}$$

where K is the wave number of the electron, and L is the scattering length of s-wave electron [9]. These theoretical calculations show fairly good agreement with the experimental results. This finding indicates that the naive model, in which an extra electron in the anion is treated as a free electron moving at the same velocity of the anion, would be not so far from reality.

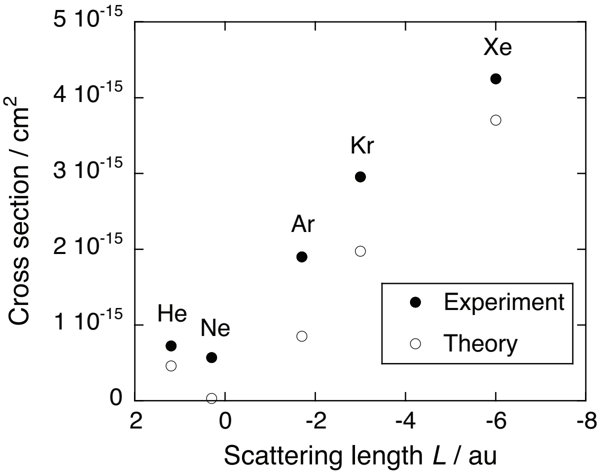

Figure 4: Measured detachment cross sections in collisions of C^- with rare gases at 20 keV, and theoretical cross sections of the elastic collision of an electron with rare gases, as a function of the scattering lengths of s-wave electron.

6. Observation of weakly bound excited states of C_n^- $(1 \leq n \leq 8)$

For C^- ions, we observed that the lifetime of the excited state ($2p^3\,{}^2D$) depends on the environmental temperature, because this state has the binding energy of a few ten meV and can be easily photo-detached by the black-body radiation at the room temperature. This measurement has been achieved with the cooling of the electrodes by liquid nitrogen. The observed lifetime of the excited state at room temperature of 2.7 ms became about 6.0 ms after the cooling, with contract of a constant storage lifetime of the ground state ($2p^3\,{}^4S$) determined by only the collisional cross-section with the residual gas.

Not only atomic anions, but also the small carbon cluster anions, C_n^- $(n \geq 2)$, were also produced by the same sputter ion source. The decay curves of C_n^- $(2 \leq n \leq 8)$ were measured to find the short lifetime components for every size of the clusters. The metastable states of carbon cluster ions is reported by J. U. Anderson *et al.* by using the magnetic storage ring ASTRID [10] only for $n = 2$, 3, 5, 7, and 9. The difference between the works done in the ASTRID and in the TMU E-ring might be due to the different operation conditions of the cesium sputter ion source.

7. Conclusion

Using the electrostatic storage ring, we perform several types of experiments on light and heavy ions. The metastable states and highly excited states of ions have been investigated from the various viewing points. Very recently, we measured the absorption spectra of zinc phthalocyanine anions, and time evolution of the spectra as a function of the storage time allows us to observe the hot anions undergoing radiative cooling [11].

Acknowledgement

This work is in part supported by the Grant-in-Aid for Scientific Research (Nos. 14204062 and 14340124) from the Japanese Society for the Promotion of Science and the JSPS-CAS Core-University Program in the field of “Plasma and Nuclear Fusion”.

References

[1] S. P. Møller, Nucl. Instrum. Meth. A **394**, 281 (1997).
[2] T. Tanabe *et al.*, Nucl. Instrum. Meth. A **482**, 595 (2002).
[3] S. Jinno *et al.*, Nucl. Instrum. Meth. A **532**, 477 (2006).
[4] S. Jinno *et al.*, Nucl. Instrum. Meth. A **572**, 568 (2007).
[5] M. Goto *et al.*, Eur. Phys. J. D **43**, 65 (2007).
[6] T. Takao *et al.*, J. Phys. Conf. Ser. **88**, 012044 (2007).
[7] L. H. Andersen *et al.*, Phys. Rev. Lett. **71**, 1812 (1993).
[8] K. Hansen *et al.*, Phys. Rev. Lett. **87**, 123401 (2001).
[9] N. F. Mott and H. S. W. Massey, *The Theory of Atomic Collisions*, (Oxford University Press, 1965)
[10] J. U. Anderson *et al.*, Z. Phys. D **40**, 365 (1997).
[11] M. Goto *et al.*, *to be submitted.*

Production of nanometer sized charged particle beams with glass capillary

Tokihiro Ikeda[1], Yasuyuki Kanai[1], Takao M. Kojima[1], Yoshio Iwai[1],
Yuu Kanazawa[2], Masamitsu Hoshino[2], Tomohiro Kobayashi[3],
Grigory P. Pokhil[4] and Yasunori Yamazaki[1,5]

(1) *Atomic Physics Laboratory, RIKEN, 2-1 Hirosawa, Wako, Saitama 351-0198, Japan*
(2) *Department of Physics, Sophia University, 7-1 Kioicho, Chiyoda, Tokyo 102-8554, Japan*
(3) *Beam Application Team, RIKEN, Wako, Saitama 351-0198, Japan*
(4) *D.V. Skobeltsyn Institute of Nuclear Physics, Moscow State University, 119992 Moscow, Russia*
(5) *Institute of Physics, University of Tokyo, Meguro, Tokyo 153-8902, Japan*

e-mail: tokihiro@riken.jp

Abstract

We have developed methods to produce nanometer-sized beams of keV highly charged ions and MeV charged particles with various glass-made beam optics. The beam size of 900 nm was obtained for keV ions. (1) For keV energy region, a focusing effect for an Ar^{8+} beam of 8 keV through a cm-long tapered capillary was obtained with a density enhancement of the transmitted beam compared with that of the input beam, which increases from 1 to 6 as the input current decreases from 30 pA to 0.8 pA. (2) For 4 MeV He^{2+} beam, a 100 times density enhanced beam by a cm-long tapered capillary with a closed outlet was utilized to irradiate a biological cell in liquid. The range of the beam was controlled by the closed outlet with accuracy of $\sim$1 μm. Moreover, muon beams with an energy of 13 MeV were also focused with a density enhancement of a factor of $\simeq$2 using 40 cm-long tapered glass tubes.

Keywords: atomic processes, highly charged ion, glass capillary, insulator surface, microbeam, cell irradiation, muon

1 Introduction

Interaction of slow (kV - 10 kV accelerated) highly charged ions (HCI) with multiple nano-capillaries in insulator foils has recently been intensively studied experimentally [1-11] as well as theoretically [12-14]. One of the most prominent features is a so-called guiding effect, a transportation of slow HCIs along the capillary axis keeping their initial charge states even when the capillary axis was tilted against the beam direction. The fact that most of the guided ions keep their initial charge suggests that the ions do not touch the inner wall of the capillaries during transportation, *i.e.,* an amazingly well-tuned electric field is automatically formed in each capillary. In other words, a self-organized charge-up of the inner wall plays an important role in realizing the guiding effect.

A somewhat similar but qualitatively different phenomenon has been reported for MeV ion beams by Nebiki *et al.* [15], where a 2 MeV He^{+} beam was transmitted through a cm-long single tapered glass capillary and focused down to several hundreds nm in size. In this case, multiple small angle scatterings are expected to be dominant to induce the phenomena, and the beam density at the capillary outlet was found to be much higher than that at the inlet, which is called a focusing effect. It is then an interesting question whether various charged particles are guided and focused by a tapered single capillary. We briefly describe here how slow HCI's [16-18], MeV ions [19, 20], and positive/negative muons [21] are really focused by a tapered single glass capillary (tube).

2 Transmission of keV-energy HCI beams

A beam with the diameter of less than 1 μm (hereafter, nanobeam) of slow HCIs is not yet practically available because HCI beams are sometimes so weak that the beam intensity is reduced drastically by a collimator or slit. In addition, collisions of the beam with the inner wall of the collimator or the slit induce contamination due to charge-changed ions. When magnetic and/or electrostatic lenses are combined, good emittance is required. Single tapered glass capillary has the following advantages. (1) Slow HCI can be reflected from the inner wall without a close collision, keeping its initial charge state. (2) The taper can enhance the density of the output beam. (3) The size of the output beam is the same size of the outlet inner diameter. Considering these points, single tapered glass capillaries are one of the feasible techniques to produce a nanobeam of slow HCI.

The first experiment of the transmission of slow HCI beam through insulator capillaries was performed by Stolterfoht *et al.* [1]. They found that most of the transmitted ions kept their initial charge state for a 3 keV Ne^{7+} beam through a multi-capillary foil of polyethylene terephthalate (PET). The phenomenon can be explained as follows: The incident ions entering the capillary hit the inner wall and consequently cause it to become charged. When the accumulated charge becomes large enough to prevent the following incident ions from touching the inner wall, the ions travel more or less parallel to the wall, and then the ions can exit from the outlet. If the diameter of the outlet is smaller than that of the inlet, and is in μm/nm order, a density enhanced micro-/nanobeam of slow HCI is realized.

Experimental setup

An ion beam of 8 keV Ar^{8+} was extracted from a 14.5 GHz Caprice ECR (Electron Cyclotron Resonance) ion source at RIKEN, and then transported to an experimental chamber, where the vacuum level was $\sim 10^{-5}$ Pa, via a mass/charge selecting magnet. The ion beam was then cut by a 2 mmϕ aperture (see Fig. 1), injected in a tapered glass capillary made of borosilicate, and finally detected by a PSD (Position Sensitive Detector) set at 125 mm downstream from the capillary inlet via a deflector. The divergence of the incoming beam after the aperture was at most ±3.3 mrad. The deflector was used for the charge-state analysis of the transmitted ions. The tapered capillary was prepared by heating a straight glass tube, and then stretched by pulling both ends with a constant force. The taper angle can be controlled by tuning the temperature and the force [17]. The outer and inner diameters of the capillary at the inlet were 2 mm and 0.8 mm, respectively, and those at the outlet were 55 μm and 24 μm, respectively. (Hereafter, D_{in} for the inlet inner diameter and D_{out} for the outlet inner diameter.) A typical length of the capillary was 50 mm.

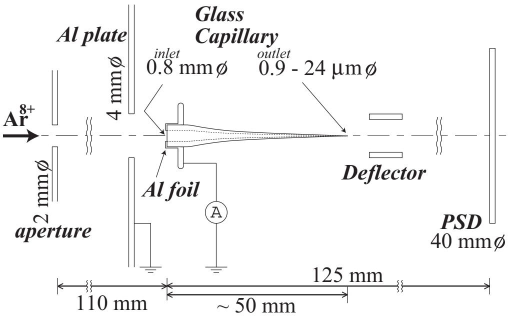

Figure 1: A schematic view of the experimental setup[16].

Density enhancement of the output beam

For a capillary of $D_{\mathrm{out}} = 24$ μm, the transmitted beam was guided within as large as ±87 mrad (=±5°), and had a circular spot at the PSD and the divergence of ±5 mrad without the charge transfer inside the capillary, where the transmission rate was at most 1% [16]. Without tilting the capillary with respect to the beam axis, we have observed stable transmission for more than 1200 sec as seen in Fig. 2, where the maximum counts at the PSD was about 1600 cps for the entering current of 0.2 pA. The density enhancement factor, σ, was introduced and defined by the ratio of N_t/S_o to N_i/S_i, where N_t is the number of transmitted ions, N_i the number of injected ions into the capillary, and S_o and S_i the geometrical outlet and inlet cross sections of the capillary, respectively. For this

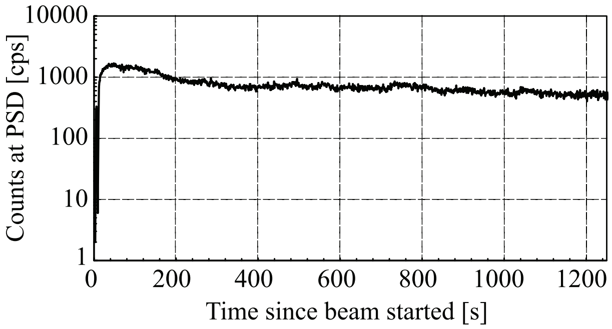

Figure 2: Time dependence of the number of transmitted ions. The maximum counts at the PSD was about 1600 cps [16].

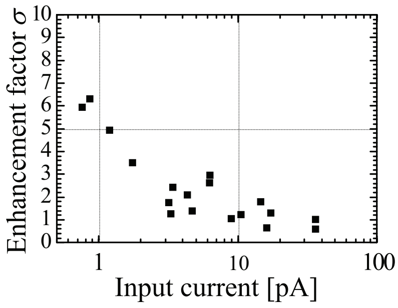

Figure 3: Input current dependence of the enhancement factor for 8 keV Ar^{8+} beam.

measurement, the density of the output beam was larger than that of the input beam, where the factor, σ, was approximately 10 [16]. However, the density enhancement could depend on the beam energy, the charge state of the ion, the ion mass, the input current intensity, outlet size and surface resistivity of the capillary and so on. We examined the input current dependence of the density enhancement. Figure 3 shows the enhancement factor as a function of the input current without tilting the capillaries of $D_{\text{out}}=$ 20 μm. The horizontal and vertical errors were estimated to be about 10 % due to the input beam fluctuation. The enhancement factor was found to decrease from 6 to 1 with the input current varying from 0.8 pA to 30 pA.

Nano-meter sized beam

Slow HCIs have high ability to modify surfaces and cause efficient sputtering without damaging the substrate very much. For example, a single HCI induces a nanometer sized dot on graphite [22-24] and Al_2O_3 surfaces [22]. It was also found that the F-Si bond direction of a Si(001)-F surface can be reconstructed from the 3D momentum distribution of F^+ ions desorbed by slow HCIs, *i.e.,* a stereo-chemical analysis can be done with slow HCIs [25]. Once a nanobeam is available, these functions specific to slow HCIs can be used to realize various nano-fabrications, *e.g.,* nano-patterning of nanodots and element-sensitive nano-imaging.

The transmitted beam through a capillary with $D_{\text{out}}=$ 900 nm was successfully obtained for Ar^{8+} ions with an energy of 64 keV. The spot at the PSD had widths (FWHM: full width at half maximum) of 0.30 mm and 0.40 mm in the vertical and horizontal directions, respectively. The corresponding divergences were ±2.0 mrad and ±2.7 mrad, respectively [17]. An outlet with D_{out} more than $\sim$ 900 nm has been obtained by cutting around

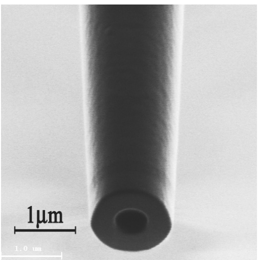

Figure 4: A manufactured outlet (D_{out}= 500 nm) of a glass capillary by FIB.

the outlet under an optical microscope. However, for the outlet with D_{out} smaller than several hundreds of nm, a focused ion beam (FIB) of 40-keV Ga^+ was employed to realize such smaller outlet sizes. Figure 4 shows a thus manufactured outlet of a glass capillary with D_{out}= 500 nm. The scanning parameters of the Ga^+ beam, *e.g.,* scanning directions, interlace rate, scanned region, etc., were tuned to prevent the Ga^+ beam from being bent due to the charge up around the capillary outlet.

3 Transmission of MeV-energy beams

An application of μm-/nm-sized He ion beams in a MeV region with glass capillaries has already been performed for the analysis of materials [15, 26]. In the work of [15], transmission of 2 MeV He^+ ions without significant energy loss was reported. We have developed another technique using MeV-energy ions for biological applications with closed outlet capillaries.

Considering the focusing of MeV ion beams due to multiple small angle scatterings, a muon beam with an energy of more than MeV could be focused by a tapered glass tube. Consequently experiments investigating the focusing of muon beams were performed.

Range control with a closed outlet

If the outlet of a glass capillary is closed by a thin lid for a beam injection into liquid, it is possible to control the range of the beam in the liquid, because the energy-loss of ions within the lid can be controlled by adjusting the thickness of the lid. Recently, glass capillary with a sub-micron-thick glass lid was introduced to realize the irradiation of wet samples, especially biological cells. As a calibration, 4 MeV He^{2+} ions were injected into liquid scintillator and the scintillation volume [19, 20], which corresponds to the range and struggling of the ions, showed good agreement with a simulation by SRIM-2006 [27]. The enhancement factor was observed to be more than 100. Figure 5(a) shows how to fabricate a capillary outlet with a thin lid, where FIB is used to cut the thick lid, which is already made by filling with melted glass. Figures 5(b) and (c) are the photographs of the fabricated outlet taken by an FIB device and an optical microscope, respectively. The thickness was set to 1μm. The arrows in Figs. 5(a) and (b) are the trace of Ga$^+$ beam.

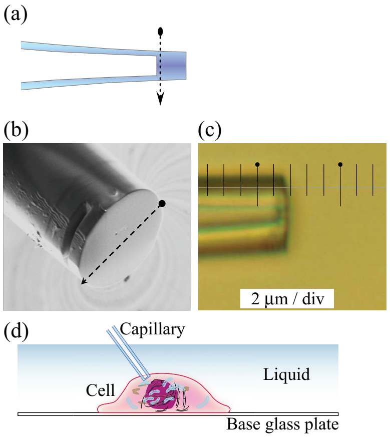

Figure 5: (a) FIB is used to cut the thick lid, which is already made by filling with melted glass. (b) and (c) are photographs of the fabricated outlet taken by an FIB device and an optical microscope, respectively. Arrows in (a) and (b) are the trace of the Ga$^+$ beam. (d) ion irradiation of a cell in liquid.

Application to cell irradiation

Figure 5(d) explains how to use the capillary for ion irradiation of a cell in liquid without breaking the vacuum of the beam transport. A typical animal cell is about 50 μm in diameter, composed of complex intracellular organelles and assembled macromolecules with various shapes and sizes. Selective inactivation or disruption of appropriate cellular structures, ranging in size from several μm down to 100 nm or less, would be an attractive approach to investigate their function in living cells.

The distance from the outlet to the Bragg peak can be set inside a cell with the accuracy of $\sim$1 μm for 2 $\sim$ 4 MeV He^{2+} ions. The experiment with a biological cell, a HeLa cell, is described elsewhere [20].

Focusing of muon beams

Muons implanted into a sample are quickly thermalized and then localized at characteristic sites. These muons interact with the local magnetic field, resulting in muon spin precession and/or depolarization. This makes spin polarized muons very sensitive and versatile microscopic probes to study magnetic properties in various materials. One of the obstacles of this technique is that the size of the polarized muon beam from accelerator facilities is relatively large; typically a few tens of mm FWHM at the focal point. However, most of intriguing samples, such as newly synthesized chemical compounds and biological samples, are often much smaller in size than the beam diameter. Therefore, density enhancement of muon beams by capillary focusing should have many potential applications.

The experiment was performed in RIKEN-RAL Muon Facility at Rutherford Appleton Laboratory, U.K. [28]. Figure 6 schematically shows the experimental setup. Muons with specified momentum are transported to the beam port, and extracted into atmosphere through a thin Mylar foil and an aluminum collimator. Typical beam intensity is about 10^4 muons per pulse for the momentum of 54 MeV/c. Considering the size of the muon beam, we used tapered glass tubes with $D_{\text{in}} = 46$ mm. The tubes were made of Pyrex, whose components are similar to those of borosilicate. The length of the tubes was 400 mm. In order to make variations of taper angles, D_{out} varied from 3 to 20 mm. The wall thickness of the tube was 2 mm. A plastic scintillation counter with thickness of 0.5 mm and diameters of 20 mm was placed 3 mm downstream of the tube.

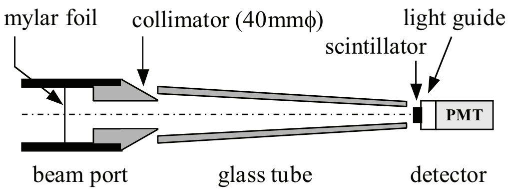

Figure 6: A schematic view of the experimental setup (not to scale). The scintillator was placed 3 mm downstream of the tube [21].

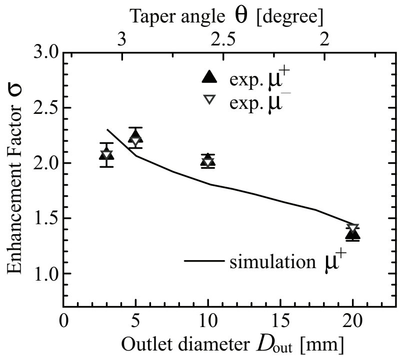

Figure 7: The beam density enhancement σ for 54 MeV/c $\mu^{\pm}$ as a function of D_{out}.

Figure 7 shows the enhancement factor σ as a function of D_{out} together with the results of the numerical simulation. The enhancement factor σ increases from ∼1.5 to ∼2.3 as D_{out} decreases from 20 to 3 mm. This enhancement occurs because a certain fraction of muons is reflected from the inner wall via small angle scattering and transported to the outlet of the tube. It is worth noting that the enhancement for negative muons was almost identical to that of positive muons [21]. The enhancement factor of ∼2 can reduce beam time by half.

Acknowledgment

This work was partly supported by a Grant-in-Aid for Scientific Research (No. 17654079) from the Ministry of Education, Culture, Sports, Science, and Technology, Japan, a Grant of "Developments and Applications of Exotic Quantum Beams" from RIKEN, a Grant of Special Projects for Basic Science of RIKEN, a RIKEN's FY2006 DRI Research Grant, and the JSPS-CAS Core-University Program in the field of "Plasma and Nuclear Fusion".

References

[1] N. Stolterfoht *et al.*, Phys. Rev. Lett. **88**, 133201 (2002).
[2] N. Stolterfoht *et al.*, Nucl. Instrum. Methods B **225**, 169 (2004).
[3] R. Hellhammer *et al.*, Nucl. Instrum. Methods B **232**, 235 (2005).
[4] Gy. Vikor *et al.*, Nucl. Instrum. Methods B **233**, 218 (2005).
[5] M. Fursatz *et al.*, J. Phys.: Conf. Series **58**, 319 (2007).
[6] R. Hellhammer *et al.*, Nucl. Instrum. Methods B **258**, 159 (2007).
[7] Y. Kanai *et al.*, Nucl. Instrum. Methods B **258**, 155 (2007).
[8] R. T. Rajendra Kumar *et al.*, Nanotechnology **16**, 1697 (2005).
[9] M. B. Sahana *et al.*, Phys. Rev. A **73**, 040901 (2006).
[10] H. F. Krause *et al.*, Phys. Rev. A **75**, 042901 (2007).
[11] P. Skog *et al.*, Nucl. Instrum. Methods B **258**, 145 (2007).
[12] K. Schiessl *et al.*, Nucl. Instrum. Methods B **232**, 228 (2005).
[13] K. Schiessl *et al.*, Phys. Rev. A **72**, 062902 (2005).
[14] K. Schiessl *et al.*, Nucl. Instrum. Methods B **258**, 150 (2007).
[15] T. Nebiki *et al.*, J. Vac. Sci. Technol. A21, No.5, 1671 (2003).
[16] T. Ikeda *et al.*, Appl. Phys. Lett. **89**, 163502 (2006).
[17] T. Ikeda *et al.*, J. Phys.: Conf. Series **58**, 68 (2007).
[18] A. Cassimi *et al.*, to be published in Int. J. Nanotechnology.
[19] Y. Iwai *et al.*, Abstract of 22nd Int. Conf. on Atomic Collisions in Solids (Germany), 76, (2006).
[20] Y. Iwai *et al.*, to be published.
[21] T. M. Kojima *et al.*, J. Phys. Soc. Jpn. **76**, 9, 093501 (2007).
[22] I. C. Gebeshuber *et al.*, Int. J. Mass Spectrometry **229**, 27 (2003).
[23] N. Nakamura *et al.*, Nucl. Instrum. Methods Phys. Res., Sect. B **232**, 261 (2005).
[24] M. Terada *et al.*, Nucl. Instrum. Methods Phys. Res., Sect. B **235**, 452 (2005).
[25] N. Okabayashi *et al.*, Nucl. Instrum. Methods Phys. Res., Sect. B **205**, 725 (2003).
[26] T. Nebiki *et al.*, Nucl. Instr. and Meth. B **249**, 226 (2006).
[27] computer code SRIM-2006.01 (http://www.srim.org/)
[28] T. Matsuzaki *et al.*, Nucl. Instr. and Meth. A **465**, 365 (2001).

Sub-Shell Excitations of Rare Gas Atoms by Electron Impact

Y. Sakai*, N.Umeda†, L.F.Zhu‡§, Z.S.Yuan‡§, Y.Fujita†, N.Miyauchi*,
T.Takayanagi¶, C.Yamada†, N.Nakamura†, K.Z.Xu‡§, and S.Ohtani†

* Dept. of physics, Toho University, Chiba 274-8510, Japan
† Inst. for Laser Science, University of Electro-Communications, Tokyo 182-8585, Japan
‡ Hofei National Lab. for Physical Science at Microscale, Hofei 230026, China
§Dept. of Modernphyasics, University of Science and Technology of China, Hofei 230026, China
¶ Dept. of physics, Sophia University, Tokyo 102-8554, Japan

Abstract

The sub-shell excitations of rare gas atoms have been investigated by electron energy-loss spectroscopy at various impact energies. In energy-loss spectra, we have observed several structures involving ones by the optically forbidden transitions, which are embedded in a continuum. Besides, we have found new states formed by two-electron excitations. In this region, above the first ionization limit the rare gas atoms can be ionized either directly or via the other excited states like inner-shell excited states or doubly excited states, which are coupled to the ionization continuum. These resonance line profiles have been theoretically studied by Fano. We have found that the line profile depend on the incident electron energy and scattering angle. In particular, the line profile parameters q for each state of spectra of argon have been determined. Besides, for 3s → 4p excitation it has been found that the q parameters which are described as a function of momentum transfer has fallen on the straight line.

Keywords: electron energy-loss spectroscopy, Fano profile, rare gas, excitation, q-parameter, sub-shell, resonance

1.Introduction

It is well known that sub-shell excitations like an inner-valence excitations of a neon 2s, an argon 3s, a krypton 4s, and a xenon 5s electron have resonance shapes which show a dip structure in photo-absorption spectra. This is a window resonance. When there is a discrete state embedded in a continuum, they interact with each other, and give rise to characteristic structures in absorption spectra, which are called Fano profiles.[1] There have been many works reported about these resonance shapes, energy levels, and electron correlation effects since Fano's theoretical pioneer work in 1960's and experimental reports by Codling and co-workers.[2,3] They had found the window resonance in photo-absorption spectra of rare gas atoms. Brion and co-workers[4] had also found the window resonance in electron energy-loss spectra of rare atoms. They carried out the electron impact experiments at the condition of optical limit. In this case, the electron energy-loss spectra are obtained by using fast incident electrons and observing forward scattering electrons. In general, compared with the photo-absorption method, the electron impact method has a lower energy resolution, but it can be obtain the information of the optically forbidden transitions, i.e. higher order electric transitions and spin-exchange ones under varying experimental conditions of impact energy and scattering angle. Therefore we have started the electron impact experiment about the sub-shell excitation of rare gas atoms as a collaboration project of the Core-University Program on Plasma and Nuclear Fusion. Recently, electron impact experiments of xenon using a relative lower incident electron beam have been carried out, and the energy levels, the Fano profile, and quantum defects of autoionization Rydberg series of xenon have been obtained from electron energy-loss spectra. These results have been already published by Yuan et al. [5]

In this paper, line profiles and excitation states in electron energy-loss spectra of argon and krypton are reported. Besides, we discuss the new experimental results about the line profile factor q for 3s → 4p excitation of argon as a function of the magnitude of momentum transfer.

2. Experimental set-up and procedure

Figure 1 shows the experimental apparatus which is in the Institute for Laser Science, University of Electro-Communications. The detail information for this apparatus has been described in the previous papers.[6,7] Briefly, the electron energy loss spectrometer consists of an electron energy selector situated in front of the interaction region to get a monochromatic electron beam and an energy analyzer to analyze the scattered electrons. Both energy selector and analyzer are simulated hemi-spherical analyzers called "Jost type" [8], and each mean trajectory radius is 50 and 80 mm, respectively. The typical energy resolution is about 50 - 70 meV full width at half maximum (FWHM) at the incident electron current over 10 nA for all incident electron energies. The energy selector is rotatable around the collision center from -5° to +110°. Calibration of the scattering angles was performed by use of the symmetrical nature and the value of the scattering intensity ratio of the peaks for 2^1S excitation to 2^1P excitation in electron energy-loss spectra of helium [9]. The 2^1P excitation peak was also used for the calibration of the excitation energy.

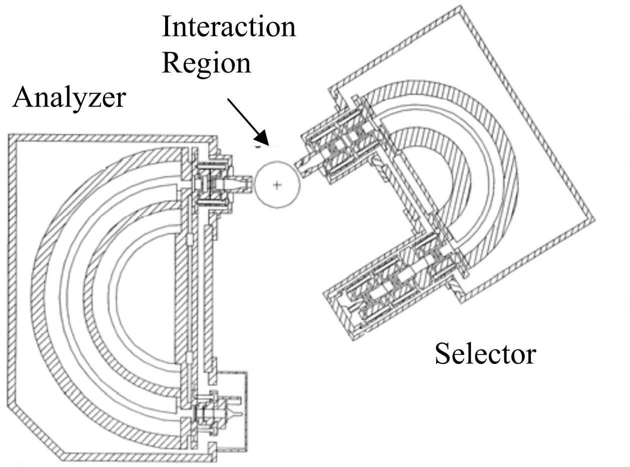

Fig.1 Schematic diagram of the Experimental apparatus

The Fano profile is described as follows,

$$\sigma(E) = \frac{(q+\varepsilon)^2}{1+\varepsilon^2} \qquad . (1)$$

Where q is the line profile factor which is sometimes called q-parameter for each resonance and ε indicates the departure of energy-loss E from an idealized resonance energy E_r which pertains to the discrete auto-ionizing level of atom with a line width Γ as given by the equation,

$$\varepsilon = \frac{E - E_r}{\Gamma/2} \qquad . (2)$$

In order to estimate the q factors, after the electron energy-loss spectra were obtained, we fitted the peak shape to the equation (1). In fact, when the q was estimated, our apparatus function was considered as the Gaussian function. Because the obtained spectra $\sigma_{EXP}(E)$ contains the apparatus function.

3. Result and Disscussion

3.1 Electron energy-loss spectra

Typical electron energy loss spectra of argon are shown in Fig. 2. We have observed several peaks and dips in each energy loss spectrum. The dips are due to the transitions of 3s → np, which are window resonances. There are some difference between the spectra by electron impact experiment and photon impact one. The peaks of 3s → nd series which are very weak in photo-absorption spectrum have been observed as clear peaks. The structure located at about 25 eV has clearly appeared only in the energy loss spectrum by 35 eV electron impact. This is due to the 3s → 4s forbidden transition, ^1S and/or ^3S. Even the spectrum by 200 eV electron impact, this structure has been remained as a step. This had been also found in the energy-loss spectrum by fast electron impact experiment using the fast 2.5 keV incident electron and detecting 4 degrees scattered electrons, by Zhu et.al.[10] It is worthy of special mention in the present results that the line profile of the 3s → 4p excitation depended on the impact energy and were changed. The line shape which shows a dip in the experiment by 200 eV incident electron impact changes the profile to a peak in the experiment by 35 eV. This means that the q-parameter which characterizes the line profile decreased to minus value from near zero value. It can be seen to have appeared like for other experiments.

Figure 3 shows the typical energy-loss spectra of krypton. Several structures by 4s → np series and 4s → nd series have been clearly observed in each spectrum as well as the case of the results of argon. The line profile of the 4s → 5p excitation also changes from a dip to a peak along with the decrease of the incident energy. Comparing with the case of argon, the structure of 4s → 5s forbidden transitions is clear. In particular, the ^3S peak can be remarkably confirmed in a spectrum by 35 eV electron impact.

It is strange that two unknown peaks exist in the spectrum by 200 eV. One is located near the 4s → 4d transition peak at 25.75 eV. This is not the 4s → 6s transition, because the peak of 4s → 5s does not appear at the position in which it should be located at about 23.5 eV. There is no single excitation corresponding to this peak, so it might be attributed to a two-electron excitation. In fact, this peak had been also observed by Yuan et.al.[11] and Baxter et al. Although our assign agrees with them, a detailed electron configuration is not understood.

Another unknown peak is located at about 26.5 eV. This is not the 4s → 6s transition, too. In the 2.5 keV fast electron impact experiments by Yuan et al.[11], this peak had been not observed, instead, the peak of the 4s → 6s transition had been observed. But, in our energy-loss spectrum, the structure by 4s → 5s transition is very weak compared with the

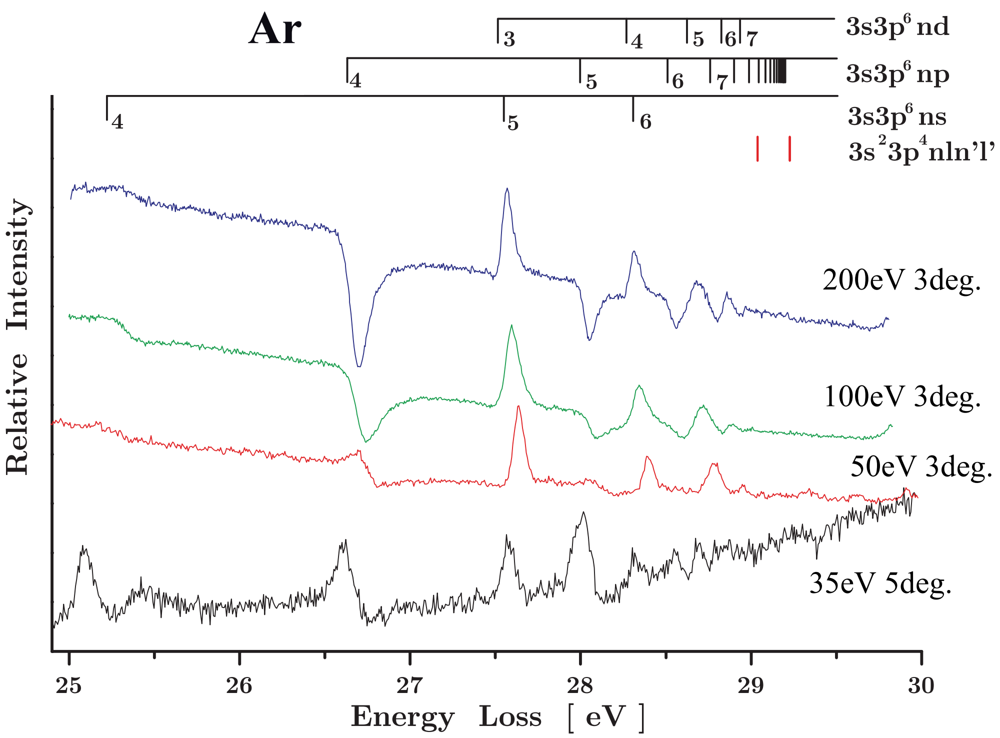

Fig.2 Typical electron energy-loss spectra in auto-ionizing region of argon.

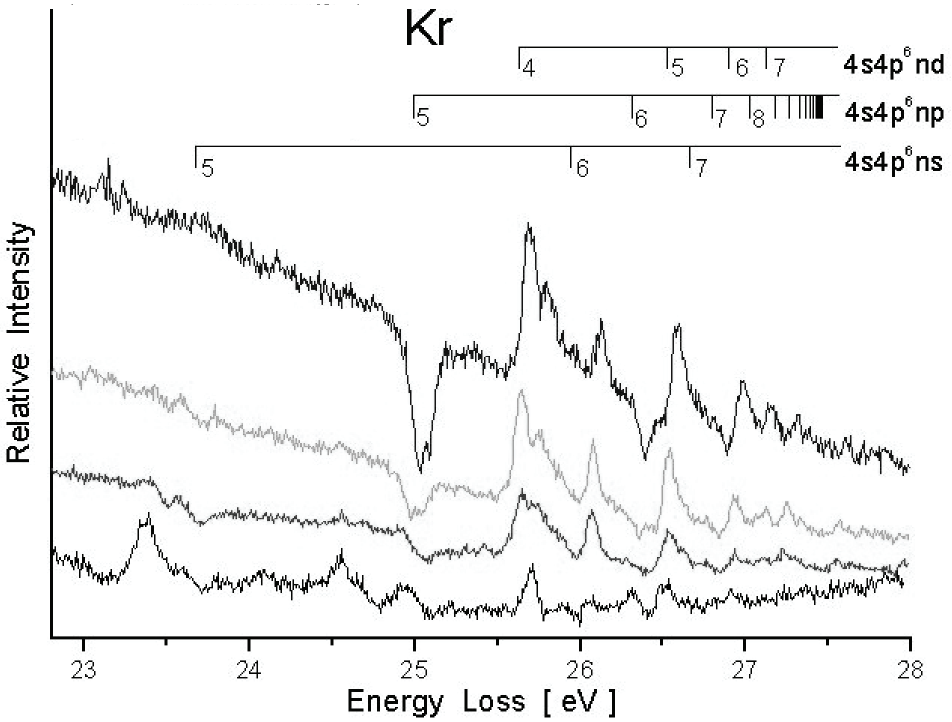

Fig.3 Typical electron energy-loss spectra in auto-ionizing region of krypton.

spectra by fast electron impact. Normally, the peak by 4s → 6s transition is weaker than the peak by 4s → 5s one. Therefore it is reasonable that this peak is also assigned as a double excitation.

We have found that a lot of new double excitation states have existed in the sub-shell excitation region of xenon though it doesn't put on this paper.

3.2 Line profile parameter q for Ar 3s → 4p excitation

In this section, we discuss the line profile parameter q for Ar 3s→ 4p excitation, again. Using equation (1), we have estimated the q-parameters for this resonance from the energy-loss spectra by 200 eV electron impact and various scattering angles. In the case of the experiment obtained at 3 degrees scattering angle, the q-parameter was estimated to be -0.25 with a least square fitting method. The q-parameter obtained from the photo-absorption spectrum by Madden et al.[3] was -0.22, while Wu et al.[12] had obtained that by fast electron impact experiment to be -0.31. Thus, it seems that our result is in good agreement with the previous ones. But, recently, Zhu et al.[10] had carried out the another fast electron impact experiments, and estimated the q-parameter for this transition from their energy-loss spectrum measured at 4 degrees. The q-parameter estimated by them had positive value, 0.08. Since the difference between the experiments by Wu et al, and Zhu et al is in the scattering angle, each momentum transfer K is different. The magnitude of momentum transfer defined as

$$K^2 = k_i^2 + k_f^2 - 2k_i k_f \cos\theta \qquad , (3)$$

where θ is the scattering angle, k_i and k_f are the initial and final momenta, respectively. Then the value of K^2 for the result by Zhu et al. was 0.90, while the experiment by Wu et al. was carried out at near-zero momentum transfer. This means that the q-parameter depend on the value of K^2.

In order to discuss this topic, we have plotted q-parameters estimated from the energy-loss spectra measured at various scattering angles as a function of the magnitude of momentum transfer, K^2. This result is shown in Fig.4. Surprisingly, our data line up on the straight line, and connect two different results by fast electron impact. This fact means that the quantum interference between the discrete state and continuum changed with the increase of the momentum transfer. The q-parameter is proportional to the ratio of the transition matrix elements as follows,

$$q \propto \frac{\langle \Psi_i | T | \Psi_f \rangle}{\langle \Psi_i | T | \Psi_{con} \rangle} \qquad . (4)$$

Where T is the interaction potential, Ψ is the wave function, besides subscript i, f, and con mean the initial, final, and continuum states, respectively. The change of q-parameter might be due to the transition matrix element $\langle \Psi_i | T | \Psi_f \rangle$, because it may be sensitive to the changes in momentum transfer squared.

Very recently, using the linear density response theory, Tong and Watanabe[13] have succeeded in the representation of the q-parameter as a function of the momentum transfer squared for 3s→ 4p transition of argon under the Born approximation. They have

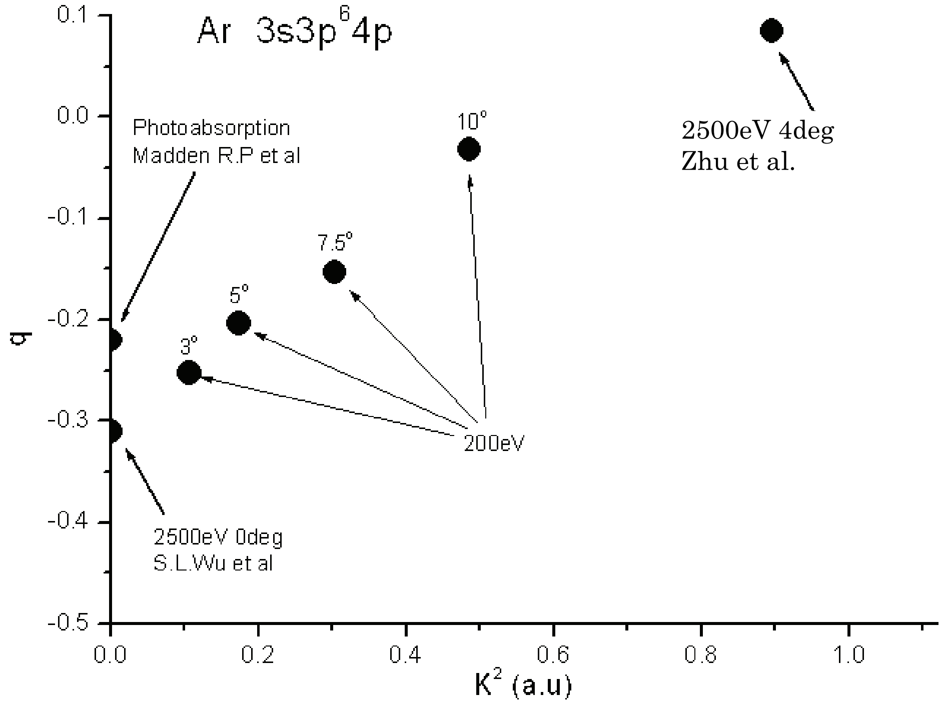

Fig.4 Fano q parameter of 3s to 4p resonance state as a function of the magnitude of momentum transfer, K^2

calculated the generalized oscillator strength, have indicated that the change of q-parameter is due the quantitative problem. Furthermore, they have predicted that the resonance shape of the 3*s* to 4*p* transition changes from a diplike resonance to a peaklike resonance as the momentum transfer K increases.

The energy dependence of q-parameter may be also due to the similar reason. But in the low energy electron impact experiments, the Born approximation is not valid. Then the quantum interference between the discrete state and continuum may not be depend on the momentum transfer but directly depend on the incident energy. This phenomenon is a feature of the optically allowed transition.

4. Conclusion

In order to investigate the sub-shell excitations, the electron energy-loss spectra of rare gas atoms have been measured at a various scattering angles and different incident energies. The several structures by optical allowed and forbidden transition have been observed in each energy-loss spectrum, and new resonance states formed by two-electron excitations have been found by careful analysis. Besides, the q-parameters for the several optical allowed transitions of rare gas atoms have been estimated, we have found the phenomena that the q-parameters have been changed with change of the incident energy and scattering angle. In particular, the change of q-parameters for Ar 3s→ 4p excitation can be described as a function of momentum transfer, which line up on the straight line.

However detail mechanism has not been clear, yet. In order to discuss the mechanism of the interference between the discrete state and continuum, the further experimental investigates are needed. An of course theoretical research is indispensable, and we need those help.

Acknowledgement

This work was supported from the Core-University Program on Plasma and Nuclear Fusion. The authors would like to thank Professor T. Watanabe and X.M.Tong for their helpful theoretical discussions.

References

[1] U.Fano, Phys. Rev. **124**, 1866 (1961).
[2] R.P.Madden and K.Codling, Phys. Rev. Lett. **10**, 516(1961).
[3] R.P.Madden D.L.Ederer, and K.Codling, Phys. Rev. **177**, 136(1969).
[4] W.F.Chan, G.Cooper, X.Guo, G.R.Burton, and C.E.Brion, Phys. Rev. A **46**,149(1992).
[5] Z.S.Yuan, Y.Sakai, N.Umeda, Y.Fujita, T.Takayanagi, C.Yamada, N.Nakamura, S.Ohtani, L.F.Zhu, and K.Z.Xu, J.Phys. B **39**, 5097(2006).
[6] G.P.Li, T.Takayanagi, K.Wakiya, H.Suzuki, T.Ajiro, S.Yagi, S.S.Kamo, and H.Takuma, Phys. Rev. A **38**,1240 (1988).
[7] T.Takayanagi, G.P.Li, K.Wakiya, H.Suzuki, T.Ajiro, T.Inaba, S.S.kano, and H.Takuma, Phys. Rev. A **41**, 5948 (1990).
[8] K.Jost, J. Phys. E **12**, 1006(1979).
[9] T. Y. Suzuki, H. Suzuki, F. J. Currell, S. Ohtani, Y. Sakai, T. Takayanagi, and K. Wakiya, Phys. Rev. A **57**, 1832 (1998).
[10] L.F.Zhu, H.D.Cheng, X.J.Liu, P.Tian, Z.S.Yuan, W.B.Li, and K.Z.Xu, Chin.Phys.Lett. **20**, 1718(2003).
[11] Z.S.Yuan, L.F.Zhu, X.J.Liu, Z.P.Zhong, W.B.Li, H.D.Cheng, and K.Z.Xu, Phys.Rev. A. **66**, 062701(2002).
[12] S.L.Wu, Z.P.Zhong, R.F.Feng, S.L.Xing, B.X.Yang, and K.Z.Xu, Phys.Rev. A. **51**, 4494(1995).
[13] X.M.Tong and T.Watanabe, Phys.Rev. A. **76**, 042715(2007).

Ab Initio Design of Laser Pulse for Controlling Photochemical Reactions

Shiyang Zou
Institute of Applied Physics and Computational Mathematics, Beijing P.O.Box 8009, P.R. China
e-mail: shiyang.z@gmail.com

Abstract

With high level *ab initio* description of molecule-field interaction, we have developed an optimal control algorithm for manipulating molecular transformation and quantum populations. High order molecule-field interactions are fully taken into account through the use of electric-nuclear Born-Oppenheimer (ENBO) approximation [J. Chem. Phys. **122**, 084110(2005)]. The present algorithm is demonstrated on the control of molecular post-pulse (transient)alignment and orientation. High degrees of alignement and orientation are achieved in a vibrationally selective manner by optimized infrared laser pulses of duration on the order one rotational period of molecule. To reveal the control mechanism behind the complicated optimal pulses, an analytical pulse design method is developed within the ENBO approximation, which is based on a two-state treatment of the dynamics in a Floquet picture. This analytical method is also illustrated on the control of the alignment of homonuclear diatomics.

Keywords: optimal control, alignment, orientation

1.Introduction

Recent years have witnessed rapid acceleration of research activity in the general area of coherently controlling the quantum phenomena in atomic and molecular motions. Cohenertly controlling molecular transformation and quantum population using shaped or specially designed laser pulses began as a theoretical concept[1-4] but has now been realized in an increasing numbers of successful experiments[5-9] especially those guided by closed loop techniques[10].

The work described here attempts to apply high level *ab initio* theory to designing laser pulses in a quantitaive manner which should be amenable to direct experimental verification. The calculations begin with *ab initio* electronic structure calculations of the energy of a molecule in a static (electric) field[11]. This is known as the Electric-Nuclear Born-Oppenheimer (ENBO) approximation. In this method the energy of the molecule is computed as a function of: 1)the geometry of the molecule, 2)the electric field strength and 3)the orientation of the molecule with repect to the electric field direction. The validity of this approximation is discussesed in detail of Ref. [11] and it is shown to be applicable to infreared excitation of H_2. The ENBO approximation takes account of the interaction of the molecule with the electric field to all orders of the field strength. The application of the ENBO approximation, in conjunction with optimal control theory and numerical solution of the time-dependent Schrödinger equation, provides an alogrithmic method to design laser pulses to achaive the desired control goals.

In one recent application [12] of the formualtion presented above, we have successfully optimized the laser pulses to manipulted the post-pulse (transient) alignment and orientation of carbon monoxide in a vibrationally selective manner. High degress of alignment and orientation are achieved by optimized infrared laser pulses of duration on the order of one roational period of the molecule. In Ref. [12], we have also established an algorithm, within the optimal control procedure, by incorporating a projection operator into the objective functional that permits the final wavefunction to be restricted to lie within a prescribed subspace of the Hamiltonian.

Beased on the ENBO approximation, we have formulated an analytical method for design infrared laser pulses for controlling the vibrational and rotational excitation of homonuclear diatomic molecules[13], which is beased on an two-state treatment of the dynamics in a Floquet picture. The analytically derived pulses provide a transparent explanation of the control mechanism. In Ref.[14], this analytical method is extened to control the alignment of H_2.

2. Optimal Control of Molecular Alignment and Orientation

Optimal control theory proceeds by defining an objective functional, J, which is maximized by varying the control parameters. For our purposes the objective functional is written in the following form:

$$J = \left\langle \psi(T) \left| \hat{O} \right| \psi(T) \right\rangle - \alpha_0 \int_0^T |\epsilon(t)|^2 \, dt - 2\Re \left[\int_0^T \left\langle \chi(t) \left| \frac{\partial}{\partial t} + \frac{i}{\hbar} \hat{H}[\epsilon(t)] \right| \psi(t) \right\rangle dt \right] \tag{1}$$

where T is the target time, α_0 is a positive real number which weights the penalty on the total fluence of the laser pulses, and $\chi(t)$ is an undetermined Lagrange multiplier which ensures that the function $\psi(t)$ satisfies during the pulse. The opeator $\hat{O}$ defines the control objectives:

$$\hat{O}_{alignment} = \hat{P}_v \cos^2 \theta \hat{P}_v \quad , \tag{2}$$

and

$$\hat{O}_{orientation} = \hat{P}_v \cos \theta \hat{P}_v \quad . \tag{3}$$

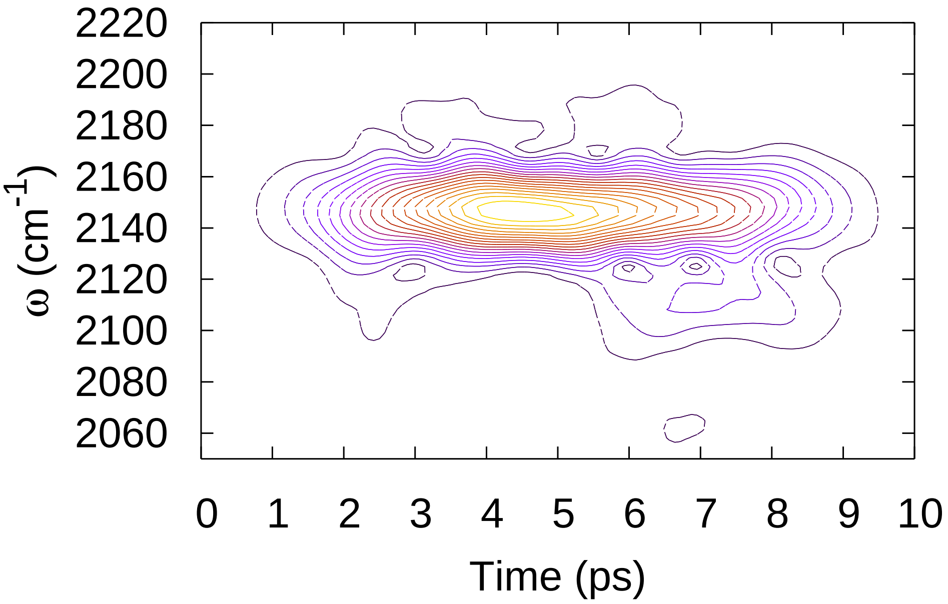

Figure 1: Contour map of the square of the electric field of the optimized laser pulse as a function of both frequency and time for the alignment of CO with the final vibrational state restricted to be $v = 1$.

In the above equations, $\hat{P}_v$ is a projection operator defined as:

$$\hat{P}_v = \sum_{jm} |vjm\rangle\langle vjm| \quad . \tag{4}$$

The use of this projection operator permits us to limit the target wavefunction of the system to be mixture of rotational states associated with a single vibrational manifold. Without these projection operators a higher degree of alignment or orientation then occurs on a very much longer time scale.

Functional variation of this objective function provides us with an expression for derivative of J with respect to the electric field, $\epsilon(t)$, at time t. Armed with this expression we can find the time varying electric field which maximizes J with a standard optimization procedure such as conjugate gradient method.

As an illustration, we show in Fig. 1 the results of the optimal control calculations for the design of a laser pulses to achieve the alignment of CO in a vibrationally selective manner. With this pulse, a vibrationally restricted alignment of $\langle \hat{O}_{alignment} \rangle =$

$\langle \hat{P}_v \cos^2\theta \hat{P}_v \rangle = 0.886$ has been obtained, with 99.3% of CO molecules being in the $v = 1$ vibrational manifold.

In an attempt to gain insight into the vibrationally selective alignment, the time evolution of the wavepacket is illustrated in Fig. 2 during the action of the optimal laser field. Figure 2 shows snapshots, at various stages of the action of the laser pulse, of the probability density of the nuclear wavefunction of CO, $|\psi(t)|^2$, represented in cartesian coordinates. The z-axis is positioned along the laser polarization vector. The first snapshot, at $t = 0$, shows an isotropic angular distribution corresponding to an initial state with $j = 0$. As the laser pulse acts on the molecule it is excited rotationally and vibrationally. At $t = 2.5\,\text{ps}$, it can be seen that some radial nodes have formed, implying that the molecule has been excited to the vibrationally excited states with quantum numbers $v = 1$ and $v = 2$ with a significant probability. At this point the molecule is already slightly aligned, with an alignment of about 0.18. This arises because the $v = 1, j = 1$ level is populated. At $t = 3.75\,\text{ps}$ and $t = 5\,\text{ps}$, the molecule is clearly concentrated around $\theta = 0$ and $\theta = \pi$ in the density plot. However, we know that the alignment in the vibrational manifold $v = 1$ is nearly zero, i.e. $\langle \hat{P}_{v=1} \cos^2\theta \hat{P}_{v=1} \rangle$=0. This is simply because the $v = 1$ manifold is not significantly populated at these times, the main states populated being $(v = 0, j = 0)$, $(v = 0, j = 2)$, $(v = 2, j = 0)$ and $(v = 2, j = 2)$. At $t = 7.5\,\text{ps}$ CO exhibits some degree of anti-alignment, i.e. a significant portion of system concentrated around $\theta = \pi/2$. By $t = 8.75\,\text{ps}$ an alignment of about 0.42 is achieved. Although at this time the rovibrational state populations are almost the same as those attained at the end of the pulse, the alignment is not yet optimal. To achieve the best alignment, the relative phases of the rotational states must be adjusted. At the end of the pulse, $t = 10\,\text{ps}$, the system is strongly confined in two narrow angular regions around $\theta = 0$ and $\theta = \pi$ as shown in Fig. 2. A high alignment of 0.886 is then attained in the vibrational manifold $v = 1$. The presence of a single radial node shows that only states with the vibrational quantum $v = 1$ are populated at the end of pulse. Since only odd rotational states in the manifold of $v = 1$ are populated at the end of pulse, the total wavefunction of CO corresponding to an odd parity state. This leads to an angular distribution of CO molecules which is symmetric with respect to reflection in the xy plane at the end of the pulse.

3. Analytical Pulse Design for Vibrational-Rotational Excitation of Homonuclear Diatomics

Our underlying model for the analytical design of IR laser pulses for vibrational-

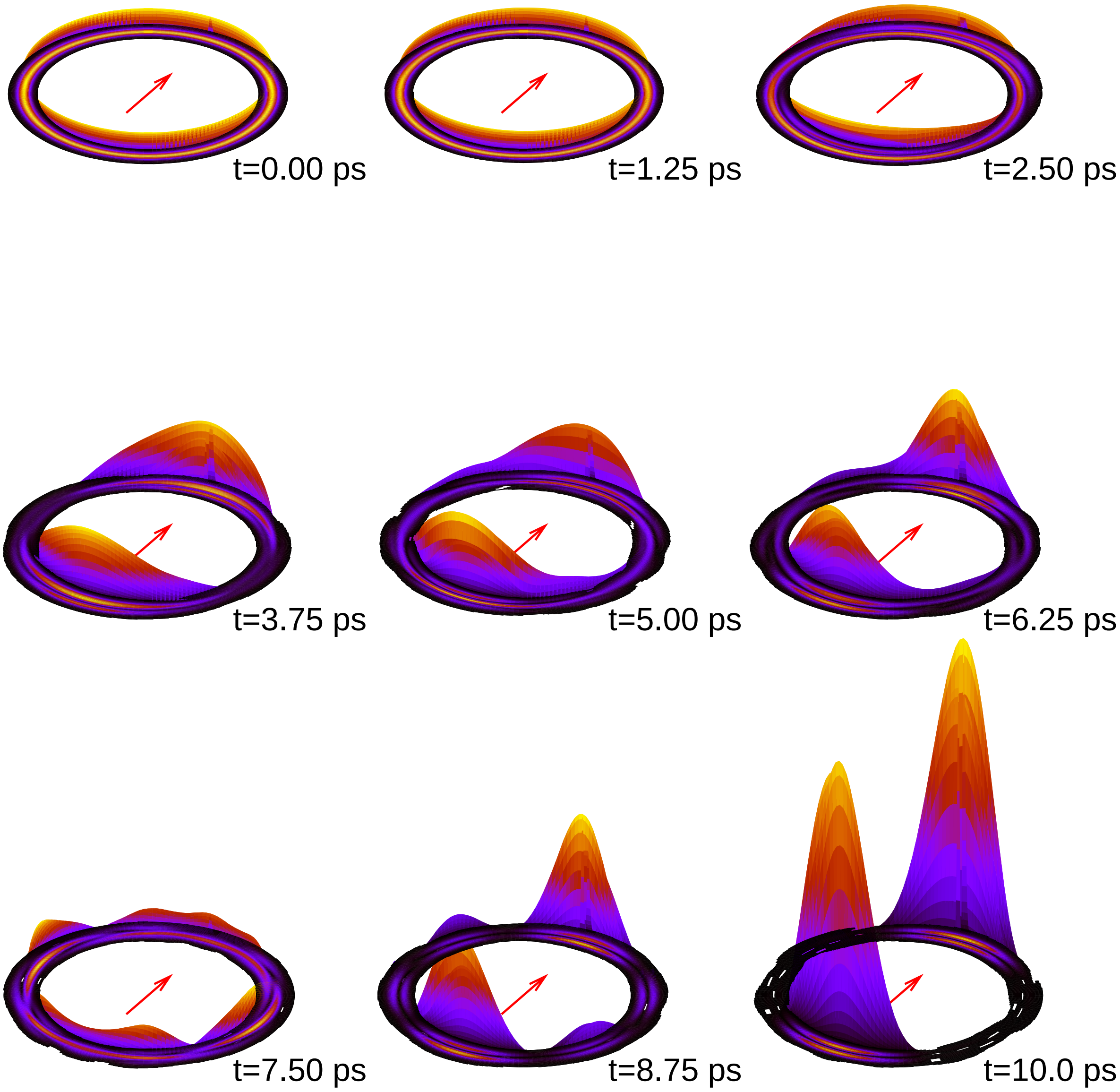

Figure 2: Time evolution of CO wavepacket being driven by the optimal field $\epsilon(t)$ given in Fig. 1 towards the alignment in the vibrational manifold $v = 1$ at $t = 10\,\text{ps}$. In this figure snapshots of $|\psi(t)|^2$ are plotted at selected times during the action of the laser pulse. A cartesian coordinate system is used and the z-axis (denoted by the arrow) is taken to be along the laser polarization vector.

rotational excitation fo homonuclear diatomic molecules is a two state model consisting of a ground state $|g\rangle$ and an excited state $|e\rangle$. The states are coupled by a laser field

$$\epsilon(t) = \hat{\epsilon}\epsilon_0 f(t) \cos\Phi(t) \quad , \tag{5}$$

where $\hat{\epsilon}$ is the polarization vector, $\hat{\epsilon_0}$ is the field strength, $f(t)$ is the normalized pulse envelope, and $\Phi(t)$ is the temporal phase of th field. The Hamiltonian of this two level model may be written as

$$H = \begin{pmatrix} E_g - \alpha_{gg}\epsilon^2(t)/2 & -\alpha_{eg}\epsilon^2(t)/2 \\ -\alpha_{ge}\epsilon^2(t)/2 & E_e - \alpha_{ee}\epsilon^2(t)/2 \end{pmatrix} \tag{6}$$

where E_i is the field-free energy of state $|i\rangle$ energy of state $|i\rangle$ and $\alpha_{ij} = \langle i|\hat{\epsilon}| \cdot \alpha \cdot \hat{\epsilon}|j\rangle$ is a matrix element of th epolarizability tensor *alpha*. If the pulse envelope $f(t)$ and laser frequency $\omega(t) \equiv d\Phi/dt$ are both slowly varied in comparision to the fast optical oscillations, we can invoke the two-photon rotating wave approximation (RWA), transform Eq. (6) into a Floquet representation ans solve it analytically.

Under two-photon resonance

$$2\hbar\omega(t) = E_e - E_g - \frac{\alpha_{ee} - \alpha_{gg}}{4}\epsilon_0^2 f^2(t) \quad , \tag{7}$$

the final populations of the states $|g\rangle$ and $|e\rangle$ may be written as

$$|a_g(T)\rangle|^2 = \cos^2\frac{\varphi}{2}, \quad |a_e(T)\rangle|^2 = \sin^2\frac{\varphi}{2} \tag{8}$$

where φ is the pulse area

$$\varphi = \frac{\alpha_{eg}\epsilon_0^2\tau s_0}{4} \tag{9}$$

where $s_0 = \int_0^T f^2(t)dt/tau$ and τ is the duration of pulse. We can see that the populations of states $|g\rangle$ and $|e\rangle$ depends on the pulse area φ only, which can be controlled through the adjustments in laser amplitude ε_0 or the pulse duration τ. On the other hand, the relative phase between the levels $|g\rangle$ and $|e\rangle$

$$\arg a_e(T) - \arg a_g(T) = \int_0^T [\omega_{eg} - q\varepsilon_0^2 f^2(t)]dt - 2\phi_0 \tag{10}$$

can be fully controlled with the changes of the carrier-envelope phase (CEP) ϕ_0 of the pulse. We can the manipulate the populations and the phases of the levels $|g\rangle$ and $|e\rangle$ through the adjuestments of th epulse area φ and the CEP ϕ_0, which enables us to create an arbitrary cohereent superposition of the two levels $|g\rangle$ and $|e\rangle$.

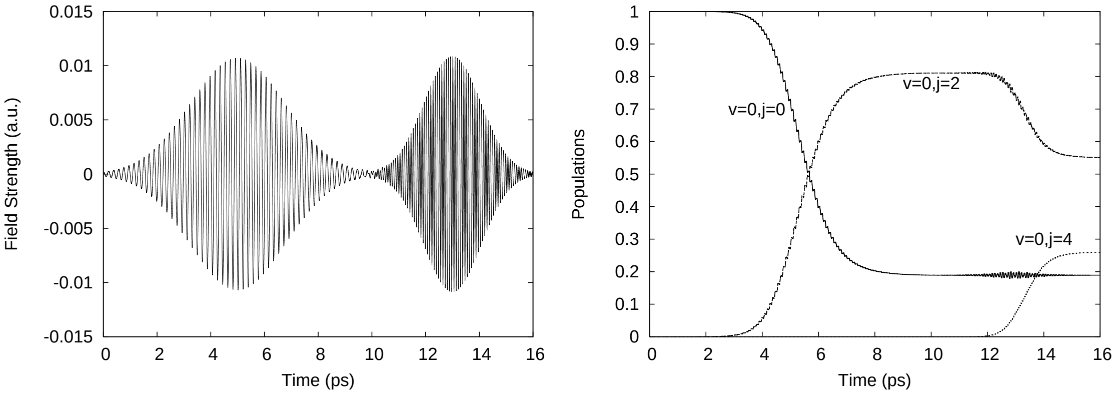

Figure 3: Rovibrational populations of H_2 (upper panel) in the states $(v = 0, J = 0)$, $(v = 0, J = 2)$ and $(v = 0, J = 4)$ under the action of two subsequent two-photon resonant pulses (lower panel) which are optimized to align the H_2 at $t_f = 16\,\text{ps}$.

As a demonstration, we consider the alignment of H_2 by two subsequently two-photon resonant pulses. In the left panel of Fig. 3 we plot the time variation of the rovibrational populations of H_2 under the action of two subsequent two-photon resonant pulses. The corresponding laser pulses are shown in the right panel of Fig. 3. The first pulse couples the states $(v = 0, J = 0)$ and $(v = 0, J = 2)$ through the two-photon resonant interaction, which transforms 82.87% of the population of the system from $(v = 0, J = 0)$ into $(v = 0, J = 2)$ and also controls the relative phase between the two states with its CEPD. The second pulse then induces an excitation from $(v = 0, J = 2)$ to $(v = 0, J = 4)$ with a transition probability of 33.14%, with respect to the 82.87% obtained in the excitation to $J = 2$. At the end of the two pulses $t = 16\,\text{ps}$, the alignment obtained is $\langle\psi(t_f)|\cos^2\theta|\psi(t_f)\rangle = 0.8692$ and the overlap of the controlled wave packet with the optimized aligned state of $J_{\text{max}} = 4$ is $|\langle\psi^a|\psi(t_f)\rangle|^2 = 0.9993$. We should point out that the two pulses employed in the two subsequent pulses are long pulses, they contain 53 and 75 optical cycles respectively. High alignment of H_2 is also achieved by using two short pulses which includes 13 and 18 optical cycles, respectively.

4. Conclusion

In conclusion, we have developed an optimal control algorithm for manipulating molecular transformation and quantum populations, where the molecule-field interaction is represented by high level *ab initio* calculations. The present algorithm provides optimal control pulses in a quantitaive relabile manner, which is amenable to direct experimental verification. In the present work, we applied this algorithm to the control of the alignment and orientation dynamics of carbon monoxide. High degrees of alignment and orientation are obtained in a vibrationally selective manner with laser pulses with a duration of the order of one rotational period.

To reveal the control mechanism, we have aslo developed an analytical scheme to manipulate the field-free alignment of molecules by using a series of optimized two-photon resonant pulses. The laser frequency is tailored continuously and smoothly to maintain the two-photon resonance as suggested in Ref. [13]. Under the two-photon resonant condition, the transition probability is controlled by changing the time integral of laser-molecule interaction, which depends on the field amplitude and pulse duration only for a given pulse envelope. The relative phase between two coupled levels is controlled with the changes in the CEP of associated two-photon resonant pulse. The effectivness of this analytical scheme is illustrated on the alignment of H_2.

Acknowledgement

I am grateful to Balint-Kurti, F.R. Manby and C.S. Sanz for collabroations in these joint works.

References

[1] D.J. Tannor and S.A. Rice, J. Chem. Phys. **83**, 5013 (1985).
[2] P. Brumer and M. Shapiro, Chem. Phys. Lett., **126**, 541(1986).
[3] S. Shi and H. Rabitz, J. Chem. Phys., **92**, 364 (1990).
[4] A.P. Perice, M.A. Dahleh, and H. Rabitz, Phys. Rev. A., **37**, 4950(2002).
[5] A. Assion et al., science, **282**, 919(1998).
[6] R. Bartels et al., Nature, **406**, 164(2000).
[7] R.J. Levis, G.M. Menkir, and H. Rabitz, Science, **292**, 709(2001).
[8] T.C. Weinacht, J.L. White, and P.H. Bucksbaum, J. Phys. Chem. A., **103**, 1016(1999).
[9] T. Hornung, R. Meier, and M. Motzkus, Chem. Phys. Lett., **326**, 445(2000).
[10] R.S. Judson and H. Rabitz, Phys. Rev. Lett., **68**, 1500(1992).
[11] G.G. Balint-Kurti et al, J. Chem. Phys., **122**, 084100(2005).
[12] S. Zou et al, J. Chem. Phys., **127**, 044107(2007).
[13] S. Zou et al, Phys. Rev. Lett., **96**, 243003(2006).
[14] S. Zou et al, Phys. Rev. Lett., (submitted).

Resonant Processes in Electron - Highly Charged Ion Collisions Observed with The Tokyo Electron Beam Ion Trap

Nobuyuki Nakamura, Anthony P. Kavanagh[1], Hirofumi Watanabe[2],
Hiroyuki A. Sakaue[3], Yueming Li[4], Daiji Kato[3], Fred J. Currell[1], and Shunsuke Ohtani
Inst. for Laser Science, The Univ. of Electro-Communications, Tokyo 182-8585, JAPAN
1) Queen's University Belfast, Belfast BT7 1NN, Northern Ireland, U.K.
2) CREST, Japan Science and Technology Agency, Chofu, Tokyo 182-8585, JAPAN
3) National Institute for Fusion Science, Toki, Gifu 509-5292, JAPAN
4) Inst. of Appl. Phys. and Comp. Math., P.O.Box 8009, Beijing 100088
e-mail: n_nakamu@ils.uec.ac.jp

Abstract

Resonant processes in electron-highly charged ion collisions have been observed with the Tokyo electron beam ion trap. In addition to the ordinary X-ray measurements, charge abundance measurements were used in the present study. Results obtained for very highly charged heavy ions, such as Li-like Bi^{80+}, are presented.

Keywords: highly charged ions, dielectronic recombination (DR), electron beam ion trap (EBIT)

1.Introduction

In the collisions of highly charged heavy ions with electrons, relativistic effects become very important as the atomic number, the charge state, and the interaction energy increase. The electron beam ion trap in Tokyo (Tokyo-EBIT) [1] is suitable for studying such relativistic collision processes because it can produce and trap very highly charged heavy ions which interact with a mono-energetic and unidirectional relativistic electron beam with an energy of up to 200 keV. In particular, recently we have been studying resonant processes in ionization [2] and recombination [3]. In the interactions with highly charged ions, a free electron is captured with a large probability and simultaneously a bound electron is excited to form a doubly excited state resonantly. This unstable intermediate state may decay by photon emission: Dielectronic Recombination (DR), or by emission of two electrons due to successive autoionization: Resonant Excitation/ Double Autoionization (REDA).

DR: $A^{q+} + e^- \rightarrow A^{(q-1)+**} \rightarrow A^{(q-1)+} + h\nu$.

REDA: $A^{q+} + e^- \rightarrow A^{(q-1)+**} \rightarrow A^{q+*} + e \rightarrow A^{(q+1)+} + e + e$.

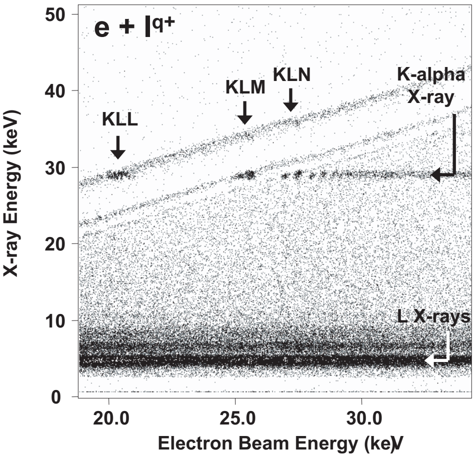

Figure 1: Typical results for X-ray measurements.

In this paper, we present new experimental technique for measuring these resonant processes for various charge states and various elements.

2. Experiments

Up to now, DR processes have been studied with an EBIT through X-ray observation, where the X-ray intensity is measured as a function of electron beam energy [4]. Typical result obtained for highly charged iodine ions is shown in Fig. 1. The lines whose X-ray energy is independent on electron energy are the characteristic X-rays from iodine, e.g. K-likes at around 29 keV and L-lines at around 4 keV. The lines whose X-ray energy linearly increases with electron energy correspond to radiative recombination (RR) X-rays whose energy is the sum of the electron beam energy and the binding energy of the captured level. As seen in the figure, enhancement of X-ray intensity can be found at several electron beam energies, e.g. around 20 keV and 25 keV. These enhancements correspond to DR processes. For example at an electron energy of around 20 keV, the beam electron is captured into the L-shell of highly charged iodine ions with exciting a K-shell electron to the L-shell. As a result, K X-rays are enhanced at that energy. This process is labelled as KLL using the inverse Auger notation. The DR cross section can be obtained by normalizing the X-ray intensity arising from DR to that arising from RR, for which reliable theoretical cross section can be obtained [3].

There exists a few problems on DR measurements through X-ray observation with an EBIT. First, since an EBIT confines several charge states at the same time, contributions from them are mixed in the spectrum. Although the charge state distribution can be concentrated to closed shell states, it is practically impossible to concentrate the charge

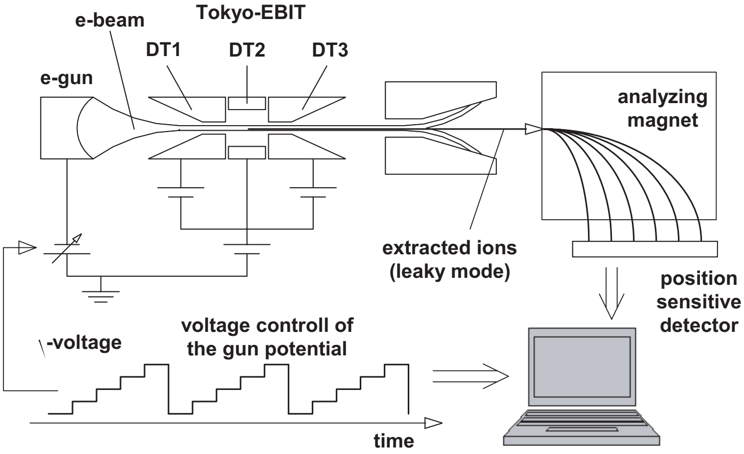

Figure 2: Diagram for the experimental setup and procedure used in the charge abundance measurements.

state to open shell states, so that most of the previous studies were devoted to closed shell ions. Second, since the observation solid angle is usually less than 10^{-3}, the efficiency is quite limited so that weak processes can not be measured.

Recently, we are studying resonant processes such as DR by measuring charge abundance inside the EBIT at the equilibrium. The abundance ratio between adjacent charge states can be represented at the equilibrium as follows [5],

$$\frac{n_{q-1}}{n_q} = \frac{\sigma_q^{re} + \langle \sigma_q^{CX} \rangle}{\sigma_{q-1}^{ion}}, \tag{1}$$

where σ_q^{re} is the recombination cross section which is the sum of RR (σ_q^{RR}) and DR (σ_q^{DR}) cross sections, $\langle \sigma_q^{CX} \rangle$ is the effective charge exchange cross section for the collisions with residual gas, and σ_{q-1}^{ion} is the ionization cross section. For off-resonance region, the ratio varies slowly with the electron energy. However, when the electron energy coincides with the resonant energy at which ionization or recombination is enhanced, the abundance ratio can drastically change. Thus, the resonant processes can be studied by measuring the abundance ratio between adjacent ions as a function of electron beam energy.

In the present study, the ion abundance ratio was obtained by measuring the intensity of ions extracted from the EBIT. Figure 2 shows the diagram for the present experimental setup and procedure. The ions escaping from the trap were extracted into a beam line [6], and detected after the charge separation with an analysing magnet. Several charge states were detected at the same time by using a position sensitive detector. Here, we assumed that the total efficiency (extraction, transport, and detection) should be practically the same for the ions with adjacent charge states. Actually we compared the charge abundance

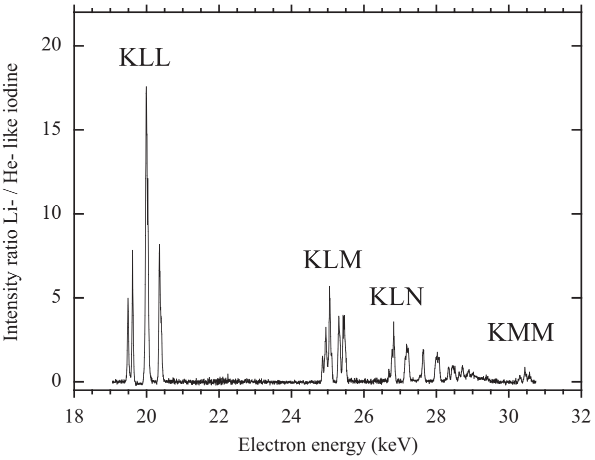

Figure 3: Intensity ratio of Li-like to He-like iodine extracted from the EBIT. Structures correspond to the Knn' DR resonances of He-like iodine.

obtained from x-ray observation of trapped ions to that obtained from the observed ion intensity, and found that there was no significant difference between them [7]. Thus, the intensity ratio between adjacent charge states is considered to give the ion density ratio inside the trap.

The extracted ion measurements have the following advantages compared to the ordinary X-ray measurements:
(1) The ion measurements have higher efficiency because the total (extraction and transport) efficiency is an order of 10%. This advantage enabled us to study weak resonant processes.
(2) The charge state of extracted ions can be clearly separated by using an analyzing magnet while it is difficult to separate the charge state by X-ray observation with an ordinary solid state Ge detector. This advantage enabled us to study any charge state including open-shell systems [7].

3. Results and discussion

Figure 3 shows the intensity ratio of extracted Li-like to He-like iodine obtained as a function of electron beam energy. A background obtained by fitting a second-order polynomial function to the non-resonance region has been subtracted. Thus the structures in the figure correspond to $\sigma_q^{DR}/\sigma_{q-1}^{ion}$, the DR cross section for He-like iodine scaled with the ionization cross section of Li-like iodine. As seen in the figure, the Knn' DR series

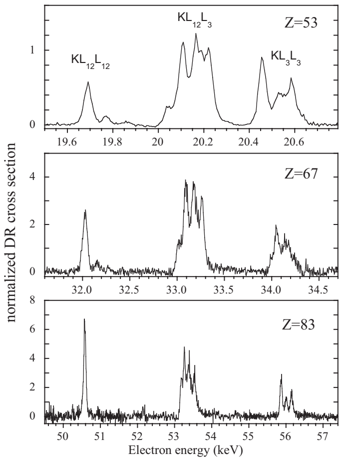

Figure 4: DR cross sections of Li-like ions normalized to the ionization cross sections of Be-like ions for iodine($Z = 53$), holmium ($Z = 67$) and bismuth ($Z = 83$). The horizontal energy scale was calibrated with the theoretical resonance energy.

has been clearly observed.

In this way, DR processes have been measured for a wide range of the atomic number. Figure 4 shows the intensity ratio of extracted Be-like to Li-like ions obtained for I ($Z =$ 53), Ho ($Z = 63$), and Bi ($Z = 83$). Similarly to Fig. 3, the structures in Fig. 4 correspond to DR cross sections of Li-like ions normalized to the ionization cross sections of Be-like ions. For all the elements studied, three manifolds were observed in the KLL DR resonance region, which correspond to $KL_{12}L_{12}$, $KL_{12}L_3$ and KL_3L_3 DR resonances (L_{12} denotes the $2s_{1/2}$ and $2p_{1/2}$ levels and L_3 the $2p_{3/2}$ level). As seen in Fig. 4, it was found that the resonance at the lowest energy side has strong Z-dependence; i.e. its relative intensity with respect to that of the other resonances rapidly increases as Z increases. By comparing the present results with theoretical calculations [8], we found that the strong Z dependence of the resonance at the lowest energy side is due to the generalized Breit interaction (GBI) effect, which is one of the quantum electrodynamics (QED) effects. As shown here, the present result showed that the Z-dependence of DR resonant strength can be quite different among resonant levels.

4. Conclusion

As shown in this paper, the present method has been confirmed to be very useful to study DR for a wide range of atomic number and charge state. In addition to DR, the present method is very useful also to observe recombination in ionization, such as REDA.

The cross section for REDA is usually very small for highly charged heavy ions because radiative rates predominate over Auger rates. The highest charge state for which REDA was observed so far is Na-like Fe^{15+}. On the other hand, through the ion abundance measurements, we have successfully observed REDA for Li-like I^{50+} [2]. This shows the high efficiency of the present method.

Acknowledgement

This work was supported by the JSPS program under the Japan-UK Research Cooperative Program, and partially supported by the CREST program, “Creation of Ultrafast Ultralow Power, Super-performance Nanodevices and Systems” in the Japan Science and Technology Agency, and the National Natural Science Foundation of China under Grant No.10674020 and No.10434050. This work was also a part of the 21st Century Center of Excellence Program, ”Innovation in Coherent Optical Science” at the University of Electro-Communications. FJC and APK thank the Royal Society for support which allowed them to participate in this research program. This work is also partly supported by the Leading Project for advanced semiconductor technology of MEXT.

References

References

[1] N. Nakamura et al., Rev. Sci. Instrum. **69**, 694 (1998).

[2] N. Nakamura et al., Phys. Rev. A **73**, 020705 (2006).

[3] H. Watanabe et al., J. Phys. B **34**, 5095 (2001).

[4] D. A. Knapp et al., Phys. Rev. Lett. **62**, 2104 (1989).

[5] R. E. Marrs et al., Phys. Rev. A **56**, 1338 (1997).

[6] N. Nakamura et al., Can. J. Phys. in press (2007).

[7] H. Watanabe et al., Phys. Rev. A **75**, 012702 (2007).

[8] Y. M. Li et al., to be published elsewhere.

Ab Initio Study of Charge Transfer Processes in Ion-atom Collisions at Low to Intermediate Energies

Yong Wu[†], Bin Yan[‡] and Jian-Guo Wang[†]

[†] *Key Laboratory of Computational Physics, Institute of Applied Physics and Computational Mathematics, PO Box 8009-57, Beijing 100088*

[‡] *Institute of Atomic and Molecular Physics, Jilin University, Changchun 130012*

e-mail: wu_yong@iapcm.ac.cn

Abstract

The single charge transfer process in $He^+ + H$ collisions is investigated using the quantum-mechanical molecular-orbital close-coupling method, in which the adiabatic potentials and radial couplings are calculated by using the *ab initio* multireference single- and double-excitation configuration interaction methods. Total and state-selective cross sections for the single charge transfer are presented for incident energy range from 5eV/u to 15keV/u for the projectile He^+. Obvious discrepancy is found in comparing with the calculations by B. Zygelman *et al* [*Phys. Rev. A* 40, 2340 (1989)] in the low-energy range and the charge transfer processes to higher states become more important with increment of the incident energy.

Keywords: single charge transfer, MOCC, MRDCI, state-selective, ion-atom.

1. Introduction

The investigations of ion-atom collisions are important for both fundamental physical research and applied fields, and thereinto the charge transfer in collision of ions with neutral atoms and molecules has attracted much attention. In addition to the necessity of a clear understanding of the fundamental collision dynamics in many-electron systems, the requirements of detailed cross sections for various collision processes in some applied research fields such as astrophysics and plasma physics are partly responsible for the profusion of work in this subfield of atomic collisions. Charge transfer provides a recombination mechanism for multiply charged ions in x-ray ionized astronomical environments which may have sparse electron abundances. [1] In the diverter region of tokamak fusion device, charge exchange of impurity ions with neutral atoms and molecules plays an important role in the ionization balance and production of radiative energy loss leading to cooling. [2, 3] In the core of the plasma, charge exchange spectra produced by neutral beam injection are also an important method to diagnose the populations of impurities.

The quantum-mechanical molecular-orbital close-coupling (MOCC) method has been described thoroughly in the literature [4 - 8] and we only give a brief introduction in this paper. It involves solving a coupled set of second-order differential equations and the solutions are the scattering amplitudes of total system wave function expanded over a truncated set of molecular eigenfunctions. The differential cross section for single charge transfer (SCT) is given by

$$\frac{d\sigma(\theta)}{d\Omega}=\frac{1}{4k^2}[\sum_l(2l+1)S^lP_l(\cos\theta)]^2, \tag{1}$$

where the S matrix is

$$S^l=\frac{I+iK^l}{I-iK^l}. \tag{2}$$

and k is the initial momentum. The K matrix is obtained from the scattering amplitude after a partial-wave decomposition [4] and I is the identity matrix.

The state-selective cross sections for the charge transfer process $He^+(1s)+H(1s)\rightarrow$ He (1*snl*) + H^+ has been investigated using the MOCC method. The multireference single- and double-excitation configuration interaction (MRDCI) programs[9-13] were employed to obtain the adiabatic potentials and radial couplings for HeH^+ system, in which the Gaussian ($6s3p2d1f$)basis sets of cc-pVTZ type were used for helium or hydrogen atom and three additional diffuse (3*s*3*p*3*d*) set of functions centered on helium or hydrogen atom are also used to describe the molecular Rydberg states,[14] in which the exponent factors have been optimized to obtain accurate dissociation limits for a few low-lying states. Total and state-selective cross sections for the single charge transfer (SCT) are calculated and compared with that of B. Zygelman[15] et al. for the incident energies from 5eV/u to 15keV/u for the projectile He^+.

2. Adiabatic potential and radial coupling calculation

The calculated adiabatic potentials for the lowest eight $^1\Sigma_g$ and $^3\Sigma_g$ states are shown in Fig. 1(a) and Fig. 1(b) respectively, and the corresponding potential curves for the lowest six $^1\Sigma_g$ of Green *et al.,*[16] which are calculated using the method of superposition of configurations, are also shown in Fig. 2 for comparison, in which the solid lines are the present calculations and the solid circles are results of Green *et al.* [16]. It can be found from Fig.2 that there is a good agreement between the present calculations and the results of Green *et al*[16] in the whole internuclear distance considered. For the avoided crossing positions, it can be observed that the ones between each two adjacent potential curves are very close for the two calculations, as shown in Figs. 2. The radial couplings for the adjacent molecular states in $^1\Sigma_g$ symmetries are displayed and compared with the corresponding results of Green *et al*[17] and Zygelman *et al*[15]., as shown in Fig. 3. It can be found that the present calculation agrees well with the result of Green *et al*[17] for the radial coupling between the $3^1\Sigma_g$ and $4^1\Sigma_g$, as shown in Fig. 3 (b). And for the radial coupling between the $1^1\Sigma_g$ and $2^1\Sigma_g$, there are obvious differences between the present calculation and the results of Green *et al* [17] and Zygelman *et al* [15] at the small internuclear distance, which is due to the strong electrons correlation effect, and large numbers of configurations are needed in the calculation for radial coupling. It can also be found that there is a better agreement between the present calculation and that of Green *et al*[17].

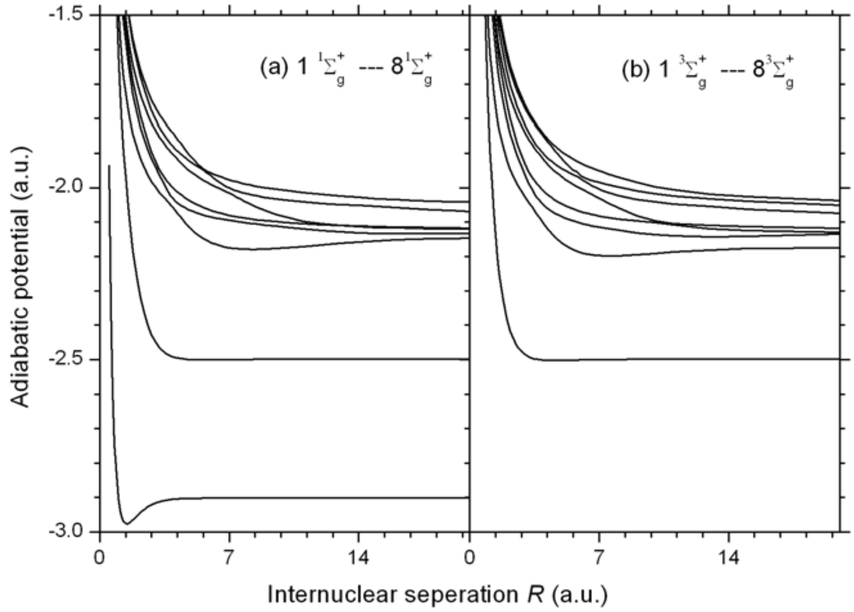

Fig.1. Adiabatic potentials for the (HeH)$^+$. (a) the lowest eight for $^1\Sigma_g$ symmetry states; (b) the lowest eight for $^3\Sigma_g$ symmetry states.

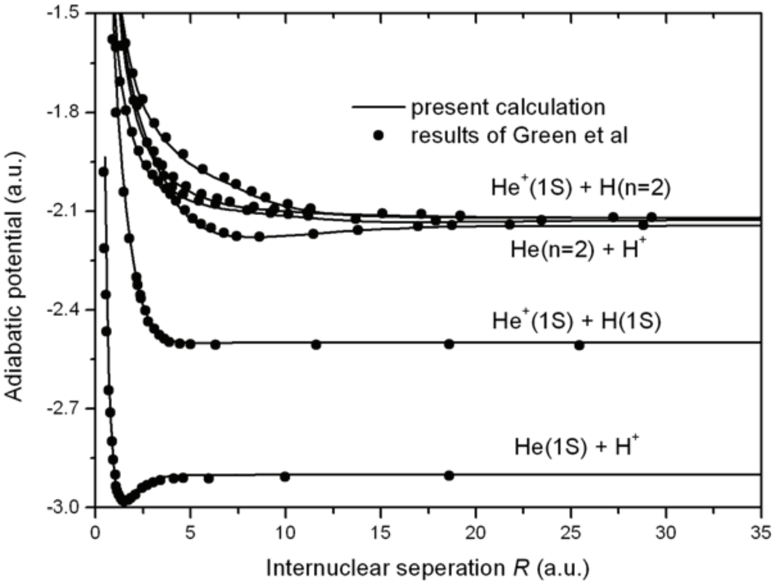

Fig.2. Adiabatic potential comparison between the present calculation (solid lines) and the results of Green *et al*[16] (solid circles) for $^1\Sigma_g$ state.

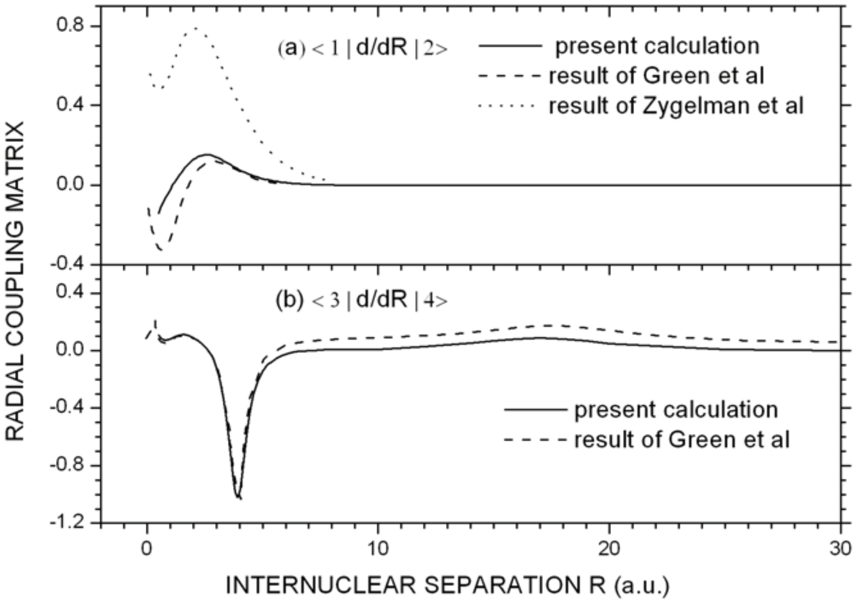

Fig.3. Comparison of the adiabatic radial couplings between the present calculation and the results of Green *et al*[17] and Zygelman *et al*[15].

3. SCT cross section

With the adiabatic potentials and the radial coupling matrix elements shown in Figs. 1 and Figs. 3, the state selective cross sections for the single charge transfer processes are calculated with the MOCC method at the incident energies range from 5eV/u to 15keV/u for the projectile He^+, which are presented and compared with the corresponding theoretical results of Zygelman *et al*[15], as shown in Figs.4 (a) and Fig.4 (b). In the calculation of the SCT cross sections, $1^1\Sigma_g$, $2^1\Sigma_g$, $3^1\Sigma_g$, $4^1\Sigma_g$, and $1^3\Sigma_g$, $2^3\Sigma_g$, $3^3\Sigma_g$ channels are included, where $2^1\Sigma_g$ and $1^3\Sigma_g$ are the incoming channels, and the total SCT cross section is obtained by summing the partial SCT cross sections for all the outgoing channels in both $^1\Sigma_g$ and $^3\Sigma_g$ symmetries. It is found from Fig. 4 (a) that the charge transfer cross section to $1^1\Sigma_g$ increases with the increment of the incident energy, which is consistent qualitatively for the present calculation and the results of Zygelman *et al*[15]. But quantitatively, the charge transfer cross section increases more quickly with the increment of the incident energies in the present calculation, which is due to the different radial coupling used in the calculation, as shown in Fig. 3 (a). Furthermore, it can be observed from Fig. 4 (b) that the charge transfer processes to higher states ($2^3\Sigma_g$, $3^3\Sigma_g$ and $3^1\Sigma_g$, $4^1\Sigma_g$) become more important as the incident energies increase beyond about 60eV, which differs from the estimation of Zygelman *et al*[15] who neglected these contributions.

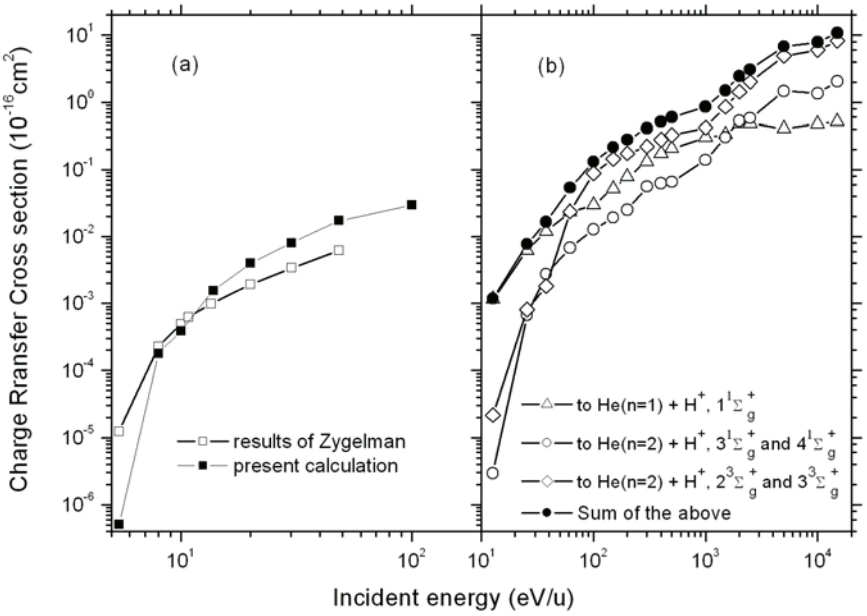

Fig.4. Single charge transfer cross section in the He^++H collision.

(a) Comparison between the present calculation and the results of Zygelman *et al*[15] for the charge transfer process of $He^+(1s) + H(1s) \rightarrow He(1s, n=1) + H^+$;

(b) States selective and total cross section for $He^+(1s) + H(1s) \rightarrow He(1s, nl)+H^+$

4. Conclusion

In summary, using the *ab initio* MRD-CI method the adiabatic potentials and radial coupling matrix elements for the $(HeH)^+$ system are obtained, on which the state selective cross sections for the SCT process of $He^+ + H \rightarrow He + H^+$ are calculated in the quantum-mechanical molecular-orbital close-coupling (MOCC) method at the incident energies from 5eV/u to 15keV/u for the projectile He^+. Comparison with the exiting data of Zygelman *et al* reveals that accurate potential and radial coupling calculations are very important for the collision process investigation and the charge transfer process to higher states become more dominant while the incident energies increase beyond 60eV/u.

Acknowledgement

This work is supported by the National Natural Science Foundation of China under Grant Nos 10604011, 10604022, 10574018, 10574020, and the National High-Tech ICF Committee in China.

References

[1] Lepp S and McCray R, Astrophys. J. **269** 560 (1983)

[2] Krasheninnikov S I, Pgarov A Yu and Sigmar D J Phys. Lett. A **214** 295 (1996); Phys. Lett. A **222** 251(1996)

[3] Janev R K, Kato T and Wang J G Phys. Plasmas **7** 4364 (2000)

[4] B. Zygelman, D. L. Cooper, M. J. Ford, A. Dalgarno, J. Gerratt, and M. Raimondi, Phys. Rev. A **46**, 3846 (1992)

[5] P. O. Lo¨wdin, Phys. Rev. **97**, 1474 (1955)

[6] M. Kimura and N. F. Lane, Adv. At., Mol., Opt. Phys. **26**, 79 (1990)

[7] J. G. Wang, P. C. Stancil, A. R. Turner and D. L. Cooper, Phys. Rev. A **67**, 012710 (2003)

[8] J. G. Wang, P. C. Stancil, A. R. Turner and D. L. Cooper, Phys. Rev. A **69**, 062702 (2004)

[9] Buenker R J and Peyerimhoff S D 1975 Theor. Chim. Acta **39** 217

[10] Buenker R J and Peyerimhoff S D 1976 *New Horizons of Quantum Chemistry* ed Löwdin P O and Pullman B (New York: Reidel) p183

[11] Buenker R J, Peyerimhoff S D and Butscher W 1978 Mol. Phys. **35** 771

[12] Buenker R J 1986 Int. J. Quantum Chem. **29** 435

[13] Knowles D B, Alvarez-Collado J R, Hirsch G and Buenker R J 1990 J. Chem. Phys. **92** 585

[14] Woon D E and Dunning T H Jr 1994 J. Chem. Phys. **100** 2975

[15]B. Zygelman, A. Dalgarno, M. Kimura and N. F. Lane, Phys. Rev. A 40, 2340 (1989)

[16] T. A. Green, H. H. Michels, J. C. Browne and M. M. Madsen, J. Chem. Phys. **61**, 5186 (1974)

[17] T. A. Green, J. C. Browne, H. H. Michels and M. M. Madsen, J. Chem. Phys. **61**, 5198 (1974)

Calculations of Electron Impact Excitation Cross Sections related with Plasmas

Luyou Xie[1], Jun Jiang[1], Chenzhong Dong[1,2,†] and Ninxuan Yang[1]

1) *College of Physics and Electronic Engineering, Northwest Normal University, Lanzhou, 730070, China*
2) *National Laboratory of Heavy-Ion Accelerator of Lanzhou, Lanzhou 730000, China*

†*e-mail: dongcz@nwnu.edu.cn*

Abstract

Fully relativistic distorted-wave (RDW) calculations of electron impact excitation (EIE) cross sections for Ne-like iron and neutral xenon have been performed. In the present method, Multi-configuration Dirac-Fock wavefunctions are used to describe the target-ion states, and the relativistic continuum wavefunctions are calculated in the frozen orbital self-consistent-field (SCF) approach with inclusion of exchange effects between the continuum electron and the target-ion. And in the calculations, the effects of electron correlation, Breit interaction and high partial wave contributions on EIE cross sections are considered systematically. The results are compared with previous calculations and experiments, good agreement is obtained.

Keywords: RDW, EIE, Cross Sections

1. Introduction

Electron impact excitation (EIE) cross sections are widely required for calculating level populations and spectral line intensities in diagnostic of plasmas occurring fusion experiments, X-ray lasers and astrophysics[1-4]. With the development of experimental techniques, such as, electron beam ion traps (EBIT), merged electron-ion beams energy-loss (MEIBEL), atom trap-based technique, synchronous photon detection, radiation trapping etc., some high accurate data of EIE have been obtained experimentally, which not only provide much valuable information for understanding electron collision dynamics, but also bring some new challenges for theorist to study EIE[1,3]. In theory, there are three methods commonly used, namely, distorted-wave approximation (DW), R-matrix method and close-coupling (CC) method[2-4]. It is well known that the R-matrix and CC methods are accurate for neutral atoms or low charged state ions, but they consume more computational efforts and are usually limited to the low collision energies. In practical applications, the DW method is more easy and effective to obtain the EIE cross sections.

Recently, to satisfy the urgent demand of large numbers of electron collision data, a new rapid and accurate fully relativistic distorted-wave (RDW) program[5]have been developed by us based on the well-known atomic structure procedure package GRASP92[6] and RATIP[7]. As a application of the program, the EIE processes of Ne-like ion and neutral xenon were investigated, which are very useful for studying of laser plasmas, solar plasmas, cataclysmic variable binary systems and cool stars etc. In the present work, the EIE cross sections connected with the ground state, metastable states and inner-shell excitated states have been calculated systematically. In the calculations, the configuration interactions (CI) of the target states were considered, which plays a very important role in low energy impact excitations. Also, the contributions of resonance excitation near threshold were discussed.

2. Theoretical method

In the independent-processes approximation, the total excitation cross section from an initial state i to a final state f is given by

$$\sigma^{T}_{i\to f} = \sigma^{DE}_{i\to f} + \sigma^{RE}_{i\to f} \tag{1}$$

where $\sigma^{RE}_{i\to f}$ is the resonant-excitation (RE) cross-section. $\sigma^{DE}_{i\to f}$ is the nonresonant background cross-section, namely the direct-excitation (DE) cross-section and is defined as

$$\sigma^{DE}_{i\to f}(\varepsilon) = \frac{\pi a_0^2}{k_i^2 g_i}\Omega_{if}(\varepsilon), \tag{2}$$

where a_0 is the Bohr radius, g_i is the statistical weight of the initial level of the N-electron target ion, and k_i is the relativistic wave number of the incident electron,

$$k^2 = \varepsilon\left(1 + \frac{\alpha^2\varepsilon}{4}\right) \tag{3}$$

with the energy ε in rydbergs. The relativistic distorted wave collision strength $\Omega_{if}(\varepsilon)$ is defined as,

$$\Omega_{if}(\varepsilon) = 8\sum_J (2J+1)\sum_{\kappa,\,\kappa'}\left|\langle\Psi_i|\sum_{p,q\,p<q}^{N+1}\left(\widehat{V}_{Coul} + \widehat{V}_{Breit}\right)|\Psi_f\rangle\right|^2, \tag{4}$$

where κ and κ' are the relativistic quantum numbers of the initial and final continuum electrons, respectively; $\widehat{V}_{Coul}$ is the Coulomb operator and $\widehat{V}_{Breit}$ is the Breit operator. Ψ_i and Ψ_f are the antisymmetric wavefunctions for both the initial and final states of the $(N+1)$-electron impact systems including the target ion plus continuum electron, which can be written as

$$\Psi = \frac{1}{(N+1)^{1/2}}\sum_{p=1}^{N+1}(-1)^{N+1-p}\sum_{M_t,\,m} C(J_t j M_t m; JM)\psi(J_t P_t M_t; N)u_{\varepsilon\kappa m}(N+1), \tag{5}$$

where C is the Clebsch-Gordon coefficient, J_t, j, and J are the angular momentum quantum numbers of the target-ion, continuum electron and the impact system, respectively. $\psi(J_tP_tM_t;N)$ is wavefunction of the target-ion with N electrons, which can be approximated by a linear combination of configuration state functions (CSFs) of well-defined total angular momentum J_t and parity P_t, and generated by using the widely used atomic structure package GRASP92[6]. $u_{\varepsilon\kappa m}$ is relativistic continuum wavefunction of the free electron with the certain energy ϵ, wich are produced by using the relativistic program COWF[7], and in the calculations, the contributions from both direct and the exchange interactions between the contimuum electron and bound electrons were considered.

In the independent-processes approximation, the resonance excitation is treated as a two-step process: dielectronic capture followed by Auger decay to a singly excited state. The RE cross section at an incident energy ε is given by

$$\sigma^{RE}_{i\to f} = \frac{(2\pi a_0 I_H)^2}{\varepsilon} \sum_k \frac{g_k}{2g_i} \tau_0 A_a(k,i) B_a(k,f) L_k(\varepsilon) \tag{6}$$

where $(2\pi a_0)^2\tau_0 = 2.6741 \times 10^{32} cm^2 s$, $A_a(k,i)$ is the radiationless excitation capture probability, which can by obtained from the autoionization transition probability from a doubly excited state k to an initial state i by detailed balance, the branching ration for autoionization from a doubly excited state k to an electron-impact excited final state f is given by

$$B_a(k,f) = \frac{A_a(k,f)}{\sum_m A_a(k,m) + \sum_n A_r(k,n)} \tag{7}$$

where $A_a(k,m)$ is the autoionization rate to all states m which lie below k, and $A_r(k,n)$ is the radiative rate to all states n which also lie below k. L_k is the lorentz profile

$$L_k(\varepsilon) = \frac{(1/2\pi)\Gamma_k}{(\varepsilon + E_i - E_k)^2 + (1/4)\Gamma_k^2} \tag{8}$$

The total width, $L_k = \hbar \sum_m A_a(k,m) + \sum_n A_r(k,n)$, and contains contributions from all radiative as well as autoionization rates.

3. EIE Cross Sections of Ne-like Iron

The highly charged neon-like FeXVII ion, because of its closed-shell nature, has become a very good candidate to test all kinds of atomic collision calculations and physical effects. In the past 20 years, there are many theoretical methods such as the distorted-wave approximation[8-10], R-matrix method[11,12], and close-coupling approach[2], have been widely used to study EIE processes of FeXVII. Also, some experimental work at electron beam ion trap (EBIT) and tokamak sources has been performed to study L-shell emission line ratios [1-3,13]. However, there are still several long-standing discrepancies and inconsistencies when calculated and measured line intensities are compared. As is well known, the collision strengths or cross sections for the resonance line $(2p^5_{1/2}3d_{3/2})_1 - 2p^6\ ^1S_0$ (labeled 3C) and the intercombination line $(2p^5_{3/2}3d_{5/2})_1 - 2p^6\ ^1S_0$ (labeled 3D) of FeVII are extremely interesting for physicists because of their potential diagnostic applications. Resently, Brown et al.[1] measured EIE cross-sections for 3C and 3D lines. Their measurements show that the resonance contributions to the cross-sections of 3C and 3D are very samll, and which are not sufficient to explain the discrepancies of 3C and 3D line intensity ratios between theoretical calculations and expermental observations. The real reason is that all previous calculations overestimate the direct cross-sections of 3C and 3D by more that 25%.

In this study, we calculated the direct electron-impact excitation cross sections of 3C and 3D with the different correlation approaches. Model A contains seven configurations $2s^22p^6$, $2s^22p^53l(l=s,p,d)$ and $2s2p^63l(l=s,p,d)$ with 37 fine-structure levels. Model B contains 15 configurations with 89 fine-structure levels, namely eight configurations $2s^22p^54l(l=s,p,d,f)$ and $2s2p^64l(l=s,p,d,f)$ are added to the seven configurations from Model A. The results are plotted in Fig. 1 as a function of electron-impact energies. As can be seen from Fig. 1, the correlation effects are much more important for the resonance line 3C than for the intercombition line 3D. When the $4l$ electron correlations are included, the cross-sections for 3C are decreased by about 3 -10%, and the results are better than the previous calculations compared to the experiment. For the 3D line, the effects of correlation on cross-section are not important, and both results calculated in Model A and B are in good agreement with the experiment[1]. Although the results from Mohan et al.[11] also agree with the experiment for the 3D line, there are limit partial wave contributions ($\kappa = 9$) considered in their calculations. In the present calculations, all partial waves in the range $\kappa = 50$ were included. In addition, we studied the contributions of Breit interaction on the 3C and 3D cross-sections, it is about 0.5% and can be negelected compared to the contribution of electron correlations.

For neon-like FeXVII, the RE contributions are much larger for the $2p^53s$ states than the $2p^53p$ and $2p^53d$ states[3,4]. To test our theory, we calculated the indirect RE cross sections of $2p^53s$ states, and studied the contributions of resonance excitation to total cross-sections. In the present calculations, we explicitly included contributions from the $2p^53pnl'$, $2p^53dnl'(7 \leq n \leq 15, l'=s,p,d,f)$ and $2p^54l4l'$, $2p^54l5l'(l,l'=s,p,d,f)$ resonance series. It is found that the $2p^53dnl$ resonances dominate the indirect contributions. In Fig.2, the RE, DE and total cross sections for $2p^6\ ^1S_0 - (2p^5_{1/2}3s_{1/2})_1$ transitions are

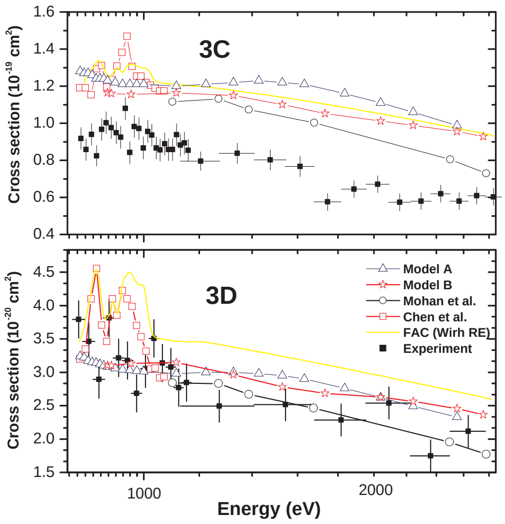

Figure 1: Comparision of the present calculations in Model A (solid line with open triangle) and Model B (solid line with open star) for 3C and 3D Cross sections of FeXVII as functions of electron elergies, with the results of the resent EBIT experiment[1] (full cicle with error bars), and the previous calculations by Mohan et al.[11](solid line with open circles), by Chen et al.[2] (solid line with open squares) and the FAC calculations with resonance excitation by Brown[1] (solid line).

presented. As can be seen from the Fig.2 (a), the larger resonance peaks occur near threshold with the incident electron energy $\varepsilon \leq 880eV$, and there are also some small resonance peaks around 960eV and 1080eV. Compared to the fully relativistic R-matrix calculations by Loch et al.[3], who employed 139 coupled atomic levels through $n = 5$, the present RE cross sections are close for both resonance positions and the shape. We found that the discrepancies are less than 10eV for resonance positions. The resonance contributions to total cross-sections are very significant, they increase the DE cross sections by 1-2 orders of magnitude near threshold. At higher collision energies with $\varepsilon > 900eV$, the DE contributions dominate the total cross sections, while the RE contributions are very small and can be neglected.

4. EIE Cross Sections of Neutral Xenon

Beside of long lifetimes, the metastable states of rare gas atoms are known for having rather large EIE cross sections, if compared with the ground state. Thus, those cross sections are highly interested for analysising of emissions from low temperature plasmas, and finding applications in the fields of gas-discharge lasers, Hg-free fluorescent lighting and plasma displays[14-17]. The neutral Xenon, because of its stronger correlation and relativistic effects, has become a typical example in the study of electron collision with heavy elements. The ground state of xenon is formed by the very stable closed-shell configuration $5p^6$. The relative low excited states are formed by the configurations $5p^5 6s$ and $5p^5 6p$. Those excited levels are separated obvious into two pairs by their parent (core) terms $5p^5(^2P_{3/2})$ and $5p^5(^2P_{1/2})$. The lower lying metastable states of the xenon

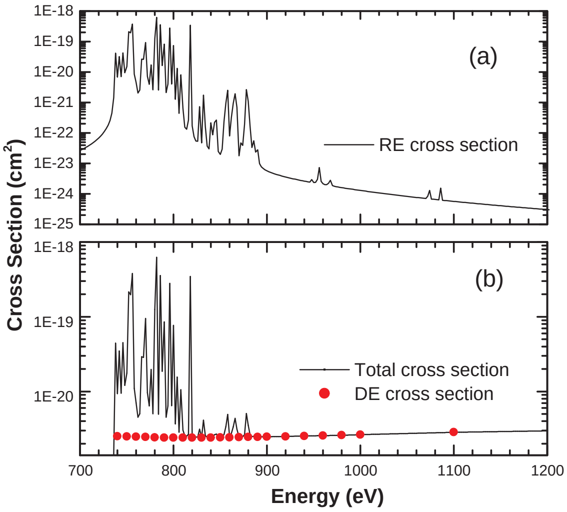

Figure 2: Cross sections for the $2p^6\ ^1S_0 - (2p^5_{1/2}3s_{1/2})_1$ transition of FeXVII as functions of electron temperature.

are the $5p^56s$ J=2 and J=0, which denoted as $1s_5$ and $1s_3$ in Paschen notation, with the core angular momentum j_c=3/2 and j_c=1/2 respectively. For the ten levels of $5p^56p$ configuration, it also exhibits the similar two pairs, namely, the upper four levels with j_c=1/2 denoted as $2p_1$ to $2p_4$ and the lower six levels with j_c=3/2 denoted as $2p_5$ to $2p_{10}$.

In this study, to obtain the convergent results of cross sections, the maximal partial wave $\kappa = 40$ were included for most of excitations at incident energy below 20eV and more high partial wave up to $\kappa = 60$ were included for the high energy region. In addition, to discuss the correlation effects of the target on EIE cross sections, two models are used to describe the target states. Model A, similar with the descriptions by Srivastava *et.al.*[18], includes the configurations of $5s^25p^6$, $5s^25p^56s$ and $5s^25p^56p$, with total 15 CSFs. And in the calculations, single electron orbital wave functions including the core ($1s_{1/2}$, $2s_{1/2}$, $2p_{1/2}$, $2p_{3/2}$ $3s_{1/2}$, $3p_{1/2}$, $3p_{3/2}$, $3d_{3/2}$, $3d_{5/2}$, $4s_{1/2}$, $4p_{1/2}$, $4p_{3/2}$, $4d_{3/2}$ and $4d_{5/2}$) and peel ($5s_{1/2}$, $5p_{1/2}$, $5p_{3/2}$, $6s_{1/2}$, $6p_{1/2}$ and $6p_{3/2}$) are obtained by using an extended optimal level (EOL) method[19]. Model B includes the configurations of $5s^25p^6$, $5s^25p^56p$, $5s^25p^56s$ and $5s^25p^55d$. To deal with the rearrangement of the valence orbits, we divided all levels into six groups according to their parity and total angular momenta, and optimized the states by using EOL method independently. In the calculations, all virtual single and double excitations from the $5s_{1/2}$, $5p_{1/2}$, $5p_{3/2}$ shells into the unoccupied $5d_{3/2}$, $5d_{5/2}$, $6s_{1/2}$, $6p_{1/2}$ and $6p_{3/2}$ shells were incorporated by using the active space method[19]. Table 1 listed in detail the number of the CSFs used for different level groups in the Model B.

Fig.3 plotted the EIE cross sections from the metastable state $1s_5$ to the six excited states of $5p^6p$ ($2p_5$ to $2p_{10}$) as functions of incident electron energy in two models. As comparisons, the results of the newly experiments[20] and calculations by Srivastava *et*

Table 1: Number of CSFs in the expansion of the target state functions of XeI in model B. J^P is the total angular momenta and parity, NL is the number of the optimized levels, NCSF is the number of CSFs.

Configurations	J^P	NL	NCSF
$5s^25p^56s + 5s^25p^55d$	2−	1	963
	0−	1	301
$5s^25p^6 + 5s^25p^56p$	0+	3	263
	1+	4	630
	2+	3	778
	3+	1	660

al.[18] are also presented. Firstly, we pay attentions to the excitations from $1s_5$ to $2p_6$ and $2p_{10}$, since these excitations are dipole allowed transitions, both the theoretical and experimental results show similar variational trends, namely, they have larger cross sections and broad peaks, which decrease slowly with increasing of incident electron energies. From the figure, we can see that our results in model A are much larger than the experiments, but in model B, which are in good agreement with experiments, except for the transition $1s_5 \rightarrow 2p_{10}$, for this transition all theoretical results including ours and Srivastava *et al.*[18] are lager than the experiments[20] a factor of 2. Comparing our results with the Srivastava[18], although the description of the target states by Srivastava *et al.*[18] are same as the present descriptions in model A, some larger differences are still existed. Secondly, for the excitation from $1s_5$ to $2p_5$, which is a dipole forbidden transition, the cross sections decrease rapidly with the increasing of incident electron energies. The difference between two models are very small and our results are excellent agree with the experiments. In addition, when the incident electron energy is higher than 4eV, because of the cascade contributions from more highly excited states are becoming important, so the experiment results are larger both than our results in two models and the results of Srivastava *et al.*[18].

5. Conclusions

In summary, the electron impact excitation cross sections of Ne-like iron from the ground state to 37 excited states, and neutral xenon from the metastable states to the ten levels of the $5p^56p$ configuration were calculated systematically by using the RDW method. It is found that the accurate description of target states plays a very important role and the more detailed description should be included especially for neutral xenon. For the high energy impact, the high partial wave contributions should be considered both

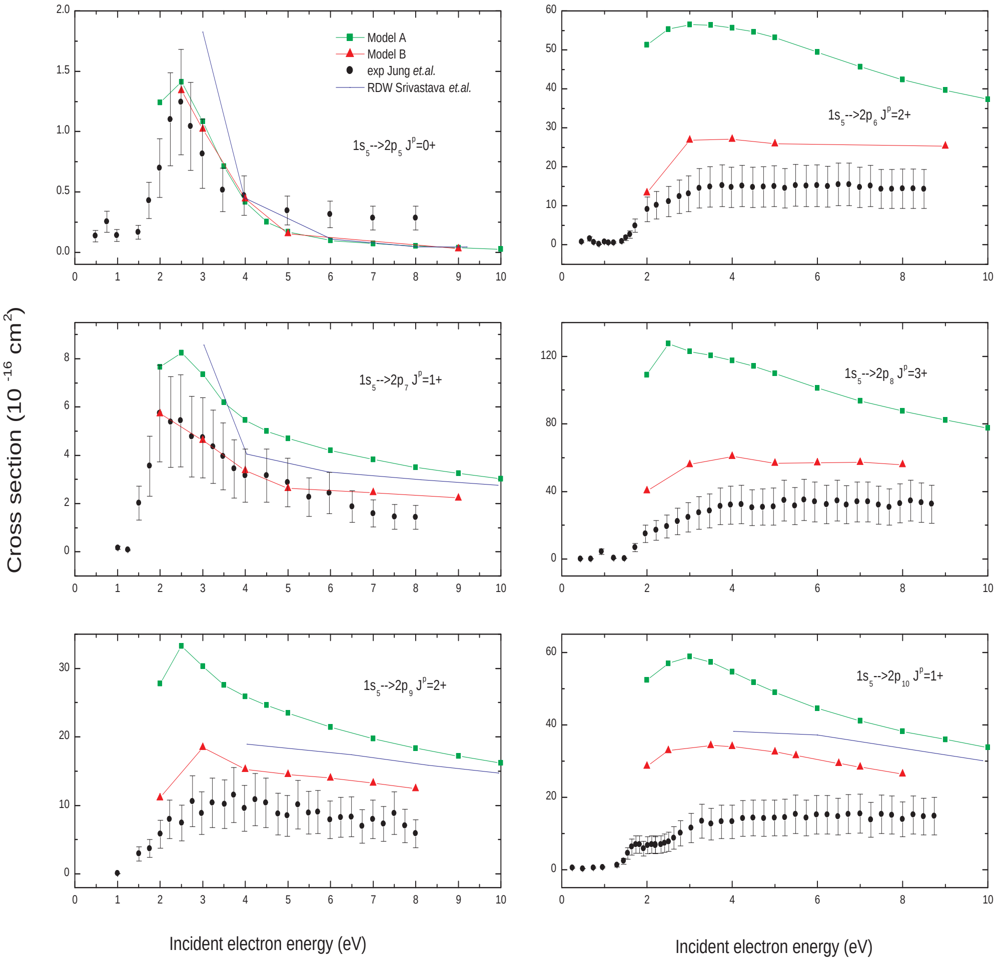

Figure 3: Electron impact excitation cross sections from the metastable state $1s_5$ to the excited states $2p_5 - 2p_{10}$. The square are the results in model A, triangle are the results in models B, circle with the error bars are the experiments of Jung *et al.*[20], the solid line are the RDW results of Srvatave *et al.* [18].

for Ne-like iron and neutral xenon, and for the electron impact excitation at low energy region, the RE contributions can not be ignored.

Acknowledgements

This work is supported by the National Nature Science Foundation of China (Grant Nos. 10434100, 10774122), China/Ireland and Technology Collaboration Research Fund (Grant No. CI-2004-07), and the Foundation of Northwest Normal University (Grant No. NWNU-KJCXGC-03-21).

References

[1] G. V. Brown, P. Beiersdorfer and H. Chen et al.,Phys.Rev. Lett. **96**, 253201 (2006).
[2] G. X. Chen and A. K. Pradhan, Phys. Rev. Lett. **89**, 013202 (2002).
[3] S. D. Loch, M. S. Pindzola and C. P. Ballance et al., J.Phys.B **39**, 85 (2006).
[4] M. S. Pindzola, S. D. Loch and C. P. Ballance et al., Phys. Rev. A **73**, 012718 (2006).
[5] J. Jiang, C. Z. Dong and L. Y. Xie et al., Chin. Phys. Lett **24**, 691 (2007).
[6] F. A. Parpia, C. F. Fischer and I. P. Grant Comput. Phys. Commun **94**, 249 (1996).
[7] S. Fritzsche et al., Nucl. Instr. and Meth. in Phys. Res. B **205**, 93 (2003).
[8] H. L. Zhang, D. H. Sampson and A. K. Mohanty, Phys. Rev. A **40**, 616 (1989).
[9] M. H. Chen and K. J. Reed, Phys. Rev. A **40**, 2292 (1989).
[10] G. X. Chen, Phys. Rev. A **53**, 3227 (1996).
[11] M. Mohan et al., Astrophys. J. **108**, 389 (1997).
[12] S. Ait-Tahar, I. P. Grant and P. H. Norrington, Phys. Rev. A **54**, 3984 (1996).
[13] G. V. Brown, P. Beiersdorfer, and K. Widmann, Phys. Rev. A **63**, 032719 (2001).
[14] Y. B. Golubovskii et al., Plasma Sources Sci. Technol. **14**, 45 (2005).
[15] D. Hayashi, G. Heusler and G. Hagelaar et al., J. Appl. Phys. **95**, 1656 (2004).
[16] G. F. Karabadzhak, Y. Chiu and R. A. Dressler, J. Appl. Phys. **99**, 113305 (2006).
[17] Y. Chui, B. L. Austiu and S. Williams et al., J. Appl. Phys. **99**, 113304(2006).
[18] R. Srivastava, A. D. Stauffer and L. Sharma, Phys. Rev. A**74**, 012715 (2006).
[19] C. Z. Dong, S. Fritzsche and B. Fricke, Eur. Phys. J. D **40**, 317 (2006)
[20] R. O. Jung, J. B. Bofford and L. W. Anderson et al., Phys. Rev. A**72**, 022723 (2005).

Scattered electron- ion coincidence measurements for the study of dissociative ionization processes

Karin Yamamoto, Naoya Miyauchi, Shunsuke Yamada, and Yasuhiro Sakai
Dept. of Physics, Toho University, Miyama Hunabashi, Chiba 2748510 Japan
e-mail: karin@ph.sci.toho-u.ac.jp

Abstract

We have developed the scattered electron- ion coincidence (SEICO) apparatus which has the capability to measure time-of-flight (TOF) mass spectra in coincidence with scattered electrons. The SEICO apparatus has the TOF mass analyzer and the electron energy analyzer, which is used to study the dissociative ionization processes under the both dipole and non-dipole electronic excitations by low energy (50-300 eV) electron impact. The TOF spectra in coincidence with inelastically scattered electrons are named "SEICO spectra", which have been measured under a variety of experimental conditions of electron energy loss value. In this study, we have obtained the SEICO spectra of methane and estimated the apparent generalized oscillator strength distributions as a function of excitation energy.

Keywords: electron- ion coincidence measurements, electron impact, methane, ionization, generalized oscillator strength

1.Introduction

The dissociative ionization process is one of the important process for physics, i.e. plasma, atmosphere of the earth and other planet, and fundamental atomic and molecular physics. We have such interests in the information of total and partial ionization cross sections, and kinetic energy distributions and angular distributions of fragments about the dissociative ionization processes on molecules. In plasma physics, many experimental data have been stored for many years since the beginning of plasma studies [1]. These experimental results were usually reported as the function of incident electron energy. However, in order to study these processes as the fundamental physics, it is desirable that the data should be described as the function of excitation energy. Therefore, recently, the experimental studies of dissociative ionization processes have been carried out by photon impact rather than electron impact. In particular, the photoionization experimants with various coincidence measurements, such as photoelectron-photoion coincidence and photoion-photoion coincidence measurements, are powerful tools. These measurements were usually carried out as the function of excitation energy.

In this paper, we have reported the new experimental apparatus. This is the scattered electron- ion coincidence (SEICO) apparatus for the study of dissociative ionization processes of simple molecule by low energy (50-300 eV) electron impact. The SEICO apparatus is a kind of (e, e+ ion) spectrometer, which has the capability to measure the intensity of fragment ions as the function of excitation energy. In SEICO experiments, we can obtain the information about not only the electric dipole allowed transition caused by photon impact or high energy electron impact, but also other electric multipole and spin-exchange transitions, under a variety of experimental conditions of impact energy, energy loss value, and scattering angle. Although a new high energy (e, e+ ion) spectrometer have been recently designed for similar studies by Cooper *et al.* [2], there have been still few studies about the dissociative ionization from non-dipole states by low energy electron impact.

Using the SEICO apparatus, we can obtain the differential and partial cross sections for every ions including fragment ions at a energy loss value that is excitation energy. Besides, the obtained differential cross section can be transformed into the generalized oscillator strength (GOS). The GOS for electron scattering provides a very useful framework for quantitative analysis of inelastic electron scattering. This is only the function of the magnitude of momentum transfer K^2 under the first Born approximation. Then the GOS $F(K^2)$ is defined as

$$F\left(K^2\right) = \frac{W}{2}\frac{k_0}{k_s}K^2\frac{d\sigma}{d\Omega}, \tag{1}$$

where W is the excitation energy, k_0 and k_s are the momentum of the incident electron and the scattered electron respectively, and $d\sigma/d\Omega$ is the measured differential scattering cross section. For continuum region, the GOS distribution $dF(K^2)/dE$ can be defined as

$$\frac{dF\left(K^2\right)}{dE} = \frac{W}{2}\frac{k_0}{k_s}K^2\frac{d^2\sigma}{dEd\Omega}. \tag{2}$$

Where $d^2\sigma/dEd\Omega$ is the differential cross section for inelastic scattering into an angle $d\Omega$ over the energy loss range dE. When the first Born approximation is not valid, the Eq.(1) and the Eq.(2) may be used to define the apparent generalized oscillator strength (apparent-GOS) for discrete region and the apparent-GOS distribution for continuum region. These are the function of not only K^2, but also the incident electron energy. In this work, we have carried out the SEICO experiment of methane, CH_4, as the first step of the dissociative ionization studies. Since the impact electron energy is not high enough, the first Born approximation is not fully valid in the present experiment.

2. Experimental set-up

The experimental set-up is shown in Fig.1. The SEICO apparatus consists of a pulsed electron-gun, an electron energy analyzer, and a time-of-flight (TOF) mass analyzer. All these components are enclosed in a vacuum chamber, which is evacuated with 500 L/s turbo molecular pump (TMP). Besides, we furnish the chamber with 150 L/s TMP for the TOF mass analyzer as a differential pumping system. The ultimate vacuum pressure was lower than a few times 10^{-7} Pa, and the pressure during the measurements was maintained below 3×10^{-4} Pa.

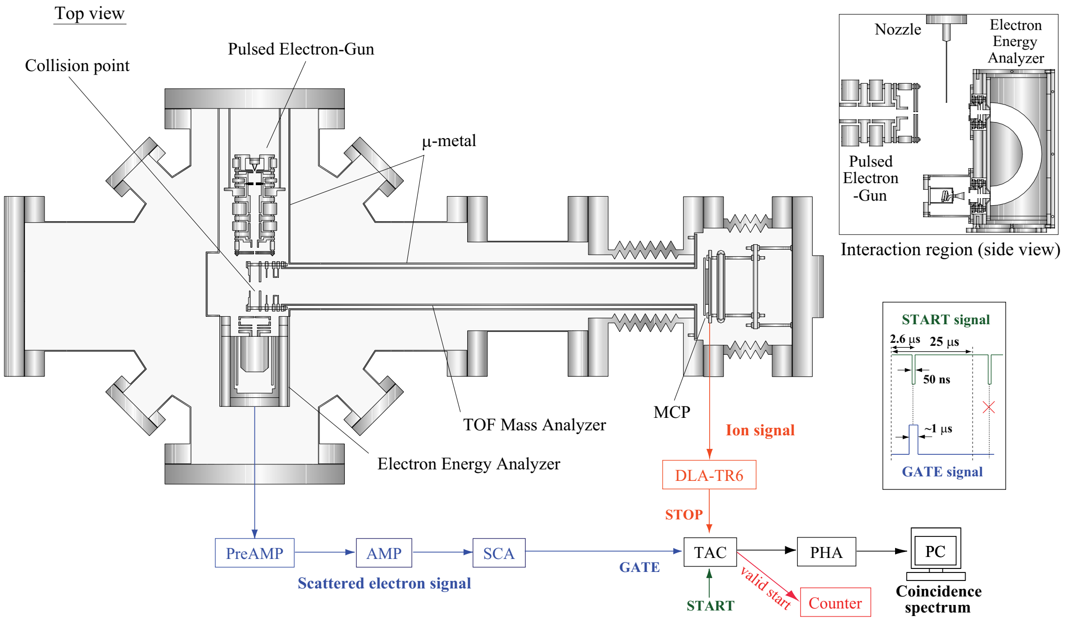

Figure 1: The experimental set-up

The sample gas is introduced through a nozzle into the centre of the interaction region. The incident electrons which are supplied as pulsed electron beam collide with the molecules sprayed from the nozzle (crossed beam geometry). The primary electron current was about 5 nA as continuous electron beam on average. The pulse width and rate were about 70 ns and 40 kHz, respectively. After colliding with the target molecules, electrons are analyzed with electron energy analyzer and detected with a channel electron multiplier. The electron energy analyzer is a simulated hemispherical analyzer called "Jost type" [3], and its mean trajectory radius is 52 mm. The typical energy resolution was 0.5 eV full width at half maximum (FWHM). The scattering angle was determined by the ratio of 2^1S peak intensity to 2^1P peak intensity in electron energy loss spectra of helium [4]. The interaction region is kept at the earth potential while ions are being produced by electrons.

After the pulsed electrons pass through the interaction region (about after 0.2 microsecond), the produced ions are extracted from that region by applying the pulse electric field of 90 V/cm, and analyzed with TOF mass analyzer which is Wiley and McLaren type analyzer [5]. The interaction region and the second accelerate region are 20 and 10 mm in length, respectively, and the drift tube length of the TOF mass analyzer is about 480 mm.

A pulse signal which was for producing electron beam was input to the time-to-amplitude converter (TAC) as the start signal with the gate signal which was a detected electron signal. The detected ion signal was used as the stop signal of TAC. Where, the start signal pulse for TAC was formed with 2.6 microseconds delay. We needed this delay time to prove the coincidence measurement between a scattered electron and an ion. Because, it takes about 2 microseconds from producing the incident electron beam to forming the scattered electron signal. When the both start signal and gate signal are coming here at same timing, the start signal is valid, otherwise not valid. Besides, valid start counts which are corresponding to energy selected electron counts were measured with a counter for normalization.

3. Results and discussion

Figure 2 shows the typical SEICO spectra which were obtained as the TOF spectra in coincidence with energy selected electrons of methane. For every spectra, the impact energy of electron is 150 eV, and the scattering angle is 4 degree. The excitation energy which are corresponded to the energy loss value of each spectrum is 14.4, 16.5, 19.7, and 22.4 eV. The intensity of CH_4^+ decreases, as the excitation energy increases, while the CH_3^+ intensity is turned to a decrease, after the maximum value is taken at 16.5 eV. These results agreed with photon impact experiments.

In order to compare with photoionization cross sections, the apparent generalized oscillator strength (apparent-GOS) distributions were estimated. The apparent-GOS distributions for CH_4^+ and CH_3^+ are shown in Fig.3, together with partial photoionization cross sections measured by Samson *et al.* [6], as the function of excitation energy. Both the apparent-GOS data of CH_4^+ and CH_3^+ were normalized at the excitation energy 16.5 eV, respectively. The data of 150 eV electron impact were good agreement with the photoionization cross sections by Samson *et al.* except for a point at 22 eV excitation energy. On the other hand, due to the statistical error, the data of 70 eV varied widely in this experiment.

In future work we will carry out several SEICO experiments at various excitation energies, under a variety of experimental conditions of impact energy and scattering angle.

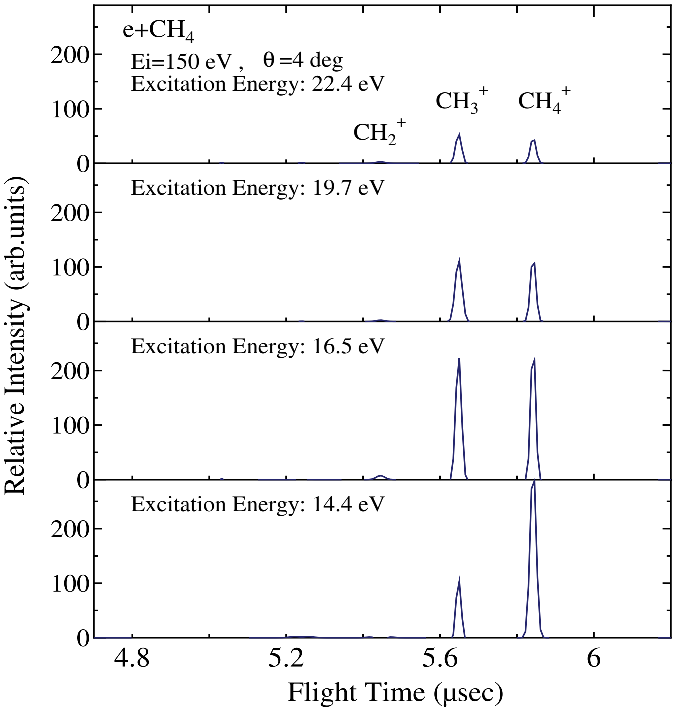

Figure 2: SEICO spectra of methane. The impact energy of electron is 150 eV and the scattering angle is 4 degree.

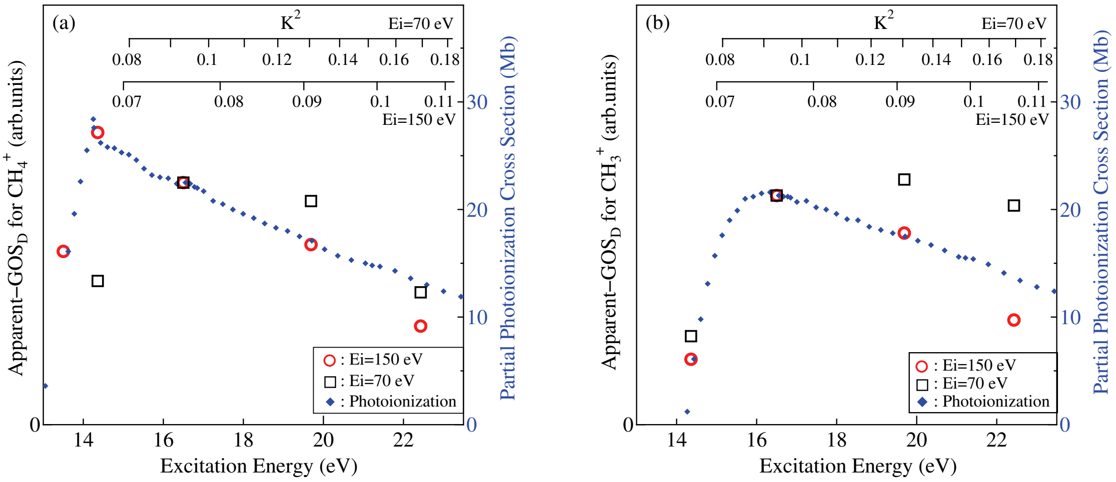

Figure 3: Apparent generalized oscillator strength distributions for CH$_4^+$ (a) and CH$_3^+$ (b) as the function of excitation energy. ○ and □, present data of 150 eV and 70 eV electron impact, ◆, Samson *et al.* (Ref. [6]).

4. Conclusion

We have developed the SEICO (scattered electron- ion coincidence) apparatus for the study of dissociative ionization processes of molecule by low energy electron impact, which is a kind of (e, e+ ion) spectrometer. We succeeded to obtain the SEICO spectra which were the TOF spectra measured in coincidence with energy selected electrons at various energy loss values. The apparent-GOS distributions estimated for CH_4^+ and CH_3^+ were good agreement with photoionization cross sections. In measuring at various scattering angles and/or various impact energies, we hope that the dissociative ionization processes will be completely characterized by low energy electron impact.

Acknowledgement

This work was partly supported by the JSPS-CAS Core-University Program in the field of “Plasma and Nuclear Fusion”. The author (Y. Sakai) also acknowledges support from the Ministry of Education, Science, Sports and Technology, Japan, Grant-in-Aid’s for Scientific Research (C), 13640406, 2003 the 15th MATSUO FUNDATION, 2002.

References

[1] M. Kimura *et al.,* NIFS-DATA-98, (2006).

[2] Glyn Cooper, Jacob Stewart-Ornstein, and Adam P. Hitchcock, *J. Electron Spectrosc. Relat. Phenom.,* **156-158**, 86 (2007).

[3] K. Jost, *J. Phys. E: Sci. Instrum.,* **12**, 1006 (1979).

[4] T. Y. Suzuki, H. Suzuki, F. J. Currell, S. Ohtani, Y. Sakai, T. Takayanigi, and K. Wakiya, *Phys. Rev. A,* **57**, 1832 (1998).

[5] W. C. Wiley, and I. H. McLaren, *Rev. of Sci. Instrum.,* **26**, 1150 (1955).

[6] James A. R. Samson, G. N. Haddad, T. Masuoka, P. N. Pareek, and D. A. L. Kilcoyne, *J. Chem. Phys.,* **90**, 6925 (1989).

Shake Up Processes in the $3d$ Photoionization of Sr I and the Subsequent Auger Decay

Xiaobin Ding[1], Chenzhong Dong[1,2,†], G O'Sullivan[3], P Hayden[3], L Gaynor[3]

1) College of Physics and Electronic Engineering, Northwest Normal University, Lanzhou ,730070, China
2) Center of Theoretical Nuclear Physics, National laboratory of Heavy-Ion Accelerator of Lanzhou, 730000, China
3) School of Physics, University College Dublin, Belfield, Dublin 4, Ireland
†e-mail: dongcz@nwnu.edu.cn

Abstract

The shake up processes accompanying $3d$ photoionization and subsequent Auger decay were studied using multi-configuration Dirac-Fock (MCDF) methods. General agreement was obtained with the experimental results both for the photoelectron and Auger electron spectra. The energy and relative intensity of the $5s \rightarrow 6s$ shake up accompanying the $3d$ photoionization process were identified quantitatively in the present investigation.

Keywords: photoionization, Auger decay, electron correlation, MCDF

1. Introduction

Recent progresses in the spectroscopic measurement and the light source technology made it possible to measure higher order processes accompanying and consequent with photoionization process [1–4]. Meanwhile, relativistic theory of atomic structure and properties were also developed to study these processes [5–7]. It is found in both theoretical and experimental research work that the shake up process accompanying with photoionization is very important in some cases [8–12]. In general, shake up processes are mainly caused by the sudden change in the potential of the residual ions after an inner-shell electron is ionized. This process is a typical multi-electron phenomenon which can not be explained by the independent particle approximation. The main motivation in the past for investigations of this process arose from the high sensitivity of the core ionized states to the effects of correlation. Understanding such processes are crucial not only to explain the basic atomic processes in various plasma but also to understand the break down of the independent particle approximation and the significance of electron correlation effects.

The alkaline earth metal element Sr is a good candidate to investigate the electron correlation effects. However, there are few results available up to date on this atom. In one of the experiments, the ratio of double to single photoionization in the 25-36 eV region ($4p$ excitation region) was measured for neutral strontium [13], while the absolute photoionization cross section for Sr^+ in the 20-41 eV region has been determined by merging beams of Sr^+ with monochromatic synchrotron radiation [14]. The photoabsorption and photoionization spectrum of the $3d$ subshell from Sr I to Sr IV was also studied by dual laser plasma (DLP) method [15]. In a very recent work, J. Nikkinen *et al* observed the $3d$ photoionization spectrum of Sr I and a detailed theoretical analysis was performed to explain their results [16, 17]. However, the dominant photoionization peaks still confused and the shake up process accompanying $3d$ photoionization was not studied quantitatively.

Recently, the multi-configuration Dirac-Fock method has been successfully applied in the study of atomic structure and spectra of complex atom [18–20]. The orbital relaxation effects due to the creation of an inner-shell hole and configuration interaction (CI) effects can be taken into account systematically in the calculations. Based on previous work, a program RERR06 for the study of the photoionization processes has been developed by our research group.

In the present paper, a detailed investigation on the shake up process accompanying $3d$ photoionization and the subsequent Auger decay of $3d$ hole state of Sr I is presented. A brief description of the theoretical method is given in section 2, the correlation model and the calculation of the wavefunction are introduced in section 3. In section 4, we will discuss the shake up process accompanying the $3d$ photoionization and subsequent Auger decay of the $3d$ hole state of Sr.

2. Theoretical method

The photoionization cross section from the initial state i to a ionic state f can be expressed as,

$$\sigma_{if} = 4\pi^2 a_0^2 \alpha \frac{df_{if}}{d\epsilon} \tag{1}$$

where $\frac{df_{if}}{d\epsilon}$ is the oscillator strength density which is defined as,

$$\frac{df_{if}}{d\epsilon} = \frac{\pi c}{(2L+1)\omega^2} | \sum_{rs} d_r^*(i) d_s(f) \sum_{kl} < U^r_{\{u_k\}} | P^{(L)} | V^s_{\{v_l\}} > D_{UV}(k|l) |^2 \tag{2}$$

where $P^{(L)}$ is the radiative field multipole tensor operator and L is the rank of the operator.

The Auger decay rates A^a_{ia} from the core excited state f to the final state k can be calculated by the following formula

$$A^a_{fk} = \frac{2\pi}{\hbar} \left| \langle \alpha_f(PJM) | \sum_{s<t} \frac{1}{r_{s,t}} + V_B | \alpha_k(P'J'M') \rangle \right|^2 . \tag{3}$$

In order to incorporate the influence of the photoionization on the subsequent Auger decay, the relative Auger intensity have been calculated using a two-step model. In this model the primary $3d$ photoionization of the Sr atom is assumed to take place independently of the Auger decay of the $3d$ hole states. The relative Auger decay intensity was defined as

$$I_{fk} = \sigma_{if} \frac{A^a_{fk}}{\sum_k A^a_{fk}}, \tag{4}$$

3. Correlation Model and calculation of wavefunction

The ground state of the neutral strontium is $3d^{10}4s^24p^65s^2\ ^1S_0$. Since the binding energy of $5s$ and $4d$ electron is quite close, it will form a set of near degenerate levels of the ground state and lower excited states, such as $3d^{10}4s^24p^64d^15s^1$ and $3d^{10}4s^24p^64d^2$. Dielectronic correlation is found to be very important to these kind of configurations [21]. Therefore, it is necessary to include dielectronic correlation in the calculation for the wavefunctions of the ground, final photoionization and final Auger states. All of the configurations included in the calculation are listed in table 1 and optimized by a two separated step same as in Ref. [17]. At first, a simple computation for the single configuration is performed to get a better approximation for the inner shells such as $1s$ to $4p$. After that, an extended calculation was carried out for the whole configuration list included in table 1 by fixing the inner-shell orbitals and optimizing the valence orbitals.

Table 1: Configurations used in the MCDF calculation for ground, final photoionization and final Auger states.

Ground State	$3d^{10}4s^24p^65s^2$
Correlation configuration	$3d^{10}4s^24p^6(5s^2, 4d^2, 4d^15s^1, 4d^16s^1, 5s^16s^1, 5p^2, 6s^2)$
$3d$ final photoionization State	$3d^94s^24p^65s^2$
Correlation Configuration	$3d^94s^24p^6(5s^2, 4d^2, 4d^15s^1, 4d^16s^1, 5s^16s^1, 5p^2, 6s^2)$
final Auger state	
A	$3d^{10}4s^24p^6$
B	$3d^{10}4s^24p^5(4d^1, 5s^1, 5p^1, 6s^1)$
C	$3d^{10}4s^14p^6(4d^1, 5s^1, 5p^1, 6s^1)$
D	$3d^{10}4s^24p^4(4d^2, 4d^15s^1, 5s^2, 5p^2, 6s^2)$

4. Results and discussion

4.1. 3d Photoelectron spectra of Sr I

The $3d$ photoionization process interested here is,

$$h\nu + 3d^{10}4s^24p^65s^2 \rightarrow 3d^94s^24p^6(4d^2, 5s^2, 4d^15s^1, 5s^16s^1) + \epsilon f, p$$

The theoretical photoelectron spectrum of this process was presented graphically for comparison with the experimental spectrum in figure 1, where a constant shift of 1 eV towards higher energy for the theoretical results seems to optimize agreement between the calculation and the observation, at least for the most pronounced features observed. In obtaining the theoretical spectrum, each transition was given an intensity proportional to its cross section, and an artificial Gaussian linewidth of 250 meV (instrumental resolution) which was found to give optimum agreement with the experimental data.

The absolute photoionization cross section, binding energy and related photoionization final states denotation and main components in jj coupling are listed in table 2. The atomic state designation is described using all of the opened relativistic subshells $[nl_j^{\omega}]_J$ in jj coupling scheme. ω is the occupation number, $\omega = -1$ represent for the hole state.

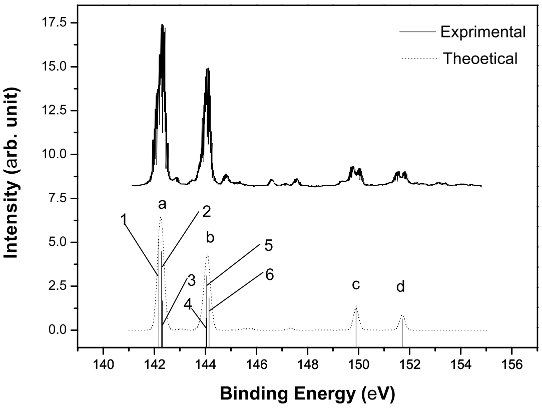

Figure 1: Experimental (upper-part) and theoretical(lower part) Sr 3d photoelectron spectrum. The solid line stands for the experimental from the reference [17], while the dash dots represent the theoretical spectrum from our calculation. The stick lines are the strongest individual photoionization lines. The photo energy is 255 eV.

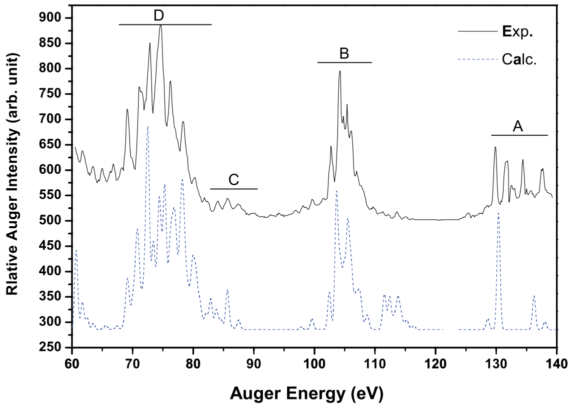

Figure 2: Experimental (upper part) and calculated (lower part) Sr 3d Auger electron spectrum to final states A-D. The intensity at the energy region E_k=120-140 eV have been multiplied by a factor of 10 in each lines.

It can be found from the table that there are very strong mixing between these states, especially between $3d^9 4s^2 4p^6 (4d^2, 5s^2, 4d^1 5s^1)$. The maximum of the main component is just about 50%. Even for the ground state of Sr I, there is also very strong mixing among $3d^{10} 4s^2 4p^6 (4d^2, 5s^2, 4d^1 5s^1, 5p^2)$.

According to the independent particle model it is forbidden that the radiative transition process involved more than two electrons. However, due to the configuration mixing of $4d^2$ with $5s^2$ in both the initial and final states, the density of oscillator strength will be redistributed. Moreover, due to the creation of the 3d hole state, the 6s orbital in the final ionic state will fell less screening from the nucleus, and the wavefunction of the 6s will contracted. The overlap integral of 5s orbital in the ground state with 6s orbital in the ionic state will become very important, as a result the shake-up – even the double shake up – photoionization process become possible. It can be found from figure 1 that the shake up lines arising from 5s to 6s shake up near 149 and 151 eV as indicated in [16] play a very important role in the profile of the photoelectron spectrum.

4.2. Auger decay of 3d hole state

From the viewpoint of single particle approximation, only normal Auger decay is valid in the case of Auger decay following 3d inner-shell photoionization. However, we may expect the appearance of spectator, participator Auger lines and so forth due to the electron correlation effects. All the final Auger states include in table 1 can be classified into (A) double participator, (B) and (C) spectator-participator and (D) double spectator.

Table 2: Bind energy, photoionization cross section, and designation of the 3d photoionization process of Sr.

	present result		Designation
	bind energy*(eV)	cross section(Mb)	
1	142.18	0.944	$37\%\ [3d^{-1}_{5/2}5s^{2}_{1/2}]_{5/2} + 22\%\ [(3d^{-1}_{5/2}4d^{1}_{3/2})_{3}5s^{1}_{1/2}]_{5/2} + 19\%\ [(3d^{-1}_{5/2}4d^{1}_{5/2})_{3}5s^{1}_{1/2}]_{5/2}$
2	142.28	0.840	$51\%\ [(3d^{-1}_{5/2}4d^{1}_{3/2})_{3}5s^{1}_{1/2}]_{5/2} + 34\%\ [3d^{-1}_{5/2}]_{5/2} + 4\%\ [3d^{-1}_{5/2}(4d^{2}_{3/2})_{2}]_{5/2}$
3	142.32	0.409	$44\%\ [(3d^{-1}_{5/2}4d^{1}_{5/2})_{2}5s^{1}_{1/2}]_{5/2} + 17\%\ [(3d^{-1}_{5/2}4d^{1}_{3/2})_{2}5s^{1}_{1/2}]_{5/2} + 15\%\ [3d^{-1}_{5/2}]_{5/2}$
4	144.03	0.258	$21\%\ [3d^{-1}_{3/2}(4d^{2}_{3/2})_{2}]_{3/2} + 12\%\ [(3d^{-1}_{5/2}4d^{1}_{3/2})_{3}4d^{1}_{5/2}]_{3/2}\ +12\%\ 3d^{-1}_{3/2}$
5	144.05	0.629	$40\%\ [3d^{-1}_{3/2}5s^{2}_{1/2}]_{3/2} + 24\ \%\ [(3d^{-1}_{3/2}4d^{1}_{5/2})_{2}5s^{1}_{1/2}]_{3/2} + 9\%\ [3d^{-1}_{3/2}(4d^{2}_{3/2})_{2}]_{3/2}$
6	144.14	0.437	$57\%\ [(3d^{-1}_{3/2}4d^{1}_{3/2})_{3}5s^{1}_{1/2}]_{3/2} + 27\%\ 3d^{-1}_{3/2} + 7\%\ [(3d^{-1}_{3/2}4d^{1}_{5/2})_{2}5s^{1}_{1/2}]_{3/2}$
7	149.90	0.367	$53\%\ [(3d^{-1}_{5/2}5s^{1}_{1/2})_{3}6s^{1}_{1/2}]_{5/2} + 43\%\ [(3d^{-1}_{5/2}5s^{1}_{1/2})_{2}6s^{1}_{1/2}]_{5/2}$
8	151.71	0.251	$63\%\ [(3d^{-1}_{3/2}5s^{1}_{1/2})_{2}6s^{1}_{1/2}]_{3/2} + 34\%\ [(3d^{-1}_{3/2}5s^{1}_{1/2})_{1}6s^{1}_{1/2}]_{3/2}$

*: The calculated energy are shifted by 1 eV.

The double participator (A) should be the weakest while the double spectator (D) should be the strongest. The theoretical Auger electron spectrum is shown in figure 2 with the experimental spectrum is also provided for comparison.

5. Conclusion

The shake up processes accompanying 3d inner-shell photoionization of Sr I and the subsequent Auger decay were investigated using MCDF methods. General agreement was obtained between the experimental and theoretical results. The good agreement between the different gauges, i.e. length and velocity, in the present theoretical calculation indicate that the wavefunction used here are good enough to describe the present states and processes. Due to strong mixing between dielectronic correlation configurations, oscillator strength redistribution occurred in some spectator satellite lines, while the shake up process for $5s \rightarrow 6s$ also becomes possible due to the relaxation effects. According to our results, there are some peaks very close to each other. In order to make a better understanding of such features, it is necessary to improve the experimental resolution.

Acknowledgments

This work was supported by the SFI/RIA China-Ireland Research Collaboration Fund(CI-2004-07), the National Natural Science Foundation of China (Grant No.10434100, 10774122), the Core-University Program between Japanese Society of Promotion of Science and Chinese Academy of Sciences, the Specialized Research Fund for the Doctoral Program of Higher Education of China (Grant No. 20070736001), the Foundation of Center of theoretical Nuclear Physics of National Laboratory of Heavy Ion Accelerrator of Lanzhou, and the Foundation of Northwest Normal University(NWNU-KJCXGC-03-21).

References

[1] Matveev V I and Parilis S 1982 *SOV PHYS USPEKHI* **25**(12) 881–897

[2] West J B 2001 *Journal of Physics B: Atomic, Molecular and Optical Physics* **34**(18) R45–R91

[3] Eichmann U, Gallagher T F and Konik R M 2003 *Phys. Rev. Lett.* **90** 233004

[4] Kjeldsen H 2006 *Journal of Physics B: Atomic, Molecular and Optical Physics* **39**(21) R325–R377

[5] Fano U 1961 *Phys. Rev.* **124**(6) 1866–1878

[6] Raksštikas N and AKupliauskiene 1998 *Physica Scripta* **58** 587–594

[7] Kupliauskiene A 2001 *Journal of Physics B: Atomic, Molecular and Optical Physics* **34**(3) 345–361

[8] Lisini A, Burke P G and Hibbert A 1990 *Journal of Physics B: Atomic, Molecular and Optical Physics* **23**(21) 3767–3776

[9] Kupliauskiene A 1997 *Journal of Physics B: Atomic, Molecular and Optical Physics* **30**(8) 1865–1878

[10] Stoica S, Petrini D and Bely-Dubau F 1998 *Astronomy and Astrophysics* **334** L26–L28

[11] Petrini D and Silva E 1999 *Astronomy and Astrophysics* **348** 659–661

[12] Zhou H L, Manson S T, L V K *et al* 1999 *Phys. Rev. A* **59**(1) 462–476

[13] Holland D M P and Codling K 1981 *Journal of Physics B: Atomic and Molecular Physics* **14**(14) 2345–2351

[14] Lyon I C, Peart B and Dolder K 1987 *Journal of Physics B: Atomic and Molecular Physics* **20**(9) 1925–1932

[15] McGuinness C, O'Sullivan G, Carroll P K, Audley D and Mansfield M W D 1995 *Phys. Rev. A* **51**(3) 2053–2062

[16] Nikkinen J, Aksela H, Fritzsche S *et al* S 2005 *Phys. Rev. A* **72** 042706

[17] Nikkinen J, Aksela H, Heinäsmäki S *et al* 2005 *Physica Scripta* **T115** 119–121

[18] Ding X B and Dong C Z 2004 *Acta Physica Sinica* **53** 3326–3329

[19] Ding X B, Dong C Z and Fritzsche S 2004 *Acta Physica Sinica* **53** 2490–2495

[20] Dong C Z and Fritzsche S 2005 *Physical Review A* **72**(1) 012507 (pages 9)

[21] Huang W 2000 *Phys. Rev. A* **61**(6) 062505

Dielectronic Recombination of $\mathrm{Sn}^{5+} \sim \mathrm{Sn}^{13+}$ Ions

Yanbiao Fu[1], Chenzhong Dong[1], Maogen Su[1], Gerry O′Sullivan[2]

1) College of Physics and Electronic Engineering, Northwest Normal University, 730070, Lanzhou, China
2) School of Physics, University College Dublin, Belfield, Dublin 4, Ireland

e-mail: fuyb@nwnu.edu.cn

Abstract

Based on the Multi-configuration Dirac-Fock method, theoretical calculations have been performed for the dielectronic recombination (DR) rate coefficients of $\mathrm{Sn}^{5+} \sim \mathrm{Sn}^{13+}$ ions. It is found that the total DR rate coefficient has its maximum value between 10 eV and 100 eV and is greater than either the radiative recombination (RR) or three-body recombination rate coefficients (the number of free electrons per unit is $10^{21}cm^3$) for $\mathrm{Sn}^{7+} \sim \mathrm{Sn}^{13+}$ ions at T_e >10 eV. Therefore, DR can strongly influence the ionization balance of laser produced multi-charged tin ions.

Keywords: dielectronic recombination, rate coefficient, MCDF, EUV

1.Introduction

Dielectronic recombination is a basic atomic process in electron-ion collisions. Accurate DR cross sections and rate coefficients are essential for studying the ionization balance of highly ionized ions in hot plasmas and calculating populations of lasing levels in research of x-ray lasers[1,2,3]. In recent years, extreme ultraviolet (EUV) sources has been extensively studied for next generation lithography. Laser-produced multi-charged tin ions are regarded as one of hopeful candidates for such EUV emission[4-8]. Observations and calculations have shown that very bright emission lines from Sn^{7+} to Sn^{12+} ions lie in the region of interest[9] . However, to our knowledge, little work has been reported on dielectronic recombination rate coefficients for tin ions up to now. In order to consider the influence of DR on the ionization balance of tin ions, as an example, this work presents a first calculation on the dielectronic recombination rate coefficient of Sn^{5+} to Sn^{13+} ions using the Flexible Atomic Code (FAC) [10] .

2. Theoretical method

The dielectronic recombination rate coefficients from initial state i $(4p^64d^m)$ to radiative final state k $(4p^64d^mnl)$ through resonant doubly excited state j $(4p^64d^{m-1}4fnl$ or $4p^54d^{m+1}nl)$, for electrons in the Maxwellian distribution, can be expressed as [3]

$$\alpha_{DR}(i,j,k;T_e) = (\frac{h^2}{2\pi m_e k_B T_e})^{3/2}\frac{1}{2g_i}\frac{g_j A^a_{ji}A^r_{jk}}{\sum_{k'}A^r_{jk'}+\sum_{i'}A^a_{ji'}}exp(-\frac{E_{ji}}{k_B T_e}), \qquad (1)$$

where T_e is the electron temperature, m_e is the electron mass, h is Plank constant, k_B is Boltzmann constant, g_i is the statistical weight of the state i, E_{ji} is the resonance energy. In practical calculations, the l_{max} is assumed as $(n-1)$ for $n < 8$ and 7 for $n > 7$. The effects of configuration interaction (CI) on considered by including $4p^5 4d^{m+1} nl$ and $4p^6 4d^{m-1} 4fnl$ doubly excited states. For comparison, the radiative recombination rate coefficient and three-body recombination rate coefficient, which are also two important recombination processes in plasmas, are estimated simply by Eq.(2) and Eq.(3) as used in Ref. [11].

$$\alpha_{RR} = 5.2 \times 10^{-14} (\phi/T_e)^{1/2} Z [0.429 + \frac{1}{2} \lg(\phi_Z)/T_e + 0.469(T_e/\phi_Z)], \tag{2}$$

$$n_e \alpha_{3b} = n_e \times 2.97 \times 10^{-27} (\xi_Z/T_e) \phi_Z^2 (4.88 + T_e/\phi_Z), \tag{3}$$

where ϕ_Z is the ionization potential and ξ_Z is the number of electrons in the outermost shell corresponding to the state of charge Z, n_e is the number of free electrons per unit volume.

3. The dielectronic recombination rate coefficients of Sn ions

The calculated DR rate coefficients of Sn^{10+} ions are given in figure 1. It can be seen that DR for $n = 4, 5$ gives an important contribution at low temperature. The values of the total DR rate coefficients are maximum between 10 eV and 100 eV. Although the contributions from $n > 5$ decrease as n increases, their sum is more than the contributions from $n = 5$, and from figure 1 it is also seen that the contributions from $n > 15$ should not be neglected. This conclusion is quite similar to the case of Xe^{10+} ions [12].

In figure 2, the DR rate coefficients, RR rate coefficients and three-body recombination rate coefficients of Sn^{10+} ions are further shown. In our calculations, the number of free electrons per unit volume is assumed as $10^{21} cm^{-3}$, the critical density for Nd:YAG laser irradiation. It can be seen that the DR rate coefficients are great than the RR rate coefficients and three-body recombination rate coefficients for $T_e >$1 eV.

Figure 3 and 4 show the DR rate coefficients, RR rate coefficients and three-body recombination rate coefficients of $\mathrm{Sn}^{5+} \sim \mathrm{Sn}^{8+}$ and $\mathrm{Sn}^{9+} \sim \mathrm{Sn}^{13+}$ ions respectively. It can be seen that the values of the total DR rate coefficients have maximum between 10 eV and 100 eV just same as Sn^{10+} ions. The DR rate coefficients are greater than the RR rate coefficients and three-body recombination rate coefficients for $\mathrm{Sn}^{7+} \sim \mathrm{Sn}^{13+}$ ions at $T_e >$10 eV and for $\mathrm{Sn}^{8+} \sim \mathrm{Sn}^{13+}$ ions at $T_e >$2 eV. Clearly, DR can greatly influence the ionization balance of laser-produced multi-charged Sn ions.

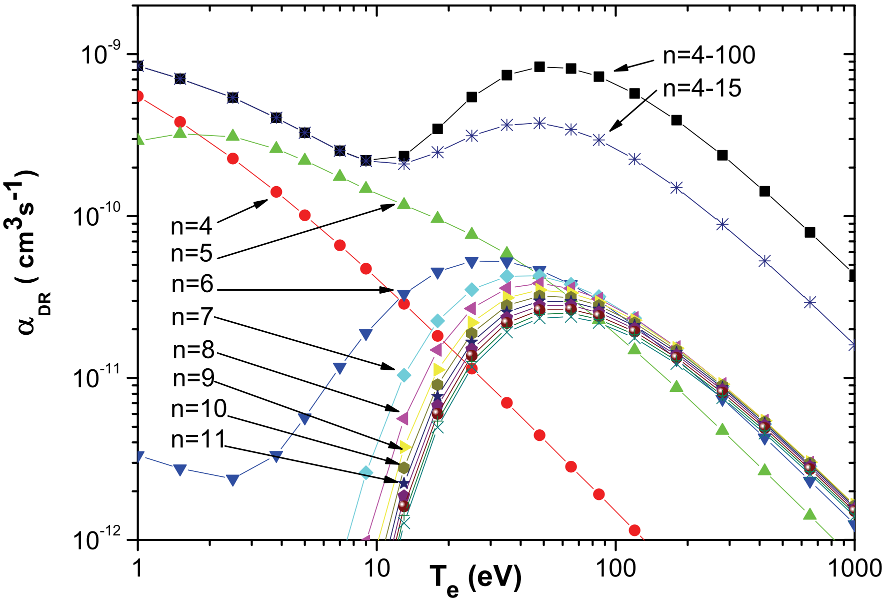

Figure 1: DR rate coefficients of Sn^{10+} ions.

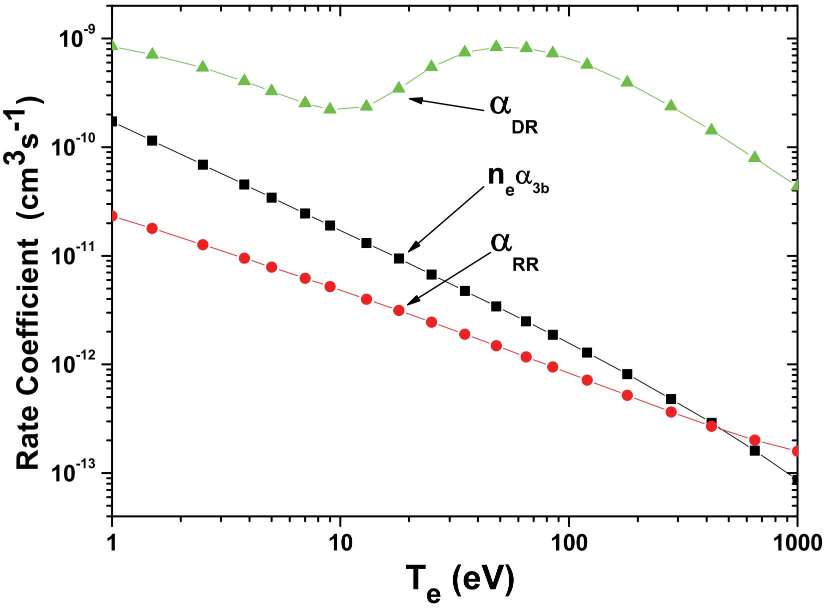

Figure 2: DR , RR and three-body recombination rate coefficients of Sn^{10+} ions.

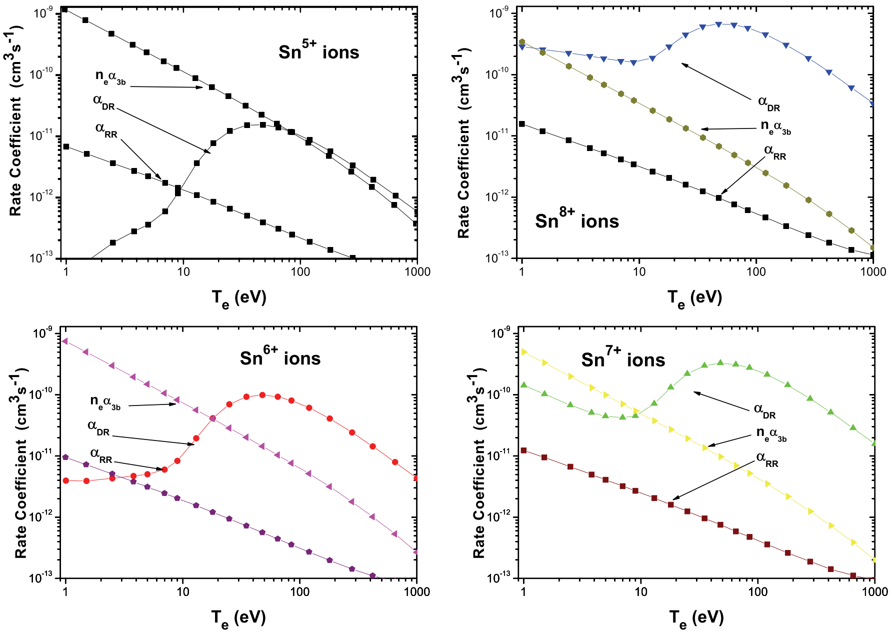

Figure 3: DR , RR and three-body recombination rate coefficients of Sn^{5+} $\sim$ Sn^{8+} ions.

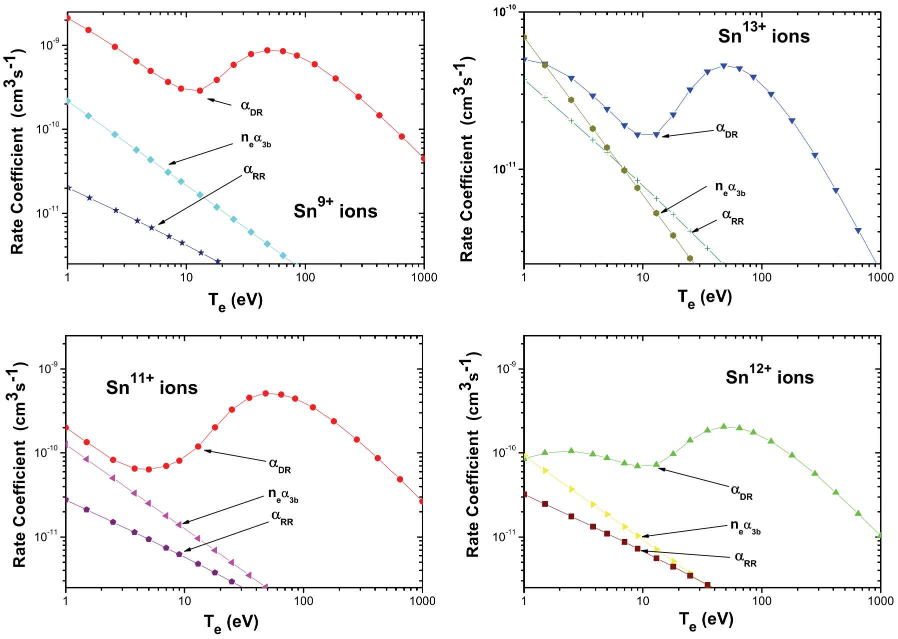

Figure 4: DR , RR and three-body recombination rate coefficients of $\mathrm{Sn}^{9+}\sim\mathrm{Sn}^{13+}$ ions.

3. Conclusions

In summary, based on the multi-configuration Dirac-Fock method, theoretical calculations have been made for the dielectronic recombination rate coefficients of $\mathrm{Sn}^{5+} \sim \mathrm{Sn}^{13+}$ ions using FAC. The results showed that the values of the total DR rate coefficients are maximum between 10 eV and 100 eV and can greatly influence the ionization balance of laser-produced multi-charged Sn ions.

Acknowledgements

This work was supported by the SFI/RIA China-Ireland Research Collaboration Fund(CI-2004-07), the National Natural Science Foundation of China (Grant No.10434100, 10774122), the Core-University Program between Japanese Society of Promotion of Science and Chinese Academy of Sciences, the Specialized Research Fund for the Doctoral Program of Higher Education of China (Grant No. 20070736001), the Foundation of Center of theoretical Nuclear Physics of National Laboratory of Heavy Ion Accelerrator of Lanzhou, and the Foundation of Northwest Normal University(NWNU-KJCXGC-03-21).

References

[1] P. Mazzotta, G. Mazzitelli, S. Colafrancesco, and N. Vittorio, Astron. Astrophys. Suppl. Ser., **133**, 403 (1998).
[2] S. M. V. Aldrovandi and D. Pequignot, Astron. and Astrophys., **25**, 137 (1973).
[3] M. Y. Song and T. Kato, JKPS, **49**, S374 (2006).
[4] G. O'Sullivan, R. Faulkner, Opt. Eng., **33**, 3978 (1994).
[5] A. Sasaki, K. Nishihara, F. Koike, T. Kagawa, T. Nishikawa, K. Fujima, T. Kawamura, H. Furukawa, IEEE J. Quantum Electronics, **10**, 1307 (2004).
[6] RC. Spitzer, TJ. Orzechowski, DW. Phillion, RL. Kauffman, C. Cerjan, J. Appl. Phys., **79**, 2251 (1996).
[7] P. Jansson, B. Hansson, O. Hemberg, M. Otendal, A. Holmberg, Applied Physics Letters, **84**, 2256 (2004).
[8] T. Aota, T. Tomie, Phys. Rev. Lett., **94**, 015004 (2005).
[9] J. White, P. Hayden, P. Dunne, A. Cum-mings, N. Murphy, P. Sheridan and G. O'Sullivan, J. Appl. Phys., **98**, 113301 (2005).
[10]M. F. Gu, Astrophys. J., **590**, 1131 (2003).
[11]D. Colombant and G. F. Tonon, J. Appl. Phys., **44**, 3524 (1973).
[12]M. Y. Song and T. Kato, NIFS-DATA, **94**, 1 (2005).

Study on the Properties of Rydberg States of Lithium in a Static Electric Field by B-spline Functions

Yonglin He, Xiaoxin Zhou and Xiaoyong Li
College of Physics and Electric Engineering, Northwest Normal University, Lanzhou 730070, China
e-mail: zhouxx@nwnu.edu.cn

Abstract

The B-spline expansion technique and the method of model potential of atom have been applied to study the properties of Rydberg states of lithium. Our results for Stark maps, oscillator strength distributions for Li are in good agreement with other reported theoretical calculations and experimental measurement. It shows that the method we used can be applied to investigate the properties of alkali-metal atoms in external static electric field. Finally, we obtain the evolution of the oscillator strength spectrum and Shannon Entropy of Li with the different static electric fields.

Keywords: B-spline function, Stark maps,Oscillator strength, Shannon Entropy

1.Introduction

With the development of laser techniques, great interest has been paid to the behaviors of highly excited atoms in the presence of electric fields. People can obtain state-selective Rydberg atoms and monitor the excited-state population. The measurement and analysis of the interactions of highly excited Rydberg atoms with electric fields has been widely reported[1,2,3]. The theoretical calculations may support the experimental data and provide a physical insight into the experimental phenomenon. One should calculate different relevant atomic properties in the presence of the static electric field, such as level splitting picture, oscillator strength distribution, lifetime, positions and widths of avoided crossings, field ionization threshold and so on.

The B-spline expansion technique and the method of model potential of atom[4,5] have been applied to study the properties of Rydberg states of lithium. Our results for Stark maps, oscillator strength distributions, avoided crossing positions and widths for Li are in good agreement with other reported theoretical calculations and experimental measurement[1,6,7]. It shows that the method we used can be applied to investigate the properties of alkali-metal atoms in external static electric field.

2. Stark maps

Li atom Stark maps are calculated. The result in the neighborhood of n=15 are presented in Fig.1. Our calculated results are excellent agree with those of experimental and theoretical results by Zimmerman[1]. The results of $|m|$=0 in Fig.1 show a striking contrast to hydrogentic features. Differently, the results of $|m|$=1 show a typical hydrogenic features, they have approximately linear Stark shifts.As a qualitative analysis, the avoided crossings for $|m|$=1 are obviously weaker than the avoided crossings for m=0. The only difference between lithium's Stark structure($|m|$=1) and hydrogen is the nondegeneracy in the ”p” state of Li at zero field strength.

3. Oscillator strength

The present theoretical spectrum of atom Li belonging to the absorption transition $|3s >\rightarrow |n, n_1, n_2, 0 >$in the form of the component oscillator strength for different electric field strength, are

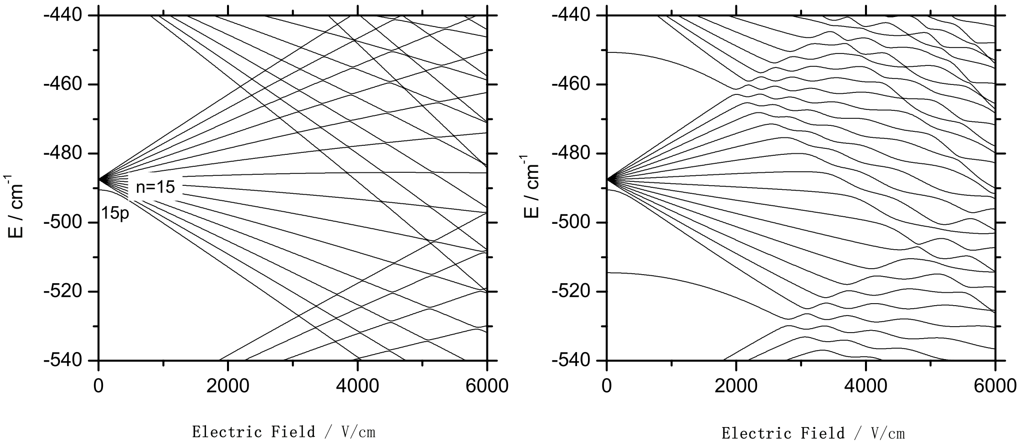

Figure 1: Stark maps of Lithium with n=15,$|m|$=1(left) and $|m|$=0(right).

plotted in Fig.2. Obviously, the oscillator strength spectrum is very regular if the magnitude of electric field is 1500v/cm, and there are some characteristic like periodicity. With the increasing of the magnitude of electric field, the characteristic of periodicity is gradually destroyed. The oscillator strength spectrum is very chaotic if the magnitude of electric field is 3500v/cm, the reason is that with the increasing of the magnitude of electric field, the mixing between different n branches gradually become strong. From the Fig.2, we could easily realize the characteristic of the mixing between different n branches. It also tell us that the component oscillator strength to the (14,0) state takes up the largest proportion of oscillator strength until the magnitude of electric field is 3500 v/cm. The reason is that there is no n-mixing for the (14,0) state even the magnitude of electric field reached 3500 v/cm. But one could easily realize that the case for the (15,13) state is not like that. The component oscillator strength to the (15,13) state takes up the largest proportion of oscillator strength when the electric field F is 1500 v/cm. With the increasing of electric field, n-mixing gradually appears. The larger the electric field F, the less proportion of oscillator strength the (15,13) state takes up. Finally, the characteristic of large oscillator strength to the (15,13) state disappear. With the strengthen of n-mixing, the redistribution of the oscillator strength component along the substates of the Stark branch gives rise to the possibility of excitations from the $|3s>$ state that are not allowed by the Laporte selection rule. The result is that the Laporte selection rule is not come into existence for atom in static electric field. Another characteristic in Fig.2 is that the positions of the oscillator spectrum are removed when the electric field F is changed, that is a result of the Stark effect.

4. Shannon Entropy

The evolvement of Shannon Entropy for Rydberg States of Lithium in static electric field is investigated in Fig.3. The fact that there is a point of intersection for Shannon Entropy as the static electric field strength is varied across the region where an avoided crossing occurs indicates the informational

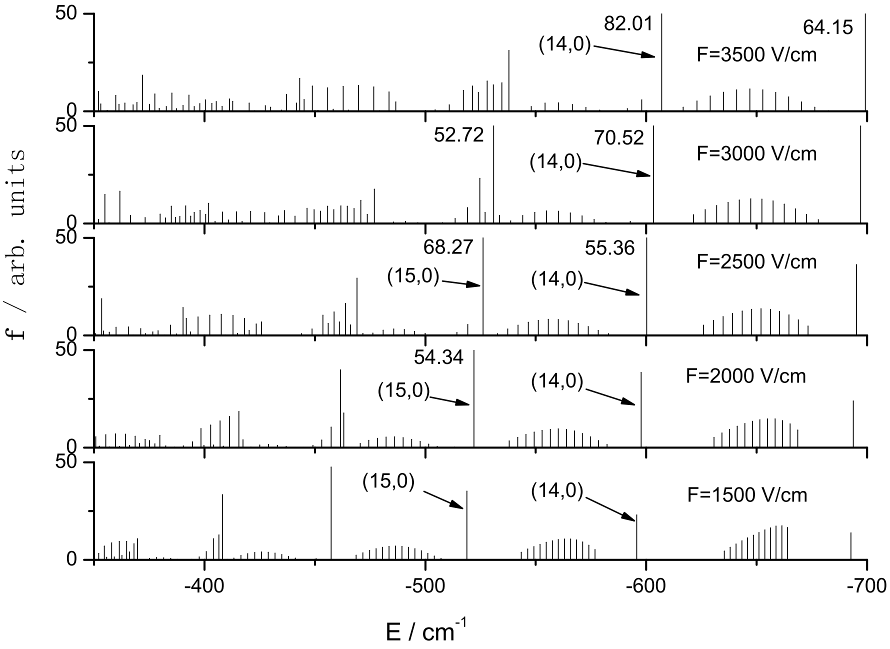

Figure 2: The evolvement of the spectrum of oscillator strength of Li, the electric field strength F are chosen from 1500 v/cm to 3500 v/cm.

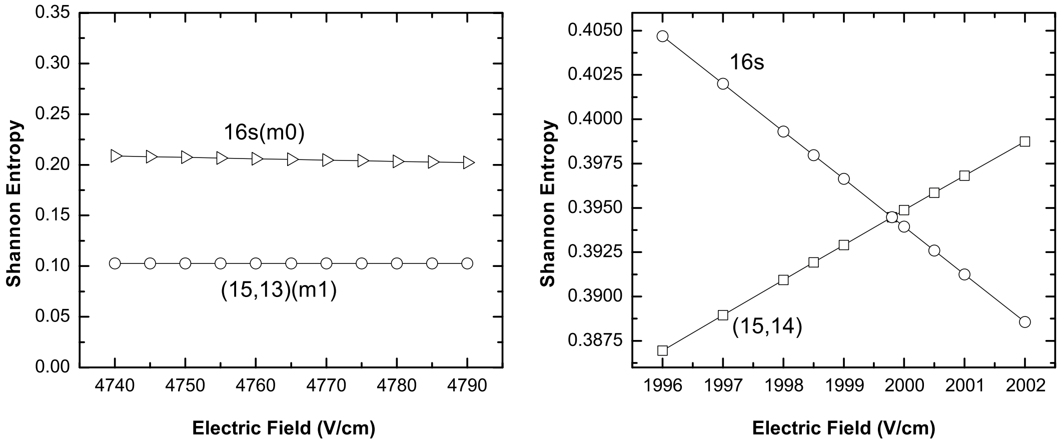

Figure 3: The evolvement of Shannon Entropy for 16s ($|m|$=0) and ((15,13), ($|m|$=1)) as the static electric field strength is varied across the region where an level crossing occurs(left); The same for 16s($|m|$=0) and ((15,14), ($|m|$=0)) as the static electric field strength is varied across the region where an avoided crossing occurs(right).

exchange of the two involved states. For level crossing, there is no point of intersection, no information exchange and no interaction between the two involved states. The result indicates that the Shannon Entropy is an indicator or predicator of the level crossing and avoided crossing for Lithium Rydberg States in static electric field, our conclusions is consistent with that of González-Férez[8] for hydrogen in the presence of parallel magnetic and electric fields. Note that we only investigate the region where an avoided crossing (level crossing) occurs. A more systematic study is required.

5. Conclusions

We have ignored the spin-orbit interaction in this paper, given the fact that the F-S interaction is too small for light atoms, the result presently obtained for Stark maps and the oscillator strength spectrum agree well with other calculations and experiment[1,6]. The accuracy of the B-spline expansion method and the potential model given by Marinescu[9] is further tested. Specially, to our knowledge, we obtain the evolvement of the spectrum of oscillator strength and the Shannon Entropy of Li in static electric field for the first time. This has encouraged us to undertake the study of other characteristics of atom in a static electric field such as the process of field ionization, the problem of atom in microwave field and some others, which are in progress.

Acknowledgements

This work is supported by the National Natural Science Foundation of China (No. 10674112), the Natural Science Foundation of the Gansu Province, (No. 3ZS061-A25-013) and the Foundation of Education Department of Gansu Province (No. 0601-23).

References

[1] M. L. Zimmerman, M. G. Littman, et al., Phys. Rev. A, **22** 2251 (1979).
[2] R. C. Stoneman, G. Janik and T. F. Gallagher, Phys. Rev. A, **34** 2952 (1986).
[3] Y. Li, and B. W. Li, J. Phys. B, **30** 547 (1997).
[4] C. Jin, X. X. Zhou and S. F. Zhao, Commun. Theor. Phys, **44** 1065 (2005).
[5] C. Jin, X. X. Zhou and S. F. Zhao, Commun. Theor. Phys, **47** 119 (2007).
[6] J. M. Menndez, I. Martn, and A. M. Velasco, J. Chem. Phys, **119** 12926 (2003).
[7] J. M. An and G. H. Zhou , J. At. Mol. Phys, **15** 407 (1998).
[8] R. González-Férez and J. S. Dehesa, Phys. Rev. Lett, **91** 113001 (2003).
[9] M. Marinescu, H. R. Sadeghpour, and A. Dalgarno, Phys. Rev. A, **49** 982 (1994).

Electron Correlation effects on the Hyperfine Induced ^{47}Ti^{18+} (2s2p ^{3}P$_0$ → 2s^2 ^{1}S$_0$) Transition Probability

Jiguang Li[1], Gediminas Gaigalas[2, 3], Chenzhong Dong[1, 4 †]

1). *College of Physics and Electronic Engineering, Northwest Normal University, Lanzhou 730070, China*
2). *Department of Physics, Vilnius Pedagogical University, Studentu 39, Vilnius LT-08106, Lithuania*
3). *Institute of Theoretical Physics and Astronomy, A. Goštauto 12, Vilnius LT-01108, Lithuania*
4). *National Laboratory of Heavy Ion Accelerator of Lanzhou, Lanzhou 730000, China*
† *e-mail: dongcz@nwnu.edu.cn*

Abstract

We calculated the hyperfine induced transition probability for ^{47}Ti^{18+} (2s2p ^{3}P$_0$ → 2s^2 ^{1}S$_0$) and analysed the influence of the electron correlation effects in order to interpret the reason for a large difference between existing experimental value and previous only one theoretical result with neglected electron correlation effects. An improved result A_{HFI}=0.3708 s^{-1} was obtained.

Keywords: hyperfine induced transition, hyperfine interaction, electron correlation effect, MCDF method

1.Introduction

Hyperfine interactions origin from magnetic field and nonspherical symmetric electric field of nuclei and are related to both atomic and nuclear properties [1]. Therefore, hyperfine interactions build a bridge between atomic physics and nuclear physics. In general instance, because the hyperfine interactions cause the coupling between the electronic angular momentum J and nuclear angular momentum I to a total angular momentum $F = I + J$, both the electronic angular momentum and the nuclear angular momentum are not good quantum numbers and different atomic state wavefunction with different electronic angular momentum are mixed. Then, some radiative transitions can be induced, such as $J = 0 \rightarrow J' = 0$ (usually viewed as allowed through two-photon decay). Therefore, the lifetime, especially for the metastates of atom with $I \neq 0$, may be affected strongly and dependent on the nuclear properties. The study on hyperfine induced transition (HFI) are attractive in view of more subtle understanding electron correlation and relativistic effects, testing theory of atomic structure and standard model [2], obtaining ultraprecise atomic clocks [3], realizing novel types of cold atomic gases, determining relative isotope and nuclear properties and diagnosing the properties of low-density plasma [4] and so on.

Recently the hyperfine induced transition probability of 2s2p ^{3}P$_0$ → 2s^2 ^{1}S$_0$ for Be-like ^{47}Ti^{18+} ion has been measured using resonant electron-ion recombination method in a heavy-ion storage ring TSR of the Max-Planck Institute for Nuclear Physics, Heidelberg, Germany [5]. However, the experimental value $A_{HFI} = 0.56(3)s^{-1}$ is almost 60% larger than only one theoretically predicted from Marques *et al.* [6]. In experimenter's opinion, the important error come form the neglected electron correlation effects.

In this paper, we studied the influence of the electron correlation effects on the electric dipole matrix elements and hyperfine interaction constants in detail, which are need in calculation of hyperfine induced transition probability, and show the significant core-valence and core-core correlation effects. The hyperfine induced transition probability are calculated using the latest program[7].

2.Theoretical Method

The Hamiltonian for the hyperfine interactions can be represented by a multipole expansion [1]

$$H_{HFS} = \sum_{k\geq 1} \mathbf{T^{(k)}} \cdot \mathbf{M^{(k)}}, \tag{1}$$

where $\mathbf{T^{(k)}}$ and $\mathbf{M^{(k)}}$ are spherical tensor operators of rank k in the electronic and nuclear spaces, respectively. The $k = 1$ term of the expansion represents the magnetic dipole interaction and the $k = 2$ term the electric quadrupole interaction.

The hyperfine interaction couples the nuclear I and electronic J angular momenta to a total momentum $F = I + J$, and only F and M_F are good quantum number, the wavefunction of atomic system can be represented by

$$|\alpha F M_F\rangle = \sum_{\alpha,J} (\sum_{M_I} \sum_{M_J} b_i |\alpha J M_J\rangle |I M_I\rangle). \tag{2}$$

where $|\alpha J M_J\rangle$ is pure atomic state function (ASF) and $|I M_I\rangle$ is pure nuclear state function. Here we assume the state of nuclear does not change and can be describe as spin I and M_I.

When the off-diagonal hyperfine interaction is weak, that is, the interaction between I and J is small in magnitude and these angular momenta remain well-defined in magnitude even though not in direction, which is called the weak coupling case, the wavefunctions of the coupled states can be approximately written as,

$$|\alpha I J F M_F\rangle = \sum_{M_I, M_J} (-1)^{J-I+M_F} (2F+1)^{-1/2} \begin{pmatrix} J & I & F \\ M_J & M_I & -M_F \end{pmatrix} |\alpha J M_J\rangle |I M_I\rangle, \tag{3}$$

which is also called the zero-order wavefunction.

Using eq.(3) the eq.(2) can be represented as,

$$|\alpha F M_F\rangle = \sum_{\alpha,J} h_{\alpha,J} |\alpha IJFM_F\rangle. \tag{4}$$

where $h_{\alpha,J}$ is the hyperfine mixing coefficients.

Hyperfine level energies and the hyperfine mixing coefficients $h_{\alpha,J}$ can be obtained by means of diagonalizing matrix of the full Hamiltonian $H = H_{FS} + H_{HFS}$. H_{FS} is usual electrons' Hamiltonian. The matrix elements for hyperfine interactions Hamiltonian H_{HFS} can be written as

$$\begin{aligned} W_{M1}(J,J') &= (-1)^{I+J'-F}[(2J+1)(2I+1)]^{1/2} W(IJ'IJ;F1) \times \\ &\quad \langle \alpha J||\mathbf{T}^{(1)}||\alpha' J'\rangle \langle I||\mathbf{M}^{(1)}||I\rangle, J' = J, J\pm 1, \qquad (5) \\ W_{E2}(J,J') &= (-1)^{I+J'-F}[(2J+1)(2I+1)]^{1/2} W(IJ'IJ;F2) \times \\ &\quad \langle \alpha J||\mathbf{T}^{(2)}||\alpha' J'\rangle \langle I||\mathbf{M}^{(2)}||I\rangle, J' = J, J\pm 1, J\pm 2, \qquad (6) \end{aligned}$$

where $W(IJ'IJ;F1)$ and $W(IJ'IJ;F2)$ are Racah's coefficients. $J' = J$ and $J' \neq J$ represent diagonal and off-diagonal hyperfine interaction energies, respectively. The nuclear tensor operator $\mathbf{M}^{(k)}$ are related to the conventional nuclear magnetic dipole moment μ_I and electric quadruple moment Q_I through the relations

$$\begin{aligned} \mu_I &= \begin{pmatrix} I & 1 & I \\ -I & 0 & I \end{pmatrix} (2I+1)^{1/2} \langle I||M_0^{(1)}||I\rangle, \qquad (7) \\ Q_I &= 2\begin{pmatrix} I & 2 & I \\ -I & 0 & I \end{pmatrix} (2I+1)^{1/2} \langle I||M_0^{(2)}||I\rangle. \qquad (8) \end{aligned}$$

Once the hyperfine level energies and corresponding wavefunctions are obtained, we can further calculate the hyperfine transition probability for an electric dipole by [8, 9]

$$\begin{aligned} A(F-F') &= \frac{2\omega}{3c} |\sum_{\alpha,J}\sum_{\alpha,J'} h_{\alpha,J} h_{\alpha',J'} \langle \alpha IJF|O^{(1)}|\alpha' IJ'F'\rangle|^2 \\ &= \frac{2\omega}{3c}(2F'+1)|\sum_{\alpha,J}\sum_{\alpha',J'} h_{\alpha,J} h_{\alpha',J'} \begin{Bmatrix} J & I & F \\ F' & 1 & J' \end{Bmatrix} \langle \alpha J||O^{(1)}||\alpha' J'\rangle|^2 \end{aligned} \tag{9}$$

where ω is hyperfine splitting energy and $\langle \alpha J||O^{(1)}||\alpha' J'\rangle$ is the electric dipole reduced matrix element.

3. Results

To reflect the electron correlation effects, different calculational models were employed in our investigation, i.e.,

1. SC: Single-Configuration,
2. nSD: formed by single and double substitutions of valence electrons (the valence electrons are $2s^2$ for ground state and 2s2p for excited state) to the nth shell (the 6th shell only including 6s, 6p, 6d);
3. CP: including single electron substitutions of core electrons ($1s^2$);
4. CC: including single and double substitutions of core electrons;
5. Breit: Breit interactions;
6. QED: vacuum polarization.

In Fig1-2 the effects of electron correlation, Breit interaction and QED effects on level energies, the electric dipole transition-matrix elements and hyperfine interaction constants which are very important for calculating hyperfine induced transition are shown. It is found from those picture that core-valence and core-core correlation effects are indispensable, especially for hyperfine interaction constants.

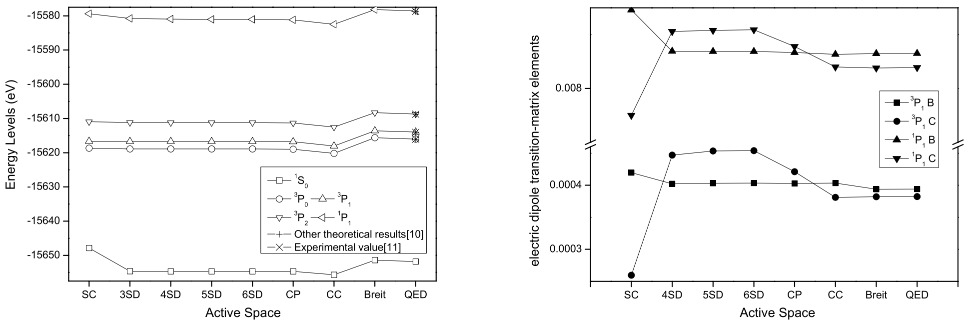

Fig.1 Level energies and electric dipole matrix elements calculated in different calculational model.

On the basis of these results, the calculated hyperfine induced transition probability is 0.3708 s^{-1}[1]. The results improve on other theoretical value due to considering the important electron correlation effects. However, the difference between theory and experiment is still exist and need to be studied further.

4. Conclusion

In this paper, we shown the important electron correlation effects on the level energies, electric dipole matrix element and hyperfine interaction constants for Be-like Ti ion.

---

[1] the nuclear magnetic dipole moment and electric quadruple moment come form Ref[9]

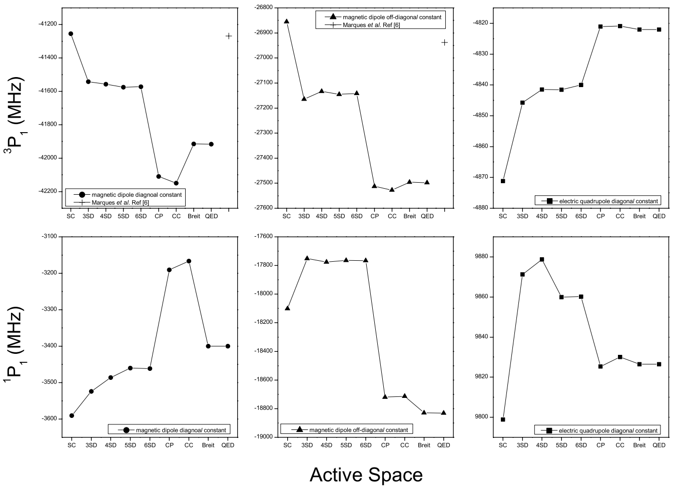

Fig.2 The hyperfine diagonal and off-diagonal constants in different calculational model.

Although we obtained improved result, the difference between experimental value and present theoretical result is still exist. Further study is necessary.

Acknowledgement

One of the author (Jiguang Li) would like to thank Mr Ding for comments on the manuscript. This work was supported by the National Natural Science Foundation of China (Grant No.10434100, 10774122), the Core-University Program between Japanese Society of Promotion of Science and Chinese Academy of Sciences, the Specialized Research Fund for the Doctoral Program of Higher Education of China (Grant No. 20070736001), the Foundation of Center of theoretical Nuclear Physics of National Laboratory of Heavy Ion Accelerrator of Lanzhou, and the Foundation of Northwest Normal University(NWNU-KJCXGC-03-21).

References

[1] L. Aemstrong, Theory of the Hyperfien Structure of Free Atoms, first ed., Wiley-Interscience, New York, 1971.

[2] S. C. Bennett, C. E. Wieman, Phys. Rev. Lett. **82** (1999) 2484.

[3] Masao Takamoto, Hidetoshi Katori, Phys. Rev. Lett. **91** (2003) 223001.

[4] Tomas Barge, Philip G. Judge, Abdellatif Aboussaïd, *et al.*, The Astrophysical Journal **500** (1998) 507.

[5] S. Schippers, E. W. Schmidt, D. Bernhardt, *et al.*, Phys. Rev. Lett. **98** (2007) 033001.

[6] J. P. Marques, F. Parente and P. Indelicato, Phys. Rev. A **47** (1993) 929.

[7] Jiguang Li, Gediminas Gaigalas and Chenzhong Dong, Comput. Phys. Commun. (in preparation).

[8] Martin Andersson, Per Jönsson and Hans Sabel, J. Phys. B **39** (2006) 4239.

[9] Robert D. Cowan, The Theory of Atomic Structure and Spectra, University of California Press, Berkeley, CA, 1981.

[10] M. S. Safronova, W. R. Johnson and U. I. Safronova, Phys. Rev. A **53** (1996) 4036.

[11] J. Sugar and C. Corliss, J. Phys. Chem. Ref. Data **14** Suppl. (1985) 2 .

[12] N. J. Stone, Atomic Data and Nuclear Data Tables **90** (2005) 75.

Effects of the Model Potential on Two-color Multiphoton Ionization of Atoms by an Intense Laser Field and One of Its Harmonics

P.C. Li, and X.X. Zhou

College of Physics and Electronic Engineering,Northwest Normal University,Lanzhou 730070,China

e-mail: lipc@nwnu.edu.cn

Abstract

We present the theoretical investigation of the effects of the model potential on two-color multiphoton ionization of atoms by solving the time-dependent Schrödinger equation of a one-dimensional model atom. We choose two different model potentials with the same ground-state energy: one is long-range(Coulomb-like), and the other is short-range(with no excited state). Some effects are observed by two-color photoionization spectra and ionization process for two different model potential. It is found that the magnitudes of the photoelectron peaks depend on the choice of the model potential, and different model potential can lead to different dynamics of the ionization of atoms.

Keywords: model potential, multiphoton ionization, intense laser field

1. Introduction

In the past decades, the study of the interaction of atoms with intense laser fields led to a comprehensive understanding of the nonlinear physics in the underlying dynamics of the ionization of atoms[1]. In particular, the simultaneous application of radiation of two different frequencies has led to interesting new phenomena in multiphoton ionization of atoms[$2-4$], and attracted many experimental and theoretical investigations. In the experimental study of two-color above-threshhold ionization(ATI) of atoms by Muller et al[5]. In the theoretical aspects, the multiphoton ionization in two-color laser fields has developed rapidly. For example, G.G.paulus et al.[6] have studied the effects of the classical rescattering on two-color ATI, R.M.Potvliege et al.[7] have discussed the multiphoton ionization of hydrogen by an intense laser field and one of its harmonics, V.Véniard et al.[8] have studied the laser-assisted single-photon ionization (LASPI) process in a strong low-frequency laser field and its high-order harmonic. All of these works, from both experiment and theory, have been demonstrated the features of the two-color multiphoton ionization and responding physical processes, and attempted to interpret the effects of the occurrence of physical processes on two-color multiphoton ionization. Fortunately, it is realized that these effects could be related to the structure of the atomic system considered.

Recently, C.Figueira de Morisson Faria et al.[9] have investigated the influence of the binding potential on the ATI of atoms. The numerical simulations were performed by choosing two classes of one-dimensional model potential, one is long-range, with a Coulomb tail, and the other is short-range, with an exponential decay. Therefore, we will choose two types of model atomic potentials commonly used in the studies on two-color multiphoton ionization. The main difference lies that our two types of model atomic potential have a uniform ground-state energy, which is convenient to compare the effects of different binding potential on the multiphoton ionization, furthermore we will consider two-color case, not a single color as mentioned above.

2. Theoretical Method

For a one-dimensional model atom under the influence of the time-dependent external laser fields, the dynamical behavior of laser-atom interaction can be described by the TDSE. In the dipole approximation, it is given by(atomic units are used throughout this paper)

$$i\frac{\partial\psi(x,t)}{\partial t} = [H_0 + xE(t)]\psi(x,t), \tag{1}$$

where H_0 is the one-dimensional atomic Hamiltonian, which is given by

$$H_0 = -\frac{1}{2}\frac{\partial^2}{\partial x^2} + V(x). \tag{2}$$

Here $V(x)$ is atomic potential. In order to model the influence of the potential on the coherent control of atomic MPI in the external laser fields, we have chosen two different model potentials: one is long-range potential[10], which is given by

$$V(x) = -\frac{1}{\sqrt{a+x^2}}, \tag{3}$$

where the choice of parameters $a = 2.0$, the ground-state energy is $E_0 = -0.5$ a.u. It behaves asymptotically as a one-dimensional Coulomb potential and supports an infinite number of bound states. And the other is short-range potential[11] with an exponentially decreasing tail, supporting only finite numbers of bound states. It is given by

$$V(x) = -bexp(-\frac{x^2}{c}), \tag{4}$$

where $b = 1.986$ and $c = 1.202$, there is only one bound state with energy $E_0 = -0.5$ a.u., i.e., the same as for the long-range potential discussed above.

For external laser fields, we choose a combination of a laser field and its seventh-order harmonics field,

$$E(t) = F_L sin(\omega_L t) + F_H sin(\omega_H t + \phi), \tag{5}$$

where F_L and F_H are the field amplitudes for the fundamental and seventh-order harmonics,respectively; ω_L and ω_H(with ω_H=7ω_L) are the corresponding frequencies; ϕ is the relative phase between the two fields.

To find the energy spectra of the ionized photoelectrons, let the evolved wave function be overlapped with the continuum-energy eigenstates. we define the photoelectron spectra as[12]

$$P(\frac{E_{n-1} + E_n + E_{n+1} + E_{n+2}}{4}) = \frac{|<\varphi_n(x)|\psi(x,T)>|^2}{E_{n+1} - E_{n-1}} + \frac{|<\varphi_{n+1}(x)|\psi(x,T)>|^2}{E_{n+2} - E_n}, \tag{6}$$

where $\psi(x,T)$ is the wave function at the end time of the laser pulse, E_n and $\varphi_n(x)$ are energy eigenvalues and eigenvectors of the one-dimensional atomic Hamiltonian H_0.

3. Effects of the Model Potential on Two-color Photoelectron Spectra

We calculate atomic two-color photoelectron spectra for the long-range potential Eq.(3) and short-range potential Eq.(4), respectively. The results are illustrate in Fig.1. Here, we consider the radiation pulses containing the fundamental frequency ω_L=0.1a.u. and its 7th harmonic with ω_H=0.7a.u., lying well in the ultraviolet range. The harmonic field intensity F_H=0.0675a.u. and F_L=0.021a.u.

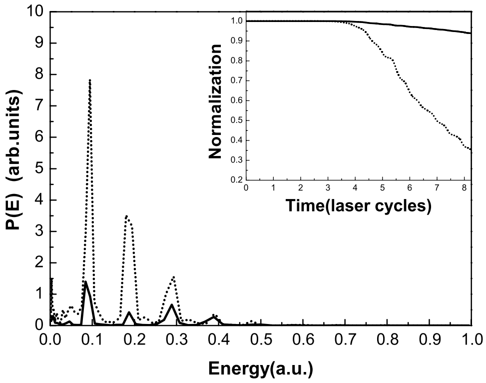

Fig.1 Comparisons two-color photoelectron spectra for the long-range potential Eq.(3)(solid line) and short-range potential Eq.(4)(dot line). The inset window shows the corresponding ionization yields.

It can be seen from Fig.1, the whole magnitudes peak of the short-range potential is higher than long-range potential. This is because ionization yields are different for the two different model potentials. For the short-rang potential, the ionization yield with the laser cycles is always higher than long-range potential's. This is illustrated in the inset window. On the other hand, we note that, every photoelectron peak for the two different model potentials is located at the same position. Actually we have obtained photoelectron spectra here, representing the LASPI is dominated process, the reason will be discuss in the following. According to the energy-conserving relation[13]

$$\varepsilon_n \approx \omega_H + n\omega_L - \mid E_0 \mid - U_p, \tag{7}$$

where E_0 is the ionization energy for the ground state, and U_p=$F_L^2/4\omega_L^2$ is the ponderomotive energy, it can be seen that Eq.(7) describes the process in which one high-frequency photon ω_H is absorbed causing ionization, and then n low-frequency photons are absorbed or emitted (for n positive or negative), causing the redistribution of the continuum states. It is just because the same ground state energy for long-rang potential and short-rang potential, therefore, the photoelectron peak is almost exactly located at ε_{-1}=0.09a.u., ε_0=0.19a.u., ε_1=0.29a.u., ε_2=0.39a.u., etc, and the energy interval of the peaks ω_L=0.1a.u.

4. Effects of the Model Potential on Two-color Ionization Process

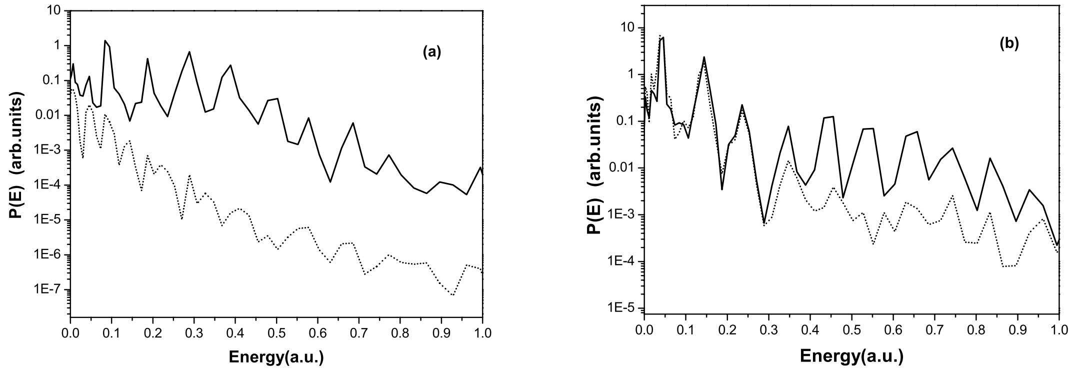

Fig.2 Effects of the high-order harmonic radiation on the photoelectron spectra for long-range potential, in the same conditions as in Fig.1. (a) F_L=0.021a.u. solid line, F_H=0.0675a.u; dot line,F_H=0. (b) Same as (a), with $F_L = 0.044$a.u.

To discuss the effects of the high-order harmonic radiation on ionization mechanism for two different model potential, we compare the two-color photoelectron spectra with those obtained with the sole radiation. This comparison is illustrated in Fig.(2) and Fig.(3) (note the logarithmic scale) for long-range potential and short-range potential, respectively. From Fig.2(a), it is clearly shown that the effects of the high-frequency field on the photoelectron spectra is much stronger. That is to say, the LASPI process is dominated here, but the ATI is almost completely negligible. Fig.2(b) corresponds to F_L=0.044a.u. In this case, the photoelectron spectra is not influenced by the harmonic radiation at the lower energies, which corresponds here to the first three peaks between 0 and 0.3a.u. Therefore, we can say that the ATI is dominated at this region. In addition, it is also seen that, at energy range in photoelectron spectra, the interplay between ATI and LASPI are dominated from 0.3a.u to 0.4a.u. On the other hand, we note that the effects of the high-frequency field on the photoelectron spectra becomes stronger gradually. That is to say, the LASPI begins to dominate at higher energies, which ranges here approximately from 0.4a.u to 1.0a.u..

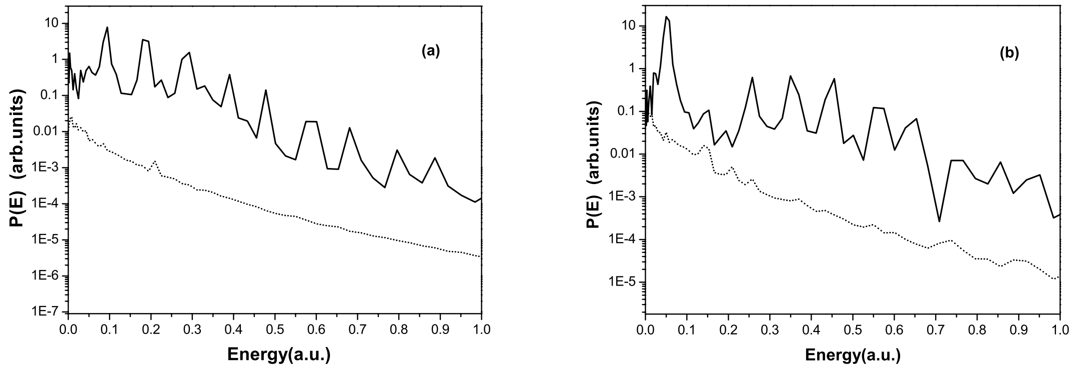

Fig.3 Effects of the high-order harmonic radiation on the photoelectron spectra for short-range potential, in the same conditions as in Fig.1. (a) F_L=0.021a.u. solid line, F_H=0.0675a.u; dot line,F_H=0. (b) Same as (a), with $F_L = 0.044$a.u.

For short-range potential, the results are shown in Fig.3. It is clearly shown that the effects of the harmonic radiation on the photoelectron spectra are much stronger, either at the lower laser intensity [as shown in Fig.3(a)], or the higher laser intensity [as shown in Fig.3(b)]. Namely, for short-range potential, the LASPI is always dominated when the fundamental field intensity is varied.

5. Conclusion

In this paper, we have investigated the effects of the model potential on two-color multiphoton ionization of atoms. Our own investigations have been based on the resolution of the TDSE for one-dimensional model potentials, either long-range or short-range. We find that the whole magnitudes peak of the short-range potential is higher than long-range potential's. On the other hand, we have also shown that the two different model potential leads to the two-color ionization process growing difference. For long-range potential, the LASPI is dominant at relatively lower laser intensities, but at higher laser field strengths, the ATI is dominant in the low-photoelectron-energy region, the LASPI is dominant in the high-photoelectron-energy region. For short-range potential, whether at lower or higher laser intensities, the LASPI is always dominant.

Acknowledgement

This work is supported by projects of the National Natural Science Foundation of China under Grant No.10274063 and the Young Teachers Foundation of Northwest Normal University under Grant No. NWNU-QN-04-25.

References

[1] M.Protopapas,C.H.Keitel,and P.L.Knight,Rep.Prog.Phy **60** (1997) 389.
[2] M.Dörr and R.Shakeshaft,Phys.Rev.A **36** (1987) 421.
[3] F.Zhou and L.Rosenberg,Phys.Rev.A **44** (1991) 3270.
[4] A.Szöke,K.C.Kulander,and J.N.Bardsley,J.Phys.B **24** (1991) 3165.
[5] H.G.Muller,H.B.V. Heuvell,and M.J.Van derWiel,J.Phys.B **19**(1986) L733.
[6] G.G.Paulus,W.Becker,and H.Walther,Phys.Rev.A **52** (1995) 4043.
[7] R.M.Potvliege,and P.H.G.Smith,J.Phys.B **25** (1992) 2501.
[8] V.Véniard,R.Taïeb,and A.Maquet,Phys.Rev.Lett.**74** (1995) 4161.
[9] C.Figueira de Morisson Faria,H.Schomerus,and W.Becker,Phys.Rev.A**66** (2002) 043413.
[10] Q.Su and J.H.Eberly,Phys.Rev.A **44** (1991) 5997.
[11] C.Figueira de Morisson Faria,D.B.Milosevic and G.G.Paulus,Phys.Rev.A **61** (2000) 63451.
[12] J.Javanainen,J.H.Eberly and Q.Su,Phys.Rev.A **38** (1988) 3430.
[13] R.Taïeb,V.Véniard and A.Maquet,J.Opt.Soc.Am.B **13** (1996) 363.

Relaxation Effects on Photoionization Processes of Lithium

Cuicui Sang[1], Jianjie Wan[1], Chenzhong Dong[1,2]*, Xiaobin Ding[1], and Jun Jiang[1]

1) College of Physics and Electronic Engineering, Northwest Normal University, Lanzhou 730070 China
2) National Laboratory of Heavy Ion Accelerator of Lanzhou, Lanzhou 730070 China

**e-mail: dongcz@nwnu.edu.cn*

Abstract

Using multi-configuration Dirac-Fock method and the corresponding packages GRASP92 and RATIP, as well as the recently developed computational program RERR06, the inner- and outer-shell photoionization cross sections related with the configurations $1s^2nl$ $(n = 2, 3; l = s, p)$ of Lithium have been calculated. In present calculations, the relaxation effects and relativistic effect are included in systematical way. It is found that relaxation effect plays important role in the inner-shell photoionization processes, but contrarily in the outer-shell photoionization processes. Furthermore, the effects of relaxation on inner-shell photoionization processes from different states is not the same. It is more important for the excited states than for the ground state, and for the higher excited states than for the lower excited states.

Keywords: Multi-configuration Dirac-Fock method, relaxation effects, photoionization cross section, photoelectron spectrum

1.Introduction

Photoionization (PI) was regarded as an inverse process of Radiative Recombination (RR), which is one of the basic processes in nature. In PI process an atom (ion) absorbs one photon and the electron in the atom (ion) will be ionized. There are two typical PI processes — main and shake up (down) PI processes. For main PI process, just one electron involved in the PI process which is a normal one and can be explained by single-electron approximation, while for shake up (down) process, accompanying the emission of photoelectron, another electron has been shaken up (down) to a higher (lower) state in residual ions, which can't be explained if neglecting the correlation effects. Investigation on PI process is very important for understanding the celestial physics, X-Ray, and especially in radiant balance of plasmas (such as high temperature plasmas and thermonuclear fusion plasmas), etc.

Lithium has been chosen as a candidate for investigation of relaxation effects because it is the simplest system with open shells and several electrons. Furthermore, the study can provide useful information to other PI of similar systems. There are many works on PI of Lithium in early times. However, most of them just investigate the process related to the ground state $1s^22s$. For example, the outer-shell photoionization cross section (PICS) have been calculated in 1975 by Bhatia et al.[1] and Chang et al.[2] using a method of polarized orbitals and many-body theory separately. And the inner-shell PICS was calculated in 1990 by Lisini et al.[3] and Armen et al.[4] by applying R-matrix and non-resonant multichannel scattering approach. In aspect of experiment advance, Hudson et al.[5] observed the outer-shell PI process as early as in 1965, and Ferrett et al.[6] measured the inner-shell PICS in 1987, afterward in 1991, Langer et al.[7] measured the inner-shell PICS again in high resolution.

However, for lithium at excited states, there are only theoretical studies available[8 – 11] in early times. Until recently, with quick development of experimental techniques, it is become possible to produce and keep Li atom at excited states (such as $1s^22p$, $1s^23s$ and $1s^23p$, etc.) for a little long time. As a result, it is possible to measure the PICS for excited states. For example, Cheng et al.[12] measured the photoelectron spectrum from main PI process for $1s^2nl$ $(n = 2, \ldots, 10, l = s, p, d)$ in 1999. And in 2006, Amin et al.[13] measured the outer-shell PICS of $1s^22p$ $^2P_{3/2}$ and $1s^23s$ $^2S_{1/2}$. At the same time, Saleem et al.[14,15] measured the outer-shell PICS of $1s^22p$ $^2P_{3/2}$ and $1s^23p$ $^2P_{3/2}$. In 2007, Hussain et al.[16] observed the outer-shell PI process of $1s^23s$ $^{1,3}S$, especially for the first time, Cubaynes et al.[17] observed the photoelectron spectrum of inner-shell PI of $1s^2nl$ $(n = 2, 3; l = s, p)$ including main and shake up process with high resolution, and discussed the intensity inversion between main and satellite lines in atomic PI processes. These latest experimental advances have provided good chances and new challenges to carry out further theoretical study.

In order to obtain the full understanding of the PI process of $1s^2nl$ $(n = 2, 3; l = s, p)$, the inner- and outer-shell PICS of this configurations have been calculated in detail by using multi-configuration Dirac-Fock (MCDF) method[18] and the corresponding packages GRASP92 and RATIP, as well as the recently developed RERR06 which could include relaxation effects, the inner- and outer-shell PICS of configurations $1s^2nl$ $(n = 2, 3; l = s, p)$ for atom Lithium have been calculated in detail , and the effect of relaxation on PI from different initial states have been studied systematically.

2. Orbital Relaxation in Lithium

Electronic density distribution will be rearranged after emitting an electron in atom (ion), because the potential of the residual ions have changed. This effect is the source of relaxation effect and can be reflected purely by the electronic average orbital radius (AOR). Fig.1 shows the electronic AOR before and after PI, it can be found that the AOR

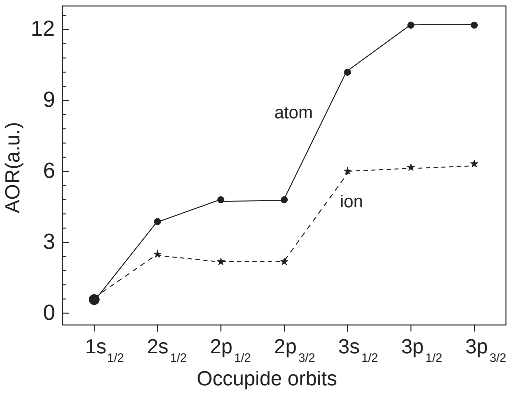

Figure 1: Electronic AOR before PI in atom and after PI in ion.

of inner-shell $1s_{1/2}$ nearly unchanged, while the AOR of outer-shell $2s_{1/2}$, $2p_{1/2}$ and $2p_{3/2}$ have been reduced about 1.3783 a_0 (35.6%), 2.6190 a_0 (54.6%) and 2.6194 a_0 (54.6%), and the outer-shell $3s_{1/2}$, $3p_{1/2}$ and $3p_{3/2}$ have been reduced about 4.1853 a_0 (34.3%), 6.0230 a_0 (49.4%) and 5.8683 a_0 (48.2%) separately. In general, the AOR of electrons in residual ion will change dramatically throughout the PI process. Furthermore, rearrangement of electron density distribution will arise acute changing of character of relevant processes, so it have to be considered in calculation of PICS for Lithium.

3. Inner-shell PICS

Fig.2-5 shows the inner-shell PICS of $1s^2nl$ $(n = 2, 3; l = s, p)$, and other experimental as well as theoretical results. Where, V and L are the present calculated result in velocity and length gauge separately. It is worth noting that in Fig.5 our results decreased gradually as photon energy approaches the ionization limit. It is because of destructive interference of configuration interaction[4,19]. Furthermore, it can be seen from Fig.2 that the shake up PICS is smaller than the main PICS, and in Fig.3 they are almost the same, but in Fig.4 the shake up PICS is a little bigger than the main PICS, while in Fig.5 the shake up PICS are quite bigger than the main PICS. It indicate that the shake up process for high excited state is stronger than for low excited and ground state. In another word, the relaxation effect in high excited states is stronger than that in low excited state

4. Outer-shell PICS

Fig.6-9 shows the outer-shell PICS of $1s^2nl$ $(n = 2, 3; l = s, p)$. Good agreements are obtained between our results in two gauge and between our results and other experimental

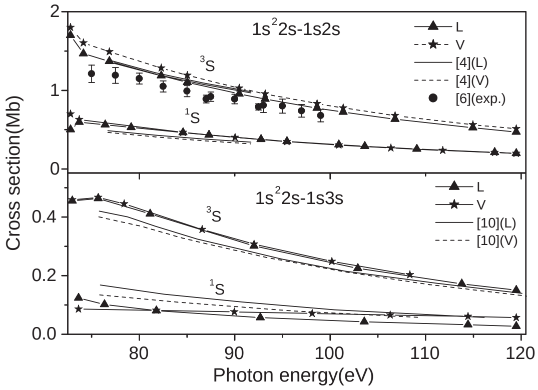

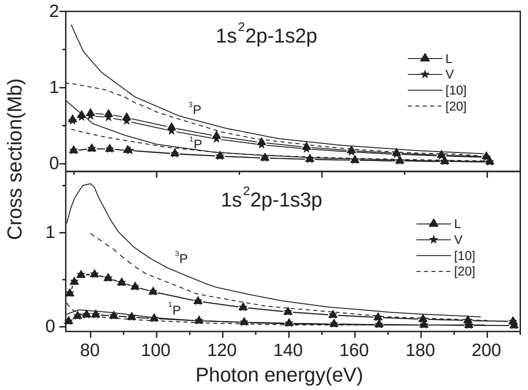

Figure 2: Inner-shell PICS from the ground state $1s^2 2s$. Corresponding to final states $1s2s(^{1,3}S)$ and $1s3s(^{1,3}S)$ are the main and shake up PICS separately.

Figure 3: Inner-shell PICS from the excited state $1s^2 2p$. Corresponding to final states $1s2p(^{1,3}P)$ and $1s3p(^{1,3}P)$ are the main and shake up PICS separately.

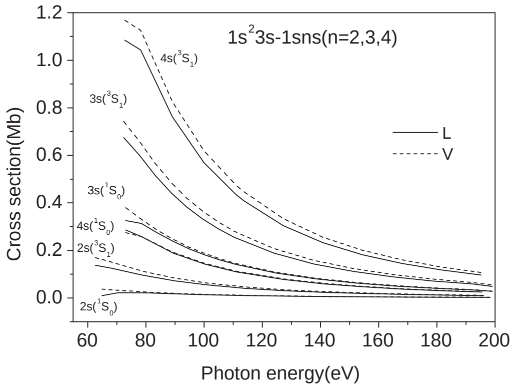

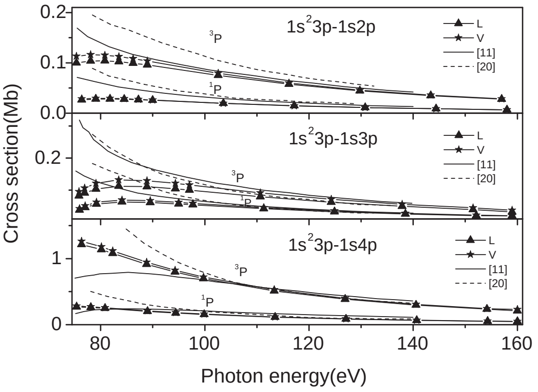

Figure 4: Inner-shell PICS from the excited states $1s^2 3s$. Corresponding to final states $1s2s(^{1,3}S)$, $1s3s(^{1,3}S)$ and $1s4s(^{1,3}S)$ are the shake down ,main and shake up PICS separately.

Figure 5: Inner-shell PICS from the ground states $1s^2 2p$. Corresponding to final states $1s2p(^{1,3}P)$, $1s3p(^{1,3}P)$ and $1s4p(^{1,3}P)$ are the shake down, main and shake up PICS separately.

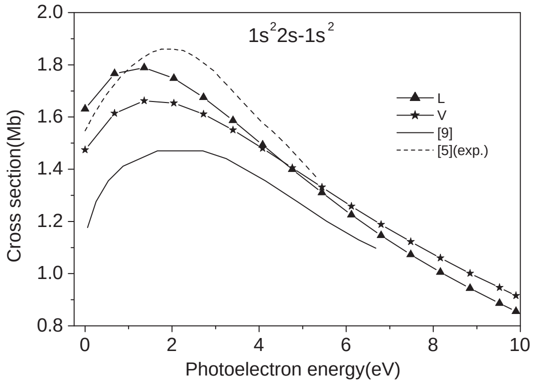

Figure 6: Outer-shell PICS from ground state $1s^22s$.

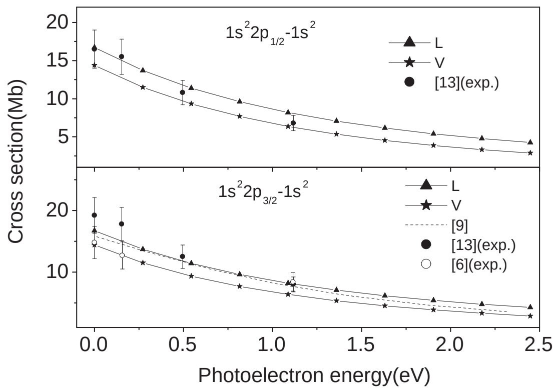

Figure 7: Outer-shell PICS from excited states $1s^22p_{1/2,3/2}$.

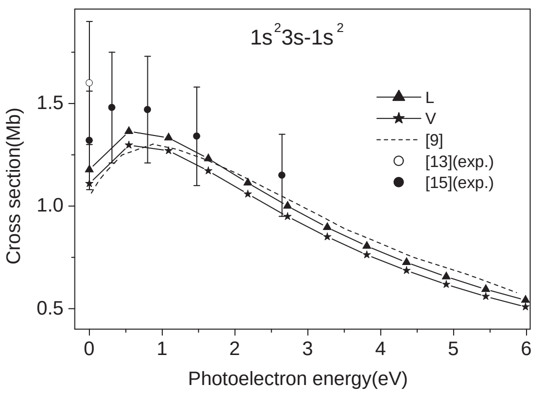

Figure 8: Outer-shell PICS from excited state $1s^23s$.

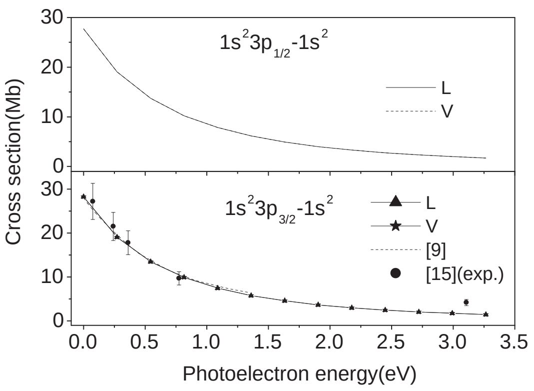

Figure 9: Outer-shell PICS from excited states $1s^23p_{1/2,3/2}$.

as well as theoretical results.

5. Relaxation effect on PICS

In the outer-shell PI process, inner-shell electronic density distribution nearly unchanged, so the relaxation effect is not obvious. While in the inner-shell PI processes, outer-shell electronic density distribution changed dramatically due to the creation of hole in inner-shell, so relaxation effect is very important. To make clear the regularity of the effect on different PI processes from different atomic states, the photoelectron spectrum (PES) of $1s^2nl$ ($n = 2, 3; l = s, p$) was shown in Fig.10 at photon energy 100eV with kinetic energy of photoelectron shifted properly. Fig.10(a) and (b) include latest experimental[17] and our calculated PES for $1s^22s$ and $1s^22p$, while Fig.10(c) and (d) include

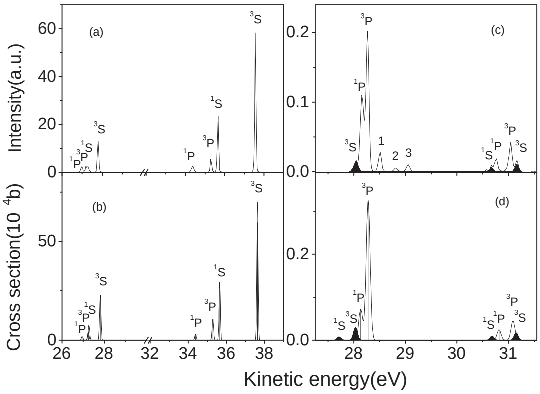

Figure 10: PES at photon energy 100eV.(a) and (b) include inner-shell PES of $1s^22s$ and $1s^22p$, (c) and (d) include inner-shell PES of $1s^23s$ and $1s^23p$.Where, (a) and (c) are experimental results from [13]. (b) and (d) are our calculated results.

PES from $1s^23s$ and $1s^23p$ for experiment[17] and our results separately. In general, shake up lines usually lies in the red wing of main PI lines. In Fig.10(c), lines 1-3 are relevant to conjugate shake up processes. It can be found from Fig.10 that the relative intensity of shake up lines to main lines is bigger for excited states than for the ground state, and becomes bigger through the first excited state to the higher excited state $1s^23p$, which indicates that the relaxation effect is more important for excited states than for the lower excited and ground state. It could be understood by the weaker penetration of the valence electron in the excited states than in the ground states, and in higher excited states than in the lower excited states. For the valence electron, the weaker penetration indicate the more evident changing of the effective nuclear charge after PI. while it will lead to the bigger changing of electron density distribution, and consequently, the more important relaxation effect is induced[20]. Moreover, these results can be explained by a systematic increase of the relative importance of electron correlation through the ground states $1s^22s$ to the excited states $1s^23p$ as in Ref.[17].

6. Conclusion

Using MCDF method and the corresponding packages GRASP92 and RATIP, as well as the recently developed RERR06, the inner- and outer-shell PICS of configurations $1s^2nl$ $(n = 2, 3; l = s, p)$ of Lithium have been calculated, and the relaxation effects on PICS have been discussed in detail. It is found that relaxation effect is important in the inner-shell PI processes, due to the creation of inner-shell hole will lead to large change in the potential of residual ions. Moreover, relaxation effect is the main reason for shake up (down)[10], so in the inner-shell PI processes, shake up (down) processes have to be considered. While in the case of outer-shell PI processes, relaxation is not evident, and it can be neglected, only the corresponding main PICS was discussed. Furthermore, the PES of shake up (down) and main lines was shown. It is found that the relaxation effect is more important for the excited states than for the ground state, and for the higher excited states than for the lower excited states. Again, through the good agreement between our results and the other experimental and theoretical results, it implies that MCDF is a good method to study the atom (ion) PI process.

Acknowledgments

This work was supported by the National Natural Science Foundation of China (Grant No.10434100, 10774122), the Core-University Program between Japanese Society of Promotion of Science and Chinese Academy of Sciences, the Specialized Research Fund for the Doctoral Program of Higher Education of China (Grant No. 20070736001), the Foundation of Center of theoretical Nuclear Physics of National Laboratory of Heavy Ion Accelerrator of Lanzhou, and the Foundation of Northwest Normal University(NWNU-KJCXGC-03-21).

References

[1] A. K. Bhatia, A. Temkin and A. Silver, Phys. Rev. A, **12**, 2044 (1975).
[2] T. N. Chang and R. T. Poe, Phys. Rev. A, **11**, 191 (1975).
[3] A. Lisini, P. J. Burke and A. Hibbert, J. Phys. B: At. Mol. Opt. Phys., **23**, 3767 (1990).
[4] G. B. Armen and F. P. Larkins, J. Phys. B: At. Mol. Opt. Phys., **24**, 2675 (1991).
[5] R. D. Hudson and V. L. Carter, Phys. Rev. A, **137**, 1648 (1965).
[6] T. A. Ferrett, D. W. Lindle, P. A. Heimann et al., Phys. Rev. A, **36**, 3172 (1987).
[7] B. Langer, J. Viefhaus, O. Hemmers et al., Phys. Rev. A, **43**, 1652 (1991).
[8] M. Aymer, E. L. Koenig and F. C. Farnoux, J. Phys. B: At. Mol. Opt. Phys., **9**, 1279 (1976).
[9] J. Lahiri and S. T. Manson, Phys. Rev. A, **48**, 3674 (1993).
[10] A. Kupliauskienë, Phys. Scr., **53**, 149 (1996).
[11] H. L. Zhou, S. T. Manson, L. Vo Ky et al., Phys. Rev. A, **59**, 462 (1999).
[12] W. T. Cheng, E. Kukk, D. Cubaynes et al., Phys. Rev. A, **62**, 062509 (1999).
[13] N. Amin, S. Mahmood, M. Saleem et al., Eur. Phys. J. D, **40**, 331 (2006).
[14] M. Saleem, S. Hussain, M. Rafiq et al., J. Appl. Phys., **100**, 053111 (2006).
[15] M. Saleem, S. Hussain, M. Rafiq et al., J. Phys. B: At. Mol. Opt. Phys., **39**, 5025 (2006).
[16] S. Hussain, M. Saleem and M. A. Baig, Phys. Rev. A, **75**, 022710 (2007).
[17] D. Cubaynes, S. Diehl, F. J. Wuilleumier et al., Phys. Rev. Lett., **99**, 213004 (2007).
[18] F. A. Parpia, C. F. Fischer, I. P. Grant et al., Comput. Phys. Commun., **94**, 249 (1996).
[19] S. Fritzsche, H. Aksela, C. Z. Dong et al., Nucl. Instrum. Methods Phys. Res. B, **93-98**, 205 (2003).
[20] Z. Felfli and S. T. Manson, Phys. Rev. Lett., **68**, 1687 (1992).
[21] C. C. Sang, J. J. Wan, C. Z. Dong et al., Acta. Phys. Sin., **4**, (2008) (in print)

Theoretical Calculation of Photoionization Cross Sections for Ions N^{2+}, N^{3+}, O^{3+}, O^{4+} and F^{4+}

Guoli Wang and Xiaoxin Zhou

College of Physics and Electronic Engineering, Northwest Normal University, Lanzhou,730070, China

e-mail: wanggl@nwnu.edu.cn

Abstract

There exist notable discrepancies with regard to the resonance structures when compared R-matrix calculations from the Opacity Project and other sources with recent absolute experimental measurements by Bizau et al. (2005 *Astronomy & Astrophysics.* **439** 387) for Be-like ions N^{3+} and O^{4+} and B-like ions N^{2+},O^{3+} and F^{4+}. To remove the differences between theory and experiment, we performed close-coupling calculations based on the R-matrix formalism for the photoionizations of ions mentioned above both for the ground states and the first excited states in the near threshold regions. The present results are compared with experimental ones by Bizau et al. and earlier theoretical ones. Excellent agreement is obtained between our theoretical predictions and the experimental photoionization cross sections. The present calculations show a significant improvement in comparison with previous theoretical results.

Keywords: photoionization, resonance structure, Be-like ions, B-like ions

1. Introduction

Absolute photoionization (PI) cross sections of atoms and ions are required to model many physical systems, such as astrophysical or laboratory plasma and the upper atmosphere. Multiply charged ions of low-Z elements such as carbon, nitrogen, and oxygen have been concerned in a number of theoretical and experimental studies due to their importance in astrophysics [1-11].

The accuracy of these data is very important for practical application. Recently, in order to test the R-matrix calculations of the Opacity Projects, Bizau et al. [11] measured absolute photoionization cross sections for the light multiply charged ions of astrophysical relevance: N^{2+}, N^{3+}, O^{3+}, O^{4+}, F^{3+}, F^{4+} and Ne^{4+}. In the experiment they used the merged-beam technique combined with the synchrotron radiation from an undulator at the storage ring ASTRID with ions produced by an ECR ion source. Although there have been many theoretical studies for those ions, very significant deviations between the experimental data and the previous R-matrix calculations are observed as concerning the spectral structure of some ions studied. To improve the accuracy of theoretical calculation, we calculated the photoionization cross sections of some Be-like and B-like ions mentioned above using the R-matrix method [12] and the corresponding program [13]. In this paper, all cross sections are obtained by using a fine energy mesh of $10^{-6}\times z^2$ Ry, z is the charge on the N-electron target system, $z=Z-N$ where Z is the charge on the nucleus.

2. Be-like ions N^{3+} and O^{4+}

For N^{3+} and O^{4+} ions, the present R-matrix calculation includes five lowest Li-like LS target states. In the wave-function expansion of these target ions, six real and three pseudo-orbitals (1s, 2s, 2p, 3s, 3p, 3d, $\overline{4s}$, $\overline{4p}$, $\overline{4d}$) are employed. The 1s and 2s orbitals are Hartree-Fock orbitals for the Li-like ground state $1s^22s$ ^2S given by Clementi and Roetti [14]. The pertinent parameters and coefficients for other orbitals are obtained by optimizing on the energy of given states using the structure CIV3 code of Hibbert [15].

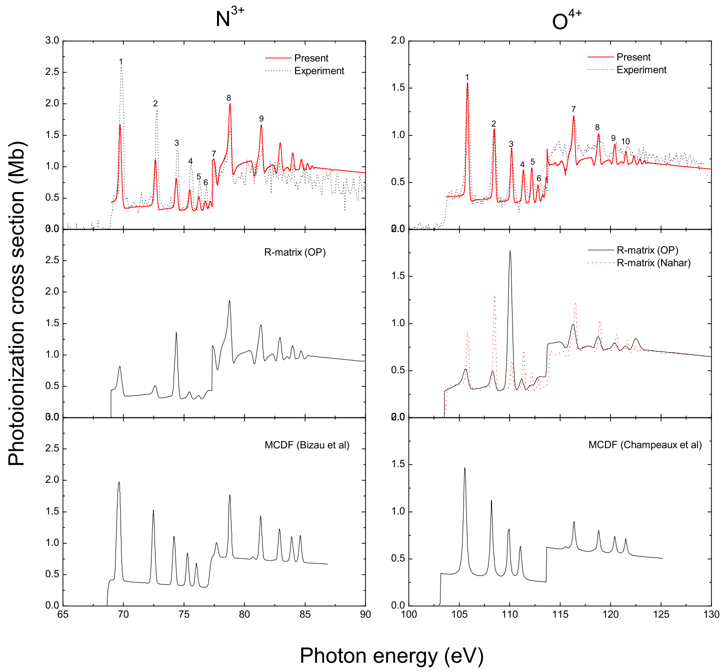

Figure 1: Comparison of different results for the photoionization cross sections of the Be-like ions N^{3+} (*left*), O^{4+}(*right*). *Top*: dotted (black) line was experimental data of Bizau et al. [11], solid (red) line was present R-matrix calculations; *middle*: previous R-matrix calculations, solid (black) line was result of Tully et al. [1] from Opacity Project, dotted (red) line was calculation of Nahar [5]; *bottom*: the MCDF calculations, calculated by Bizau et al. [11] and Champeaux et al. [6] for N^{3+} and O^{4+}, respectively.

We calculate photoionization cross sections of N^{3+} and O^{4+} from the ground state $2s^2$ ^1S and excited state 2s2p $^3P^o$ near the thresholds. In order to make a comparison with the recent measured absolute photoionization cross sections of Bizau et al. [11] directly, we convolute our calculated cross sections with the resolutions used in the experiment (230 and 250 meV for N^{3+} and O^{4+}, respectively), and the final result is a sum of the ground and metastable contributions, weighted by their relative abundance (65% and 50% for N^{3+} and O^{4+} for ground states, respectively). Figure 1 displays the comparison between different results, besides the present R-matrix calculation, the earlier R-matrix and MCDF calculations are also included. For N^{3+}, the strength of the resonances obtained by both the MCDF and R-matrix calculations is not agreed very well with the experimental measurements. For O^{4+}, either the magnitude of the continuum cross section or the strength of the resonances gets a good agreement between the present R-matrix calculation and the experiment. To match the experimental results, we have shifted calculated energy scale by 0.15 eV to the higher side for excited state in the case of O^{4+}.

As a part of the Opacity Project (OP), Tully et al. [1] calculated total photoionization cross sections from all terms with $L \leq 3$ lying below the first ionization threshold of Be-like ions including N^{3+} and O^{4+} in LS coupling using the R-matrix method. It can be found that though the magnitude of the continuum cross section was reproduced correctly in the calculations of Tully et al., the relative intensities of resonances are not agreed well with experimental results especially for the excited states. More recently, Nahar [5] calculated photoionization cross sections of several oxygen ions using both LS coupling and relativistic Breit-Pauli R-matrix approach. For O^{4+}, Nahar obtained PI cross sections for the ground $2s^2(^1S)$ and excited $2s2p(^3P^o,^1P^o)$ states. The calculated spectra reproduced all observed resonant features, shapes, and energy positions in measurements of Champeaux et al. [6], see Fig.7 in Ref.[5], but there are also differences. In comparison with recent experimental results of Bizau et al. [11], Fig.1 (right, middle panels), some discrepancies for the intensity of the peaks still existed. The MCDF calculations (N^{3+} by Bizau et al. [11], O^{4+} by Champeaux et al. [6]) described the resonance structures very well, but it is not the case for the absolute values. For N^{3+} the strength of resonances is underestimated in the spectra of the metastable state. For O^{4+} the magnitude of the continuum cross section is smaller than that in measurements of the ground state part. It also can be observed that the MCDF calculations are not able to produce all resonances for the excited state of N^{3+} and O^{4+}. The present R-matrix calculations reproduces all resonances observed in experimental spectra. For N^{3+}, it is the same as what happened in the MCDF calculation of Bizau et al., the strength of resonances calculated at present is underestimated in comparison with experimental measurements. The resonance structures and intensities all agree very well with recent experiment by Bizau et al. [11] for O^{4+}.

3. B-like ions N^{2+}, O^{3+} and F^{4+}

In the calculations for B-like ions, we include twelve lowest target states. In the wave-function expansion of these target ions, six real and three pseudo-orbitals (1s, 2s, 2p, 3s, 3p, 3d, $\overline{4s}$, $\overline{4p}$, $\overline{4d}$) are included. The 1s, 2s and 2p orbitals are Hartree-Fock orbitals for the Be-like ground state $1s^22s^2$ ^1S given by Clementi and Roetti [14]. The pertinent parameters and coefficients for other orbitals are obtained by optimizing on given energy of states using the CIV3 code [15]. The calculated energies for target states and ionization energies agree very well with experimental values.

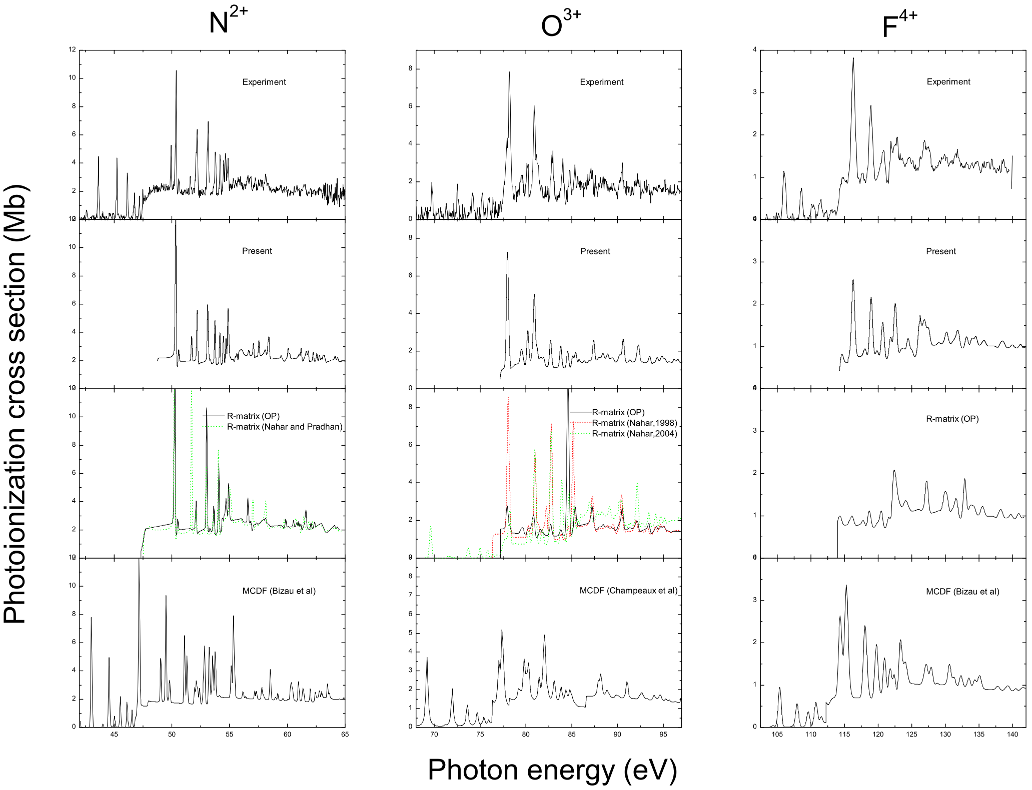

Figure 2: Comparison of different results for the photoionization cross sections of the B-like ions N^{2+} (*left*), O^{3+}(*center*), F^{4+}(*right*). *Top*: the experimental data of Bizau et al.; *Second*: present R-matrix calculations; *Third*: previous R-matrix calculations; *bottom*: the MCDF calculations. The theoretical spectra have been convoluted with Gaussian distributions of 100, 250 and 500 meV (FWHM), respectively, and are calculated under the assumption of a ($^2P^o$:^4P) fraction of (0.90:0.10) for N^{2+} and F^{4+} and (0.84:0.16) for O^{3+}. For N^{2+} and F^{4+}, we have shifted calculated energy scale by about 0.15, 0.25 eV, respectively, to the higher-energy side for ground state.

Figure 2 displays the comparison between the experimental and theoretical results. The calculated results are convoluted with 100, 250 and 500 meV and summed with mixing fractions 10%, 16% and 10% for ^4P, 90%, 84% and 90% for $^2P^o$ in the case of N^{2+}, O^{3+} and F^{4+}, respectively. For N^{2+} and F^{4+}, we have shifted calculated energy scale by about 0.15, 0.25 eV, respectively, to the higher-energy side for the ground state. It can be observed from Figs.2 that some resonances observed in the experiment were missed in the LS coupling results. The missed resonances lie in the energy range $E(2s^2\ {}^1S)$-$E(2s2p\ {}^3P^o)$ for metastable state ^4P, they can be formed in this range from allowed transitions with relativistic fine structure, but not via LS coupling, $^4P_{1/2,3/2,5/2}+h\nu \rightarrow 2s^2(^1S)np\ {}^2P^o_{1/2,3/2}$. In present paper, we focus on the photoionizations which can be produced in LS calculations.

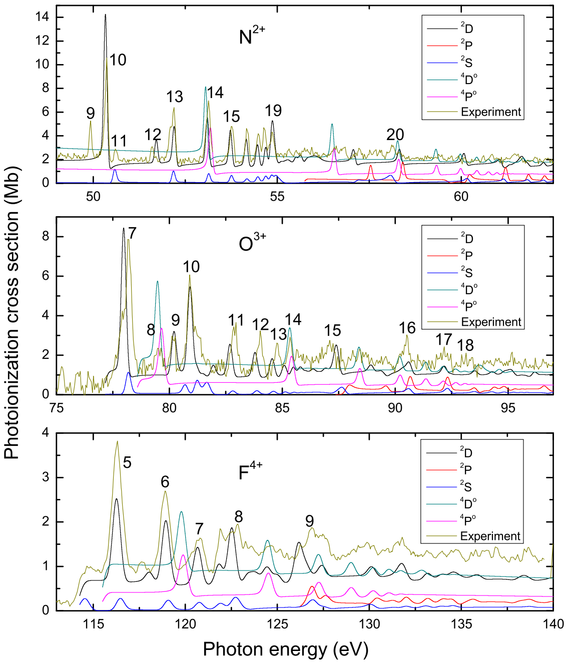

Figure 3: photoionization cross sections of N^{2+}(*top*), O^{3+}(*middle*), F^{4+}(*bottom*). The theoretical spectra have been convoluted with experimental bandwidth.

The photoionization cross sections of the B-like ions N^{2+}, O^{3+} and F^{4+} have been calculated utilizing the R-matrix method by Fernley et al. [2] as part of the Opacity Project. Employing the same method, Nahar and Pradhan [3] calculated the cross sections of the ions of C and N. Nahar [4] calculated the cross sections for oxygen and its ions. All the above investigations were non-relativistic and R-matrix calculations including relativistic effects have been carried out for oxygen ions by Nahar [5]. These results are also showed in Fig.2 (third panels) and we can see that these calculations can be able to reproduce the magnitude of the continuum cross sections, but fail to describe many details of the spectral structures, especially for O^{3+} and F^{4+}.

Using MCDF method Bizau et al. [11] and Champeaux et al. [6] calculated photoionizations for N^{2+}, F^{4+} and O^{3+}, respectively. And the results are displayed in Fig.2 (bottom panels). The MCDF description of the cross sections is fairly good for the gross features but fails to give resonances positions correctly. As can be seen later the peaks are shifted in energy by up to ±1 eV.

Present calculations show a significant improvement in comparison with previous theoretical results. Either the magnitude of the continuum cross sections or spectral structures and peak positions agree very well with recent experimental results of Bizau et al. [11].

Although the R-matrix approach can not identify the peaks straightforwardly, the partial cross sections can still provide some useful information. In figure 3 we display the partial cross sections and for the sake of clarity the convoluted results are given. We can see that beside the resonances coming from the ground state there are also some strong peaks due to transitions from the metastable state. We identify these resonances from NIST as $2p^2(^3P)np\ ^4D^o,^4P^o$ two-electron transition from the metastable state and compare with their energies in table 1. We can see that the present results are in good agreement with NIST values, the difference between them is less than 0.1 eV.

Table 1: Energies of the resonances $2p^2(^3P)np\ ^4D^o,^4P^o$ (in eV) for N^{2+}, O^{3+} and F^{4+}.

	N^{2+}		O^{3+}		F^{4+}
Level	NIST[16]	Present	NIST[16]	Present	Present
$2p^2(^3P)4p\ ^4D^o$	53.11	53.05	79.52	79.46	120.79
$^4P^o$	53.25	53.19		79.65	120.88
$2p^2(^3P)5p\ ^4D^o$	56.57	56.49		85.33	125.47
$^4P^o$	56.63	56.54		85.41	125.52
$2p^2(^3P)6p\ ^4D^o$	58.36	58.27		88.40	128.24
$^4P^o$	58.39	58.30		88.44	128.26
$2p^2(^3P)7p\ ^4D^o$	59.41	59.31		90.20	130.01
$^4P^o$	59.42	59.33		90.22	130.02

4. Conclusion

In conclusion, we have calculated photoionization cross sections of Be-like ions N^{3+} and O^{4+} and B-like ions N^{2+}, O^{3+} and F^{4+} that are in excellent agreement with recent experimental determinations. In cross sections of B-like ions we find resonances $2p^2(^3P)np$ $^4D^o,^4P^o$ for the first time. Present calculations show that we must employ a very fine energy mesh in the R-matrix calculation to obtain a perfect result. Our results show a good improvement in comparison with previous theoretical results. For excited states of B-like ions we need a relativistic calculation in comparison with recent experimental result.

Acknowledgement

This work is partly supported by the National Natural Science Foundation of China (Grant No. 10674112) and the Foundation of Northwest Normal University (Grant No.

NWNU-KJCXGC-03-21).

References

[1] J. A. Tully et al., J. Phys. B, **23**, 3811 (1990).
[2] J. A. Fernley et al., J. Phys. B, **32**, 5507 (1999).
[3] S. N. Nahar, et al., ApJS, **111**, 339 (1997).
[4] S. N. Nahar, Phys. Rev. A, **58**, 3766 (1998).
[5] S. N. Nahar, Phys. Rev. A, **69**, 042714 (2004).
[6] J.-P. Champeaux et al., ApJS., **148**, 583 (2003).
[7] H. Kjeldsen et al., Astrophys. J., **524**, L143 (1999).
[8] S. N. Nahar, Astrophys. J. Suppl. Ser., **101**, 423 (1995).
[9] S. N. Nahar, Phys. Rev. A, **65**, 052702 (2002).
[10] S. Schippers et al., J. Phys. B, **36**, 3371 (2003).
[11] J.-M. Bizau et al., Astro. Astrophy., **439**, 387 (2005).
[12 Burke P G and Berrington K A, Atomic and Molecular Processes: an R-matrix Approach (Bristol, UK: Institute of Physics Publishing) (1993).
[13] Y Yan et al.., J. Phys. B, **20**, 6399 (1987).
[14] E. Clementi and C. Roetti, At. Data Nucl. Data Tables, **14**, 177 (1974).
[15] A. Hibbert, Comput. Phys. Commun., **9**, 141 (1975).
[16] http://physics.nist.gov/PhysRefData/contents.html

Study on the Characteristic of Lightning Discharge Plasmas

Ping Yuan[1,2], Jie Wang[1], Xiaozhi Shen[1], Huaming Zhang[1], Yuhua Ouyang[1], Xueyan Zhao[1], Yixiao Guo[1] and Hongzhen Qiao[1]

1) College of physics and electronic engineering, Northwest Normal University, Lanzhou 730070, China
2) Cold and Arid Regions Environmental and Engineering Research Institute, Chinese Academy of Sciences, Lanzhou 730000, China

e-mail: yunap@nwnu.edu.cn

Abstract

According to the wavelengths, relative intensities and transition parameters of lines in lightning spectra obtained by a Slit-less Spectrograph, and by theoretical calculations of plasma, the average temperature and electron density for individual lightning discharge channel have been calculated, and then, using Saha equations, electric charge conservation equations, particle conservation equations, the particle densities of every ionized-state, the mass density, pressure and the average ionization degree are obtained. This work gives another way on the study of lightning physical mechanism besides the electric observation method.

Keywords: spectra of lightning, temperature, electron density, conductivity, particle densities, pressure, ionization degree

1. Introduction

Lightning is an important way in global atmosphere electrical circulations. The researches on the characteristics of lightning return stroke have became one of the most interesting subjects in atmospheric physics, atmospheric chemistry, laboratory long arc discharge and other relevant fields. As the occurrence of lightning is very random, and the transport and development happen at high velocity, the diagnostics of lightning discharge plasma are hardly to be achieved while optical observation could record the emission information. The high temperatures in and around the discharge channels of a lightning stroke cause the dissociation of the major atmospheric constitutions and the formation of atoms and ions. As we know that lightning is a significant source of nitrogen oxide to the atmosphere, this work will give some reference to the research of lightning producing nitrogen oxide and the effects on the local climate[1,2].

2. Temperature of lightning discharge plasma

The temperature of lightning discharge channel is calculated based on the two essential assumptions: (a) channel plasma is in the local thermodynamic equilibrium (LTE);

(b) channel is optically thin. Under LTE assumption, the line intensity can be given by[3]

$$I = \frac{h\nu}{4\pi}\frac{gA}{Z}Ne^{-E/kT} \tag{1}$$

Where ν is the line frequency, g, A, Z and E are the statistical weight, transition probability, partition function and upper excitation energy of corresponding transition, T is the temperature, and this function can be changed into

$$\ln(\frac{I\lambda}{gA}) = -\frac{E}{kT} + c \tag{2}$$

If we take the value $\ln(\frac{I\lambda}{gA})$ as the y-axis and E as the x-axis, then a slope parameter can be obtained by a linear fit. This parameter is equal to $-\frac{1}{kT}$, then the temperature can be calculated.

Table 1: Channel temperatures calculated for NII lines applying multiple-line method.

Position(height/km)	Temperature/K
0.123	29164
1.392	27172
1.827	29100
2.585	28473
3.248	27509
4.516	27369
4.999	27272
Average temperature	28000 ± 1000

Temperatures at given positions of a discharge channel A (time: 19:24:16, Aug 15, 2002, place: Qinghai) are listed in table 1. It can be seen that temperatures are all above 24,000K. In such high temperature circumstance, the channels will take plasma state. In general, the more intensive lightning discharge is, the higher the value of channel temperature is. For a certain return stroke channel, temperatures of different positions show a tiny trend of falling away with increasing height alone the discharge channel.

3. Electron density of lightning discharge plasma

The ratio of densities between atoms and ions are expressed by the relative intensities of the atomic and ionic lines. The electron density could be calculated by Saha equation[3].

$$n_e = 2 \cdot \frac{(2\pi mkT)^{3/2}}{h^3}(\frac{I_A}{I_I}) \cdot (\frac{gA}{\lambda})_I \cdot (\frac{\lambda}{gA})_A \cdot \exp(-(V + E_I - E_A)/kT) \tag{3}$$

Where I_A, I_I are the relative intensities of atom and ion lines, and E_A, E_I are the upper excitation energies while V is ionization energy.

If we make following assumptions: (a) The $H\alpha$ line is predominantly radiated while the stroke has one value of electron density; (b) The densities of electron, ion, and neutral hydrogen across the stroke are approximately constants; (c) All effects which may broaden the $H\alpha$ line are negligible in comparison with the Stark effect; (d) There is little self-absorption of $H\alpha$ within the stroke, then the electron density can be measured from Stark-broadening of $H\alpha$, and that can be express by[4]

$$n_e = C(n_e, T)\Delta\lambda_s^{3/2} \tag{4}$$

Where $\Delta\lambda$ is the full Stark width, and C is a coefficient which is only a weak function of the electron density. The values of electron densities calculated by the above two methods are listed in table 2 and table 3. The result shows that the electron density changes from 10^{17} to 10^{18} cm^{-3}. Generally speaking, the more intensive lightning discharge is, the higher the values of channel temperature and electron densities are. For a certain return stroke channel, electron densities at different positions show signs of falling away with increasing height alone the discharge[11], with the same changing rules as temperature.

Table 2: Electron density of discharge A at different heights by stark broadening method.

Height(km)	Stark width(nm)	Electron density (cm^{-3})
8.5	2.562	5.03×10^{17}
4.6	2.674	5.36×10^{17}
0.64	3.105	6.71×10^{17}
Average electron density		5.7×10^{17}

Table 3: Electron density of discharge A at heights 8.5 km by Saha equation.

Lines(nm)	Electron density (cm^{-3})
600.8/463.0	2.54×10^{18}
600.8/568.0	1.25×10^{18}
600.8/594.2	1.45×10^{18}
Average electron density	1.75×10^{18}

The electron density calculated by stark broadening method are lower than that of Saha equation, that's because the maximum intensities of the lines belong to NI, NII and $H\alpha$ don't emit at the same time. Lightning channels are almost completely ionized.

4. Particle densities of lightning discharge plasma

Based on the temperature and electron density that have been calculated according to the above methods, and using the Saha function again, the particle densities could be obtained. Further more, the particle distributions represent by the occupation of particle in same element total amount, number of particles per air atom, pressure, mass density and average ionization degree are also worked out and listed in table 4 and table 5.

Table 4: The particle densities and distribution of lightning return stroke A at 28000K with ne=1.75E18

Particles	Particles density	Particle distribution	Number of particles per air atom
electron	—	—	1.022E+00
NI	2.827E15	0.209E-01	2.156E-02
NII	1.270E18	0.941E00	7.129E-01
NIII	5.192E16	0.384E-01	4.653E-02
NIV	2.777E11	0.206E-06	4.715E-07
OI	1.100E16	0.304E-01	1.010E-02
OII	3.465E17	0.959E00	1.952E-01
OIII	3.938E15	0.109E-01	3.715E-03
OIV	7.564E09	0.209E-07	1.427E-08
ArI	1.318E14	0.762E-02	6.852E-05
ArII	1.297E16	0.750E00	6.600E-01
ArIII	4.186E15	0.242E00	3.325E-03
ArIV	4.793E12	0.277E-03	6.732E-06
ArV	2.025E06	0.117E-09	5.919E-12

Table 5: The characteristic parameters of lightning discharge channel A.

Channel temperature T	28000K
Electron density n_e	$1.750 \times 10^{18} cm^{-3}$
Mass density ρ	$4.217 \times 10^{18} kg \cdot m^{-3}$
Pressure P	13.048 atm
Average ionization degree	0.977

From the date in table 4 and table 5, we know Lightning channels are almost completely ionized, and the singly ionized particles occupy the main station while NII has the highest particle density. Comparing with data of other lightning discharge channels, the relative concentrations of NII and OII are nearly a constant in lightning channels with different discharge intensities. Generally speaking, the more intensive lightning discharge is, the higher the values of channel temperature, electron density and relative concentrations of highly ionized particles are, but lower for the neutral atoms. At a temperature of 30,000K, the electron pressure is about 6.7 atmospheres and the pressure due to heavy air particles (include atoms and ions) is about 6.8 atmospheres. The mass density of channel is lower and changes from 0.01 to 0.1 times the value of air at standard temperature and pressure (STP)[5].

5. Conductivity of lightning discharge plasma

Generally speaking, the temperatures of lightning discharge channel are about 24,000K, lightning channels are almost completely ionized, and the singly ionized particles occupy the main station. If we ignore the neutral atoms and highly charged ions, and consider that the channel is quasi-neutral, thus the conductivity can be calculated from [6].

$$\sigma = \frac{e^2}{\sqrt{3mkT}} \frac{T^2}{(20.2 \times 10^{-6}) \lg(221 \times T/n_e^{1/3})} \tag{5}$$

Table 6: Channel temperatures, electron density and conductivity at different heights of natural and triggered lightning discharge channels.

Cloud to ground flash	Natural lightning discharge channel					Triggered
Height(km)	1.862	1.878	2.099	2.266	2.656	—
Temperature(k)	26589	24745	24608	23678	24524	23899
Electron density($10^{18} cm^{-3}$)	2.505	2.470	2.463	2.343	2.478	0.293
Conductivity(10^6S/m)	2.28	2.07	2.06	1.93	2.05	1.3

From table 6, we can see that the lightning discharge channel is a fine conductor of electricity, and the electrons are the main carrier of lightning current. Meanwhile, from the conductivity characteristic of lightning channel, the phenomenon that the actual luminance of natural lightning are brighter than triggered ones can be inferred.

6. Conclusion

The result shows that the characteristics of lightning discharge plasma have close relationships with lightning intensities. The transitions from excited states of n=3 in NII ions are main composition of lightning spectra. Geographic situation and absolute altitude of observation site have a obvious influence on the feature of lightning spectra[7,8]. In general, temperature of lightning discharge channel can reach about 24,000K, and the electron density changes from 10^{17} to 10^{18} per cubic centimeter. For a certain return stroke channel, both temperatures and electron densities of different positions show tiny trends of falling away with increasing height alone the discharge channel [9-11]. Lightning channels are almost completely ionized, and the singly ionized particles occupy the main station while NII has the highest particle density. On the other hand, the relative concentrations of NII and OII are nearly constants in lightning channels with different discharge intensities. Generally speaking, the more intensive lightning discharge is, the higher are the values of channel temperature, electron density and relative concentrations of highly ionized particles are, but lower for the neutral atoms. At the temperature of 28,000K, the electron pressure is about 6.7 atmospheres and the pressure due to heavy air particles (include atoms and ions) is about 6.8 atmospheres. The mass density of channel is lower and changes from 0.01 to 0.1 times the value air at standard temperature and pressure (STP)[5].

Acknowledgement

This work is supported by the National Natural Science Foundation of P. R. China (Grant No.40475007) and the Foundation of Northwest Normal University (Grant No. NWNU-KJCXGC-03-21).

References

[1] L. E. Salanave, The optical spectrum of lightning, Science, **134**, 1395-1399 (1961).
[2] M. A. Uman, Lightning, New York: Cambridge University Press, 264, (1969).
[3] D. R. Qiu, Atomic spectra analysis, Shanghai: Fudan University Press, 37, (2001).
[4] H. R. Griem, Plasma Spectroscopy, NewYork: McGraw-Hill book company, 305, (1964).
[5] J. Wang, P. Yuan, H. M. Zhang, et al, Study on the Characteristics and Particle Densities of Lightning Discharge Plasma, Plateau meteorology, **in press**, (2007).
[6] B. Gross, B, Grycz, K. Miklossy, Plasma Technology, London : Iliffe, 176, (1980).
[7] P. Yuan, X. S. Liu, Y. J. Zhang, et al, Spectral Properties of the Lightning Return Stroke, Plateau meteorology, **22**, 235-239 (2003).
[8] P. Yuan, X. S. Liu, Y. J. Zhang, et al, Spectral study on lightning return stroke in plateau area, Chinese J. Geophys., **47**, 42-47 (2004).
[9] Y. H. OuYang, P. Yuan, X. S. Qie, et al, Temperature Study on Lightning Return Stroke in the Coastal Area of Guangdong, Spectroscopy and Spectral Analysis, **26**, 1988-1992 (2006).
[10] P. Yuan, Y. H. OuYang, S. H. Liu, et al, Characteristic of Temperature on Lightning Return Stroke in Qinghai Area, Plateau meteorology, **25**, 503-508 (2006).
[11] H. M. Zhang, P. Yuan, S. H. Liu, et al. Electron Density Study on Lightning Return Stroke, Plateau meteorology, **26**, 264-269 (2007).

Radiative Electron Capture in Collisions of Li-like Uranium Ions with N_2 Targets

Jianjie Wan[1], Yongjun Wang[1], Xiaobin Ding[1], Chenzhong Dong[1,†], Xinwen Ma[2], Jacek Rzadkiewicz[3,4], Thomas Stöhlker[4] and Stephan Fritzsche[4,5]

1)College of Physics and Electronic Engineering, Northwest Normal University, 730070, Lanzhou China
2) Institute of Modern Physics, 730000, Lanzhou, China
3) The Soltan Institute for Nuclear Studies, 05-400 Świerk, Poland
4) Gesellschaft für Schwerionenforschung (GSI), D-64291 Darmstadt, Germany
5) Max-Planck-Institut für Kernphysik, D-69029 Heidelberg, Germany

†*e-mail: dongcz@nwnu.edu.cn*

Abstract

The radiative electron capture (REC) in collisions of U^{89+} ions with N_2 target molecules has been studied theoretically. In this study, the REC cross sections and photon energies of the capture into the levels of the $1s^2 2snl$ ($2 \le n \le 9$, $0 \le l \le 6$) configurations, starting from the $1s^2 2s$ ground configuration of U^{89+} ions, have been calculated by applying the recently developed program RERR06. This program is based on the RATIP package and includes the contributions of most important multipole transitions. The REC spectra were generated by convoluting the RR cross sections with the Compton profile of the N_2 molecule. The calculated REC spectra are in good agreement with the observations of new experiments at GSI.

Keywords: REC, Compton profile, relativistic theory, MCDF

1. Introduction

The importance of electron-capture processes in laboratory fusion and astrophysical plasmas is well known[1-2]. Radiative recombination (RR) and radiative electron capture (REC) are two elementary processes for plasma equilibrium. RR involves collisions of highly-charged ions with free electrons, where the free electron undergoes a direct transition into a bound state of the stationary ion via the emission of a photon with the energy of difference between the initial and final state of the whole system. The energy of emitted photon is continuous and depend on the initial kinetic energy of the incoming electron. Another process–REC–occurs in ion-atom/molecule collisions in which the captured electrons are provided by target atoms/molecules and the final projectiles emit radiation during the capture. This is analogous to RR when viewed in the projectile ion rest frame in the context of the impulse approximation[3].

REC was identified in experiments by Raisbeck and Yiou[4] and by Schnopper *et al.*[5] who first observed unusually energetic x-rays from fast heavy-ion collisions in which the projectile ion captured a weakly bound target electron. Subsequently this process was extensively studied both experimentally and theoretically including the direct observation of REC photons, the angular distribution, and the interference effects in REC processes[6-11]. Recently the formation of singly excited states $1s2s\ ^1S_0$ and $1s2s\ ^3S_1$ in He-like uranium by K-shell ionization of the initially Li-like species colliding with nitrogen atoms/molecules has been studied by Rzadkiewicz *et al.*[12].

In this paper, the following REC processes,

$$U^{89+}(1s^22s) + N_2 \longrightarrow U^{88+}(1s^22snl) + N_2^+ + \hbar\omega^{REC}(2 \leq n \leq 9, 0 \leq l \leq 6),$$

is of our interest. According to the impulse approximation, the process mentioned above can be viewed as its related RR process,

$$U^{89+}(1s^22s) + e^- \longrightarrow U^{88+}(1s^22snl) + \hbar\omega^{RR}(2 \leq n \leq 9, 0 \leq l \leq 6),$$

which should be studied firstly, and additionally the Compton profile of N_2[13] should be given to reproduce the final REC x-ray spectra[12]. The REC cross section is found to be convolution between the RR cross sections and the Compton profile of the N_2 molecule.

2. REC cross sections

The RR cross sections have been calculated using the recently developed program RERR06[14] which is based on the RATIP package[15]. The present calculation was compared with the experimental spectra which was recorded at an observation angle of $\theta = 30°$[12]. Figure 1(a) shows experimental spectra associated with electron capture (outgoing charge state of U^{88+})[12]. From this figure, in the mid-energy region, the observed radiation is dominated by radiative electron capture (REC) into L, M, and higher shell of the projectile. The appearance of broader feature results from the distribution of electron momentum projection along the direction of the projectile in the target N_2 molecules. The theoretical REC and related RR spectra in the projectile frame have been shown in figure 1(b) and (c). Firstly, it is found in the present results that with the decreasing of photon energy the loosely bound electron in the target is captured into L-shell, M-shell, and up to S-shell by the highly charged Li-like uranium. Secondly, the probabilities of capture into L-shell, M-shell, and up to S-shell decrease gradually, which gives less probability of capture by highly charged Li-like uranium for higher shells. At the same time it is found that the energy levels quite close to one another near the ionization limit of the projectile, many RR lines can contribute to the peak in lower energy, however, there were eight shells (L-, M-, N- and O-S-shell) considered in the present calculation. As a result, the experimental spectrum is broader than the present theoretical spectra. As seen in figure 1, excellent agreement between the experimental and theoretical results

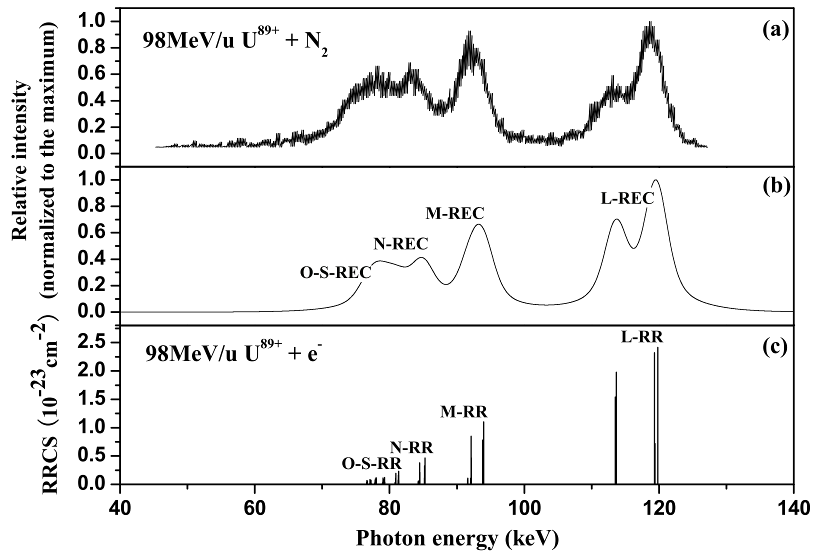

Figure 1: Projectile x-ray spectra for 98 MeV/u $U^{89+} \rightarrow N_2$ collisions (a) simulated by folding the initial electronic momentum distribution in the cross section for radiative recombination, (b) calculated RRCS to identify the contribution of the RR processes and (c) measured coincidence with electron capture (U^{88+})[12], including the relevant Doppler shift in (a) and (b).

is obtained, and the five marked peaks can be identified, which have been designated by the dominant RR lines.

3. Conclusion

In summary, REC spectra in collisions of Li-like uranium ions with N_2 targets at the projectile energy of 98MeV/u has been reproduced and compared with the normalized experimental spectra. A good agreement between the present results for the relative intensity and the experiment has been found. At the same time it also has been proved that the resulting line can be used to identify the contribution in each experimental peak. In addition, such a good agreement also implies another way to study the Compton profile of the target N_2. Here, it is suggested that if the related RR cross sections for the REC processes and the experiment REC spectra could be obtained exactly, the Compton profile of the target atoms or molecules could be evaluated and further the electron momentum distribution in the targets by using the method similar to deconvolution.

Acknowledgments

This work was supported by the National Natural Science Foundation of China (Grant No.10434100, 10774122), the Core-University Program between Japanese Society of Promotion of Science and Chinese Academy of Sciences, the Specialized Research Fund for the Doctoral Program of Higher Education of China (Grant No. 20070736001), the Foundation of Center of theoretical Nuclear Physics of National Laboratory of Heavy Ion Accelerrator of Lanzhou, and the Foundation of Northwest Normal University(NWNU-KJCXGC-03-21).

References

[1] J. Eichler, Phys. Rep., **193**, 165 (1990).
[2] C. R. Vane, S. Datz, P. F. Dittner *et al.*, Phys. Rev. A, **49**, 1847 (1994).
[3] D. Brandt, Phys. Rev. A, **27**, 1314 (1983).
[4] G. Raisbeck and F. Yiou, Phys. Rev. A, **4**, 1858 (1971).
[5] H. W. Schnopper, Hans D. Betz, J. P. Delvaille *et al.*, Phys. Rev. Lett., **29**, 898 (1972).
[6] A. Ichihara, T. Shirai, and J. Eichler, Phys. Rev. A, **49**, 1875 (1994) .
[7] Th. Stöhlker, C. Kozhuharov, P. H. Mokler *et al.*, Phys. Rev. A, **51**, 2098 (1995).
[8] R. Anholt, S. A. Andriamonje, E. Morenzoni *et al.*, Phys. Rev. Lett., **53**, 234 (1984).
[9] Th. Stöhlker, H. Geissel, H. Irnich *et al.*, Phys. Rev. Lett., **73**, 3520 (1994).
[10] X. W. Ma, Th. Stöhlker, H. F. Beyer *et al.*, Nuclear Physics Review, **19**, 131 (2002).
[11] A. Gumberidze, Th. Stöhlker, G. Bednarz *et al.*, Nucl. Instr. and Meth. B, **205**, 374 (2003).
[12] J. Rzadkiewicz, Th. Stöhlker, D. Banaś *et al.*, Phys. Rev. A, **74**, 012511 (2006).
[13] J. S. Lee, J. Chem. Phys., **66**, 4906 (1977).
[14] C. Z. Dong, X. B. Ding, L. Y. Xie *et al.* (unpublished).
[15] S. Fritzsche, J. Electron Relat. Phenom., **114-116**, 1155 (2001).

Theoretical Study on Low-lying Level Structures and Excited States Properties of the Super-heavy Elements Uub(Z=112) and Uuq(Z=114)

Youjun Yu[1], Jiguang Li[1], Chenzhong Dong[1,2,*], Xiaobing Ding[1]
Stephan Fritzsche[3] and Burkhard Fricke[4]
1) College of Physics and Electronic Engineering, Northwest Normal University, 730070 Lanzhou, China
2) National Laboratory of Heavy Ion Accelerator of Lanzhou,730000 Lanzhou, China
3) Gesellschaft für Schwerionenforschung, D-64291 Darmstadt, Germany
4) Institut für Physik,Universität Kassel, D-34132 Kassel, Germany
* *e-mail: dongcz@nwnu.edu.cn*

Abstract

Multi-configuration Dirac-Fock method (MCDF) is employed to calculate the ionization potentials, excitation energies and oscillator strengths for all neutral and ionized species of element Uub, as well as the homologue elements Zn, Cd and Hg. And a similar calculation was performed for the element Uuq and it's homologues. Using an extrapolative scheme, improved ionization potentials of Uub were obtained with an uncertainty of less than 0.5 eV and for Uuq within 2000 cm^{-1}. Some relatively stronger resonance transitions are predicted for the elements Uub and Uuq.

Keywords: low lying levels structure, oscillator strength, ionization potentials, MCDF method

1. Introduction

Studying on the physical and chemical properties of the super-heavy elements is always a common problem with interests, especially, since the mid-1960s the existence of an "island of stability" for the super-heavy elements has been predicting by nuclear theoy. Great excitement about the possible existence of super-heavy elements is the driving force for a large number of experimental and theoretical studying of these elements.

Recently, some chemical properties and atomic spectra of a few super-heavy elements have been studied using the gas-phase chromatography technique by Sch*ä*del group [1] or two photons resonance ionization spectroscopy on-line technique by Sewtz group [2]. However, the experiment is still difficult due to the short half-life and very low production rate for super-heavy element. In addition, it is well known theoretically that some chemical properties might not follow the trends of the lighter homologue in the chemical groups due to the strong relativistic effects and electron correlation effects in the super-heavy elements [3]. In order to obtain reliable information in limited time, it is desirable to make good theoretical predictions. Theoretical work has made a progress in molecular calculations for element Uub [4] or Uuq compounds [5], but the reliable basic atomic structure calculations is still little. A more direct approach to investigate relativistic effects of these elements is to study the atomic level schemes as well as the first ionization potentials theoretically.

In this paper, the ionization potentials, excitation energies and oscillator strengths for neutral and ionized species of elements Uub(Z=112) and Uuq(Z=114) as well as their lighter homologues have been calculated using the MCDF method by which the relativistic effects and electron correlation effects taken into account as complete as possible. Moreover, the extrapolated ionization potentials were obtained for the two elements Uub and Uuq.

2. Theoretical method

In this study, wave functions have been generated by the widely–used atomic structure package GRASP92 [6] which is an implementation of the multi-configuration Dirac-Fock (MCDF) method. In the MCDF method, an atomic state wavefunction $|\alpha(\Gamma PJM) >$ (ASF) is approximated by a linear combination of configuration state functions $\Psi(\gamma_r PJM)$ (CSFs) of the same symmetry

$$|\alpha(\Gamma PJM) >= \sum_{r=1}^{n_c} c_r(\alpha)\, \Psi(\gamma_r PJM) \tag{1}$$

In standard calculations, the CSFs are constructed from the summation of antisymmetrized products of a common set of *orthonormal* orbitals which are optimized by vibrational method on the basis of the Dirac–Coulomb Hamiltonian.

According to the time-dependent perturbation theory, the Einstein spontaneous transition probability for the electric dipole transition from an upper state β to the lower state α can be given by [7],

$$A_{\beta\alpha} = \frac{2\pi}{2j_\beta + 1} \sum_{M_\beta} \sum_{M_\alpha} |\langle \alpha(P_\alpha J_\alpha M_\alpha)|O^{(1)}|\beta(P_\beta J_\beta M_\beta)\rangle|^2$$

where $O^{(1)}$ is the electric dipole operator, j_β is the total angular momentum of the upper state β, $|\beta(P_\beta J_\beta M_\beta)\rangle$ and $|\alpha(P_\alpha J_\alpha M_\alpha)\rangle$ are the wave functions of the upper atomic state β and the lower atomic state α, respectively. Then, absorption oscillator strengths can be obtained from[7],

$$f_{\beta\alpha} = \frac{2j_\beta + 1}{(2j_\alpha + 1)2\alpha\omega^2} A_{\beta\alpha}$$

where j_α is the total angular momentum of the lower state α, ω is frequency of the photon absorbed by an atom from the lower state α to the upper state β.

3. Results and discussions

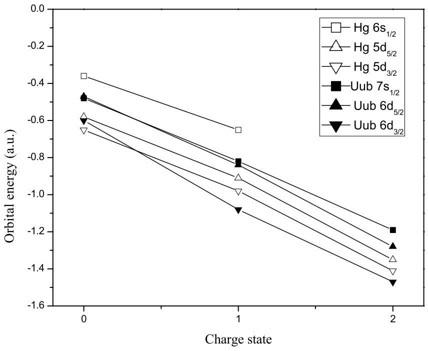

Figure 1: The orbital energy diagrams for neutral atom, monocation and dication of the elements Hg and Uub.

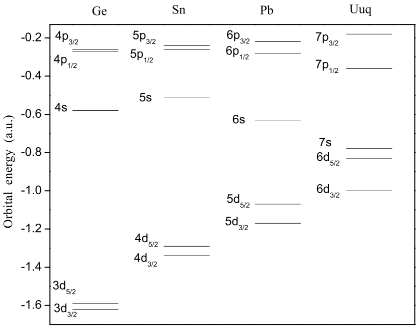

Figure 2: The orbital energy diagrams for the ground state configurations $[\text{core}](n-1)d^{10}ns^2np^2$ for Ge (n= 4), Sn (n=5), Pb (n=6) and Uuq (n=7), respectively.

It is well known that the electron correlation effects are very important for calculating atomic structures of many-electron atoms, especially for the super-heavy element. In MCDF method, the electron correlation effects can be included via increasing the number of CSFs by using active space method. In our calculations, the CSFs have been restricted to all possible configurations which can be constructed from the $\{(n-1)d, ns\}$ subshells with single, double, triple and quadruple excitations into $\{(n-1)d, ns, np\}$ (n= 4, 5, 6, 7 for Zn, Cd, Hg and Uub, respectively) and from the $\{(n-1)d, ns, np\}$ subshells with single and double excitations into $\{(n-1)d, ns, np, (n+1)s, (n+1)p, nd\}$ (n= 4, 5, 6, 7 for Ge, Sn, Pb and Uuq, respectively) subshells for a specific total angular momentum and parity, where the core of each configuration is kept fully occupied and the valence electrons are excited in all possible ways given above.

3.1 Orbital properties

As can be seen from Figure 1 , comparing with the light homologue element Hg, for the neutral atom of element Uub, the stronger relativistic effects lead to the bound energies of the $7s_{1/2}$ orbital and $6d_{5/2}$ orbital to reverse. For the element Uuq, as shown in Figure 2, due to the stronger relativistic effects, the 7s orbital contracted distinctly and 7p orbital split so large as to form a lower $7p_{1/2}$ and higher $7p_{3/2}$ spinor orbital for element Uuq, which results in an inert $7p_{1/2}^2$ pair of electrons. Thus, a stabilized electronic structure $7s^2 7p_{1/2}^2$ for the ground state of element Uuq [20] was predicted.

3.2 Ionization potentials

The ionization potentials for the Uub and its ions as well as for the homologous elements Zn, Cd, Hg and for the Uuq as well as its ions and for the homologous Ge, Sn and Pb are shown in Table1 and 2, respectively, including the experimental ionization potentials for the homologous elements [8] and other theoretical results from references [9,10,12] for Uub and from references [11,12,13,14] for Uuq.

As can be seen from Table 1, for element Uub, the difference for the ionization potentials (IP) between our results and the values in reference [9], which are Dirac–Coulomb–Breit interaction, is large. In addition there exist very old results from reference [10], which are Dirac–Fock–Slater calculations. The same holds true for the modern coupled cluster results from reference [12] for the first IP. The results which we have calculated here can be improved by extrapolation methods given in [17,18]. We obtain more accurate ionization potentials for Uub, Uub^{+} and Uub^{2+} which are 11.73 eV, 21.98 eV and 32.62 eV, respectively. This extrapolation leads to ionization potentials for element Uub probably within an uncertainty of 0.5 eV [19].

As can be seen from Table 2, the difference between experimental and MCDF ionization potentials is about 3000 to 8000 cm^{-1} per charge state. Based on above procedure, the ionization potentials for element Uuq have been obtained using the extrapolation schemes given in [17] that reduced the uncertainty within 2000 cm^{-1}. At the same time we find that the ionization potentials of element Uuq are lager than the values of the lighter homologue elements per charge state, which indicates that in the group IVA, element Uuq [20] is stronger chemically inert than e.g. Pb.

3.3 Excitation energies and absorption oscillator strengths

Table 3 presents the resonance excitation energies and absorption oscillator strengths for the neutral atoms of the elements Zn, Cd, Hg and Uub as well as experimental values [8]. As can be seen from Table 3, our results are in good agreement with experimental values for Zn, Cd and Hg, however, the difference increases with the charge state almost like the results of ionization potentials. For the oscillator strengths, we present our results with length gauge and velocity gauge respectively, and the values in two gauges are consistent with each other. Moreover, the results for Cd and Hg are in good agreement with the experimental values given in references [15,16]. This further indicates that our wave functions for the calculation of the element Uub are appropriate. Furthermore, we give more precise results for the low excitation energies and resonant oscillator strengths using a extended MCDF calculations and predict some relatively stronger resonance transitions for Hg and Uub [19].

Table 4 presents the resonance excitation energies and absorption oscillator strengths for the neutral atoms of the elements Pb and Uuq and experimental [8] as well as other theoretical results [11,13]. As can be seen from Table 4, the discrepancies between experimental and present excitation energies are about 5000 cm^{-1}, especially for the neutral

Table 1: Ionization potentials (in eV) for Zn, Cd, Hg and Uub in the charge states 0 to +4.

Elements	Transitions			Our calc.	Expt.[8]	Extrapolated	Other theory
Zn	$[3d^{10}4s^2]_0$	→	$[3d^{10}4s_{1/2}]_{1/2}$	8.48	9.39		
Cd	$[4d^{10}5s^2]_0$	→	$[4d^{10}5s_{1/2}]_{1/2}$	8.07	8.99		
Hg	$[5d^{10}6s^2]_0$	→	$[5d^{10}6s_{1/2}]_{1/2}$	9.33	10.43		
Uub	$[6d^{10}7s^2]_0$	→	$[6d^4_{3/2}6d^5_{5/2}7s^2]_{5/2}$	10.75		11.73	11.97 [9] 11.4 [10] 11.5 [12]
Zn^{1+}	$[3d^{10}4s_{1/2}]_{1/2}$	→	$[3d^{10}]_0$	16.85	17.96		
Cd^{1+}	$[4d^{10}5s_{1/2}]_{1/2}$	→	$[4d^{10}]_0$	15.62	16.90		
Hg^{1+}	$[5d^{10}6s_{1/2}]_{1/2}$	→	$[5d^{10}]_0$	17.73	18.75		
Uub^{1+}	$[6d^4_{3/2}6d^5_{5/2}7s^2]_{5/2}$	→	$[6d^4_{3/2}6d^4_{5/2}7s^2]_4$	20.84		21.98	22.49 [9] 21.1 [10]
Zn^{2+}	$[3d^{10}]_0$	→	$[3d^4_{3/2}3d^5_{5/2}]_{5/2}$	37.46	39.70		
Cd^{2+}	$[4d^{10}]_0$	→	$[4d^4_{3/2}4d^5_{5/2}]_{5/2}$	36.07	37.47		
Hg^{2+}	$[5d^{10}]_0$	→	$[5d^4_{3/2}5d^5_{5/2}]_{5/2}$	32.56	34.20		
Uub^{2+}	$[6d^4_{3/2}6d^4_{5/2}7s^2]_4$	→	$[6d^4_{3/2}6d^5_{5/2}]_{5/2}$	30.86		32.62	32.8 [10]
Zn^{3+}	$[3d^4_{3/2}3d^5_{5/2}]_{5/2}$	→	$[3d^4_{3/2}3d^4_{5/2}]_4$	56.76			
Cd^{3+}	$[4d^4_{3/2}4d^5_{5/2}]_{5/2}$	→	$[4d^4_{3/2}4d^4_{5/2}]_4$	50.70			
Hg^{3+}	$[5d^4_{3/2}5d^5_{5/2}]_{5/2}$	→	$[5d^4_{3/2}5d^4_{5/2}]_4$	46.44			
Uub^{3+}	$[6d^4_{3/2}6d^5_{5/2}]_{5/2}$	→	$[6d^4_{3/2}6d^4_{5/2}]_4$	42.36			

elements the discrepancies are within 3000 cm^{-1}. In addition, it is found that two relatively stronger resonance transitions are predicted for Pb and Uuq. In particular, the strongest line of Uuq, corresponding to the $[6d^{10}7s^27p_{3/2}8s_{1/2}]_1 \rightarrow [6d^{10}7s^27p^2_{3/2}]_2$ transition at 22 343 cm^{-1}, just lies in the prime energy region, which is planned for observing low-lying level structure for (super-)heavy atoms using the Resonance Ionization Spectroscopy (RIS) technique [21]. So the present result is helpful to be observed in the future for element Uuq [20].

4. Conclusion

We have presented our results of the ionization potentials, excitation energies and oscillator strengths in the charge states 0 to 4+ of the elements Uub and Uuq and their homologues. It is found that the super-heavy elements Uub and Uuq show some exotic chemical properties, e.g. more inert than their homologues Hg or Pb, respectively, because of the stronger relativistic effects. Using an extrapolative scheme, improved ionization potentials of Uub were obtained with an uncertainty of less than 0.5 eV and for Uuq within 2000 cm^{-1}. Some relatively stronger resonance transitions are predicted for the elements Uub and Uuq and we hope that these results are helpful for observing the low-lying level structure for the two elements using the Resonance Ionization Spectroscopy

Table 2: Ionization potentials (in cm^{-1}) for Ge, Sn, Pb and Uuq in the charge states 0 to +4.

Elements	Transitions			Our calc.	Expt.[8]	Extrapolated	Other theory
Ge	$[3d^{10}4s^24p^2_{1/2}]_0$	$\rightarrow$	$[3d^{10}4s^24p_{1/2}]_{1/2}$	57814	63600		
Sn	$[4d^{10}5s^25p^2_{1/2}]_0$	$\rightarrow$	$[4d^{10}5s^25p_{1/2}]_{1/2}$	54635	59232		
Pb	$[5d^{10}6s^26p^2_{1/2}]_0$	$\rightarrow$	$[5d^{10}6s^26p_{1/2}]_{1/2}$	56748	59821		
Uuq	$[6d^{10}7s^27p^2_{1/2}]_0$	$\rightarrow$	$[6d^{10}7s^27p_{1/2}]_{1/2}$	65533		66748	68868 [13]
							68476 [14]
							68791 [12]
							68452 [11]
Ge^{1+}	$[3d^{10}4s^24p_{1/2}]_{1/2}$	$\rightarrow$	$[3d^{10}4s^2]_0$	122360	128518		
Sn^{1+}	$[4d^{10}5s^25p_{1/2}]_{1/2}$	$\rightarrow$	$[4d^{10}5s^2]_0$	113688	118017		
Pb^{1+}	$[5d^{10}6s^26p_{1/2}]_{1/2}$	$\rightarrow$	$[5d^{10}6s^2]_0$	115364	121243		
Uuq^{1+}	$[6d^{10}7s^27p_{1/2}]_{1/2}$	$\rightarrow$	$[6d^{10}7s^2]_0$	133960		138888	136074 [13]
							135080 [14]
Ge^{2+}	$[3d^{10}4s^2]_0$	$\rightarrow$	$[3d^{10}4s_{1/2}]_{1/2}$	266358	276036		
Sn^{2+}	$[4d^{10}5s^2]_0$	$\rightarrow$	$[4d^{10}5s_{1/2}]_{1/2}$	237268	246020		
Pb^{2+}	$[5d^{10}6s^2]_0$	$\rightarrow$	$[5d^{10}6s_{1/2}]_{1/2}$	248913	257592		
Uuq^{2+}	$[6d^{10}7s^2]_0$	$\rightarrow$	$[6d^{10}7s_{1/2}]_{1/2}$	279453		288914	288256 [13]
Ge^{3+}	$[3d^{10}4s_{1/2}]_{1/2}$	$\rightarrow$	$[3d^{10}]_0$	361647	368701		
Sn^{3+}	$[4d^{10}5s_{1/2}]_{1/2}$	$\rightarrow$	$[4d^{10}]_0$	319217	328550		
Pb^{3+}	$[5d^{10}6s_{1/2}]_{1/2}$	$\rightarrow$	$[5d^{10}]_0$	329971	341350		
Uuq^{3+}	$[6d^{10}7s_{1/2}]_{1/2}$	$\rightarrow$	$[6d^{10}]_0$	362456		375649	373208 [13]

Table 3: Calculated resonance excitation energies (in eV) and oscillator strengths for Zn, Cd, Hg and Uub in the charge states 0 to 4+. (L: length gauge, V: velocity gauge)

				Transition energies		Oscillator strengths		
Elements	Transitions			Our calc.	Expt.[8]	L	V	Expt.
Zn	$[3d^{10}4s^2]_0$	$\rightarrow$	$[3d^{10}4s_{1/2}4p_{1/2}]_1$	4.05	4.03	1.84×10^{-4}	4.69×10^{-4}	
Cd	$[4d^{10}5s^2]_0$	$\rightarrow$	$[4d^{10}5s_{1/2}5p_{1/2}]_1$	3.67	3.80	1.20×10^{-3}	1.85×10^{-3}	$(2.00 \pm 0.003) \times 10^{-3}$ [a]
Hg	$[5d^{10}6s^2]_0$	$\rightarrow$	$[5d^{10}6s_{1/2}6p_{1/2}]_1$	4.76	4.89	2.25×10^{-2}	1.59×10^{-2}	$(2.37 \pm 0.08) \times 10^{-2}$ [b]
Uub	$[6d^{10}7s^2]_0$	$\rightarrow$	$[6d^{10}7s_{1/2}7p_{1/2}]_1$	6.57		9.24×10^{-2}	3.42×10^{-2}	
Zn^+	$[3d^{10}4s]_{1/2}$	$\rightarrow$	$[3d^{10}4p_{1/2}]_{1/2}$	5.75	6.01	6.48×10^{-1}	5.88×10^{-1}	
Cd^+	$[4d^{10}5s]_{1/2}$	$\rightarrow$	$[4d^{10}5p_{1/2}]_{1/2}$	5.16	5.47	6.64×10^{-1}	5.92×10^{-1}	
Hg^+	$[5d^{10}6s]_{1/2}$	$\rightarrow$	$[5d^{10}6p_{1/2}]_{1/2}$	6.11	6.38	6.09×10^{-1}	5.21×10^{-1}	
Uub^+	$[6d^4_{3/2}6d^5_{5/2}7s^2]_{5/2}$	$\rightarrow$	$[6d^4_{3/2}6d^4_{5/2}7s^27p_{1/2}]_{7/2}$	5.46		1.04×10^{-4}	5.94×10^{-3}	
Zn^{2+}	$[3d^{10}]_0$	$\rightarrow$	$[3d^4_{3/2}3d^5_{5/2}4p_{3/2}]_1$	15.88	17.37	5.00×10^{-3}	6.80×10^{-3}	
Cd^{2+}	$[4d^{10}]_0$	$\rightarrow$	$[4d^4_{3/2}4d^5_{5/2}5p_{3/2}]_1$	16.75	17.20	2.71×10^{-2}	2.98×10^{-2}	
Hg^{2+}	$[5d^{10}]_0$	$\rightarrow$	$[5d^4_{3/2}5d^5_{5/2}6p_{3/2}]_1$	13.85	14.71	5.38×10^{-2}	6.65×10^{-2}	
Uub^{2+}	$[6d^4_{3/2}6d^4_{5/2}7s^2]_4$	$\rightarrow$	$[6d^4_{3/2}6d^4_{5/2}7s_{1/2}7p_{3/2}]_4$	6.36		8.22×10^{-2}	3.58×10^{-2}	
Zn^{3+}	$[3d^4_{3/2}3d^5_{5/2}]_{5/2}$	$\rightarrow$	$[3d^4_{3/2}3d^4_{5/2}4p_{1/2}]_{7/2}$	23.02		1.62×10^{-4}	1.15×10^{-3}	
Cd^{3+}	$[4d^4_{3/2}4d^5_{5/2}]_{5/2}$	$\rightarrow$	$[4d^4_{3/2}4d^4_{5/2}5p_{1/2}]_{7/2}$	20.53	21.37	4.26×10^{-4}	1.92×10^{-3}	
Hg^{3+}	$[5d^4_{3/2}5d^5_{5/2}]_{5/2}$	$\rightarrow$	$[5d^4_{3/2}5d^4_{5/2}6p_{1/2}]_{7/2}$	15.79		2.23×10^{-3}	4.88×10^{-3}	
Uub^{3+}	$[6d^4_{3/2}6d^5_{5/2}]_{5/2}$	$\rightarrow$	$[6d^4_{3/2}6d^3_{5/2}7s_{1/2}7p_{1/2}]_{3/2}$	8.73		7.85×10^{-2}	4.47×10^{-2}	
Zn^{4+}	$[3d^4_{3/2}3d^4_{5/2}]_4$	$\rightarrow$	$[3d^4_{3/2}3d^3_{5/2}4p_{1/2}]_4$	34.23		2.48×10^{-2}	3.28×10^{-2}	
Cd^{4+}	$[4d^4_{3/2}4d^4_{5/2}]_4$	$\rightarrow$	$[4d^4_{3/2}4d^3_{5/2}5p_{1/2}]_4$	26.77		8.44×10^{-2}	1.10×10^{-1}	
Hg^{4+}	$[5d^4_{3/2}5d^4_{5/2}]_4$	$\rightarrow$	$[5d^4_{3/2}5d^3_{5/2}6p_{1/2}]_4$	20.09		7.06×10^{-2}	1.20×10^{-1}	
Uub^{4+}	$[6d^4_{3/2}6d^4_{5/2}]_4$	$\rightarrow$	$[6d^4_{3/2}6d^3_{5/2}6p_{1/2}]_4$	10.97		7.53×10^{-3}	5.29×10^{-2}	

[a] Reference [15]; [b] Reference [16].

Table 4: Resonance excitation energies (in cm^{-1}) and oscillator strengths for Pb and Uuq from $(n-1)d^{10}ns^2np(n+1)s$ to $(n-1)d^{10}ns^2np^2$. (n= 6, 7 for Pb and Uuq, respectively. L: length gauge, V: velocity gauge)

		Excitation energies				Oscillator strengths	
Elements	Transitions	Our calc.	Expt.[8]	Ref.[11]	Ref.[13]	L	V
Pb	$[5d^{10}6s^2 6p_{1/2}7s_{1/2}]_0 \rightarrow [5d^{10}6s^2 6p_{1/2}6p_{3/2}]_1$	25898	27141	26833	26874	2.79×10^{-1}	3.71×10^{-1}
	$[5d^{10}6s^2 6p_{1/2}7s_{1/2}]_1 \rightarrow [5d^{10}6s^2 6p^2_{1/2}]_0$	34458	35287	34239	34711	1.96×10^{-1}	2.02×10^{-1}
	$[5d^{10}6s^2 6p_{1/2}7s_{1/2}]_1 \rightarrow [5d^{10}6s^2 6p_{1/2}6p_{3/2}]_1$	26578	27468	26275	27180	1.35×10^{-1}	1.48×10^{-1}
	$[5d^{10}6s^2 6p_{1/2}7s_{1/2}]_1 \rightarrow [5d^{10}6s^2 6p_{1/2}6p_{3/2}]_2$	23242	24637	23453	24404	5.37×10^{-1}	6.54×10^{-1}
	$[5d^{10}6s^2 6p_{1/2}7s_{1/2}]_1 \rightarrow [5d^{10}6s^2 6p^2_{3/2}]_2$	12269	13829	12580	13858	3.22×10^{-2}	1.10×10^{-1}
	$[5d^{10}6s^2 6p_{3/2}7s_{1/2}]_2 \rightarrow [5d^{10}6s^2 6p_{1/2}6p_{3/2}]_1$	39396	40369		39883	2.61×10^{-1}	2.74×10^{-1}
	$[5d^{10}6s^2 6p_{3/2}7s_{1/2}]_2 \rightarrow [5d^{10}6s^2 6p_{1/2}6p_{3/2}]_2$	36060	37538		37107	6.24×10^{-1}	5.87×10^{-1}
	$[5d^{10}6s^2 6p_{3/2}7s_{1/2}]_2 \rightarrow [5d^{10}6s^2 6p^2_{3/2}]_2$	25086	26731		26561	5.00×10^{-1}	3.69×10^{-1}
	$[5d^{10}6s^2 6p_{3/2}7s_{1/2}]_1 \rightarrow [5d^{10}6s^2 6p^2_{1/2}]_0$	48855	49440		48682	1.10×10^{-3}	4.58×10^{-3}
	$[5d^{10}6s^2 6p_{3/2}7s_{1/2}]_1 \rightarrow [5d^{10}6s^2 6p_{1/2}6p_{3/2}]_1$	40976	41620		41151	3.80×10^{-2}	3.70×10^{-2}
	$[5d^{10}6s^2 6p_{3/2}7s_{1/2}]_1 \rightarrow [5d^{10}6s^2 6p_{1/2}6p_{3/2}]_2$	37640	38789		38375	3.95×10^{-2}	6.94×10^{-2}
	$[5d^{10}6s^2 6p_{3/2}7s_{1/2}]_1 \rightarrow [5d^{10}6s^2 6p^2_{3/2}]_2$	26666	27982		27829	8.41×10^{-1}	9.13×10^{-1}
	$[5d^{10}6s^2 6p_{3/2}7s_{1/2}]_1 \rightarrow [5d^{10}6s^2 6p^2_{3/2}]_0$	16702	19973		19423	1.98×10^{-1}	4.85×10^{-1}
Uuq	$[6d^{10}7s^2 7p_{1/2}8s_{1/2}]_0 \rightarrow [6d^{10}7s^2 7p_{1/2}7p_{3/2}]_1$	13410		16769	17122	3.06×10^{-1}	4.26×10^{-1}
	$[6d^{10}7s^2 7p_{1/2}8s_{1/2}]_1 \rightarrow [6d^{10}7s^2 7p^2_{1/2}]_0$	39725		43243	43441	1.48×10^{-1}	2.01×10^{-1}
	$[6d^{10}7s^2 7p_{1/2}8s_{1/2}]_1 \rightarrow [6d^{10}7s^2 7p_{1/2}7p_{3/2}]_1$	13915		17436	17099	1.57×10^{-1}	1.84×10^{-1}
	$[6d^{10}7s^2 7p_{1/2}8s_{1/2}]_1 \rightarrow [6d^{10}7s^2 7p_{1/2}7p_{3/2}]_2$	10162		14852	14458	0.54	1.24
	$[6d^{10}7s^2 7p_{1/2}8s_{1/2}]_1 \rightarrow [6d^{10}7s^2 7p^2_{3/2}]_2$	-23264		-16018	-17515	6.91×10^{-3}	1.94×10^{-3}
	$[6d^{10}7s^2 7p_{3/2}8s_{1/2}]_2 \rightarrow [6d^{10}7s^2 7p_{1/2}7p_{3/2}]_1$	51182			53131	2.41×10^{-1}	3.06×10^{-1}
	$[6d^{10}7s^2 7p_{3/2}8s_{1/2}]_2 \rightarrow [6d^{10}7s^2 7p_{1/2}7p_{3/2}]_2$	47429			50490	3.40×10^{-1}	4.23×10^{-1}
	$[6d^{10}7s^2 7p_{3/2}8s_{1/2}]_2 \rightarrow [6d^{10}7s^2 7p^2_{3/2}]_2$	14003			18517	7.55×10^{-1}	9.87×10^{-1}
	$[6d^{10}7s^2 7p_{3/2}8s_{1/2}]_1 \rightarrow [6d^{10}7s^2 7p^2_{1/2}]_0$	85332			80455	1.24×10^{-2}	3.00×10^{-3}
	$[6d^{10}7s^2 7p_{3/2}8s_{1/2}]_1 \rightarrow [6d^{10}7s^2 7p_{1/2}7p_{3/2}]_1$	59522			54113	3.36×10^{-2}	3.25×10^{-2}
	$[6d^{10}7s^2 7p_{3/2}8s_{1/2}]_1 \rightarrow [6d^{10}7s^2 7p_{1/2}7p_{3/2}]_2$	55769			51472	9.24×10^{-2}	1.40×10^{-1}
	$[6d^{10}7s^2 7p_{3/2}8s_{1/2}]_1 \rightarrow [6d^{10}7s^2 7p^2_{3/2}]_2$	22343			19499	1.15	0.65
	$[6d^{10}7s^2 7p_{3/2}8s_{1/2}]_1 \rightarrow [6d^{10}7s^2 7p^2_{3/2}]_0$	13256			12638	2.34×10^{-1}	6.34×10^{-1}

(RIS) technique.

Acknowledgement

This work was supported by the National Natural Science Foundation of China (Grant No.10434100, 10774122), the Core-University Program between Japanese Society of Promotion of Science and Chinese Academy of Sciences, the Specialized Research Fund for the Doctoral Program of Higher Education of China (Grant No. 20070736001), the Foundation of Center of theoretical Nuclear Physics of National Laboratory of Heavy Ion Accelerrator of Lanzhou, and the Foundation of Northwest Normal University(NWNU-KJCXGC-03-21).

References

[1] M. Schädel, J. Nucl. Radiochim. Sci. **3**, 113 (2002).
[2] M. Sewtz, H. Backe, A. Dretzke, et al., Phys. Rev. Lett. **90**, 163002 (2003).
[3] V. Pershina and B. Fricke, in *Heavy Elements and Related New Phenomena* (World Scientific, New Jersey,1999), Vol.1, p. 194.
[4] V. Pershina, T. Bastug, T. Jacob, et al., Chem. Phys. Lett. **365**, 176 (2002).
[5] V. Pershina, J. Anton, B. Fricke, J. Chem. Phys. **127**, 134310 (2007)
[6] F. A. Parpia, C. F. Fischer, I. P. Grant, Comput. Phys. Commun. **94**, 249 (1996).
[7] R. D. Cowan, *The theory of atomic structure and spectra.* (University of California Press, Berkeley, 1981).
[8] C. E. Moore, Atomic Energy Levels (II,III). Natl. Bur. Stand. (U.S.) Cire. (U.S. GPO. Washington DC,1971).
[9] E. Eliav, U. Kaldor, Y. Ishikawa, et al., Phys. Rev. A **52**, 2765 (1995).
[10] B. Fricke, W. Greiner, J. T. Waber, Theoret. Chim. Acta **21**, 235 (1971).
[11] V. A. Dzuba, V. V. Flambaum, P. G. Silvestrov, et al., Phys. Rev. A **44**, 2828 (1991).
[12] C. S. Nash, J. Phys. Chem. **109**, 3493 (2005).
[13] A. Landau, E. Eliav, Y. Ishikawa, et al., J. Chem. Phys. **114**, 2977 (2001).
[14] O. L. Keller, J. L. Burnett, T. A. Carlson, et al., J. Phys. Chem. **74**, 1127 (1970).
[15] F. W. Jr. Byron, M. N. McDermott, R. Novick, Phys. Rev. **134**, 615 (1964).
[16] J. A. Halstead, R. R. Reeves, J. Quant. Spectrosc. Radiat. Transfer **28**, 289 (1982).
[17] E. Johnson, B. Fricke, T. Jacob, et al., J. Chem. Phys. **116**, 1862 (2002).
[18] E. Johnson, B. Fricke, et al., J.Chem. Phys. **93**, 8041 (1990).
[19] Y. J. Yu, J. G. Li, C. Z. Dong, et al., Eur. Phys. J. D **44**, 51 (2007).
[20] Y. J. Yu, C. Z. Dong, J. G. Li, et al., J.Chem. Phys. (accepted).
[21] S. Fritzsche, C. Z. Dong, F. Koike, et al., Eur. Phys. J. D **45**, 107 (2007).

Investigation of the High-order Harmonic Generation and Ionization of Model Hydrogen Atom and Real Hydrogen Atom in Intense Laser Field

Songfeng Zhao[1], Xiaoxin Zhou [1,2] and Cheng Jin[1]

1) College of Physics and Electronic Engineering, Northwest Normal University, Lanzhou, 730070, China
2) Center of Theoretical Nuclear Physics, National Laboratory of Heavy Ion Accelerator of Lanzhou, Lanzhou 730000, China

e-mail: zhouxx@nwnu.edu.cn

Abstract

Solving time-dependent Schrödinger equation numerically, we investigate the high-order harmonic generation and ionization probability of one dimensional, two dimensional and three dimensional hydrogen atom exposed to intense laser field. In the tunneling ionization regime, our results show that the HHG plateau features and cutoff positions of model hydrogen atoms are well agreement with those of real hydrogen atom, and the trend of changing of the ionization probabilities with time is similar, but the values of ionization probabilities for model atoms are different from ones for three dimensional hydrogen atom. We explain the reason for the difference of ionization probabilities between model atoms and real hydrogen atom according to the semiclassical three-step model.

Keywords: intense laser field, high-order harmonic generation, ionization probability.

1.Introduction

High order harmonic generation(HHG) is a topic of great interest because of its potential applications for a coherent high frequency EUV radiation[1], a coherent soft x-ray source[2] and the generation of attosecond pulses[3].

HHG can be investigated by solving three dimensional time-dependent Schrödinger equation numerically, however, it is very time-consuming[4]. So people use one dimensional model atom[5, 6] and two dimensional model atom[7] instead of three dimensional real atom to escape huge calculations. Rae et al[8] have compared HHG by one dimensinal model hydrogen atom with results by real hydrogen atom, however, there is no report about the differences of HHG from two dimensional model atom and real atom subjected to an intense laser field. In this paper, we study the differences of HHG spectra from two dimensional model hydrogen atom and real hydrogen atom by solving time-dependent Schrödinger equation numerically.

2. Theoretical method

In the length gauge, the TDSE of hydrogen atom in the presence of linearly polarized laser field can be written as (in atomic units)

$$i\frac{\partial}{\partial t}\psi(t) = \hat{H}\psi(t) \tag{1}$$

The Hamiltonian of one dimensional hydrogen atom as such

$$\hat{H} = -\frac{1}{2}\frac{\partial^2}{\partial x^2} - \frac{1}{\sqrt{0.5 + x^2}} - xE(t) \tag{2}$$

The Hamiltonian of two dimensional hydrogen atom is

$$\hat{H} = -\frac{1}{2}\frac{\partial^2}{\partial x^2} - \frac{1}{2}\frac{\partial^2}{\partial y^2} - \frac{1}{\sqrt{0.64 + x^2 + y^2}} - xE(t) \tag{3}$$

The Hamiltonian of three dimensional hydrogen atom as follow

$$\hat{H} = -\frac{1}{2}\frac{\partial^2}{\partial r^2} + \frac{\hat{L}^2}{2r^2} - \frac{1}{r} - zE(t) \tag{4}$$

The time-dependent wave function is determined by solving Equation(1) with the second-order split-operator method.

According to the Ehrenfest's theorem, the time-dependent induced dipole acceleration is given by

$$d_A(t) = \langle\psi(t)|\frac{d^2}{dt^2}|\psi(t)\rangle \tag{5}$$

and the HHG power spectra can be determined by

$$P_A(\omega) = \left|\frac{1}{t_f - t_i}\frac{1}{\omega^2}\int_{t_i}^{t_f} d_A(t)e^{-i\omega t}dt\right|^2 \tag{6}$$

The ionization probability of hydrogen atom can be calculated with the normalization of the time-dependent wave function

$$I(t) = 1 - \langle\psi(t)|\psi(t)\rangle \tag{7}$$

In this work, the electric field of the laser pulse is given by

$$E(t) = \begin{cases} E_0 \sin^2\left(\frac{\pi t}{6T}\right)\sin\omega t & 0 \le t \le 3T \\ E_0 \sin\omega t & t \ge 3T \end{cases} \tag{8}$$

3. Results and discussion

In the tunneling ionization regime, we calculate the HHG power spectra and the ionization probability of three kinds of atoms in the presence of an intense laser field, corresponding to the laser parameters: intensity of electric field is $1.26 \times 10^{14} W/cm^2$, and central wavelength is 908nm. Figure 1 show the HHG power spectra from model hydrogen atoms and real hydrogen atom. All the HHG spectra show a typical feature, namely the first few orders harmonics decline, then exhibit a broad plateau with almost constant intensity for many harmonics, and finally the intensity of high harmonics decrease sharply at cutoff. One can see that the HHG plateau features and cutoff positions of model hydrogen atoms are well agreement with those of real hydrogen atom. Figure 2 show the variation of ionization probability with the time (in units of T). We can see that the trend of changing of the ionization probabilities with time is similar, but the values of ionization probabilities for the model atoms are different from ones for three dimensional hydrogen atom. To explain the difference of ionization probabilities of model hydrogen atoms and real hydrogen atom, The semiclassical three-step model[9] is adopted. According to the simpleman model, firstly the electron tunnels through the barrier formed by Coulomb potential and the laser field, then it oscillates quasifreely drived by the Lorenz force and acquires additional kinetic energy, finally it can recombine with the parent ion and emit a harmonic photon. The highest harmonic energy is $I_p + 3.17U_p$, where U_p is the ponderomotive energy and I_p is the ionization potential. In one dimensional case, the electron can move only along x axis (the direction of polarization). In two dimensional case, the electron can not only move along x axis (the direction of polarization), but also along y axis. In three dimensional case, the electron can not only move along z axis (the direction of polarization), but also along x axis and z axis. According to quantum mechanism, the probability of electron lies in the whole space is 1, and so the probability of electron move along the polarized direction is highest in one dimensinal case, smaller in two dimensional case, and smallest in three dimensional case. Therefore, the ionization probability of one dimensional atom is largest, then smaller in two dimensional case, and smallest in three dimensional case.

4. Conclusion

By solving time-dependent Schrödinger equation numerically, we investigate the high-order harmonic generation and ionization probability of one dimensional, two dimensional and three dimensional hydrogen atom exposed to intense laser field. In the tunneling ionization regime, our results show that the HHG plateau features and cutoff positions of model hydrogen atoms are well agreement with those of real hydrogen atom, and the trend of changing of the ionization probabilities with time is similar, but the values of ionization probabilities for the model atoms are different from ones for three dimensional hydrogen atom because of the different momentum distributions of the elec-

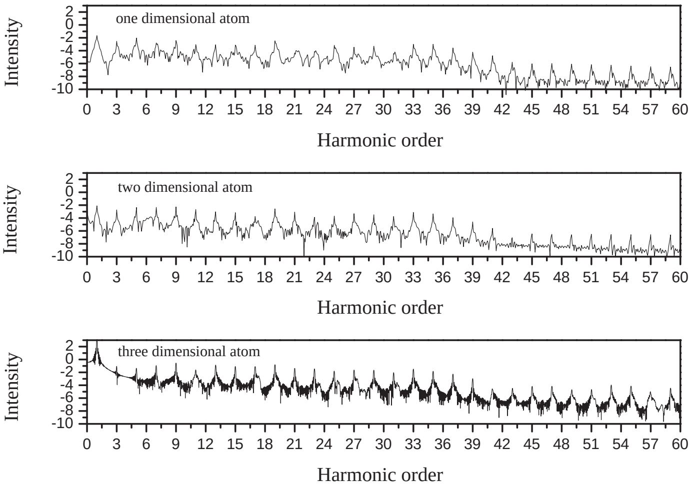

Figure 1: The high-order harmonic power spectra from hydrogen atom exposed to an intense laser field (in the tunneling ionization regime).

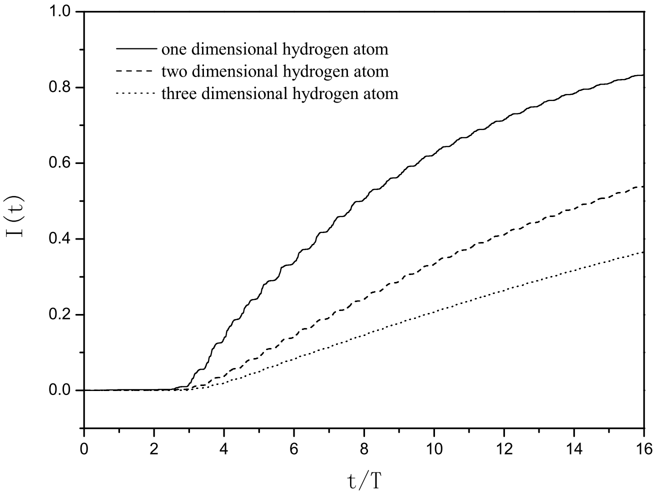

Figure 2: The ionization probability of hydrogen atom subjected to an intense laser field (in the tunneling ionization regime).

tron.

Acknowledgement

This work is supported by the National Natural Science Foundation of China(Grant No.10274063) and by the Foundation of Science and Technology Research of the Mininstry of Education of China (Grant No.03126)

References

[1] R. A. Bartels, A. Paul, H. Green et al, Science**297**, 376 (2002).
[2] T. Shiraishi, M. Mori and K. Kondo, Phys. Rev. A **65**, 045201 (2002).
[3] P. Agostini and L. F. Dimauro, Rep. Prog.Phys. **67**, 813 (2004).
[4] K. C. Kulander et al, Atoms in Intense Laser Fields,(Academic, New York,1992) 247
[5] J. H. Eberly, Q. Su and J. Javanainen, Phys. Rev. Lett.**62**, 881 (1989).
[6] X. X. Zhou, C. D. Lin, Phys. Rev. A **61** 053411 (2000)
[7] M. Protopapas, D. G. Lappas and P. L. Knight, Phys. Rev.Lett. **79**, 4550 (1997).
[8] S. C. Rae, X. Chen and K. Burnett, Phys. Rev. A **50**,1946(1994).
[9] P. B. Corkum, Phys. Rev. Lett. **71**, 1994 (1993).

RESONANCE PROCESS OF Co-, Ni-, AND Cu-LIKE IONS

Chen Chong-Yang[1,2], Meng Fan-Chang[1,2], Shen Tian-Ming[1,2], Zhang Yang[1,2], Wang Yan-Sen[1,2], Zou Ya-Ming[1,2]

[1] Shanghai EBIT lab, Modern Physics Institute, Fudan University, Shanghai 200433
[2] The Key lab of Applied Ion Beam Physics (Ministry of Education), Fudan University, Shanghai 200433

Theoretical investigations of resonance excitation (RE) and dielectronic recombination (DR) of Co-, Ni, and Cu-like ions are presented employing relativistic multi-confiugration distorted-wave approximation. The basic atomic data such as energy levels, radiative rates and Auger rates involved in presen work are obtained from the Flexible Atomic Code [1].

Ab initio calculation of the total DR rate coefficient from the ground state and the first excited state of Co-like gold is performed [2]. The DR contributions are explicitly taken into account from the relevant complexes of Ni-like ion: $3d^3_{3/2}3d^6_{5/2}n'l'$, $3p^5 3d^{10}n'l'$, $3s3p^6 3d^{10}n'l'$, $3d^8 4ln'l'$, $3p^5 3d^9 4ln'l'$ and $3s3p^6 3d^9 4ln'l'$ with $n' \leq 25$, and $3d^8 5ln'l'$ with $n' \leq 9$. The contributions from higher complex are evaluated by extrapolation procedure. The DR contributions mainly come from complex series $3d^8 4ln'l'$ and $3p^5 3d^9 4ln'l'$. The complex series $3p^5 3d^{10}n'l'$ and $3d^8 5ln'l'$ also contribute significantly to the total DR rates at low and high electron temperature, respectively. The possible important decays into autoionizing levels followed by radiative cascade (DAC) from the resonant levels are taken into account as well as the resonant stabilizing and non-resonant stabilizing transitions. The inclusion of DAC transitions enlarge the total DR rate coefficients by a factor about 10% and may break down the usual n'^{-3} scaling law of the partial DR rates along some complex series. To evaluate the high contributions from these complex series, the level-by-level extrapolation method is developed to include DAC effects. The total DR rate coefficients are fitted to an empirical formula.

The detailed and large-scale calculations on the resonant excitation rate coefficients from the ground state to the 106 fine-structure levels belonging to $3l^{17}4l' (l = 0, 1, 2; l' = 0, 1, 2, 3)$ configurations of Ni-like ions Gd^{36+}, Ta^{45+}, and W^{46+} have been performed [3]. The contributions through all possible Cu-like doubly excited states $3l^{17}4l'n''l''$ and $3l^{17}5l'n''l'' (n'' \leq 15,\ l'' \leq 8)$ are explicitly calculated. The validity of n''^{-3} scaling law is investigated. The contributions from resonant excitation are found to be as important as direct excitation processes for most transitions. In some cases, the resonant excitation can enhance the excitation rate coefficients by an order of magnitude. Large discrepancies between the present resonant excitation rate coefficients with previously published values are found, and the present results should be more reliable and accurate.

The effects of configuration interaction on dielectronic recombination of Cu-like gold ions through the $3d + e \rightarrow 4l'4l''$ capture process are studied in the models of isolated configurations approximation, configuration mixing within $3d^9 4s4l'4l''$, and configuration mixing within $3d^9 4l4l'4l'' (l \geq 0)$ [4]. Nonresonant raditive stabilizing transitions and decays to autoionizing levels followed by radiative cascades, as well as resonant stabilizing transitions from the resonant levels, are taken into account. The additional mixing with $3d^9 4l4l'4l'' (0 < l \leq l' \leq l'' \leq 3)$ shift slightly the peaks of cross section towards low energy. The rate coefficient at low temperature is dramatically changed. And the rate coefficient at temperature above 100eV is enhanced by a factor between 26% and 13%.

References

[1] M. F. Gu, Astrophys. J. **582**, 1241(2003)

[2] F. C. Meng *et al*, J. Phys. B **40**, 4269(2007)

[3] T. M. Shen *et al*, Phys. Rev. A **76**, 022703 (2007); Chin. Phys. Lett. **24**, 925(2007); J. Phys. B **40**, 3075(2007)

[4] F. C. Meng *et al*, Chin. Phys. Lett. **24**, 3404(2007)



JSPS-CAS Core University Program Seminar
The 2nd China-Japan Joint Seminar on Atomic and Molecular Processes in Plasma (AMPP)

Scientific Program

(Sessions 8-11 are organized as “Technical Workshop on Plasma Simulations and Diagnostics”)

➢Monday, October 8: Welcome

08:30 – 18:00 Arrival and Registration

18:00 – 19:30 Welcome Reception

➢Tuesday, October 9: Sessions 1-4

07:00 – 08:10 Breakfast

08:30 – 09:10 Opening Remarks (Chair: Prof. Chenzhong Dong)

i. Yulong Sun, Mayor of Dunhuang City.

ii Limin Wang, President of Northwest Normal University, China

iii Baonian Wan, Coordinator of the Core University Program

iv F. Koike, Representative of AMPP 2007

v Taking Photo for all participants

09:20 – 10:40 Session 1 (Chair: Prof. M. Kimura)

1. Short wavelength photon sources and atoms and ions
   E. Kennedy, Dublin City University, Ireland
2. One and two color photoionization experiments with laser plasma and free electron laser EUV light source
   J. Costello, Dublin City University, Ireland

10:40 – 11:00 Coffee Break

11:00 – 12:20 Session 2 (Chair: Prof. B. Fricke)

3. Similarities and differences between electron and positron scatterings from molecules: inelastic processes and resulting fragmentations
   M. Kimura, Kyushu University, Japan
4. Spectroscopy and dynamics of ion by XUV laser and velocity mapping imaging method
   Yuxiang Mo, Tsinghua University, China

12:20 – 14:10 Lunch Break

14:30 – 16:30 Session 3 (Chair: Prof. Xinwen Ma)

5. X-ray imaging and Compton polarimetry of atomic transitions in heavy ions
   T. Stöhlker, GSI, Germany
6. Theoretical study of EUVL-emissions from 4d open-shell atomic ions of heavy ion plasmas and charge transferred excited states
   F. Koike, Kitasato University, Japan
7. Dynamic behaviors for valence excitation processes of noble atoms studied by fast electron impact
   Linfan Zhu, University of Science and Technology of China, China

16:30 – 16:50 Coffee Break

16:50 – 18:10 Session 4 (Chair: Prof. T. Stöhlker)

8. Non-equilibrium and anisotropic K-shell radiation in ultra-intense laser-produced plasmas

T. Kawamura, Tokyo Institute of Technology, Japan

9. Analysis and simulation of XUV/EUV spectra of laser-produced Au, I and Sn plasmas

Maogen Su, Northwest Normal University, China

18:10 – 20:00 Conference Banquet

➢Wednesday, October 10: Session 5 - 7

07:00 – 8:10 Breakfast

08:30 – 10:30 Session 5 (Chair: Prof. E. Kennedy)

10. Spectroscopy of atoms and ions under external confinement

B. Fricke, Kassel University, Germany

11. State-selective charge transfer for keV ions impact on two electron target studied by coltrims

Xinwen Ma, Institute of Modern Physics, Chinese Academy of Sciences, China

12. Spectroscopy of highly charged ion with an EBIT

H. Sakaue, NIFS, Japan

10:30 – 10:50 Coffee Break

10:50 – 12:10 Session 6 (Chair: Prof. J. Costello)

13. Electron stereodynamics in Coulomb explosion of molecules by slow highly charged ions

A. Ichimura, Institute of Space and Astronautical Science, Japan Aerospace Exploration Agency, Japan

14. Analysis of D_α (H_α) spectra emitted in front of the limiter in HT-7

Wan Baonian, Juan Huang, Institute of Plasma Physics, Chinese Academy of Sciences, China

12:10 – 14:10 Lunch Break

14:00 – 16:00 Session 7 (Chair: Prof. Chongyang Chen)

15. Correlated relativistic dynamics and nuclear effects in dielectronic and visible spectra of highly charged ions

Z. Harman, Max Planck Institute for Nuclear Physics, Germany

16. Atomic properties from high-resolution Laser spectroscopy

Wei-guo Jin, Toho University, Japan

17. Theoretical study on KLL Dielectronic Recombination of highly charged ions

Denghong Zhang, Northwest Normal University, China

16:00 – 18:00 Visiting Dunghuang City

18:00 – 20:00 Dinner with Local Dishes

Technical Workshop on Plasma Simulations and Diagnostics

➢Thursday, October 11: Session 8 – 11

07:00 – 08:10 Breakfast

08:30 – 10:30 Session 8 (Chair: Prof. N. Nakamura)

18. Storage and cooling of ions in an electrostatic ring

H. Tanuma, Tokyo Metropolitan University

19. Resonance process of Co-, Ni- and Cu-Like Ions

Chongyang Chen, Fudan University, China

20. Production of nanometer sized charged particle beams with glass capillary

T. Ikeda, RIKEN, Japan

10:30 – 10:50 Coffee Break

10:50 – 12:10 Session 9 (Chair: Prof. Linfan Zhu)

21. Sub-shell excitations of rare gas atoms by electron impact

Y. Sakai, Toho University

22. Ab initio design of laser pulses for controlling photochemical reactions

Shiyang Zou, Institute of Applied Physics and Computational Mathematics, Beijing

12:10 – 14:10 Lunch Break

14:30 – 16:30 Session 10 (Chair: Prof. Yuxiang Mo)

23. Resonant processes in electron-highly charged ion collisions observed with the Tokyo electron beam ion trap

N. Nakamura, The Univ. of Electro-Communications, Japan

24. An investigation on the laser-induced breakdown spectroscopy of the liquid jet

Zhifeng Cui, Anhhui Normal University, China

25. Ab Initio study of charge transfer processes in ion-atom collisions at low to Intermediate energies

Yong Wu, Institute of Applied Physics and Computational Mathematics, China

16:30 – 16:50 Coffee Break

16:50 – 18:30 Session 11 (Chair: Dr. A. Ichimura)

26. Constructions of non-equilibrium plasma model for applications to laboratory and solar plasmas

N. Yamamoto, Osaka University, Japan

27. Calculations of electron impact excitation cross section related with plasmas

Luyou Xie, Northwest Normal University, China

28. Scattered electron-ion coincidence measurements for the study of dissociative ionization processes

K. Yamamoto, Toho University, Japan

18:30 – 18:50 Closing Remarks (Chair: Dr. Koike)

18:50 – 20:00 Conference Dinner

20:30 – 22:00 Local Dance about Dunhuang

➢Friday, October 12: Session 12

➢Saturday, October 13: Adjourn

ℵ Monday, October 8 through Thursday, October 11: Posters

1. Shake Up Processes in the 3d Photoionization of Sr I and the Subsequent Auger Decay
   Xiaobin Ding, Chenzhong Dong, G O'Sullivan, P Hayden, L Gaynor
2. Dielectronic Recombination of Sn^{5+} ~ Sn^{13+} Ions
   Yanbiao Fu, Chenzhong Dong, Maogen Su, Gerry O'Sullivan
3. Study on the Properties of Rydberg States of Lithium in a Static Electric Field by B-spline Functions
   Yonglin He, Xiaoxin Zhou and Xiaoyong Li
4. Electron Correlation effects on the Hyperfine Induced $^{47}Ti^{18+}$ ($2s2p\ ^3P_0$ - $2s^2\ ^1S_0$) Transition Probability
   Jiguang Li, Gediminas Gaigalas, Chenzhong Dong
5. Effects of the Model Potential on Two-color Multiphoton Ionization of Atoms by an Intense Laser Field and One of Its Harmonics
   P.C. Li, and X.X. Zhou
6. Relaxation Effects on Photoionization Processes of Lithium
   Cuicui Sang, Jianjie Wan, Chenzhong Dong, Xiaobin Ding, and Jun Jiang
7. Theoretical Calculation of Photoionization Cross Sections for Ions N^{2+}, N^{3+}, O^{3+}, O^{4+} and F^{4+}
   Guoli Wang and Xiaoxin Zhou
8. Study on the Characteristic of Lightning Discharge Plasmas
   Ping Yuan, Jie Wang, Xiaozhi Shen, Huaming Zhang, Yuhua Ouyang,
   Xueyan Zhao, Yixiao Guo and Hongzhen Qiao
9. Radiative Electron Capture in Collisions of Li-like Uranium Ions with N_2 Targets
   Jianjie Wan, Yongjun Wang, Xiaobin Ding, Chenzhong Dong, Xinwen Ma,
   Jacek Rzadkiewicz, Thomas Staehlker and Stephan Fritzsche
10. Theoretical Study on Low-lying Level Structures and Excited States Properties of the Super-heavy Elements Uub(Z=112) and Uuq(Z=114)
    Youjun Yu, Jiguang Li, Chenzhong Dong, Xiaobing Ding
11. Investigation of the High-order Harmonic Generation and Ionization of Model Hydrogen Atom and Real Hydrogen Atom in Intense Laser Field
    Songfeng Zhao, Xiaoxin Zhou and Cheng Jin

List of Participants

Name	Affiliation	e-mail
Chongyang Chen	Fudan University, China	chychen@fudan.edu.cn
John Costello	Dublin City University, Ireland	john.costel1o@dcu.ie
Zhifeng Cui	Anhhui Normal University, China	zfcui@mail.ahnu.edu.cn
Burkhard Fricke	University of Kassel, Gemany	fricke@physik.uni-kassel.de
Yanbiao Fu	Northwest Nomal University, China	fuyb@nwnu.edu.cn
Zoltan Haman	Max Planck Institute fuer Nuclear Physics Gemany	Zoltan.harman@mpi-hd.mpg.de
Juan Huang	Institute of Plasma Physics, Chinese Academy of Sciences, China	janejoy@ipp.ac.cn
Atsushi Ichimura	Institute of Space and Astronautical Science, Japan Aerospace Exploration	ichimura@isas.jaxa.jp
Tokihiro Ikeda	RIKEN, Japan	tokihiro@riken.jp
Weiguo Jin	Toho University, Japan	jin@ph.sci.toho-u.ac.jp
Tohru Kawamura	Tokyo Institute of Technology, Japan	kawamura@es.titech.ac.jp
Eugene Kennedy	Dublin City University, Ireland	Eugene.kemedy@dcu.ie
Mineo Kimura	Kyushu University, Japan	mineo.kimura@gmail.com
Fumihiro Koike	Kitasato University, Japan	koikef@kitasato-u.ac.jp
Xinwen Ma	Institute of Modern Physics, Chinese Academy of Sciences, China	x.ma@impcas.ac.cn
Nobuyuki Nakamura	The Univ.of Electro－Communications,	nakamu@ils.uec.ac.jp
Yuxiang Mo	Tsinghua University, China	ymo@mai1.tsinghua.edu.cn
Yasuhiro Sakai	Toho University, Japan	sakai@ph.sci.toho-u.ac.jp
Hiroyuki Sakaue	National Institute for Fusion Science, Japan	sakaue@nifs.ac.jp
Thomas Stoehlker	GSI, Gemany	T.stoehlker@gsi.de
Hajime Tanuma	Tokyo Metropolitan University, Japan	tanuma@phys.metro-u.ac.jp
Baonian Wan	Institute of Plasma Physics, Chinese Academy of Sciences, China	bnwan@ipp.ac.cn
Yong Wu	Institute of Applied Physicsand Computational Mathematics, China	wu_yong@iapcm.ac.cn
Luyou Xie	Northwest Normal University, China	xiely@nwnu.edu.cn
Norimasa	Osaka University, Japan	yamamoto.norimasa@nifs.ac.jp
Karin Yamamoto	Toho University, Japan	karin@ph.sci.toho-u.ac.jp
Linfn Zhu	University of Science and Technology of China, China	lfzhu@ustc.edu.cn
Shiyang Zou	Institute of AppIied Physics and Computational Mathematics, China	zou_shiyang@iapcm.ac.cn

List of Participants (continued)

Name	Affiliation	e-mail
Chenzhong Dong	Northwest Normal University, China	dongcz@nwnu.edu.cn
Zhimin Yang	Northwest Normal University, China	yangzm@nwnu.edu.cn
Xiaoxin Zhou	Northwest Normal University, China	zhouxx@nwnu.edu.cn
Hongshan Chen	Northwest Normal University, China	hschen@nwnu.edu.cn
Ping Yuan	Northwest Normal University, China	yuanp@nwnu.edu.cn
Denghong Zhang	Northwest Normal University, China	zhangdh@nwnu.edu.cn
Maogen Su	Northwest Normal University, China	sumg@nwnu.edu.cn
Jiguang Li	Northwest Normal University, China	Phys_ljg@yahoo.com.cn
Jun Jiang	Northwest Normal University, China	phyjiang@yeah.net
Jiaqjie Wan	Northwest Normal University, China	Jack_Wan1982@163.com
Guoli Wang	Northwest Normal University, China	Wanggl@nwnu.edu.cn
Xiaobin Ding	Northwest Normal University, China	dingxb@nwnu.edu.cn
Pengchen Li	Northwest Normal University, China	lipc@nwnu.edu.cn